Inverse Problems in Astronomical Imaging

by

Rachel Anne Johnston

Department of Electrical and Electronic Engineering

submitted in fulfilment of the requirements
for the degree of
Doctor of Philosophy

University of Canterbury, November 2000

Statement of Originality

This thesis contains no material which has been accepted for the award of any other degree or diploma in any tertiary institution. To the best of my knowledge and belief, the thesis contains no material previously published or written by another person, except when due reference is made in the text.

Rachel Johnston

Abstract

The imaging of astronomical objects is limited by atmospheric turbulence, which consists of layers of varying refractive index surrounding the earth. These refractive index fluctuations are a direct consequence of the warming and cooling of air and water vapour in the atmosphere. Wavefronts entering the atmosphere acquire phase distortions, which when propagated result in amplitude fluctuations known as scintillation. Hence the practical manifestation of the atmosphere is a degradation of the signals passing through it, for example it severely limits the resolution of images captured by ground-based telescopes.

A variety of solutions, or inverse problems, have been proposed and trialed in the attempt to obtain the best possible images from astronomical telescopes. An orbiting telescope (for example the Hubble space telescope) is one solution. In this case light is captured before it is distorted by the atmosphere. Less expensive ground-based solutions include the post processing of short exposure images and real-time compensation using adaptive optics, both of which are investigated in this thesis.

However, the success of an inverse problem lies in the accurate modelling of the processes that give rise to the corresponding forward problem, in this case the random refractive index fluctuations that characterise the atmosphere. Numerical simulation of atmospheric turbulence is achieved using phase screens in which the assumption of Kolmogorov statistics is often made. A previously presented method for modelling Kolmogorov phase fluctuations over a finite aperture, the midpoint displacement method, is both formalised and improved. This enables the accurate generation of atmospheric speckle images for the development and testing of post processing methods.

Another aspect of the forward problem is the accurate simulation of scintillation, resulting from the propagation of phase distorted wavefronts. Commonly used simulation methods achieve this by assuming periodic boundary conditions. A technique for the accurate modelling and simulation of scintillation from an aperiodic Kolmogorov phase screen is presented. The more physically justifiable assumption of smoothness is shown to result in a propagation kernel of finite extent. This allows the phase screen dimensions for an accurate simulation to be determined and truncation can then be used to eliminate the unwanted spectral leakage and diffraction effects usually inherent in the use of finite apertures.

Deconvolution methods are popular for the post processing of atmospheric speckle images to compensate for the effects of the atmosphere. Conventional deconvolution algorithms are applied when the distortion is known or well-characterised, whereas, blind deconvolution algorithms are used when the distortion is unknown. Conventional deconvolution techniques are not often directly applied to astronomical imaging problems as the distortion introduced by the atmosphere is unknown. However, their extension to blind deconvolution is straightforward and hence their development is valuable. The ill-conditioning of the deconvolution problem requires the addition of prior information, such as positivity, to enable its solution. It is shown that the conventional deconvolution problem can be reformulated as an equivalent quadratic programming problem. Consequently, an accelerated quadratic programming approach is applied and shown to be an improvement to an existing method used for enforcing positivity in deconvolution applications. The main algorithmic differences of the new method are implementation via the fast Fourier transform (FFT) and guaranteed convergence to the constrained minimum.

Blind deconvolution is also an interesting problem that may arise in many fields of research. It is of particular relevance to imaging through turbulence where the point spread function can only be modelled statistically, and direct measurement may be difficult. The extension of the quadratic programming method to blind deconvolution, combined with Tikhonov-Miller regularisation (energy constraints), smoothness constraints, penalty terms and statistical priors produced a series of new algorithms. The performance of these algorithms is illustrated on simulated astronomical speckle images.

Ground-based adaptive optics (AO) technologies are an alternative to post processing methods and aim to compensate for the distortion introduced by the atmosphere in real-time. Knowledge of the vertical structure of the atmosphere combined with AO provides the potential for compensation over a wide field of view. However, the continually changing nature of atmospheric turbulence places strict requirements on techniques for determining the turbulence structure. The remote sensing of scintillation data to estimate this information is known as scintillation detection and ranging (SCIDAR). Application of SCIDAR methods to the capture and analysis of experimental data, as demonstrated in this thesis, highlighted a number of problems with the technique. Methods for overcoming these difficulties are discussed and demonstrated. Finally, alternative approaches to the estimation of atmospheric turbulence profiles and a proposed new technique are investigated.

Acknowledgements

I greatly appreciate the support and direction provided by my supervisor Dr. Richard Lane.

I gratefully acknowledge the financial support I have received at various stages throughout my PhD studies. I thank the University of Canterbury for a University of Canterbury Doctoral Scholarship. I would also like to thank Telecom New Zealand for their support in the form of a Telecom Fellowship in Telecommunications Engineering and more recently the Royal Society of New Zealand for their support in the form of the R. H. T. Bates Postgraduate Scholarship 2000. Thanks also go to the IEEE for conference funding assistance.

I thank Imperial College for the use of their SCIDAR equipment, and Nick Wooder and Florence Rigal for operating it.

I extend my thanks to Cressida Harding, Roy Irwan, Valerie Leung, Sharee McNab and Philippa Martin for their friendship and support. Special thanks go to Valerie Leung and Marcos van Dam for their efforts in proof reading this large document.

Finally I wish to thank Darryl for the support, understanding and love he has given me over the last few years and especially during the task of preparing this thesis.

Contents

Preface

I began my postgraduate studies in 1997, under the supervision of Dr. Richard Lane, intending to examine the fundamental limits of blind deconvolution. During my first year I attended a number of Masters lecture courses including: *Adaptive Optics* by Prof. Chris Dainty and *Image Recovery* jointly taught by Dr. Richard Lane, Assoc. Prof. Phil Bones and postdoctoral fellow Dr. John Connolly. The result being that my research diverged to include not only image restoration but also more astronomically related research, culminating finally in a thesis entitled "Inverse Problems in Astronomical Imaging".

A project I undertook in the first year of my research was the interpolation of "Systeme Probatoire d'Observation de la Terre" (SPOT) satellite images. This is in some senses the reverse of astronomical imaging where space objects are imaged from earth. Instead the SPOT satellites record optical images of the earth's terrain from space. They are equipped with panchromatic and multispectral sensors enabling the capture of data at several fixed resolutions. Resampling, and subsequent interpolation, is frequently required for the rectification of images and comparison with other data. The availability of a pair of matching images, one at twice the resolution of the other, allowed the direct computation of an interpolator for the low resolution data, referred to as the upsampling inverse filter (UIF). A comparison between the UIF and the best performing classical interpolator resulted in the submission and subsequent publication of this work in the joint IVCNZ'97/DICTA'97 proceedings. However, since this work is not directly related to the remainder of the research presented in this thesis no further mention of it is made.

Astronomical imaging is an area of continuing research in the attempt to obtain diffraction-limited images from ground-based telescopes. This is made difficult by the atmosphere, a region of random refractive index fluctuations surrounding the earth, which separates the ground-based observer from the objects of interest. Incoming light is distorted and information lost before the imaging of this incomplete data is made by ground-based telescopes. Attempts to recover the lost information and improve the resolution of the measured data require the solution of many inverse problems. The aim of this thesis is to provide an overview of selected inverse problems in the field of astronomical imaging and the original contributions I have made during my PhD studies.

The inverse problem of interest throughout this thesis is the compensation of the degradations introduced by the atmosphere to images captured by ground-based telescopes. New methods for the processing of single and multiple speckle data frames are discussed in detail in chapters 5 and 6. Prior information, for example positivity, is necessary to attempt to recover the lost information and resolution. Positivity is commonly enforced in the majority of algorithms developed for astronomical applications, as it is intensities, which cannot be negative, that are measured. A main result presented in this thesis is the development of an improved technique for enforcing positivity using quadratic programming methods. The extension of this method to blind deconvolution is also demonstrated, as are a variety of related deconvolution problems.

Alternative compensation techniques include adaptive optics (AO) technologies, designed to compensate for the distortion introduced by the atmosphere in real-time. My investigations in this area involved researching the estimation of atmospheric turbulence profiles from scintillation measurements. This information can then be used to improve the compensation performance of AO systems by enabling the dominant turbulence to be targeted. Existing scintillation detection and ranging (SCIDAR) approaches are reviewed and improved. Alternative methods for turbulence profiling are discussed in chapter 9 along with a proposed new method.

0.0.1 Thesis organisation

A brief description of the contents of each chapter is now given.

A general introduction to image processing and inverse problems is presented in chapter 1. The astronomical imaging problem is outlined along with an in-depth introduction to the atmosphere and its effects. This chapter concludes with a brief description of each of the research areas detailed in later chapters.

Chapter 2 introduces the notation and much of the mathematics necessary for the understanding of this thesis. Linear systems, transform, probability and information theories are all introduced. The linear system model describes a variety of degradations including the instantaneous effects of atmospheric turbulence. Transforms, in particular the Fourier transform, are fundamental to the algorithms developed in this thesis and are outlined in some detail in both continuous and discrete forms. Relevant aspects of probability theory, necessary for the investigation of the random refractive index fluctuations characteristic of the atmosphere, are also introduced. Finally, basic information theory concepts are outlined as required for an understanding of the maximum entropy error metric used in image restoration algorithms.

An introduction to imaging through atmospheric turbulence is presented in chapter 3. Basic geometrical and Fourier optics theory is outlined. This includes diffraction, a key component of Fourier optics theory, which provides the basis for the simulation of scintillation outlined in chapter 4. Also presented is the imaging of atmospherically distorted images, important for providing an understanding of the forward problem relevant to astronomical imaging. This chapter concludes with a short introduction to emerging adaptive optics technologies for further improving the compensation of the effects of the atmosphere.

Chapter 4 describes and demonstrates new and improved methods for the simulation of atmospheric turbulence and its effects. The assumptions made by many of the commonly used approaches are physically unjustified and hence do not accurately model the processes of interest. A previously presented method (Lane *et al* [94]) is both formalised and improved,

enabling the rapid simulation of accurate and realistic phase screens. These phase screens are then used in the simulation of accurate scintillation necessary for the testing of SCIDAR and related techniques and also in the simulation of accurate speckle images required for the testing and development of post processing techniques. In addition, extension to the simulation of non-Kolmogorov statistics is shown to be straightforward.

Chapter 5 is concerned with estimating positive reconstructions from degraded measurements using conventional deconvolution methods. Much of the work presented in this chapter is shown to be an improvement to a method proposed by Nakamura *et al* [117]. The resulting algorithm, developed from standard quadratic programming methods, is implemented using the fast Fourier transform (FFT) and guarantees convergence to the constrained minimum for only a trivial amount of extra computation over other methods in common use, e.g. projected least squares methods.

Chapter 6 investigates the blind deconvolution of astronomical images and includes a thorough review of existing methods. The improved method for enforcing positivity, outlined in chapter 5, is extended to blind deconvolution. A variety of forms of prior information are used to regularise the problem, resulting in several original iterative blind deconvolution algorithms. The performance of these algorithms is demonstrated for the effects of noise, turbulence severity, starting estimate and form of prior information.

Chapter 7 addresses the problem of estimating atmospheric turbulence profiles from measured scintillation data as necessary for site profiling and improving the performance of AO systems. The majority of the work in this area has been carried out by Vernin and his co-workers [4,5,8,26–28,38,42,57,58,111,132,133,165,166,168–170]. More recent contributions have been made to this field by Tyler and Steinhoff [161], Tyler [159] and Kluckers *et al* [85]. The inversion of the scintillation covariance is required to obtain an estimate of the turbulence profile $C_N^2(h)$, the refractive index structure constant as a function of altitude. It is shown that the positivity enforcement outlined in chapter 5 can also be successfully applied to this problem. Experimental scintillation data, obtained during an observing run to the Mount John observatory, a University of Canterbury field station, is processed and

analysed. Finally, difficulties that arose during the processing of the experimental data are addressed.

Alternative techniques for the estimation of atmospheric turbulence profiles are presented in chapter 8. Established differential image motion monitor (DIMM) [142] and Hartmann differential image motion monitor (HDIMM) [10, 147] technologies are introduced. The extension of these methods to turbulence height estimation by the imaging of binary stars, as suggested by Bally *et al* [10], is demonstrated. Finally, a new technique requiring only single star scintillation is proposed and demonstrated.

Conclusions and recommendations for future work are presented in chapter 9.

0.0.2 Supporting publications

Journal and conference papers prepared during the course of this thesis are listed below in order of preparation.

1. "SPOT image interpolation", R. A. Johnston, N. Alwesh, R. G. Lane and P. Bones, in joint proceedings of Image and Vision Computing NZ 1997 (IVCNZ'97) and Digital Image Computing: Techniques and Applications 1997 (DICTA'97), Hodgson and Page (Editors), Albany, December 1997, pp 183 - 188.

2. "Fast simulation of a Kolmogorov phase screen", C. M. Harding, R. A. Johnston and R. G. Lane, Applied Optics, Vol. 38, No. 11, April 1999, pp 2161-2170.

3. "Regularized blind deconvolution", R. G. Lane, R. A. Johnston, R. Irwan and T. J. Connolly, in Signal Recovery and Synthesis, Vol. 11, OSA Technical Digest Series, (Optical Society of America, Washington DC, 1998), pp 5 - 7.

4. "Efficient blind deconvolution", R. A. Johnston, T. J. Connolly and R. G. Lane, in proceedings of Image and Vision Computing NZ 1998 (IVCNZ'98), G. Gimel'farb and R. Kakarala (Editors), Auckland, November 1998, pp 387 - 392.

5. "Results from Mount John SCIDAR experiments", R. A. Johnston and R. G. Lane, in Proceedings of Image and Vision Computing NZ 1999 (IVCNZ'99), D. Pairman and H. North (Editors), Christchurch, 1999, pp 271 - 276.

6. "An improved method for deconvolving a positive image", R. A. Johnston, T. J. Connolly and R. G. Lane, Optics Commun., Vol. 181, July 2000, pp 267-278.

7. "Modelling scintillation from an aperiodic Kolmogorov phase screen", R. A. Johnston and R. G. Lane, Applied Optics, Vol. 39, No. 26, September 2000, pp 4761-4769.

8. "Estimating turbulence profiles in the atmosphere", R. A. Johnston and R. G. Lane, in proceedings of SPIE Conference 4123 - Image Reconstruction from Incomplete Data, July-August 2000.

Glossary

0.0.3 Notation

j	$\sqrt{-1}$
A^{-1}	inverse of the matrix A
A^T	matrix transpose of A
$\approx$	approximately equal to
$f^*(x,y)$	complex conjugate of $f(x,y)$
$\odot$	convolution operation
$*$	correlation operation
$\langle\rangle$	ensemble average
$\leftrightarrow$	Fourier transform pair
$Im()$	imaginary part of
∞	infinity
$Ph()$	phase of
$P\{x\}$	probability of x
$\prod$	product
$\propto$	proportional to
$Re()$	real part of
$\sum$	summation
σ^2	variance
$\lvert\ \rvert$	magnitude of
$C_N^2(h)$	refractive index structure constant as a function of height
D	telescope aperture dimension
D_p and D_ϕ	phase structure function
d_0	focal anisoplanatism parameter
r_0	Fried's parameter

θ_0	isoplanatic angle
τ_0	turbulence time constant
$v(h)$	velocity profile as a function of height
k	wavenumber
λ	wavelength of light
ζ	zenith angle

$f(x,y)$	object
$h(x,y)$	point spread function
$g(x,y)$	noise free convolution of $f(x,y)$ and $h(x,y)$
$n(x,y)$	measurement noise
$d(x,y)$	measured noisy data
$\delta(x,y)$	delta function
$\text{rect}(x,y)$	rectangle function
$\text{sinc}(x,y)$	sinc function
$\text{circ}(x,y)$	circle function
$q(x,y)$	chirp function

0.0.4 Abbreviations

AO	adaptive optics
CCD	charge coupled device
CDF	cumulative distribution function
CG	conjugate gradient
CT	cosine transform
DCT	discrete cosine transform
DFT	discrete Fourier transform
DHT	discrete Hankel transform
DIMM	differential image motion monitor
DM	deformable mirror
fBm	fractional Brownian motion
FFT	fast Fourier transform
FOV	field of view
FT	Fourier transform
HDIMM	Hartmann differential image motion monitor
HST	Hubble space telescope
HT	Hankel transform
IBD	iterative blind deconvolution
IFFT	inverse fast Fourier transform
MAP	maximum *a posteriori*
ML	maximum-likelihood
MSE	mean squared error
PDF	probability density function
PET	positron emission tomography
PSF	point spread function
OTF	optical transfer function
SCIDAR	scintillation detection and ranging
SNR	signal to noise ratio
SVD	singular value decomposition

0.0.5 Astronomical and technical terms

A glossary of relevant astronomical and technical terms is presented here. Much of this material has been taken from Barlow [12] and Ridpath [131].

Angular resolution A telescope's ability to distinguish, or resolve, an adjoining pair of objects (such as double stars) into two separate objects.

Binary star A system of two stars bound together by their mutual gravitation, that orbit about their common centre of mass.

Coherent imaging The imaging of an object illuminated by coherent light, where coherent illumination implies the optical field is perfectly correlated or deterministic, i.e. laser light.

Double star A system of two stars located close to each other without having any real physical attraction.

Diffraction-limited image An optical image whose resolution is limited only by the optics with which it is captured.

Incoherent imaging The imaging of objects illuminated by incoherent light, where each object point is assumed to be statistically independent of all other object points, e.g. self-luminous objects.

Magnitude A measure of the brightness of a star expressed according to a logarithmic scale in which a difference of 5 magnitudes defines a brightness ratio of 100 to 1.

Phase screen A single realisation of the phase distortion introduced by the atmosphere.

Pixel A contraction of picture element. The smallest element of a digital image, e.g. an individual element in a CCD array.

Primary mirror The main light-gathering mirror of a reflecting telescope, that collects and focuses incoming light.

Scintillation The amplitude fluctuations, or twinkling, resulting from the propagation of phase distorted wavefronts through the atmosphere.

Secondary mirror Any mirror second in the optical path after the primary mirror.

Seeing The angular extent to which a star's image is spread by turbulence in the earth's atmosphere; good seeing refers to atmospheric conditions in which most of the light is concentrated in a diameter smaller than 1 arc second.

Spider The supports, in a telescope, holding the secondary mirror in place above the primary mirror.

Wavefront A surface found by connecting points an equal optical path length from the source.

Zenith angle The angular distance from the zenith to the observed object, where the zenith describes a point directly above the observer.

Chapter 1

Introduction

Image processing deals with the capture, storage, interpretation, manipulation and improvement of images, where an image is defined to be,
" *A physical likeness or representation of a person, animal, or thing, photographed, painted, sculptured, or otherwise made visible*" [150],
or alternatively,
" *An optical appearance or counterpart of an object, such as is produced by rays of light either reflected as from a mirror, refracted as through a lens, or falling on a surface after passing through a small aperture* " [183].

Image processing can be split into four general areas; rectification, enhancement, restoration and reconstruction [13]. *Image rectification* is concerned with the removal or correction of geometric and system induced distortions in digital images, e.g. the correct alignment of images with each other. Essentially it describes the operations that are used to transform an image into standard format. For example, airborne side looking radar images are subject to severe geometric distortions and may require geometric correction before interpretation [29]. *Image enhancement* aims to improve the visual appearance of an image or

convert it to a form better suited for display or analysis. This could be in the form of edge enhancement, pseudocolouring, noise filtering, sharpening or magnifying [79]. It should be noted that the information content of the image is not increased during image rectification and enhancement, it is merely manipulated to suit a specific purpose. Real world images often suffer from unwanted distortion. The identification, modelling, estimating and reversing of degradations associated with images is known as *image restoration*, and is an area of particular interest in this thesis. The restoration of an image degraded by atmospheric turbulence is an example of an image restoration problem, where a large number of diverse methods have been proposed for this application. *Image reconstruction* on the other hand deals with the reconstruction of detail in severely distorted images, when the distortion is known *a priori*, e.g. the deblurring of an image when the blurring function is known.

1.1 Image formation, detection and recording

The desire to manipulate and improve images leads to the need for accurate understanding and modelling of the image formation, detection, recording and degradation processes. The relationships or transformations between an object and its measured quantity must be understood in order for it to be accurately modelled. The *object*, the quantity being measured, is defined in object space using the (ξ, η) coordinate system.

An object can be illuminated by an independent source of light or radiant energy. For example a planet, which is illuminated by the sun. Alternatively, an object can be self-luminous, e.g. a star, whereupon it emits its own light. An image is formed when the radiant energy from the object, whether it is emitted or reflected, is intercepted by an image forming system, e.g. the eye or a man-made optical system. An *image* is defined by a different coordinate system, (x, y), in image space (see Fig. 1.1).

Image formation in visible light is hindered by the non-penetrating nature of the radiation at that wavelength. Consider the situation illustrated in Fig. 1.2, only the light passing through the aperture can be used to form the image. The truncation of light waves by the aperture, resulting in the distortion of the image, is due to the physical phenomenon called

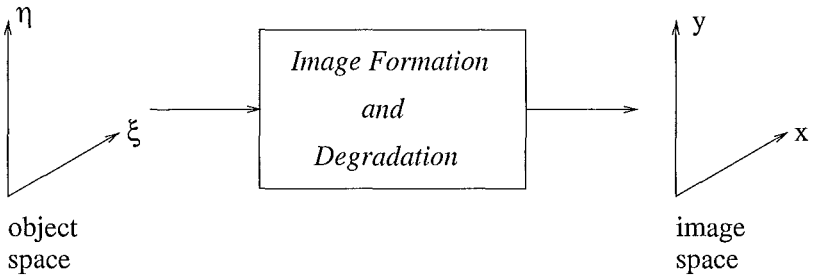

Figure 1.1: *Mapping between object and image spaces.*

diffraction, which is of the utmost importance in the theory of optical imaging systems. Diffraction effects are generally thought to be harmful, since the best images are formed when all the light from the object travels undistorted to the detector. Diffraction effects occur wherever light waves are truncated, an example being the propagation of light through an imaging system, and cannot be removed. The resolution limit imposed by diffraction is termed the *diffraction-limit*. Diffraction theory is presented in chapter 3 and simulation of the diffraction phenomenon is detailed in chapter 4.

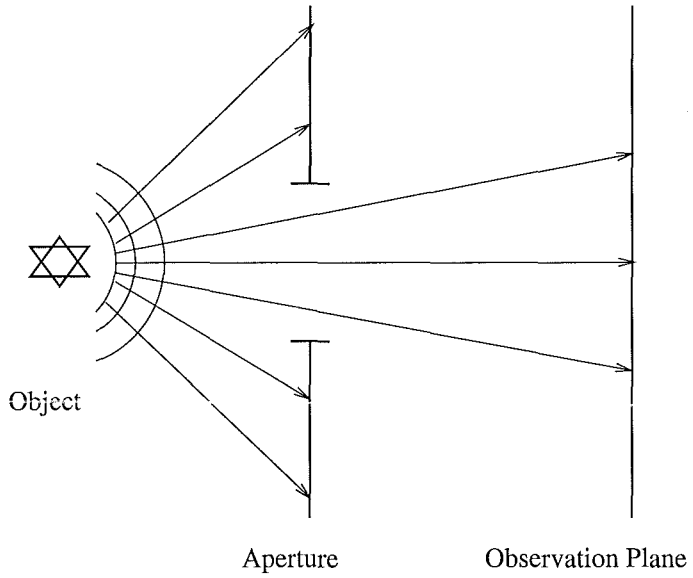

Figure 1.2: *The general diffraction problem.*

Image detection and recording are also important processes, as it is not possible to process

an image without a system to sense and record it [3]. Photochemical, e.g. film, and photoelectronic, e.g. a charge coupled device (CCD) camera, technologies are available. The silver halides on the surface of photographic film change after exposure to light, and hence record the scene of interest. The human eye also detects and records images. Here the image is formed on the retina, the surface of which is covered by millions of light receptors which become excited by light energy. Photoelectronic imaging devices, however, separate the detection and recording processes. A photoactive surface detects the image and then scanning electronics record the image formed on the surface.

Noise and measurement artifacts are inherent to the image detection and recording processes. Finite storage capacity and finite measurement times place limits on the amount of information that can be recorded and hence the quality of the corresponding image restoration. In addition, noise can be a major problem as noise sources are varied and are found everywhere. Components in the imaging and readout electronics of a system introduce signal independent noise, often modelled as Gaussian noise. Astronomical imaging applications also suffer from photon or shot noise, which is described by Poisson statistics and is due to the random arrival times and locations of photons in the detector. In some cases the light propagating from an object undergoes mechanical or thermal degradation that further reduces its resolution. A good example of this is the imaging of an object that is located behind a heat haze.

The transformation, distortion and loss of information the object suffers before and while it is imaged is referred to here as the *forward* or *direct problem*. Investigation of the forward problem is essential to its successful inversion. For example, an estimate of the object is obtained when the measured data is passed through an appropriate inverse transformation. The forward transformation could simply be a Fourier transform (described in section 2.4.1) as is the case in a number of engineering and optics problems. The corresponding inverse transformation is then performed with use of the inverse Fourier transform. However, often the transformation is not so simple and as a result the forward problem must be accurately modelled and understood before the corresponding inversion can be addressed.

1.2 The image model

A simple degradation model has four parts to it; $f(x,y)$ represents the object, $h(x,y;\xi,\eta)$ the degradation or point spread function (PSF), $n(x,y)$ the additive noise and $d(x,y)$ the observed image. Assuming that the system is linear, the degraded image can be represented as [79]

$$d(x,y) = \int_{-\infty}^{\infty}\int_{-\infty}^{\infty} f(\xi,\eta)h(x,y;\xi,\eta)d\xi d\eta + n(x,y). \tag{1.1}$$

For implementation on a digital computer these continuous quantities must be approximated by a series of discrete points, a process known as sampling (see section 2.5.1). This leads to the discrete form of Eq. (1.1), given by [11]

$$d(x,y) = \sum_{k=-\infty}^{\infty}\sum_{l=-\infty}^{\infty} f(k,l)h(x,y;k,l) + n(x,y), \tag{1.2}$$

where $d(x,y)$, $f(x,y)$, $h(x,y;k,l)$ and $n(x,y)$ now represent matrices and k and l take on integer values. This model can incorporate both space variant and invariant distortions. Space variant blurs can be very complicated and are not required in this thesis. Instead the distortion is considered to be linear space invariant (LSI). The PSF can now be expressed as

$$h(x,y;k,l) = h(x-k,y-l). \tag{1.3}$$

A number of simple distortion models, for example blur due to camera motion or atmospheric turbulence, are described by this model. The 2D superposition summation for a space invariant PSF becomes

$$d(x,y) = \sum_{k=-\infty}^{\infty}\sum_{l=-\infty}^{\infty} f(k,l)h(x-k,y-l) + n(x,y). \tag{1.4}$$

This can also be expressed in an equivalent and more compact form

$$d(x,y) = h(x,y) \odot f(x,y) + n(x,y), \tag{1.5}$$

where $\odot$ denotes the 2D convolution operator. The model described by Eq. (1.5) is illustrated in Fig. 1.3.

The digital image degradation process is often represented in terms of a matrix vector formulation,

$$d = Hf + n, \tag{1.6}$$

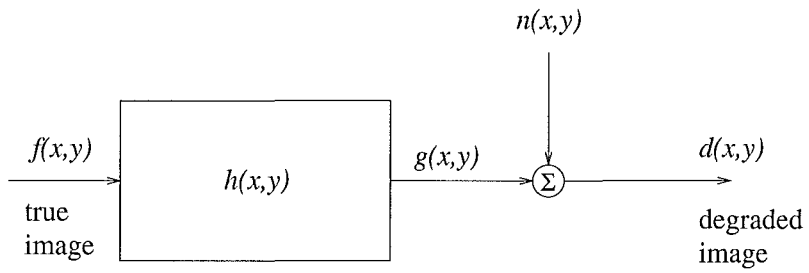

Figure 1.3: *Simple degradation model.*

where d the observed data, f the original image and n the noise are now represented by vectors and H is a matrix representing the linear convolution with h. The vectors d, f and n are created by stacking the rows (or columns) of the original matrices. Assuming the original image has dimensions $N \times N$, the corresponding dimensions after the stacking operation are $N^2 \times 1$, i.e.

$$f^T = [f(1,1)f(1,2) \ ... \ f(1,N), f(2,1) \ ... \ f(N,N)]^T, \tag{1.7}$$

and the corresponding H matrix has dimensions $N^2 \times N^2$.

A large part of the work presented in this thesis is directed towards estimating the true object from degraded image measurements, with and without prior knowledge of the PSF. The simple convolution model of Eq. (1.2) models the forward problem for many real world processes, and therefore permits a thorough investigation of the behaviour and possible outcomes of processes of this nature. An understanding of the forward problem is essential to the success of inversion techniques. As a result the forward problems relevant to the areas presented in this thesis are addressed in some detail in the following chapters.

1.3 Inverse problems

Scientific measurements of physical quantities are made in the fields of physics, astronomy, electrical engineering and in everyday life. In many cases the desired measurements can be made directly. Often, however, the object of interest is not directly measurable, so indirect, incomplete or distorted measurements are made. This process results in a significant loss

of information which must then be inferred or recovered from these measurements. The relationships or transformations between the object and its measured quantity must be understood and modelled before an inversion can be performed, where this inversion is typically referred to as an *inverse problem.* Many inverse problems occur in everyday life, for example geophysicists are interested in the earth's interior but are restricted to measurements from the surface [39], whereas astronomers try to infer information about the stars from their measurements of them [155]. In fact, image restoration and reconstruction problems are examples of inverse problems.

1.4 Astronomical imaging

Astronomical imaging is an example of an image restoration or inverse problem. This thesis investigates inverse problems related to the improvement of astronomical images. The objects of interest are generally celestial bodies such as stars, planets, galaxies, nebulae and moons. These are separated from ground-based telescopes by the atmosphere, which optically consists of layers of varying refractive index surrounding the earth. The incoming wavefronts are distorted by the atmosphere, reducing the quality and resolution of the observed and recorded images. As is the case with all inverse problems it is necessary to investigate the forward problem, in this case the atmosphere, to aid the reversal of its effects.

1.4.1 The atmosphere

The atmosphere consists of an envelope of gases and particles surrounding the earth. Turbulence arises because the atmosphere is warmed during the day and cooled at night. The combination of these temperature fluctuations with water vapour and the wind result in the mixing of air with water vapour and warm air with cool air. This in turn varies the refractive index, which is a function of the temperature and the concentration of water vapour. The heating of air in this manner results in large scale motions. As the turbulence develops, the kinetic energy of the large scale motions is transferred to smaller and smaller scale motions [87], eventually resulting in randomly sized and distributed pockets of air

known as turbulent eddies [139]. The scale of motions giving rise to turbulence is from the outer scale, L_0, which is in the order of 10s of metres down to the small scale motions described by the inner scale, l_0, which is usually in the order of millimetres.

The atmosphere can be divided into four sections; the troposphere, stratosphere, mesosphere and thermosphere, where the elevation of each layer is displayed in Fig. 1.4. The tropopause separates the troposphere and stratosphere. The stratopause and mesopause separate the stratosphere and mesosphere, and mesosphere and thermosphere respectively. Atmospheric turbulence is considered to be restricted to the troposphere and stratosphere regions.

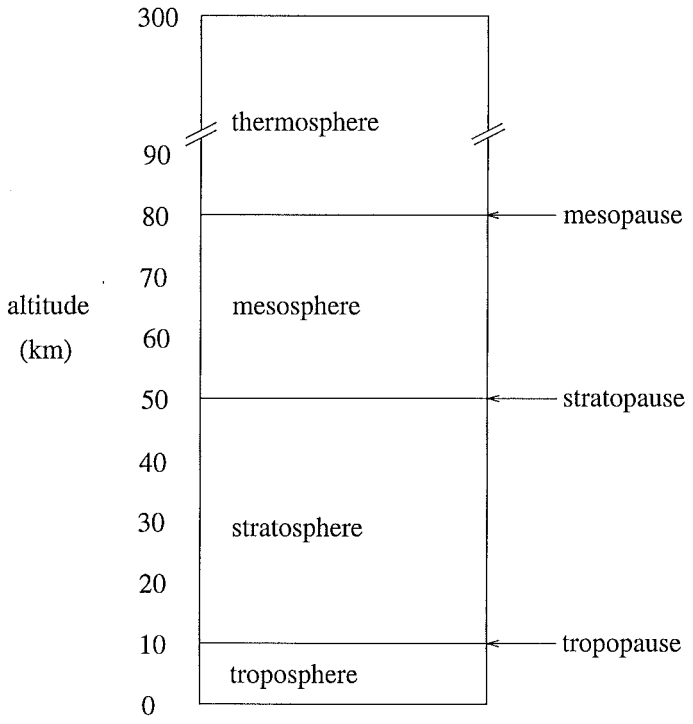

Figure 1.4: *The structure of the atmosphere.*

The statistical distribution of the size and number of turbulent eddies is characterised by the power spectral density (PSD) of the refractive index fluctuations, $\Phi_N(\kappa)$, where atmospheric turbulence is often modelled by Kolmogorov statistics [139]. The PSD for Kolmogorov statistics is given by

$$\Phi_N(\kappa) = 0.033 C_N^2 \kappa^{-11/3}, \tag{1.8}$$

where κ denotes the scalar-wavenumber vector $(\kappa_x, \kappa_y, \kappa_z)$, and C_N^2 is the structure constant of refractive index fluctuations. C_N^2 gives a measure of the turbulence severity and is measured in units of $\mathrm{m}^{-2/3}$. Turbulence can also be characterised by its temperature and humidity PSDs, $\Phi_T(\kappa)$ and $\Phi_C(\kappa)$ respectively, both of which also obey a -11/3 power law.

Kolmogorov's theory assumes an infinite outer scale and zero inner scale. These are explicitly taken into account by the von Karmen spectrum, which has a power spectrum given by [139]

$$\Phi_{N(VK)}(\kappa) = \frac{0.033 C_N^2}{(\kappa^2 + K_o^2)^{11/6}} \exp\left\{-\frac{\kappa^2}{K_m^2}\right\}, \tag{1.9}$$

where $K_o = 2\pi/L_o$ and $K_m = 5.92/l_o$.

Large amounts of research have been directed at analysing, measuring and understanding the atmosphere. There is considerable evidence that turbulence in the free atmosphere is confined to thin, horizontal layers separated by non-turbulent regions [134, 163]. The thickness of the layers is thought to be in the order of 100-200m with C_N^2 values increasing by more than an order of magnitude above the background levels in these distinct layers.

A number of turbulence models have been suggested that mathematically describe C_N^2 values for a range of altitudes, h. Daytime turbulence models include the Hufnagel-Valley and submarine laser communications day (SLC-Day) models [139]. The Hufnagel-Valley turbulence model is given by

$$\begin{aligned} C_N^2(h) &= 5.94 \times 10^{-53} (v/27)^2 h^{10} \exp\{-h/1000\} + 2.7 \times 10^{-16} \exp\{-h/1500\} \\ &+ A \exp\{-h/100\}, \end{aligned} \tag{1.10}$$

where A sets the turbulence strength near the ground and v is the high altitude wind speed. Whereas, nighttime models include a modified Hufnagel-Valley profile and the Greenwood profile. The modified Hufnagel-Valley profile is

$$\begin{aligned} C_N^2(h) &= 8.16 \times 10^{-54} h^{10} \exp\{-h/1000\} + 3.02 \times 10^{-17} \exp\{-h/5000\} \\ &+ 1.90 \times 10^{-15} \exp\{-h/100\}. \end{aligned} \tag{1.11}$$

Although the natural atmosphere is turbulent in nature and degrades resolution, turbulence is not restricted to the free atmosphere. There are five distinct contributing elements to the degradation of images of celestial bodies [169]. These are the free atmosphere, the boundary layer, the surface layer, dome seeing and mirror seeing. Mirror seeing and dome seeing correspond to the turbulence occurring inside the telescope and dome. The surface layer turbulence describes the interface between the air inside and outside the dome. This has been recognised as a significant contribution to degradation in image resolution [134]. The boundary layer extends to 10s of metres above the ground. Finally turbulence in the free atmosphere describes the natural turbulence found in the troposphere and above.

Information on boundary layer turbulence can be obtained using ground-based or tower mounted high speed temperature sensors. Acoustic, radar and aircraft soundings can also be used. Turbulence in the free atmosphere is harder to measure. Often remote measurements are made using balloon-borne instrumentation [8,25,167,169], radar soundings [41,163], laser scintillations [53] and stellar scintillation analysis [8,26,85]. However, since the atmosphere can change rapidly it is important that it can be measured efficiently. The use of balloon-borne instrumentation is not adequate as it captures only a snapshot of the turbulence that it passes through, so the information relating to higher altitudes corresponds to turbulence that may have changed considerably since the low altitude measurements were made. The remote sensing of stellar scintillation measurements is more suited to this application as it includes information relating to the entire turbulence profile at any one time and can be inferred from measurements made from a ground-based telescope.

1.4.2 The astronomical problem

Atmospheric turbulence is a major problem in astronomy or in fact any application having optical paths through the atmosphere [167]. For astronomers, the objects of interest are often distant stars, where stars are modelled as point sources that emit spherical wavefronts. After propagation over hundreds of light years, the spherical wavefronts incident on the atmosphere can be considered to be planar. These planar wavefronts encounter the atmosphere, which acts like a collection of lenses of different refractive indices [16], a few

kilometres above the earth. As the wavefronts pass through the atmosphere, they undergo a phase distortion. Propagation of this phase distortion introduces amplitude fluctuations, known as *scintillation*. As a consequence, the wavefronts entering the telescope pupil suffer from both phase and amplitude variations.

In the absence of atmospheric turbulence the planar wavefronts emitted from a distant star continue undistorted to the telescope aperture. The resolution of the recorded image is limited only by the finite size of the aperture and is defined as the *diffraction-limited* image. Diffraction effects spread the ideal image of a star from a single point to a small region of points. In practice, the effects of the atmosphere cannot be ignored. The phase distortion introduced by the atmosphere is illustrated in Fig. 1.5. Light that has passed through atmospheric turbulence results in the formation of a severely distorted image referred to as a speckle image, due to is speckled appearance. The aim is, therefore, to estimate the diffraction-limited image from single or multiple speckle images.

The phase distortion introduced by the atmosphere is more severe than the resulting scintillation and hence the scintillation is often neglected [134]. However, scintillation can be used to determine information about the structure of the atmosphere [85]. The size of the scintillation detail is given by the Fresnel length, r_f,

$$r_f = \sqrt{\lambda z}, \tag{1.12}$$

where λ is the wavelength of light and z the distance of propagation. Therefore, as the height of the turbulent layer or the distance of propagation increases the Fresnel length also increases as illustrated in Fig. 1.6. The propagation of light from the top of the atmosphere to the telescope aperture can be derived from diffraction theory and is investigated in chapter 4.

Many of the parameters used to characterise atmospheric turbulence can be derived from Fried's parameter or the turbulence coherence length, denoted by r_0. Fried's parameter can be computed from the $C_N^2(h)$ profile by [162]

$$r_0 = \left[0.42k^2 \sec(\zeta) \int C_N^2(h) dh\right]^{-3/5} \tag{1.13}$$

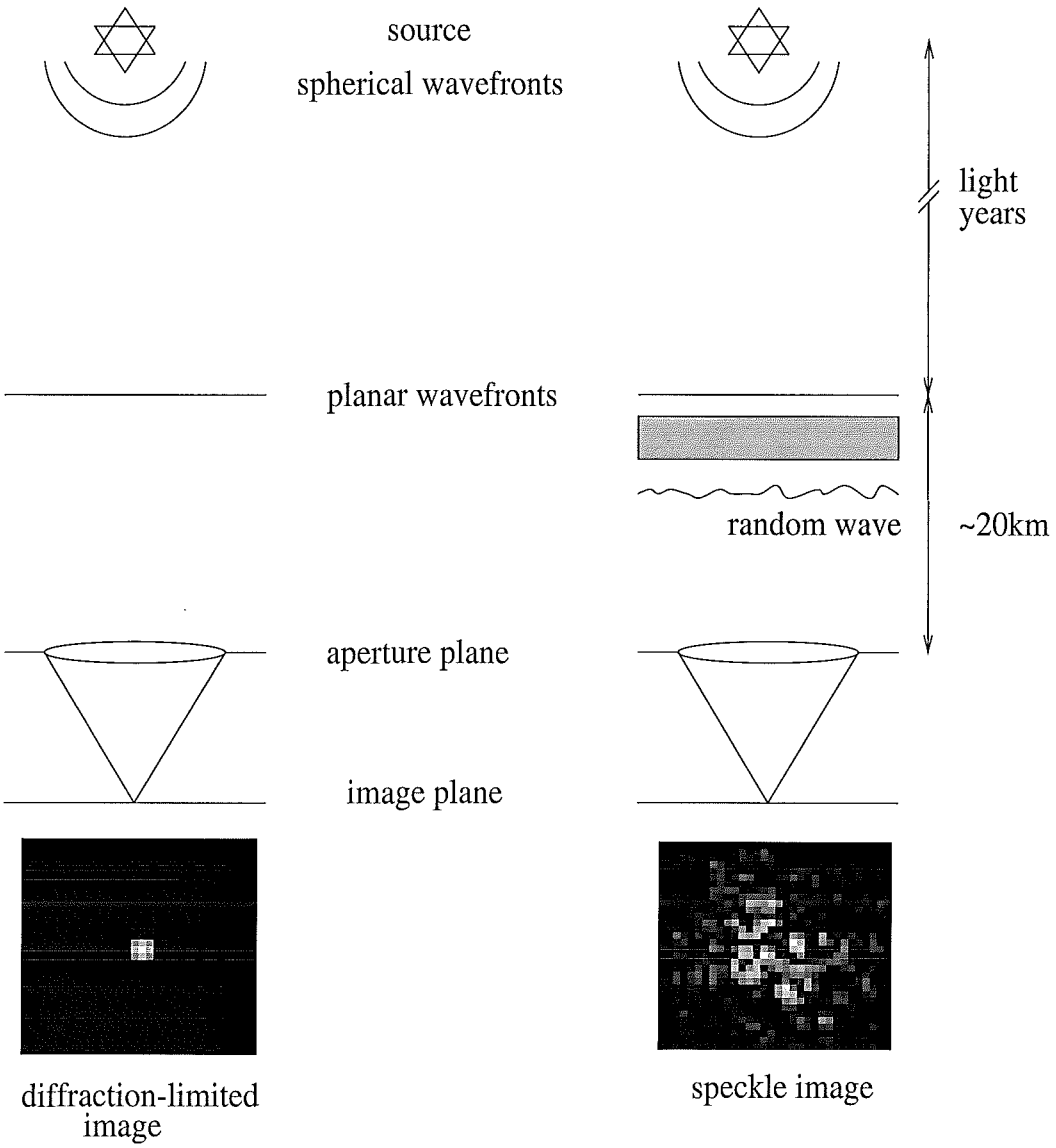

Figure 1.5: *The astronomical problem. The diffraction limited image is obtained when no distortion is introduced by the atmosphere. The speckled appearance of the speckle image is due to the effects of the atmosphere.*

where $k = \frac{2\pi}{\lambda}$ is the wavenumber and ζ is the zenith angle. It represents the effective diameter of a telescope capable of producing diffraction-limited images in the corresponding conditions. At a good astronomical site it is generally of the order of 2cm to 20cm for visible light [134]. Because the expression for r_0 contains $C_N^2(h)$, λ and the propagation path in one expression, it is widely used for scaling laws and the description of atmospheric

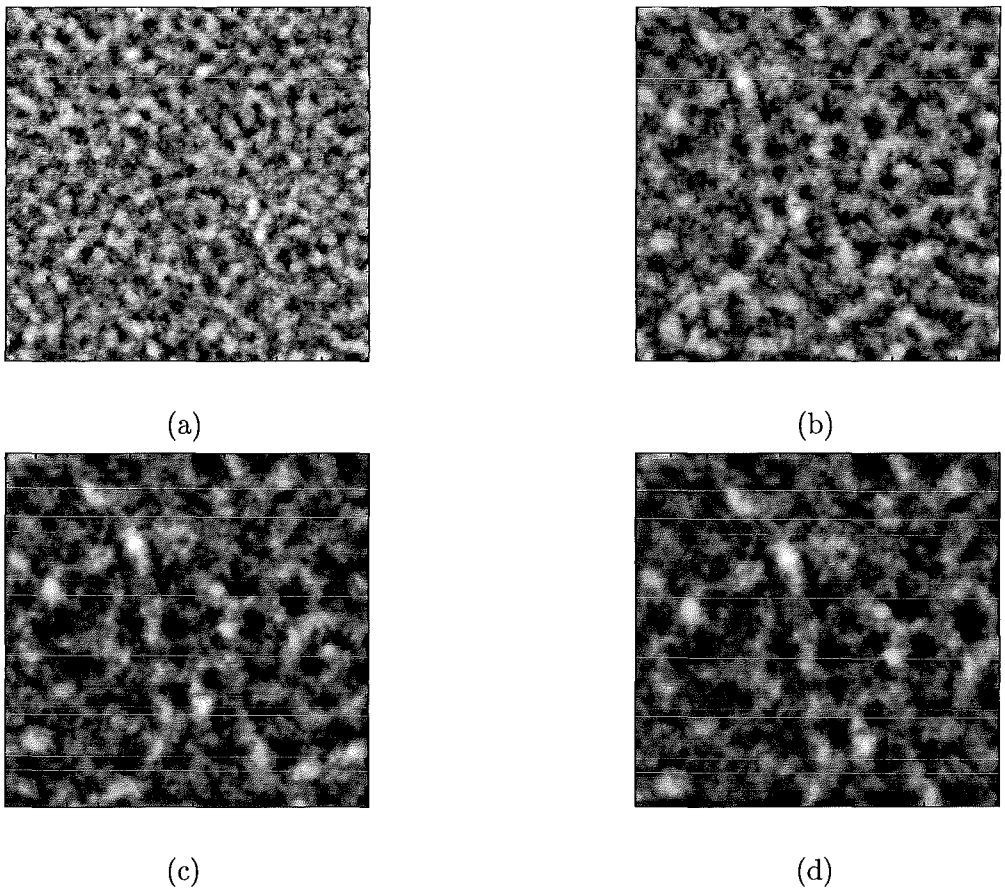

Figure 1.6: *Sample scintillation patterns for propagation distances of (a) 2.5km, (b) 5km, (c) 7.5km, and (d) 10km. Note that each scintillation pattern is of dimensions 1m by 1m.*

phenomena [162].

Other parameters often used to characterise the turbulence are the isoplanatic angle and turbulence time constant, denoted by θ_0 and τ_0 respectively. The *isoplanatic angle* is the largest angle of separation between two objects where the turbulence induced distortions of each object can be considered identical. Similarly, the *isoplanatic patch* is the patch of sky over which the distortion can be considered to be unchanging. The isoplanatic angle is small for astronomical observations in the visible wavelength range [139], typically 2-3 arcseconds. It can also be expressed in terms of $C_N^2(h)$ [162], the turbulence severity as a

function of height,

$$\theta_0 = \left[2.9k^2\sec(\zeta)\int C_N^2(h)h^{5/3}dh\right]^{-3/5}. \tag{1.14}$$

The *turbulence time constant*, τ_0, specifies the time interval over which the turbulence remains essentially unchanged and is often in the order of milliseconds. It can be expressed in terms of $C_N^2(h)$ and $v(h)$, the turbulence velocity profile [85],

$$\tau_0 = \left[2.9k^2\sec(\zeta)\int C_N^2(h)v^{5/3}(h)dh\right]^{-3/5}. \tag{1.15}$$

Turbulence is driven by winds in the atmosphere. The wind velocity, $v(h)$, can be estimated by experiment or from wind models. For example, the Bufton model [123] is an example of a wind model where

$$v(h) = 5 + 30\exp\left\{-\left[\frac{h-9400}{4800}\right]^2\right\}. \tag{1.16}$$

A number of techniques are used to eliminate the effects of the atmosphere. A good telescope above the atmosphere, for example the Hubble space telescope (HST), is able to obtain almost diffraction-limited images. Other suggestions have included placing observatories on the moon [184]. However, space telescopes are far more expensive to build and maintain than those on the ground. In addition, the size and weight is restricted by the need to place the telescope in orbit.

The general and more cost effective ground-based techniques used to deal with the effects of the atmosphere, have fallen into two general classes; freezing the turbulence by capturing short exposure images and secondly compensating the wavefront in real-time [93]. The first class of techniques refers to the post processing of short exposure frames on a computer to recover the lost resolution. Such techniques include speckle interferometry [90], bispectral analysis [7] and deconvolution techniques [91]. The second class of techniques refers to adaptive optics systems. Here the aim is to compensate for the distortion introduced by the atmosphere in real-time, that is to remove the wavefront distortion before the wavefront is detected. Aspects of these two classes of approaches are investigated in detail throughout this thesis.

Simulation of atmospheric turbulence and stellar scintillation is necessary for the research

and development of the techniques outlined above. Although many such techniques exist, improved techniques have been developed throughout the course of this research, to improve the accuracy, understanding and simulation of the astronomical problem and are presented in chapter 4. The algorithms and simulation tools developed throughout this thesis were generated using Matlab [113] and Mathematica [112].

1.5 Post processing

The majority of post processing techniques can be considered to be image restoration techniques, where image restoration describes the inversion process used to obtain an estimate of the object from distorted or incomplete data (see Fig. 1.7). The aim is to reconstruct the original object from the contaminated measurements. A main application is the reconstruction of stellar objects from astronomical speckle images. However, the post processing techniques mentioned and developed throughout this thesis can be applied to a variety of other problems also, for example medical imaging and remote sensing.

Speckle images, used by post processing algorithms, capture the instantaneous effect of the atmosphere. As a result the simple degradation model of Eq. (1.5) can be applied, where $h(x, y)$ is the distortion introduced by the atmosphere at the instant the frame was captured. The relationship between the degraded image and the object is defined as a convolution. Hence, reversing the effects of the degradation can be considered to be a deconvolution problem. Many different approaches have been used to solve this problem including filtering techniques as well as direct and iterative methods.

There are several different classes of deconvolution problems and all are investigated throughout this thesis. In a conventional deconvolution problem the aim is to recover $f(x, y)$ and $n(x, y)$ from the degraded image $d(x, y)$ and an estimate of the point spread function (PSF), $h(x, y)$. Therefore, conventional deconvolution algorithms can deblur images provided a reasonably accurate estimate of the blurring function is available. Often, the image is deblurred using a filter derived from the blurring function, for example inverse and Wiener filters [13]. In addition, many iterative techniques have been proposed and are commonly used, for

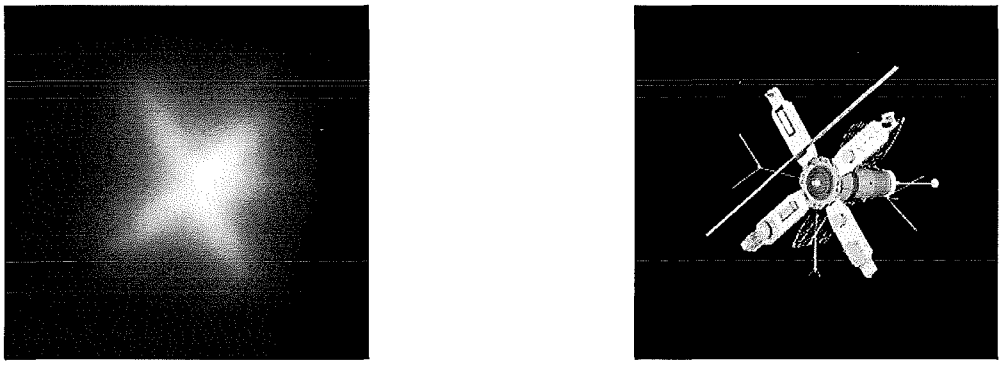

(a) (b)

Figure 1.7: *A sample restoration problem. (a) The degraded image and (b) the original image. The aim is to restore (b), often from the information given in (a).*

example the CLEAN [108] and Richardson-Lucy [104,130] algorithms.

A more complicated restoration problem is the blind deconvolution problem, which includes both single frame and ensemble varieties. In each case, no knowledge of the PSF is assumed, so the potential applications are much wider than those of conventional deconvolution. The single frame blind deconvolution problem is the most difficult to solve. Here the aim is to recover $f(x,y)$, $h(x,y)$ and $n(x,y)$ from a single observed data frame, $d(x,y)$. The difficulty arises due to measurement noise and the lack of known information. Post processing techniques suffer from a low single frame signal to noise ratio (SNR) [138], a major limiting factor of single frame methods. The extension to an ensemble of speckle data frames is used to overcome the low SNR of the single frame problem.

When more than one frame of data is considered, the simple linear degradation model of Eq. (1.5) becomes

$$d_i(x,y) = h_i(x,y) \odot f(x,y) + n_i(x,y), \tag{1.17}$$

where $1 \leq i \leq N$ and N is the number of speckle images. The aim is then to recover $f(x,y)$, $h_i(x,y)$ and $n_i(x,y)$ from $d_i(x,y)$, the observed frames. Astronomical imaging data can be used for ensemble blind deconvolution as it is easy and cheap to obtain several versions of the same distorted image. This is because the atmosphere is continually changing

while the object is assumed constant. A large number of blind deconvolution algorithms have been developed from direct single frame techniques, such as zero sheets [92], to the more common iterative ensemble techniques resulting from the iterative blind deconvolution (IBD) algorithm of Ayers and Dainty [6]. Applications include astronomical imaging [143], photography, crystallography, electron microscopy [43], medical imaging, positron emission tomography (PET) [83] and many others.

A significant problem with blind deconvolution is the issue of uniqueness. As so little information is available, there is no way of choosing one set of estimates over another. However, the use of *a priori* information about the object and/or the PSF can be used to narrow down the possible solution sets. *A priori* information can include energy, smoothness, positivity and support information, however, even with the addition of prior information, ambiguities still exist. Enforcing positivity is particularly relevant in the astronomical arena since negative photons have no physical meaning. Numerous techniques exist for enforcing positivity, each with their associated advantages and disadvantages. A new technique for enforcing positivity in deconvolution problems is presented in chapter 5 and is extended to blind deconvolution in chapter 6.

1.6 Adaptive optics

" *... refers to a set of techniques that corrects turbulence-induced phase distortions by mechanically deforming a reflective surface in the optical train of the telescope*" [122].

The adaptive optics (AO) concept was first proposed by Babcock in the early 1950s [9] and the first small scale AO systems were constructed during the mid 1970s [122]. The aim of an AO system is to remove the wavefront distortion introduced by the atmosphere before the wavefront is detected. AO technology covers a wide range of disciplines from chemistry to electrical engineering. However, it is the data processing and performance aspects of AO systems that are of interest here.

A standard AO system consists of four main parts; a bright reference source, a wavefront sensor, a correction element and a control system. A sample system containing the four main elements is illustrated in Fig. 1.8. An AO system found in nature is the eye. The eye can adapt to various conditions and improve the quality of the image perceived. In this case the control system is the brain as it interprets an image, determines a correction and applies the necessary changes through the biomechanical movement of the eye.

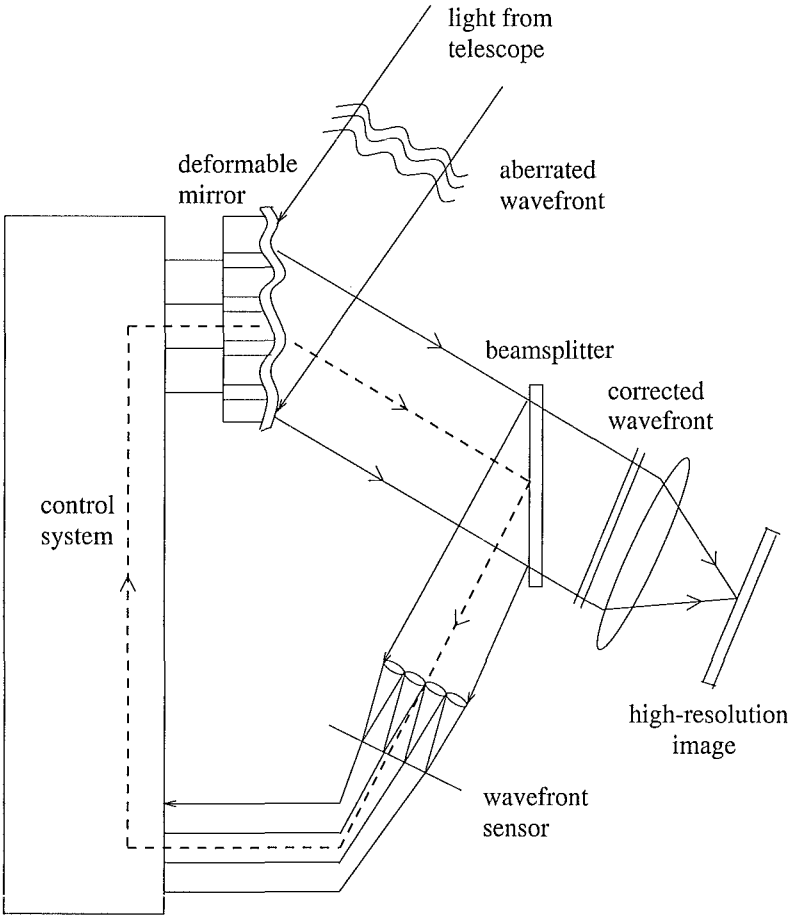

Figure 1.8: *A simple adaptive optics system.*

Astronomers are often interested in very faint objects, those that do not emit enough light to enable wavefront measurement, and extended objects such as planets. A suitable reference source along the propagation path is required to estimate the wavefront distortion. Often, the reference source is chosen to be a bright unresolvable star. However, suitable stars are

not always available. A solution in the form of artificial sources, known as synthetic beacons or laser guide stars, was first proposed by Feinlieb in 1982 [123] and independently by Foy and Labeyrie in 1985 [52]. They can be placed at specific locations in the sky and used to obtain accurate measurements of the phase distortion. One technique for generating a laser guide star is to focus a laser beam on a relatively low altitude portion of the atmosphere, i.e. 10-20km. The back scattered or Rayleigh scattered light in the direction of the telescope is used to measure the turbulence induced distortions. An alternative to the laser guide star is the sodium beacon [34]. In this case the sodium atoms in the sodium layer, 90km above the earth, are excited and give off light energy which can be used for wavefront measurements.

The wavefront sensor obtains the phase measurements, representing the distortion introduced by the atmosphere, from the reference source. The distorted wavefront can be detected and analysed with a shearing interferometer [178], a Shack-Hartmann wavefront sensor [97] or a curvature sensor [135]. A shearing interferometer splits the incoming light and recombines it, forming interference patterns which correspond to distortion at points across the aperture. The average wavefront slope is then estimated from the interference patterns. The Shack-Hartmann wavefront sensor splits the aperture into many subapertures or lenslets. Each subaperture focuses a spot onto a detector in the focal plane, allowing the local wavefront slope to be determined. A curvature sensor determines the curvature in each subaperture by differencing intensities measured at equal distances before and after the focal plane. When the slope or curvature information has been obtained, the phase estimate is computed using a phase reconstruction algorithm [148]. A final alternative is that of phase retrieval which has also been suggested as a means for wavefront sensing [95].

The correction or compensation element is generally a single deformable mirror (DM), although systems with multiple correction elements are becoming more common. There are several types of deformable mirrors, including monolithic [69], segmented [77] and bimorph [144] varieties. The monolithic mirror is comprised of a single piece of glass that is controlled by a grid of ceramic piezoelectric actuators. Segmented mirrors consist of a mosaic of small lightweight mirrors, each of which can move independently and is generally controlled by a servo motor. With precise control the resulting surface can be nearly as

smooth as that due to a one piece mirror. An emerging technology is that of bimorph mirrors consisting of sandwiches of two unlike piezoelectric layers, creating an electronically controllable deformable surface or membrane.

The phase measurements made by the wavefront sensor are fed into the control system. It uses these measurements to calculate the changes necessary to make the deformable mirror the opposite or conjugate of the instantaneous atmospheric distortion. Signals are then sent to the actuators or pistons controlling the deformable mirror. The corrected light can now be detected and recorded.

The entire process, from the measurement of the degradation to the appropriate deformation of the correction element, must be performed faster than the rate of change of the turbulence. Effectively, the surface of the deformable mirror is continually changing in an effort to represent the conjugate of the turbulence, and hence eliminate its effects. However, an AO system cannot produce diffraction-limited images due to the finite limitations of the wavefront sensor, deformable mirror and the time delays between sensing and correcting for the distortion introduced by the turbulence.

As well as the problems of finite delay times and limitations inherent to the various components of the system, there are other limitations. Firstly, the reference star must be bright enough. This can be achieved by use of artificial guide stars as the reference source, if no suitable natural stars are within the same isoplanatic patch. In addition, the compensation is limited to a small region around the reference star, which is in the order of several arcseconds for visible light. Methods have been proposed and trialed for increasing the field of view (FOV) over which compensation can be performed, some of which are outlined in section 3.5. Finally, due to the limited number of degrees of freedom of the deformable mirror, restoration will not be complete, so further post processing may be required.

1.7 Estimating atmospheric turbulence profiles

An increasing number of modern telescopes are being equipped with state of the art AO systems, having the potential to compensate in real-time for the phase distortion introduced by the atmosphere. For these systems to be effective a precise characterisation of the atmosphere is required. The problem of estimating, modelling and simulating atmospheric turbulence profiles is an essential step in the design and development of AO systems.

A remote sensing technique for profiling atmospheric turbulence is the scintillation detection and ranging (SCIDAR) technique proposed by Vernin and Roddier in 1973 [170] and modified by Fuchs *et al* in 1994 [57]. Binary star scintillation patterns are measured and processed to produce $C_N^2(h)$ and $v(h)$ profiles. These techniques have been trialed at observing sites around the world, as well as at the local Mount John observatory. The development of a series of SCIDAR simulation and analysis tools presented in chapter 7, brought to light a number of problems with these techniques. New processing methods to overcome these inadequacies are discussed and demonstrated.

Problems with aspects of the inversion to obtain $C_N^2(h)$ profiles and the need to find binary stars of a suitable brightness and separation led to the investigation and development of a technique requiring only single star measurements. The advantage is that there are considerably more suitable single stars than there are binary stars. An outline of this technique and other alternatives to the SCIDAR methods are given in chapter 8.

Chapter 2

Mathematical Preliminaries

This chapter introduces the notation, terminology and some of the mathematical requirements necessary for the understanding of this thesis. Only general mathematics and concepts are outlined, with the theory necessary for specific problems in later chapters being introduced when required.

Section 2.1 introduces the notation used throughout this thesis to represent vectors, matrices, functions and complex numbers. Section 2.2 introduces a variety of special functions. A large number of special functions have been developed to help in the mathematical description of real problems. One example is the delta function, used to characterise linear systems and model point sources.

Linear systems theory which describes many real problems, including astronomical imaging, is outlined in section 2.3. The mathematical tools of convolution and correlation which are often used to simplify linear systems theory are also discussed. Section 2.4 introduces transform theory. Transforms are powerful in that they can be used to simplify the numerical processing of physical problems. Particular use is made of the Fourier transform as it describes the transformations of quantities in astronomy, microscopy and crystallography.

In addition, many of the properties of the Fourier transform are used throughout this thesis. The cosine, Hankel and Fresnel transforms, closely related to the Fourier transform, are also introduced. Throughout this thesis these transforms are used in their discrete forms and the corresponding discrete transforms are detailed in later sections of this chapter.

A number of areas relating to the processing of real images are presented in section 2.5. The majority of the computation required for image processing applications is performed on a digital computer. Consequently, there is often the need to represent continuous quantities digitally. Discretisation of a continuous quantity involves both sampling and quantisation. Sampling describes the process in which a continuous signal is approximated by a series of discrete points. The sampling theorem of Whittaker, Shannon and Nyquist is introduced in section 2.5.1. Also discussed are a variety of associated practical considerations such as undersampling and oversampling. Quantisation deals with the conversion of a sampled quantity into a quantity that is discrete in both time and amplitude. Finally, real world limitations place restrictions on the energy contained in and size of an image, and these are also discussed along with an introduction to positive images.

Physical phenomena can be described as either deterministic or random. A deterministic variable is completely predictable or "known", e.g. if a monochromatic light wave with a known complex field distribution is incident on a transparent aperture in a perfectly opaque screen, the resulting complex field distribution some distance away from the screen can be calculated precisely by using the well-established diffraction formulae of wave optics [67]. In contrast, a random quantity is "unknown" or unpredictable and is generally described by its statistical behaviour, for example the complex field resulting from a monochromatic light wave after passing through a region of unknown random atmospheric turbulence can no longer be calculated. Most signals of interest have a random component due to factors such as noise, introduced by optical components or the photon nature of light, and random distortions inherent when transmitting information through a channel or region of space. Probability theory, introduced in section 2.6, is used to model these quantities. Basic probability theory concepts are fundamental to all areas of research presented in this thesis.

The final area introduced is that of information theory (section 2.7). Information theory has made contributions to communications, statistical inference, probability, statistics and engineering and deals with mathematical modelling and analysis [71]. In particular, the key concepts of information and entropy are defined as needed for the investigation of maximum entropy based image restoration techniques discussed in chapters 5 and 7.

2.1 Notation

2.1.1 Vectors and matrices

A vector of components $(x_1, x_2, \ldots x_n)$ is often represented by the corresponding bold lower case letter, $\mathbf{x}$. A matrix describes a rectangular array of numbers, i.e.

$$\begin{bmatrix} x_{11} & x_{12} & \cdots & x_{1N} \\ x_{21} & x_{22} & & \\ \vdots & & \ddots & \vdots \\ & & & \\ x_{N1} & & \cdots & x_{NN} \end{bmatrix} \tag{2.1}$$

and is often represented by the corresponding bold upper case letter, $\mathbf{X}$. In both cases individual components are denoted by lower case subscripts. For example, x_n denotes the nth element of the vector $\mathbf{x}$ and a_{ij} is the element of the matrix $\mathbf{A}$ corresponding to the ith row and jth column. The size of a matrix or vector is given as the number of rows by the number of columns, e.g. $N \times N$ or $N \times 1$. A square matrix has the same number of rows and columns.

The transpose of a matrix $\mathbf{A}$, is denoted by $\mathbf{A}^T$. If

$$\mathbf{A} = \begin{bmatrix} a_{11} & a_{12} & \cdots & a_{1N} \\ a_{21} & a_{22} & & \\ \vdots & & \ddots & \vdots \\ & & & \\ a_{N1} & & \cdots & a_{NN} \end{bmatrix} \tag{2.2}$$

then

$$\mathbf{A}^T = \begin{bmatrix} a_{11} & a_{21} & \dots & a_{N1} \\ a_{12} & a_{22} & & \\ \vdots & & \ddots & \vdots \\ & & & \\ a_{1N} & & \dots & a_{NN} \end{bmatrix}. \tag{2.3}$$

The identity matrix, $\mathbf{I}$, is a diagonal matrix with 1s on the diagonal and 0s off the diagonal. It is analogous to 1 in numerical algebra. If there exists an $\mathbf{A}^{-1}$ such that $\mathbf{A}^{-1}\mathbf{A} = \mathbf{A}\mathbf{A}^{-1} = \mathbf{I}$, then $\mathbf{A}$ is an invertible matrix and $\mathbf{A}^{-1}$ is referred to as the inverse of $\mathbf{A}$.

When the inverse of $\mathbf{A}$ does not exist it is sometimes possible to compute the pseudoinverse of $\mathbf{A}$, denoted by $\mathbf{A}^+$, which inverts the parts of $\mathbf{A}$ that can be inverted. To compute the pseudoinverse it is first necessary to decompose the matrix $\mathbf{A}$ using the *singular value decomposition* (SVD) [137, 149]. For an $m \times n$ matrix $\mathbf{A}$ the SVD gives

$$\mathbf{A} = \mathbf{U}\Lambda\mathbf{V}^T, \tag{2.4}$$

where Λ is a diagonal matrix containing the singular values of $\mathbf{A}$, $\mathbf{U} = (U_1, U_2, \dots U_m)$, where the U_i are the left singular vectors of $\mathbf{A}$ and $\mathbf{V} = (V_1, V_2, \dots V_n)$, where the V_i are the right singular vectors of $\mathbf{A}$. The pseudoinverse of $\mathbf{A}$ is then calculated as

$$\mathbf{A}^+ = \mathbf{V}\Lambda^{-1}\mathbf{U}^T. \tag{2.5}$$

A real symmetric matrix or Hermitian matrix $\mathbf{A}$ can be decomposed into [151]

$$\mathbf{A} = \mathbf{U}\Lambda\mathbf{U}^T, \tag{2.6}$$

where Λ is a diagonal matrix containing the eigenvalues of $\mathbf{A}$ and $\mathbf{U} = (U_1, U_2, \dots, U_n)$, where the U_i are the orthonormal eigenvectors of $\mathbf{A}$.

2.1.2 Functions

Mathematical functions are used to represent various physical phenomena. Often these functions can be expressed in terms of explicit mathematical formulae of one or several

independent variables. For example, $f(x)$ denotes a function of a single variable x and $f(x,y)$ a function of two variables x and y, where the variables are enclosed in round brackets. Functions of two variables are the main focus throughout this thesis as they are used to represent images and extensively in the analysis of optical systems. A circumflex over a quantity, i.e. $\hat{f}(x,y)$, indicates that it is an estimate of the original quantity $f(x,y)$. When $f(x,y)$ is known to represent an image, i.e. the context of the problem is known, the (x,y) coordinates may be omitted leaving only f.

Consider the function

$$y = f(x). \tag{2.7}$$

If y is a *single-valued* function, then only one value of y for each x exists. Whereas, a *multiple-valued* function can have more than one value of y for each x. Functions in which the range of y values includes only real numbers are referred to as *real-valued* functions. Functions including real and complex numbers are known as *complex-valued* functions.

Many functions exhibit symmetries which can be used to simplify the data processing required for various applications. For example, functions are often assumed to be periodic for computation purposes. A *periodic* function,

$$f(x) = f(x + nT), \tag{2.8}$$

where n is an integer and T the period of f, repeats itself at intervals of T. An *even* function obeys

$$f(x) = f(-x), \tag{2.9}$$

whereas an *odd* function satisfies,

$$f(x) = -f(-x). \tag{2.10}$$

A conjugate-symmetric or *Hermitian* function satisfies,

$$f(x) = f^*(x), \tag{2.11}$$

where a superscript $*$ denotes complex conjugation.

A 2D function is said to be *separable* in a particular coordinate system if it can be written as a product of two 1D functions, each of which depends only on one of the coordinates. Thus $f(x, y)$ is separable if

$$f(x, y) = g(x)h(y) \tag{2.12}$$

where $g(x)$ is a function only of x and $h(y)$ is a function only of y.

2.1.3 Coordinate spaces

A particularly common function of space is the two-dimensional (2D) picture or image. Although images can be of any number of dimensions, the images discussed in this thesis are restricted to two dimensions.

Mathematical transforms are used to convert data represented by a particular coordinate system to an equivalent, but different, representation using a different set of coordinate vectors. An image exists in image space, spanned by its cartesian position vector, $\mathbf{x} = \{x, y\}$. Transformations between quantities in optics can often be described by the Fourier transform. The Fourier transform or spectrum of an image exists in Fourier space, (see section 2.4.1), spanned by the 2D position vector $\mathbf{u} = \{u, v\}$. Images are denoted by lower case roman letters with the corresponding upper case letters being used to denote their Fourier transforms.

2.1.4 Complex numbers

The concept of an imaginary quantity, essential to the theory of complex numbers, first appeared in the work of Giralamo Cardano in 1545 [182]. However, it was R. Bombelli who first saw the value in the use of imaginary quantities [182].

A complex number, c, is an expression of the form

$$c = a + jb, \tag{2.13}$$

where a and b are real numbers and j satisfies $j^2 = -1$. Here a and b are the *real* and *imag-*

inary parts of c, denoted by $\mathrm{Re}(c)$ and $\mathrm{Im}(c)$ respectively. Hence, an equivalent expression for c is

$$c = \mathrm{Re}(c) + j\mathrm{Im}(c). \tag{2.14}$$

Geometrically, a complex quantity $c = a + jb$ is represented by the point (a, b) in a rectangular coordinate system known as the complex plane (see Fig. 2.1), which is also spanned by the cartesian coordinates $\{x, y\}$. A complex number is said to be *real* when $b = 0$ and *pure imaginary* when $a = 0$. Real numbers exist on the x axis only, whereas pure imaginary numbers exist on the y axis.

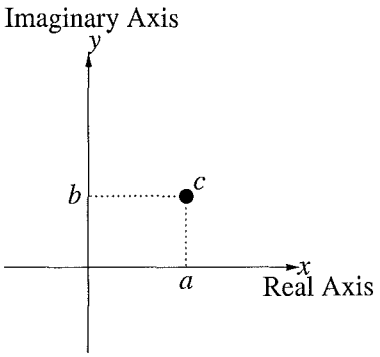

Figure 2.1: *Location of the complex number $c = a + jb$ in the complex plane.*

Perhaps the most useful way of representing complex numbers is in polar form, e.g.

$$c = r\exp(j\theta), \tag{2.15}$$

$$= |c|\exp\{j\mathrm{Ph}(c)\}. \tag{2.16}$$

Here $|c|$ and r are referred to as the magnitude, absolute value or modulus of c and θ or $\mathrm{Ph}(c)$ as the argument or phase of c, where

$$r = |c| = \sqrt{a^2 + b^2} = \sqrt{\mathrm{Re}(c)^2 + \mathrm{Im}(c)^2} \tag{2.17}$$

$$\theta = \mathrm{Ph}(c) = \tan^{-1}\left(\frac{b}{a}\right) = \tan^{-1}\left(\frac{\mathrm{Im}(c)}{\mathrm{Re}(c)}\right), \tag{2.18}$$

or alternatively,

$$a = r\cos\theta, \tag{2.19}$$

$$b = r\sin\theta \quad \text{and} \tag{2.20}$$

$$c = a + jb = r\left(\cos\theta + j\sin\theta\right). \tag{2.21}$$

The complex conjugate of c is denoted by c^* and is obtained by replacing each j with $-j$, i.e. $c^* = a - jb$. Note

$$cc^* = |c|^2 = |c^*|^2. \tag{2.22}$$

2.2 Special functions

In science and engineering a number of functions have evolved to allow for "nice" mathematical descriptions of real phenomena, where these functions tend to be piecewise in nature. The functions outlined in this section include the Dirac delta function, the comb and rectangle functions. In addition to the definition of these piecewise functions a number of additional functions are defined; the chirp, Gaussian, sinc and circle functions. The former are all separable functions and hence can be written as the product of equivalent one-dimensional functions. The circle function is a circularly symmetric function and can, therefore, be defined as a function of the radius alone.

2.2.1 Dirac delta function

The Dirac delta function, $\delta(x, y)$, often referred to as the impulse function, is used extensively in the analysis of linear systems. It is frequently used to represent point sources or model ideal realisations of physical quantities. For example, stars are often modelled as point sources.

In one-dimension (1D) the Dirac delta function is defined as

$$\delta(x) = \begin{cases} \infty & x = 0 \\ 0 & \text{otherwise} \end{cases}. \tag{2.23}$$

The two-dimensional (2D) Dirac delta function is defined as,

$$\delta(x,y) = \begin{cases} \infty & x=0, y=0 \\ 0 & \text{otherwise} \end{cases} . \tag{2.24}$$

A property of the delta function is that

$$\int_{-\infty}^{\infty}\int_{-\infty}^{\infty} \delta(x,y)dxdy = 1. \tag{2.25}$$

The delta function has a number of useful mathematical properties. The sifting property is useful in that it provides a means for "sifting" a single value of the function $f(x,y)$ [60],

$$f(x_0,y_0) = \int_{-\infty}^{\infty}\int_{-\infty}^{\infty} f(x,y)\delta(x-x_0,y-y_0)dxdy. \tag{2.26}$$

The discrete delta function is different to the continuous forms expressed in Eqs. (2.23) and (2.24). It is represented graphically as a spike of unit height, as opposed to infinity, located at the origin, (0,0). Discrete delta functions are illustrated in 1D and 2D in Fig. 2.2.

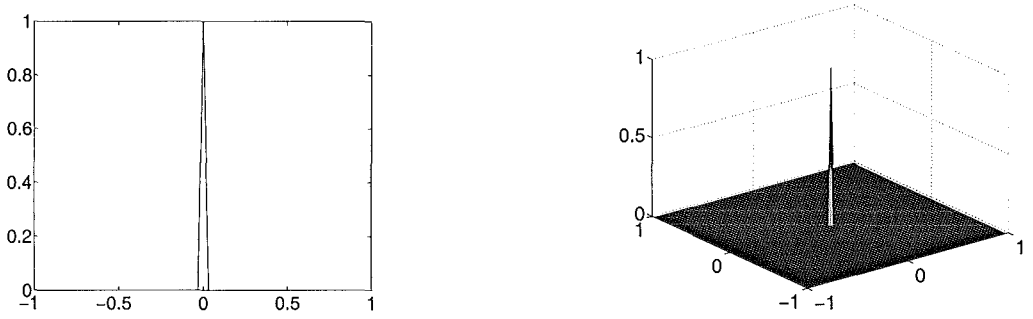

(a) (b)

Figure 2.2: *The Dirac delta function in (a) 1D and (b) 2D.*

2.2.2 Comb function

The comb function, $\text{comb}(x,y)$, is a relative of the impulse function. It describes an array of delta functions, given the name "comb" due to its physical comblike appearance. In 1D,

$$\text{comb}(x) = \sum_{n=-\infty}^{\infty} \delta(x-n), \tag{2.27}$$

where n takes on only integer values (see Fig. 2.3(a)). In 2D this becomes,

$$\text{comb}(x,y) = \sum_{n=-\infty}^{\infty}\sum_{m=-\infty}^{\infty}\delta(x-n,y-m) \tag{2.28}$$

$$= \text{comb}(x)\text{comb}(y), \tag{2.29}$$

where once again n and m are integers (see Fig. 2.3(b)). The comb function is commonly used in the sampling of continuous quantities (see section 2.5.1).

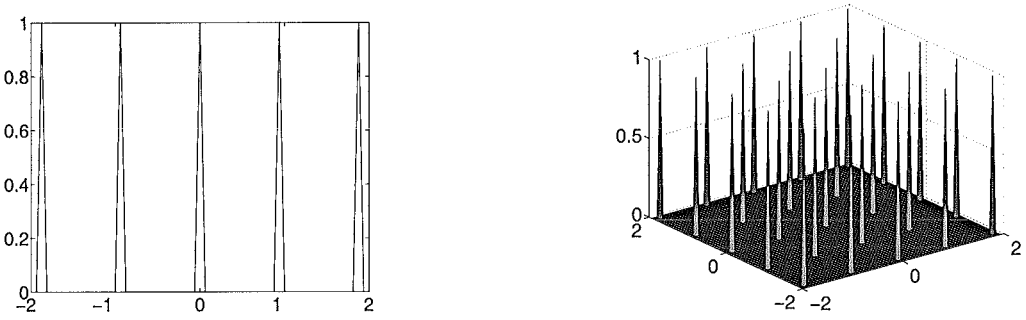

(a) (b)

Figure 2.3: *The comb function in (a) 1D and (b) 2D.*

2.2.3 Rectangle function

The rectangle function is also a piecewise function. In the time domain it can be used to represent a shutter operation in a camera, whereas in the spatial domain it is often used to describe the transmittance of an aperture. In this thesis square and rectangular apertures are used for the simulation of atmospheric turbulence, scintillation and Shack-Hartmann wavefront sensors. In 1D the rectangle function is defined as,

$$\text{rect}(x) = \begin{cases} 1 & |x| \leq \frac{1}{2} \\ 0 & \text{otherwise} \end{cases}. \tag{2.30}$$

This produces a rectangle of unity height, centred at the origin. Extension to 2D gives,

$$\text{rect}(x,y) = \begin{cases} 1 & |x| \leq \frac{1}{2}, |y| \leq \frac{1}{2} \\ 0 & \text{otherwise} \end{cases} \tag{2.31}$$

$$= \text{rect}(x)\text{rect}(y). \tag{2.32}$$

The rectangle function in one and two dimensions is illustrated in Fig. 2.4.

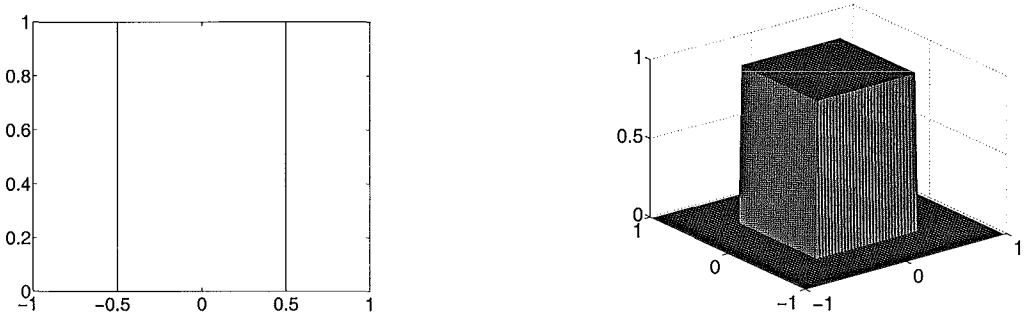

(a) (b)

Figure 2.4: *The rectangle function in (a) 1D and (b) 2D.*

2.2.4 Circle function

The circle function is useful for representing circular apertures inherent to components found in all optical systems and hence of particular relevance in this thesis. It is defined by,

$$\mathrm{circ}(r) = \begin{cases} 1 & r \leq 1 \\ 0 & \text{otherwise} \end{cases}, \tag{2.33}$$

where $r = \sqrt{x^2 + y^2}$ (see Fig. 2.5). The circle function can also be obtained by rotation of the 1D rectangle function.

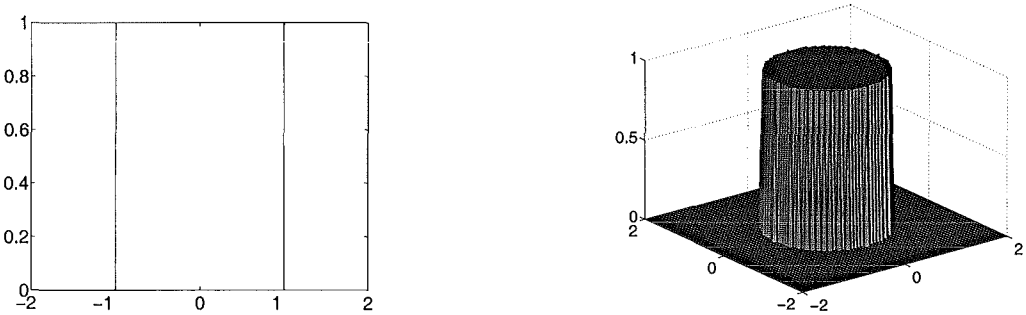

(a) (b)

Figure 2.5: *The circle function in (a) 1D and (b) 2D.*

2.2.5 Sinc function

The sinc function plays an important role in imaging theory. It is defined in 1D as [71],

$$\text{sinc}(x) = \frac{\sin(\pi x)}{\pi x}, \tag{2.34}$$

and arises from the Fourier transform of the rectangle function. It has a height of 1 at $x = 0$ and approaches 0 as $x \to \infty$, oscillating through positive and negative values. The width between the first two zero-crossings (nearest the origin) is two, with the function passing through zero at $x = \pm 1, \pm 2, \pm 3 \ \ldots \ \pm \infty$.

In 2D it is given by,

$$\begin{aligned} \text{sinc}(x, y) &= \frac{\sin(\pi x)}{\pi x}\frac{\sin(\pi y)}{\pi y} && (2.35) \\ &= \text{sinc}(x)\text{sinc}(y). && (2.36) \end{aligned}$$

Fig. 2.6 shows the sinc function in one and two dimensions.

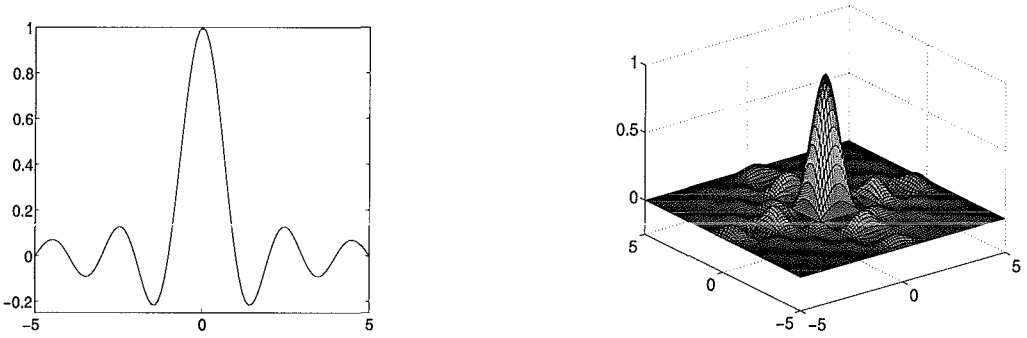

(a) (b)

Figure 2.6: *The sinc function in (a) 1D and (b) 2D.*

It should also be noted that the Fourier transform of the circle function, the Airy disk function, is important in optics and is introduced in chapter 3.

2.2.6 Gaussian function

The Gaussian function in 1D is defined as

$$\exp(-\pi x^2). \tag{2.37}$$

The corresponding representation in 2D is

$$\exp(-\pi(x^2+y^2)) = \exp(-\pi x^2)\exp(-\pi y^2). \tag{2.38}$$

See Fig. 2.7 for a graphical representation of the Gaussian function in one and two dimensions. The Gaussian function is used in chapter 4 to apply the more physically justifiable assumption of smoothness to the simulation of accurate scintillation.

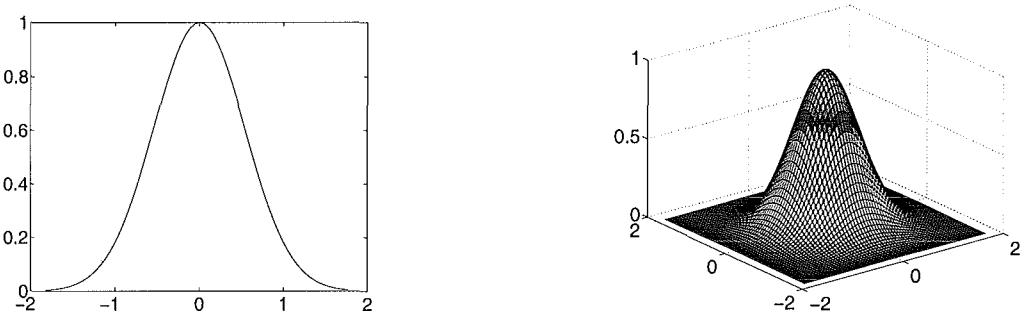

(a) (b)

Figure 2.7: *The Gaussian function in (a) 1D and (b) 2D.*

2.2.7 Chirp function

The chirp function is expressed in 1D as

$$q(x) = \exp(ja_x x^2), \tag{2.39}$$

where a_x is a real constant. In 2D this expression becomes

$$q(x,y) = \exp(ja_x x^2)\exp(ja_y y^2), \tag{2.40}$$

where a_x and a_y are real constants. It is a function of uniform magnitude and quadratic phase, hence it is a complex-valued function. The real and imaginary parts of a sample chirp function are illustrated in Fig. 2.8.

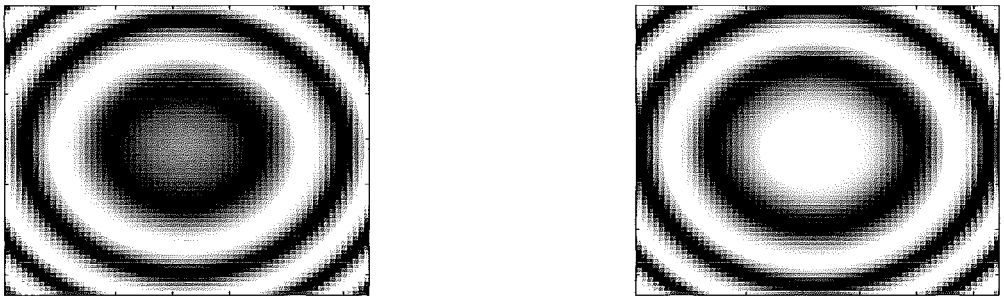

(a) (b)

Figure 2.8: *A sample chirp function. (a) Real part and (b) imaginary part.*

The chirp function has a number of useful properties and is used extensively in the analysis of the diffractive process. It describes the effect of a convex lens on the field traversing the lens and the degree of defocus in the imaging system. In addition, it describes the spreading within the diffractive process. Hence, knowledge of the chirp makes it possible to determine how the input is spread to the output.

2.3 Linear systems

Many physical processes can be described or modelled by linear systems theory. It is for this reason that many mathematical tools, for example convolution and correlation, have been developed to simplify these systems. Consider the linear system represented in Fig. 2.9 (c.f. Fig. 1.3). Let the linear system transformation that maps the input $f(x,y)$ to the output $g(x,y)$ be represented by $H\{\}$, i.e.

$$g(x,y) = H\{f(x,y)\}. \tag{2.41}$$

A linear system obeys the principle of superposition, that is the response to any number of inputs is equal to the sum of the responses to each individual input. This can be illustrated mathematically as

$$\begin{aligned} H\{c_1 f_1(x,y) + c_2 f_2(x,y)\} &= c_1 H\{f_1(x,y)\} + c_2 H\{f_2(x,y)\} \\ &= c_1 g_1(x,y) + c_2 g_2(x,y) \end{aligned}$$

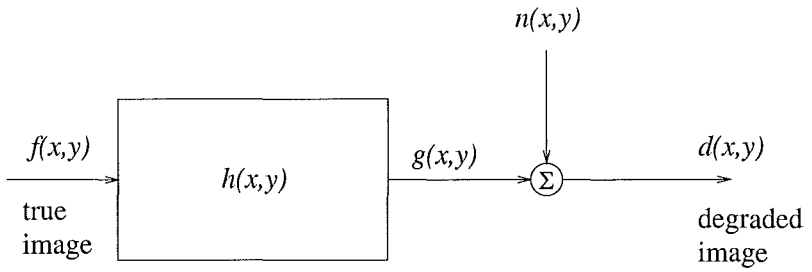

Figure 2.9: *Simple degradation model.*

where c_1 and c_2 are arbitrary constants.

A linear system is characterised by its response to a point source or delta function, which is referred to as the impulse response in 1D and the point spread function (PSF) in 2D. The point spread function is aptly named as it describes the transformation or spreading that a single point undergoes as it passes through the system. Since an image can be considered to be a sum of weighted point sources, the response of a linear system to an image is a sum of scaled and shifted versions of the point spread function. Mathematically the PSF is defined as

$$h(x, y; \xi, \eta) = H\{\delta(x, y; \xi, \eta)\}, \tag{2.42}$$

where $h(x, y; \xi, \eta)$ can describe both space variant and space invariant point spread functions. An important subset of linear systems, are linear time and space invariant systems, in which $h(x, y; \xi, \eta) = h(x-\xi, y-\eta)$. In communications theory a *matched filter* describes any system in which the output is a time reversed and delayed version of the input signal, hence linear time and shift invariant systems can be described as matched filters. Throughout this thesis a linear system is taken to mean a linear shift invariant (LSI) system. In practice, no system is shift invariant over an entire plane, but can be considered to be shift invariant over small regions, known as *isoplanatic patches*, in which the assumption is valid. It should be noted that regions of space varying phenomenon can be assumed to be isoplanatic, the images obtained from these regions are then assumed to behave as if imaged from a linear space invariant system with an appropriate choice of point spread function.

The output of a linear system to an input image $f(\xi, \eta)$ that utilises the sifting property of

the delta function (Eq. (2.26)) is

$$\begin{aligned} g(x,y) &= H\left\{\int_{-\infty}^{\infty}\int_{-\infty}^{\infty} f(\xi,\eta)\delta(x,y;\xi,\eta)d\xi d\eta\right\} \\ &= \int_{-\infty}^{\infty}\int_{-\infty}^{\infty} f(\xi,\eta)H\left\{\delta(x,y;\xi,\eta)\right\}d\xi d\eta \\ &= \int_{-\infty}^{\infty}\int_{-\infty}^{\infty} f(\xi,\eta)h(x,y;\xi,\eta)d\xi d\eta. \end{aligned} \tag{2.43}$$

2.3.1 Convolution

Substitution of the linear shift invariant PSF, $h(x-\xi, y-\eta)$, into Eq. (2.43) gives the convolution integral,

$$g(x,y) = \int_{-\infty}^{\infty}\int_{-\infty}^{\infty} f(\xi,\eta)h(x-\xi,y-\eta)d\xi d\eta \tag{2.44}$$

$$= f(x,y) \odot h(x,y) \tag{2.45}$$

which mathematically describes the process of convolution. Here $\odot$ denotes the 2D convolution operator and $f(x,y)$ and $h(x,y)$ are termed the components of the convolution $g(x,y)$. An *irreducible* function cannot be expressed as the convolution of two or more components. A function that can be expressed as a convolution of two or more components is termed a *composite* function. Hence, the function $f(x)$ is composite if

$$f(x) = f_1(x) \odot f_2(x) \ldots f_N(x), \tag{2.46}$$

for an integer value $N > 1$.

The convolution operation has a number of properties that are relevant to this thesis, and are listed below. The corresponding proofs can be found in Gaskill [60].

Commutative property

$$f(x) \odot h(x) = h(x) \odot f(x). \tag{2.47}$$

Distributive property

$$[av(x) + bw(x)] \odot h(x) = a\left[v(x) \odot h(x)\right] + b\left[w(x) \odot h(x)\right]. \tag{2.48}$$

Shift invariance

If

$$f(x) \odot h(x) = g(x), \tag{2.49}$$

then

$$f(x - x_0) \odot h(x) = g(x - x_0). \tag{2.50}$$

Associative property

$$[v(x) \odot w(x)] \odot h(x) = v(x) \odot [w(x) \odot h(x)]. \tag{2.51}$$

Convolution with delta functions

$$f(x) \odot \delta(x - x_0) = f(x_0). \tag{2.52}$$

Smoothing

Given $g(x) = f(x) \odot h(x)$ it is generally true that $g(x)$ is smoother than either $f(x)$ or $h(x)$. The process of convolution tends to round sharp detail present in the convolution components, as it can be considered to be a low pass filtering operation.

2.3.2 Correlation

The correlation of two real signals $f(x, y)$ and $h(x, y)$ is termed the cross correlation function and is defined as

$$f(x, y) * h(x, y) = \int_{-\infty}^{\infty} \int_{-\infty}^{\infty} f(\xi, \eta) h(x + \xi, y + \eta) d\xi d\eta, \tag{2.53}$$

where $*$ denotes the 2D correlation operator. It is calculated in a similar way to the convolution integral. In fact, the correlation operation can be represented in terms of the convolution operation, i.e.

$$f(x, y) * h(x, y) = f(x, y) \odot h(-x, -y). \tag{2.54}$$

When the functions are complex the cross correlation is defined by

$$f(x,y) * h^*(x,y) = \int_{-\infty}^{\infty}\int_{-\infty}^{\infty} f(\xi,\eta)h^*(x+\xi,y+\eta)d\xi d\eta, \tag{2.55}$$

where $h^*(x,y)$ denotes the complex conjugate of $h(x,y)$. The autocorrelation function, a special case of the correlation function, describes the correlation of a signal with its conjugate,

$$A_f = f(x,y) * f^*(x,y) = \int_{-\infty}^{\infty}\int_{-\infty}^{\infty} f(\xi,\eta)f^*(x+\xi,y+\eta)d\xi d\eta. \tag{2.56}$$

The correlation function behaves in a similar manner to the convolution function with one significant difference. The correlation operation does not commute, i.e.

$$f(x,y) * h(x,y) \neq h(x,y) * f(x,y), \tag{2.57}$$

indicating that the correlation operation is not shift invariant, since if f and h are identical but offset, then $f * h$ and $h * f$ will produce peaks that are displaced by equal amounts on opposite sides of the origin.

The correlation of two signals $f(x,y)$ and $h(x,y)$ gives a direct measure of the similarity of the fluctuations in each. It assigns a set of numerical values to the "closeness" between the signals $f(x,y)$ and $h(x,y)$ [176]. A single peak of the correlation function at the origin indicates an exact correlation. If the correlation function peaks for a particular (x,y), then the two signals achieve the closest match when displaced by that amount. If a negative peak occurs at the origin, the two signals are anticorrelated, in that the fluctuations are similar in a negative sense. Finally, small correlation values indicate little or no correlation.

2.4 Transform theory

Transforms are used as mathematical tools to replace a problem that cannot be solved easily with one that can be readily solved. For example, the use of a suitable transform, e.g. the Fourier transform or the Laplace transform, aids the solution of a differential equation by converting it to an algebraic expression. A number of transforms are used throughout this

thesis; the Fourier, Hankel, Fresnel and cosine transforms. However, in most cases it is the discrete versions of the transforms that are utilised.

The Fourier transform (FT) has by far the largest application in this thesis. It is a powerful tool, especially in the analysis of linear systems. The Fourier transform of a function decomposes it into a linear combination of exponentials of the form $\exp(j2\pi ft)$. The response of a linear system is then the sum of the scaled and shifted $\exp(j2\pi ft)$ terms. In addition, the Fourier transform describes many artificial and physical processes involving wave phenomena, e.g. the operation of antennae, lenses, eyes and ears.

There are many variations and special cases of the FT. The Hankel transform (HT), sometimes referred to as the Fourier-Bessel transform, is one example. It corresponds to the FT of a circularly symmetric function. The 2D FT of a circularly symmetric function reduces to the 1D Hankel transform, with the result also being circularly symmetric. Another variation of the FT is the Fresnel transform. In this case the FT kernel is modified by a quadratic phase term. It describes an approximation made to simplify calculation of diffraction patterns in diffraction theory and is introduced with the concept of diffraction in chapter 3. Finally, the cosine transform (CT) is also very similar to the FT except where the FT assumes periodicity at the image boundary the CT assumes reflection. As a result it decomposes the function of interest into a linear combination of cosines.

2.4.1 Fourier transform

The Fourier transform (FT) is an example of an integral transform, where an integral transform traditionally refers to the generalised expansion, as an integral rather than a series sum, of a function in a continuum of oscillating exponential or related functions [176]. Other integral transforms include the Hankel, Laplace and cosine transforms. The integral transform of a function $f(t)$ defined on $a \leq t \leq b$ and denoted by $I\{f(t)\}$ is [45]:

$$I\{f(t)\} = \int_a^b K(t,k)f(t)dt, \tag{2.58}$$

where $K(t,k)$ represents the kernel and k the transformation variable.

The Fourier transform is a generalisation of the Fourier series, therefore, it is necessary to introduce the concept of a Fourier series (FS). A periodic signal $f(t)$, of period T_0, can be expanded into a Fourier series provided it satisfies the Dirichlet conditions [60, 71]:

1. $f(t)$ is single-valued within the interval $-T_0/2 < t < T_0/2$
2. $f(t)$ has a finite number of discontinuities in $-T_0/2 < t < T_0/2$
3. $f(t)$ has a finite number of maxima and minima in $-T_0/2 < t < T_0/2$ and
4. $f(t)$ is absolutely integrable on $-T_0/2 < t < T_0/2$, i.e.

$$\int_{-T_0/2}^{T_0/2} |f(t)|dt < \infty. \tag{2.59}$$

The Fourier series expansion of a periodic signal $f(t)$ is given by [71]

$$f(t) = a_0 + \sum_{n=1}^{\infty}[a_n \cos(2\pi n f_0 t) + b_n \sin(2\pi n f_0 t)], \tag{2.60}$$

where

$$f_0 = \frac{1}{T_0} \tag{2.61}$$

$$a_0 = \frac{1}{T_0}\int_{-T_0/2}^{T_0/2} f(t)dt \tag{2.62}$$

$$a_n = \frac{2}{T_0}\int_{-T_0/2}^{T_0/2} f(t)\cos(2\pi n f_0 t)dt \quad n = 1, 2, \ \ldots \infty \quad \text{and} \tag{2.63}$$

$$b_n = \frac{2}{T_0}\int_{-T_0/2}^{T_0/2} f(t)\sin(2\pi n f_0 t)dt \quad n = 1, 2, \ \ldots \infty. \tag{2.64}$$

An alternative, but equivalent, expression for the Fourier series expansion of $f(t)$ is in complex or exponential form. Here,

$$f(t) = \sum_{n=-\infty}^{\infty} c_n \exp(j2\pi n f_0 t), \tag{2.65}$$

where

$$c_n = \frac{1}{T_0}\int_{-T_0/2}^{T_0/2} f(t)\exp(-j2\pi n f_0 t)dt \quad n = -\infty, \ \ldots, -2, -1, 0, 1, 2, \ \ldots \infty. \tag{2.66}$$

A FS expansion of a periodic signal is equivalent to resolving the signal into its various harmonic or complex exponential components. Decomposition of a non-periodic signal in terms of these same complex exponential functions requires use of the Fourier transform. This is obtained by setting $T_0 \to \infty$ in Eq. (2.66). Complex exponentials are the eigenfunctions of linear space invariant systems, i.e. the output of a LSI system when a complex exponential is input to it is another complex exponential.

The FT of a 1D function $f(t)$ is defined as [71],

$$\mathcal{F}\{f(t)\} = F(f) = \int_{-\infty}^{\infty} f(t)\exp(-j2\pi ft)dt \tag{2.67}$$

where $\mathcal{F}\{\}$ denotes the FT operation and has the form of an integral transform defined in Eq. (2.58). Given $F(f)$, the original signal is recovered using the inverse Fourier transform (IFT), defined as

$$\mathcal{F}^{-1}\{F(f)\} = \int_{-\infty}^{\infty} F(f)\exp(j2\pi ft)df \tag{2.68}$$

where $\mathcal{F}^{-1}\{\}$ denotes the inverse Fourier transform operation. $F(f)$ is termed the spectrum of $f(t)$ and $f(t)$ and $F(f)$ form a Fourier transform pair indicated in this thesis by a double ended arrow, i.e. $f(t) \leftrightarrow F(f)$. This also emphasises the invertible relationship existing between an image and its transform, i.e.

$$\begin{aligned} \mathcal{F}\{f(t)\} &= F(f) \\ \mathcal{F}^{-1}\{F(f)\} &= f(t). \end{aligned}$$

Throughout this thesis 2D signals are the main focus and hence the 2D FT is required. The 2D FT kernel is a function of the spatial domain variables $\{x, y\}$ and Fourier domain variables $\{u, v\}$. The 2D forward and inverse FTs of $f(x, y)$ and $F(u, v)$ are given by [66],

$$F(u,v) = \int_{-\infty}^{\infty}\int_{-\infty}^{\infty} f(x,y)\exp(-j2\pi(ux+vy))dxdy \tag{2.69}$$

and

$$f(x,y) = \int_{-\infty}^{\infty}\int_{-\infty}^{\infty} F(u,v)\exp(j2\pi(ux+vy))dudv. \tag{2.70}$$

The 2D FT is an example of a separable transform since it can be performed by a series of operations in each dimension. For example, it is possible to write Eq. (2.69) as

$$F(u,v) = \int_{-\infty}^{\infty} \left[\int_{-\infty}^{\infty} f(x,y)\exp(-j2\pi ux)dx \right] \exp(-j2\pi vy)dy \tag{2.71}$$

and perform a 1D FT in the x-direction followed by a 1D FT along the y-direction.

The FT properties relevant to this thesis are outlined below and summarised in Table 2.1 which also includes some additional properties. The relevant properties are stated here for the 2D case only. Proofs and additional properties can be found in Goodman [66] and Gaskill [60].

Linearity theorem

If $f(x,y) \leftrightarrow F(u,v)$, $h(x,y) \leftrightarrow H(u,v)$ and a and b are arbitrary constants, then

$$\begin{aligned} \mathcal{F}\{af(x,y) + bh(x,y)\} &= a\mathcal{F}\{f(x,y)\} + b\mathcal{F}\{h(x,y)\} & (2.72) \\ &= aF(u,v) + bH(u,v). & (2.73) \end{aligned}$$

Thus the spectrum of a sum of signals can be computed by adding their individual spectra.

Similarity theorem

If $f(x,y) \leftrightarrow F(u,v)$ and a and b are real non-zero constants, then

$$\mathcal{F}\{f(ax,by)\} = \frac{1}{|ab|} F\left(\frac{u}{a}, \frac{v}{b}\right). \tag{2.74}$$

This indicates that if the width of a function is increased its FT becomes narrower. Hence stretching in the spatial domain results in a contraction in the frequency domain.

Shift theorem

If $f(x,y) \leftrightarrow F(u,v)$ and a and b are real-valued constants, then

$$\mathcal{F}\{f(x-a,y-b)\} = F(u,v)\exp(-j2\pi(ua+vb)). \tag{2.75}$$

The FT of a function shifted in the spatial domain contains a linear phase shift in the frequency domain.

Parseval's theorem

If $f(x,y) \leftrightarrow F(u,v)$,

$$\int_{-\infty}^{\infty}\int_{-\infty}^{\infty} |f(x,y)|^2 dxdy = \int_{-\infty}^{\infty}\int_{-\infty}^{\infty} |F(u,v)|^2 dudv. \tag{2.76}$$

Eq. (2.76) indicates that no energy is lost as a result of the transformation process.

Convolution theorem

If $f(x,y) \leftrightarrow F(u,v)$ and $h(x,y) \leftrightarrow H(u,v)$,

$$\mathcal{F}\{f(x,y) \odot h(x,y)\} = F(u,v)H(u,v). \tag{2.77}$$

This is a very important property of the FT and is used extensively throughout this thesis. The FT of a convolution is simply given by the product of the individual transforms. The converse is also true, i.e.

$$\mathcal{F}\{f(x,y)h(x,y)\} = F(u,v) \odot H(u,v). \tag{2.78}$$

Autocorrelation theorem

If $f(x,y) \leftrightarrow F(u,v)$,

$$\mathcal{F}\{f(x,y) * f^*(x,y)\} = |F(u,v)|^2 \tag{2.79}$$

and similarly,

$$\mathcal{F}\{|f(x,y)|^2\} = F(u,v) * F^*(u,v). \tag{2.80}$$

Note that $|F(u,v)|^2$ is the power spectral density (PSD) or power spectrum of $f(x,y)$. If $f(x,y)$ is real, its autocorrelation is real and even and its power spectrum is real and even.

2.4.2 Hankel transform

Functions exhibiting radial or circular symmetry are frequently encountered in the analysis of optical systems due to the circular nature of the system components, for example, lenses and aperture stops [60]. A circularly symmetric function can be written as a function of the radius only, i.e.

$$g(r,\theta) = g(r). \tag{2.81}$$

Property	Spatial domain	Frequency domain
Definition	$f(x,y)$	$F(u,v)$
Linearity	$af(x,y)+bh(x,y)$	$aF(u,v)+bH(u,v)$
Similarity (Time scaling)	$f(ax,by)$	$\frac{1}{\lvert ab\rvert}F\left(\frac{u}{a},\frac{v}{b}\right)$
Shift (in time)	$f(x-a,y-b)$	$F(u,v)\exp[-j2\pi(ua+vb)]$
Shift (in frequency)	$f(x,y)\exp(-j2\pi(ax+by))$	$F(u-a,v-b)$
Duality	$F(x,y)$	$f(-u,-v)$
Convolution	$f(x,y)\odot h(x,y)$	$F(u,v)H(u,v)$
Cross correlation	$f(x,y)*h(x,y)$	$F(u,v)H(-u,-v)$
Autocorrelation	$f(x,y)*f^*(x,y)$	$\lvert F(u,v)\rvert^2$
Multiplication in time	$f(x,y)h(x,y)$	$F(u,v)\odot H(u,v)$
Conjugate Functions	$f^*(x,y)$	$F^*(-u,-v)$
Differentiation	$\frac{\partial f(x,y)}{\partial x}$	$j2\pi uF(u,v)$

Table 2.1: *Fourier transform properties.*

A property of a circularly symmetric function is that its transform is also circularly symmetric and can be found using the 1D Fourier-Bessel or Hankel transform of zeroth order. The Hankel transform of $g(r)$, denoted by $G(\rho)$, is given by [66]

$$G(\rho)=\mathcal{H}\{g(r)\}=2\pi\int_0^\infty g(r)J_0(2\pi\rho r)rdr, \tag{2.82}$$

where $J_0(x)$ is a zeroth order Bessel function of the first kind. The inverse Hankel transform which is used to obtain $g(r)$ from $G(\rho)$ is defined as [66]

$$g(r)=\mathcal{H}^{-1}\{G(\rho)\}=2\pi\int_0^\infty G(\rho)J_0(2\pi\rho r)\rho d\rho. \tag{2.83}$$

Eqs. (2.82) and (2.83) clearly show that the Hankel transform is self reciprocal, that is the forward and inverse kernels are identical.

The zeroth order Hankel transform is in fact a special case of the Hankel transform of order v, where [60]

$$U(\rho;v)=2\pi\int_0^\infty u(r)J_v(2\pi\rho r)rdr, \tag{2.84}$$

and

$$u(r) = 2\pi \int_0^\infty U(\rho; v) J_v(2\pi r\rho)\rho d\rho. \tag{2.85}$$

Here J_v is a vth order Bessel function of the first kind. Since only the zeroth order Hankel transform is related to the Fourier transform and of relevance to this thesis any future reference to the Hankel transform refers to the zeroth order Hankel transform.

2.4.3 Cosine transform

The cosine transform, also known as the Fourier cosine transform, is an example of another integral transform which is a special case of the Fourier transform. When the function $f(t)$, defined on $(-\infty, \infty)$, is an even function, the Fourier transform of $f(t)$ reduces to the cosine transform of $f(t)$. The cosine transform and its inverse are defined by [116]

$$F_c(k) = \mathcal{F}_c\{f(t)\} = \sqrt{\frac{2}{\pi}} \int_0^\infty \cos(kt) f(t) dt \tag{2.86}$$

and

$$f(t) = \mathcal{F}_c^{-1}\{F_c(k)\} = \sqrt{\frac{2}{\pi}} \int_0^\infty \cos(kt) F_c(k) dk. \tag{2.87}$$

The discrete version of this transform, known as the DCT, is of interest in this thesis and is outlined in section 2.5.3. It is used as an alternative to the FFT to avoid spectral leakage effects in the numerical simulation of scintillation (see chapter 4).

2.5 Real world images

2.5.1 Sampling

When processing data with the aid of a digital computer it is necessary to describe continuous data by its values at a discrete set of points. It is also often desirable to describe a function by a discrete number of points when dealing with the limited data handling capabilities of all physical devices. The value of the image at the sampled points corresponds to the original function values at those points when performing point sampling. When performing area sampling, as in CCDs [177] and Shack-Hartmann sensors, each sample value is obtained by integrating over each sensor and corresponds to the average of the light falling

on it. In most cases a set of equispaced values of an image or signal are recorded to provide an approximation to it. If the samples are taken sufficiently close to each other, the sampled values provide an accurate representation of the original function [66]. The original function can then be reconstructed from its samples by interpolation. In fact, provided a function is bandlimited it can be reconstructed exactly if sampled sufficiently closely.

For point sampling, considered here, the sample values correspond to the function values evaluated at the sampling points. The sampling interval, $\triangle$, describes the separation of the sampling points in 1D. In 2D the sampling interval is denoted by $\triangle x$ in the x coordinate direction and $\triangle y$ in the y coordinate direction. The sampling rate (sometimes referred to as the sampling frequency) is the reciprocal of the sampling interval, i.e. $f_s = 1/\triangle$. As $\triangle \to 0$ the sampled function tends to the original function.

Let $g(t)$ describe a continuous bandlimited 1D function. Its Fourier transform, $G(f)$, illustrated in Fig. 2.10(a), is clearly bandlimited since it is only non-zero for $-W < G(f) < W$. Let $g_s(t)$ denote the sampled version of $g(t)$, where

$$g_s(t) = \sum_{n=-\infty}^{\infty} \delta(t - n\triangle) g(t) \tag{2.88}$$

$$= \text{comb}\left(\frac{t}{\triangle}\right) g(t). \tag{2.89}$$

The corresponding sampling rate or frequency is $1/\triangle$. The spectrum of $g_s(t)$ is obtained by applying the convolution theorem (section 2.3.1) to Eq. (2.89),

$$\begin{aligned} G_s(f) &= \mathcal{F}\left\{\text{comb}\left(\frac{t}{\triangle}\right)\right\} \odot \mathcal{F}\{g(t)\} \\ &= \triangle \text{comb}(\triangle f) \odot G(f) \\ &= \triangle \sum_{n=-\infty}^{\infty} \delta\left(f - \frac{n}{\triangle}\right) \odot G(f) \\ &= \triangle \sum_{n=-\infty}^{\infty} G\left(f - \frac{n}{\triangle}\right) \\ &= \frac{1}{f_s} \sum_{n=-\infty}^{\infty} G(f - nf_s). \end{aligned} \tag{2.90}$$

Therefore, the sampling of a signal causes its spectrum to be repeated periodically as

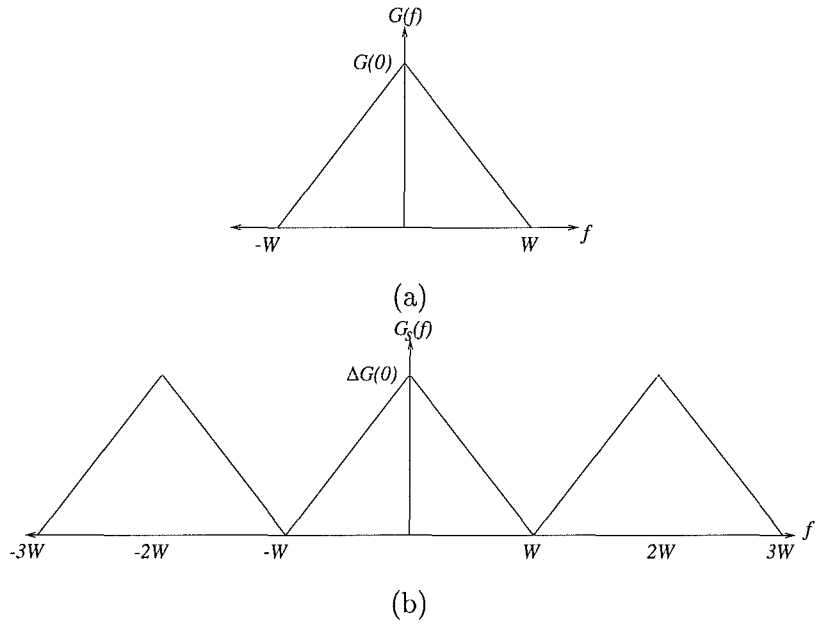

Figure 2.10: *(a) The spectrum of $g(t)$. (b) The spectrum of $g_s(t)$.*

illustrated in Fig. 2.10(b). Inspection of Eq. (2.90) indicates that the repeated spectra of $G(f)$ can be separated provided $G(f) = 0$ for $|f| \geq W$ and

$$f_s \geq 2W. \tag{2.91}$$

This is equivalent to requiring

$$\triangle \leq \frac{1}{2W}. \tag{2.92}$$

Two-dimensional spectra can be recovered provided $G(u, v) = 0$ for $|x| \geq W_u$, $|y| \geq W_v$ and

$$\triangle x \leq \frac{1}{2W_u}, \quad \triangle y \leq \frac{1}{2W_v}. \tag{2.93}$$

Eqs. (2.92) and (2.93) define the Whittaker-Shannon sampling theorem [60, 66]. The theorem states that any bandlimited function can be specified exactly by its sampled values, taken at regular intervals, provided that these intervals do not exceed some critical sampling interval. The critical sampling interval, termed the Nyquist interval, is given by Eq. (2.92) and the corresponding Nyquist sampling rate is given by equality in Eq. (2.91).

The continuous spectrum $G(f)$ can be recovered by the multiplication of $G_s(f)$ with a

rectangular window of width $2W$, i.e.

$$G(f) = G_s(f)\text{rect}\left(\frac{f}{2W}\right), \tag{2.94}$$

which is equivalent to convolving $g_s(t)$ with a sinc function in the time domain to give

$$g(t) = g_s(t) \odot 2W\text{sinc}(2Wt). \tag{2.95}$$

When the sampling rate is less than the Nyquist sampling rate the spectrum once again consists of repeated versions of $G(f)$, however they are now overlapped (see Fig. 2.11). Multiplication of $G_s(f)$ by a rectangular window, of width $2W$, will no longer return $G(f)$. Some of the signal information is lost due to *aliasing*, where high frequency components of the signal appear to take on the identity of a lower frequency in the spectrum or in other words high frequencies masquerade as low frequencies.

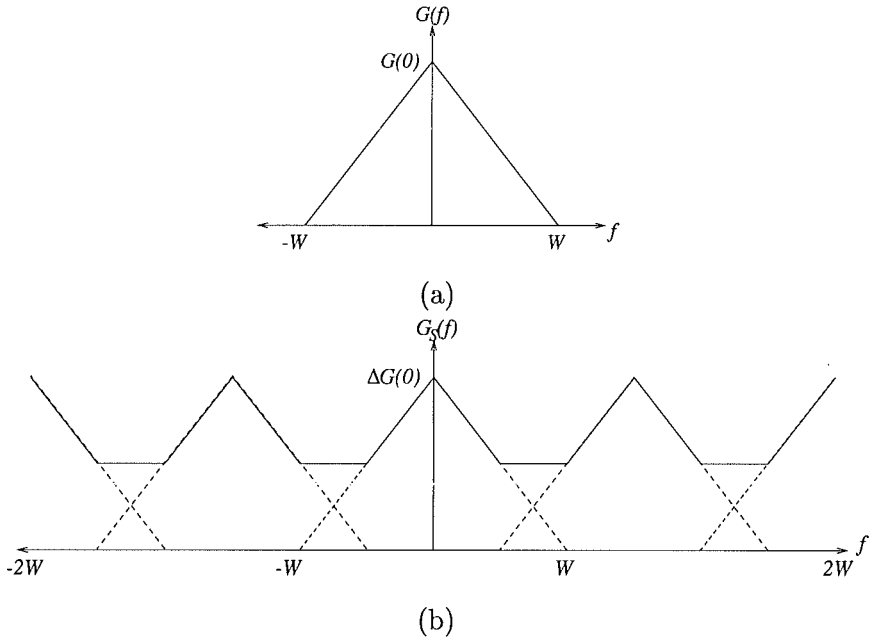

Figure 2.11: *(a) The spectrum of $g(t)$. (b) The spectrum of an under-sampled version of $g(t)$.*

Another example of aliasing is presented in Fig. 2.12, which illustrates 1rad/s and 11rad/s sinewaves. If sampled at 10rad/s, the corresponding function values at the sample points,

indicated by an 'O' in Fig. 2.12, are identical making it impossible to determine the frequency of the original signal. Generally the low frequency sinewave would be reconstructed from these samples, as it would be assumed that the original signal was sampled according to the Nyquist sampling criterion.

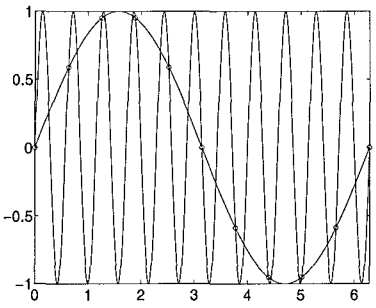

Figure 2.12: *The aliasing phenomenon. Two sinewaves of 1rad/s and 11rad/s produce identical sample values when sampled at 10rad/s.*

If $g(t)$ is now sampled at a rate higher than the Nyquist rate, its Fourier transform consists of repeated versions of $G(f)$ surrounded by empty space (see Fig. 2.13). This is often referred to as zeropacking. In this case the original spectrum can be more easily recovered since the choice of window function is not restricted to the rectangular window.

2.5.2 Discrete Fourier transform

The Fourier transform of a sampled image is given by the discrete Fourier transform (DFT). The DFT provides a simplistic approximation to the continuous FT. Consider the 1D continuous FT integral, Eq. (2.67),

$$X(f) = \int_{-\infty}^{\infty} x(t)\exp(-j2\pi ft)dt. \tag{2.96}$$

It is not practical to use this for real data as only a finite amount of data is available. To combat this the DFT assumes that the data is periodic outside the range of available data, an assumption that may not be physically justifiable.

The assumption of periodicity made by the DFT, allows the FT to be calculated via a

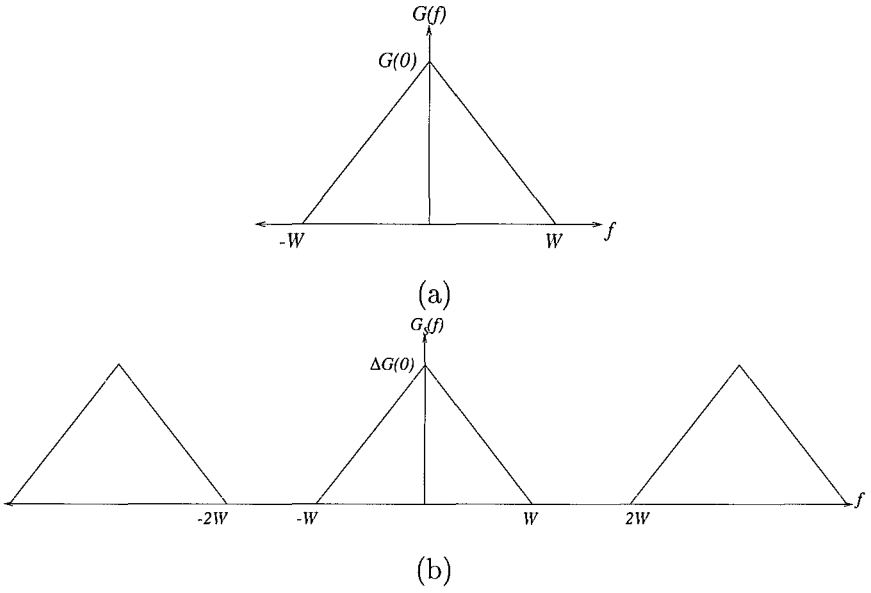

Figure 2.13: *(a) The spectrum of $g(t)$. (b) The spectrum of an oversampled version of $g(t)$.*

Fourier series calculation. Hence,

$$x(t) = \sum_{k=-\infty}^{\infty} X(k)\exp(j2\pi kft), \tag{2.97}$$

where

$$X(k) = \frac{1}{T}\int_0^T x(t)\exp(-j2\pi kft)dt \tag{2.98}$$

and T is the period of the available data. Eq. (2.98) is then converted into a summation using a crude rectangular approximation of N rectangles, each $\triangle$ wide. Ultimately, this gives the 1D DFT,

$$X(k) = \frac{1}{N}\sum_{n=0}^{N-1} x(n)\exp\left(-j\frac{2\pi nk}{N}\right). \tag{2.99}$$

The inverse discrete Fourier transform (IDFT), in 1D, is

$$x(n) = \sum_{k=0}^{N-1} X(k)\exp\left(j\frac{2\pi nk}{N}\right). \tag{2.100}$$

In 2D the forward and inverse DFTs are given by [40]

$$F(u,v) = \sum_{x=0}^{N-1}\sum_{y=0}^{N-1} f(x,y)\exp\left(-j\frac{2\pi(ux+vy)}{N}\right) \tag{2.101}$$

and

$$f(x,y) = \frac{1}{N^2} \sum_{u=0}^{N-1} \sum_{v=0}^{N-1} F(u,v) \exp\left(j \frac{2\pi(ux+vy)}{N}\right). \tag{2.102}$$

Since quantities that use the DFT are sampled, both the data and its transform are assumed periodic. This assumption of periodicity can lead to spectral leakage. If the available data is equal to the period of the original data, application of the DFT introduces no errors as illustrated in Fig. 2.14. The signal data in Fig. 2.14(a)(i) is equal to one period of the underlying signal illustrated in Fig. 2.14(a)(ii). Therefore, application of the DFT produces the correct transform (Fig. 2.14(a)(iii)). When the available signal data, Fig. 2.14(b)(i), is not equal to an exact multiple of the true period of the underlying signal, the DFT still assumes the signal is periodic, as shown in Fig. 2.14(b)(ii), producing the spectrum in Fig. 2.14(b)(iii). The periodicity assumption of the DFT means that when the signal in Fig. 2.14(b)(i) is repeated, discontinuities are introduced into the underlying signal assumed by the algorithm. Extra frequencies are required to represent this discontinuity and hence, some of the signal energy that should be located at the frequencies contained in the signal has leaked to other frequencies illustrating a phenomenon known as *spectral leakage.*

Spectral leakage can be reduced by windowing the data before performing the DFT. This reduces the extent of the discontinuities, introduced by the periodicity assumption of the DFT, when the data is repeated (see Fig. 2.15). The rectangular window is the default window used by the DFT, and not a good choice when attempting to combat spectral leakage. There are many alternative window choices, including Hamming, Bartlett and Blackman windows (see Fig. 2.16). A specific window may, however, be more suited to one application than another, so choice and use of windowing is critical when analysing real data with the DFT.

Evaluation of a 1D FT requires N^2 multiplications for a vector of length N. As a result it is computationally expensive for large N. However, the fast Fourier transform (FFT), a computationally efficient algorithm for computing the DFT, was introduced in 1965 [37]. It is most efficient for sequence lengths in which N is a power of 2. The computation

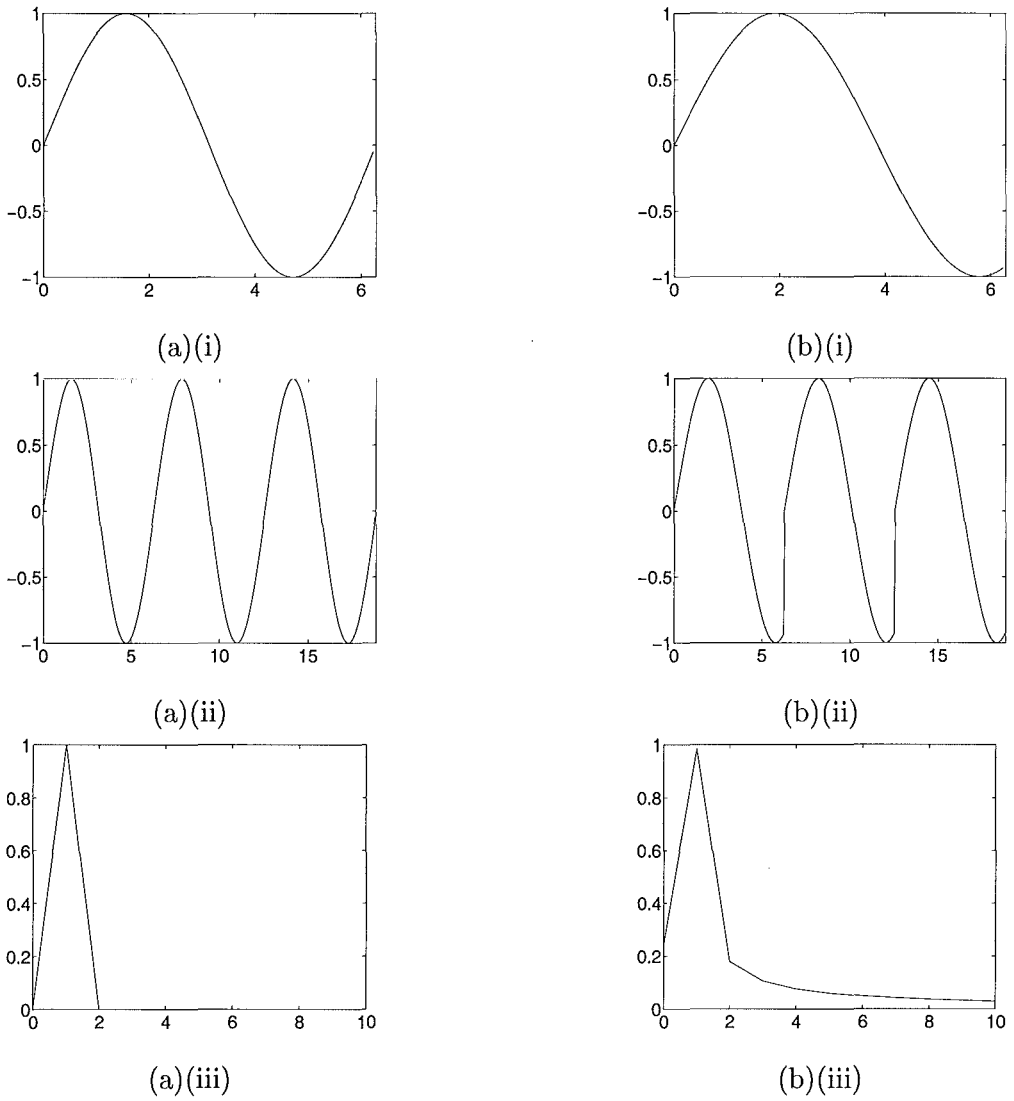

Figure 2.14: *Spectral leakage, a practical problem resulting from the periodicity assumption of the DFT. (a)(i) One period of the underlying signal. (ii) The underlying signal. (iii) The spectrum of the signal in (a)(i). (b)(i) Less than one period of the underlying signal. (ii) The underlying signal assumed by the DFT. (iii) The spectrum of the signal in (b)(i).*

required for a 1D FFT of a sequence of length N is $N\log_2 N$ multiplications. This provides a significant improvement for large N. In addition, the properties of the continuous FT are valid for the DFT and the FFT. All FTs computed in this thesis are via the FFT and are zeropacked where required to ensure that N is a power of 2.

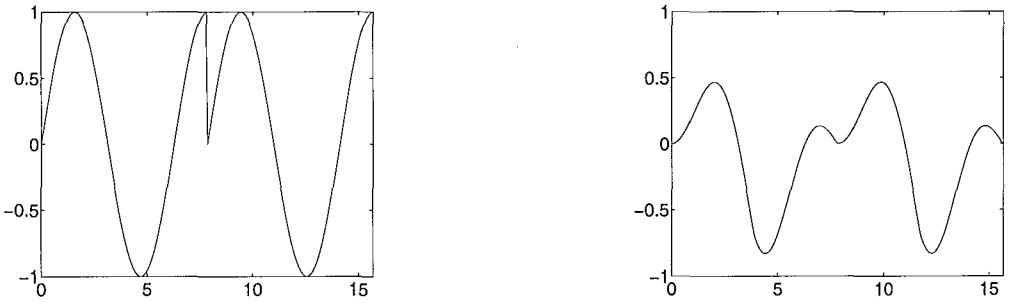

Figure 2.15: *The effect of windowing. (a) The unwindowed periodic data assumed by the DFT. (b) The same data windowed by a Bartlett window. The discontinuities present in (a) have been essentially eliminated by windowing.*

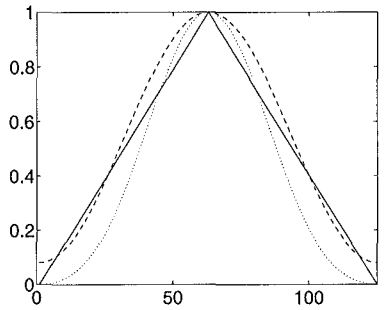

Figure 2.16: *Possible window functions; Bartlett (solid), Blackman (dotted) and Hamming (dashed).*

2.5.3 Discrete cosine transform

The discrete cosine transform (DCT) is used to calculate the cosine transform of sampled signals. The DCT, developed by Ahmed *et al* [2] in 1974, is a close relative of the DFT. In fact, the FFT is often used to compute the DCT. The DCT is widely used in image compression [172], the JPEG, MPEG and CCITT standards all use the DCT as it is very effective at image compression since most of the energy in the data can be packed into a few transform coefficients.

The DCT and IDCT of $s(x)$ and $S_c(u)$ respectively are defined in 1D as [2],

$$S_c(u) = \sqrt{\frac{2}{n}} C(u) \sum_{x=0}^{n-1} s(x) \cos\left(\left(\frac{2x+1}{2n}\right) u\pi\right) \quad \text{for} \quad u = 0, 1, \ldots\ n-1, \tag{2.103}$$

and

$$s(x) = \sqrt{\frac{2}{n}} \sum_{u=0}^{n-1} S(u)C(u)\cos\left(\left(\frac{2x+1}{2n}\right)u\pi\right), \quad x = 0, 1, \ldots\ n-1, \tag{2.104}$$

where

$$C(u) = \begin{cases} 2^{-1/2} & u = 0 \\ 1 & \text{otherwise} \end{cases}. \tag{2.105}$$

The DCT does not assume periodicity as the DFT does, however, it still has a special symmetry. Consider $s(x)$, defined on the interval $0 \leq x \leq T$. The extension outside the interval over which it is defined is the even extension of the sequence as illustrated in Fig. 2.17. The symmetry around the endpoints results in the assumption of a continuous underlying signal, producing a sequence that is even at $x = 0$ and $x = T$. As a result the DCT does not suffer from the spectral leakage problem to the same extent as the DFT. This property of the DCT is utilised in chapter 4 to combat spectral leakage effects in the simulation of scintillation.

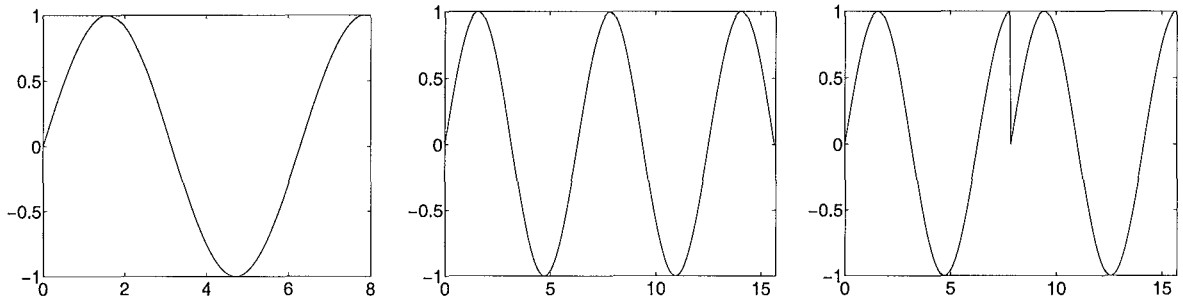

Figure 2.17: *A comparison of the symmetries assumed by the DCT and DFT. (a) The original signal, (b) the underlying signal as assumed by the DCT and (c) the underlying signal as assumed by the DFT.*

2.5.4 Finite energy, finite size and compactness

The physical size constraints of real world imaging equipment mean that only data within the field of view of the apparatus can be recorded. In some cases the object of interest may be small enough so that it fits completely within the instrument's field of view. More

often, however, the object is larger than the field of view and the resulting image of it is truncated during the capturing and recording processes. In addition, the recorded image is inevitably contaminated by noise. The noise can generally be considered to be randomly distributed with the root mean square amplitude denoted by the positive real number ϵ, which describes the background noise or uncertainty level. In addition to restricting the size of real images, the practical limitations of the recording equipment place an upper limit on the image amplitudes that can be recorded, i.e.

$$|f(x,y)| < \infty \quad \text{for all} \quad (x,y). \tag{2.106}$$

A consequence of these is that real world images must also be of finite energy, where the energy of an image $f(x,y)$ is given by

$$E_{f(x,y)} = \int_{-\infty}^{\infty}\int_{-\infty}^{\infty} |f(x,y)|^2 dxdy. \tag{2.107}$$

When noise is present the level of contamination is often described in decibels (dB), with

$$\epsilon_{\text{dB}} = 10\log_{10}\frac{E_{n(x,y)}}{E_{f(x,y)}}, \tag{2.108}$$

where $n(x,y)$ represents the noise.

It has already been established that a real image contains only a finite amount of energy. This combined with the size restriction imposed by the finite field of view of the imaging apparatus results in most of the image energy being contained in a finite region of space termed the *support*. The support of $f(x,y)$ is denoted by $S_{f(x,y)}$. Outside $S_{f(x,y)}$ the magnitude of $f(x,y)$ is in the order of ϵ and so can be considered to be negligible, i.e.

$$|f(x,y)| < \epsilon \qquad \text{outside support} \tag{2.109}$$

$$|f(x,y)| \geq \epsilon \qquad \text{inside support.} \tag{2.110}$$

If this region is finite the image is said to have *finite support*.

It is often computationally useful to define an image box $B_{f(x,y)}$, having sides parallel to the cartesian axes, which is just large enough to entirely encompass the support of the image $f(x,y)$. The length of $B_{f(x,y)}$ in the kth coordinate direction is defined as the extent, or

length of, $f(x,y)$ in that direction. The extent in the kth direction is denoted by $L_k(f)$. The image box is always larger than or equal to the support of $f(x,y)$ (see Fig. 2.18).

A finite-valued image that has finite support is said to be *compact* [13]. If $\epsilon = 0$ in Eqs. (2.109) and (2.110) an image is said to be *exactly compact*, otherwise it is *approximately compact.*

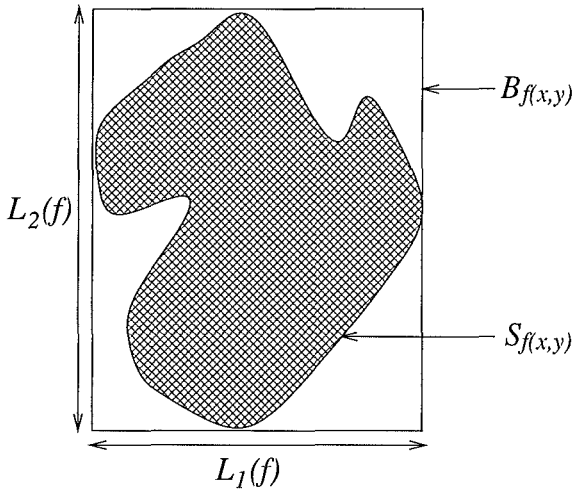

Figure 2.18: *The support, image box and extents for an image $f(x,y)$.*

2.5.5 Quantisation

It is necessary to describe real data by its values at a discrete set of points for processing and storage as outlined in section 2.5.1. The next step in the process of analog to digital conversion is *quantisation.* Each sample value of $g(t)$, represented by $g(n\triangle)$, is approximated by an integer multiple of the quantising step q. The sample values of $g(n\triangle)$ can take on one of a finite number of discrete amplitude levels. The quantised representation of $g(t)$ is, therefore, discrete in both time and amplitude. A sample quantised signal and the original signal are illustrated in Fig. 2.19. The error introduced by the quantisation process is called *quantisation noise*, and is an example of the contamination inherent to the digital processing of real world images. The maximum quantisation error introduced in the output when rounding to the closest available amplitude level is $q/2$. It is also common to assume

that any possible quantisation error in the range $-q/2$ to $q/2$ is equally likely, corresponding to the assumption of a uniform distribution of quantisation errors. The variance of the error signal is thus

$$\int_{-\infty}^{\infty} x^2 f_X(x) dx = \frac{1}{q} \int_{-q/2}^{q/2} x^2 dx = \frac{q^2}{12} \tag{2.111}$$

where $f_X(x)$ is the uniform probability distribution function defined in section 2.6. Halving the size of the quantisation step decreases the quantisation error by 4. If the discrete amplitude levels are made close enough the quantised signal is essentially indistinguishable from the sampled signal.

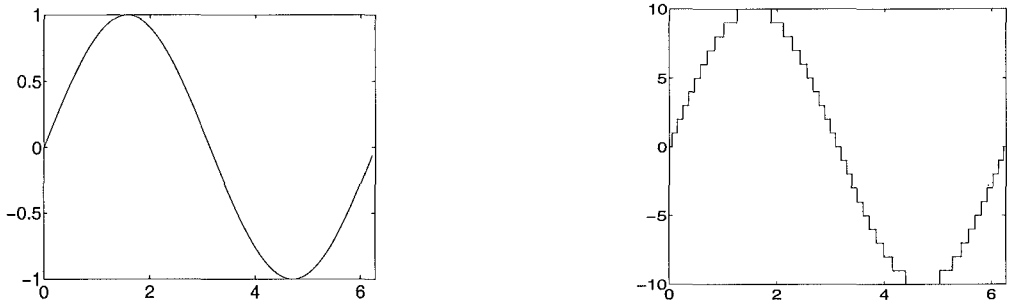

(a) (b)

Figure 2.19: *Quantisation. (a) The original signal. (b) The same signal quantised to 20 amplitude levels.*

When an image has been quantised, each sample point becomes known as a pixel (short for picture element) [3]. A pixel describes the basic unit of an image and is generally understood in 2D space where it represents a 2D area.

2.5.6 Positivity

The concept of a positive image complicates the mathematical solution to an image restoration problem. If it is known that an image is formed from positive radiant energy components then a solution containing negative components has no physical meaning. In addition, it is intensities that are measured and processed and intensities are always positive. This constraint must, therefore, be incorporated into the image restoration problem. Not only does enforcing positivity produce a more realistic solution it also helps to narrow down

the set of solutions from which the best match, according to the specified error metric, is selected. Existing and new methods for enforcing positivity are presented in chapter 5.

2.6 Statistics and random processes

Signals can be described as deterministic or random. A *deterministic* signal can be described exactly by an analytic expression or function. Therefore, the value of a deterministic signal at a specific instant in time is known. The value of a random signal, however, cannot be predicted in advance. A *random* signal could be a signal that has been transmitted through a noisy channel or a wave that has propagated through a region of inhomogeneous space. In fact, most signals of interest are random or contain a random component. As a result, statistical methods are required to describe these signals and extract the useful information contained in them. The mathematics behind the statistical characterisation of random signals is termed *probability theory* [71].

2.6.1 Probability theory

A *random experiment* is an experiment in which the outcome cannot be predicted in advance. Furthermore, if the experiment is repeated, the outcome can differ to a previous outcome. For each random experiment there is a set of possible outcomes, called the *sample space* and denoted by $\mathcal{S}$. $\mathcal{S}$ can be infinite or finite depending on the experiment. An *event*, $\mathcal{E}$, describes one possible outcome in the sample space, where each event has a probability associated with it. In the case of an event A the probability associated with it is denoted by $P\{A\}$. $P\{A\}$ describes how likely or probable the occurrence of event A is. The probability of an event is intended to represent the likelihood that a trial of an experiment will result in the occurrence of that event.

There are many possible techniques for assigning a probability to an event. However, the common approach is to find the probability of an event A, $P\{A\}$, that satisfies the axioms of probability:

1. $0 \leq P\{A\} \leq 1$.

2. $P\{\mathcal{S}\} = 1$, hence $\mathcal{S}$ is termed the sure event.

3. $P\{A+B\} = P\{A\} + P\{B\}$. If A and B are mutually exclusive, i.e the occurrence of one guarantees that the second does not occur, $P\{AB\} = \{0\}$, where $\{0\}$ denotes the null or impossible event.

All the development and properties associated with probability theory can be derived, directly or indirectly, from the axioms of probability, for example the property of conditional probability. Consider an experiment that involves a pair of events A and B. The probability of an event B occurring, given that event A has already occurred, is denoted by $P\{B|A\}$ and referred to as a *conditional probability.* It is defined mathematically as [71]

$$P\{B|A\} = \frac{P\{AB\}}{P\{A\}} \tag{2.112}$$

assuming A has non-zero probability, i.e. $P\{A\} > 0$. This can be rewritten as

$$P\{AB\} = P\{B|A\}P\{A\}, \tag{2.113}$$

or alternatively as

$$P\{AB\} = P\{A|B\}P\{B\}. \tag{2.114}$$

In some cases $P\{A|B\}$, $P\{B\}$ and $P\{A\}$ may be known, and the value of $P\{B|A\}$ desired. Combining Eqs. (2.112) and (2.114) produces Bayes' rule

$$P\{B|A\} = \frac{P\{A|B\}P\{B\}}{P\{A\}} \tag{2.115}$$

which relates $P\{A|B\}$ and $P\{B|A\}$.

If $P\{A|B\} = P\{A\}$, then the occurrence of event B provides no more information about the probability of the event A. In this case, A and B are said to be statistically independent. Statistical independence occurs if and only if

$$P\{AB\} = P\{A\}P\{B\}. \tag{2.116}$$

2.6.2 Random variables

The outcome of an experiment can take on any point in the sample space, with the value being determined by experiment. Consider $\mathcal{S} = (s_1, s_2 \ ... \ )$ as a set of possible outcomes of a random experiment. A function, X, that takes each possible outcome and assigns to it a real number $X(s_1), X(s_2), ...$ is termed a *random variable*. It is possible to define both continuous and discrete random variables as necessary for dealing with the continuous and discrete outcomes of random experiments. A *continuous random variable* can take on any value in a particular observation interval, for instance the instantaneous value of a wavefront propagating through atmospheric turbulence. Whereas, a *discrete random variable* can take on only a discrete set of values, for example the value of a pixel in a gray scale image.

Random variables are often described by their cumulative distribution function (CDF), denoted by $F_X(x)$ for a random variable X. This describes the probability that X assumes a value less than or equal to x, i.e.

$$F_X(x) = P\{X \leq x\}. \tag{2.117}$$

$F_X(x)$ is a monotonically increasing function, i.e. $F_X(x_1) \leq F_X(x_2)$ if $x_1 < x_2$. In addition, $0 \leq F_X(x) \leq 1$.

A more common characterisation of a random variable X is by its probability density function (PDF), $f_X(x)$, where

$$f_X(x) = \frac{dF_X(x)}{dx}. \tag{2.118}$$

It follows that $f_X(x)$ must obey the following properties,

1. $\int_{-\infty}^{\infty} f_X(x)dx = 1.$
2. $P(x_1 < X \leq x_2) = \int_{x_1}^{x_2} f_X(x)dx.$
3. $F_X(x) = \int_{-\infty}^{x} f_X(\xi)d\xi.$

The probability density function describes the "preferred" range of values that X assumes. It is always a non-negative function with a total area of unity. A wide variety of probability

distributions find common use. The uniform, normal (Gaussian) and Poisson probability density functions are outlined below. The uniform case gives no information on the preferred range for X between x_1 and x_2. Whereas, the Gaussian PDF is often used to describe sensor measurement noise and the Poisson PDF, photon or shot noise inherent to astronomical imaging problems.

Uniform PDF

Under the assumption of a uniform PDF X is equally likely anywhere in the interval between x_1 and x_2, i.e.

$$f_X(x) = \begin{cases} \frac{1}{x_2 - x_1} & x_1 < x \leq x_2 \\ 0 & \text{elsewhere} \end{cases} . \tag{2.119}$$

Quantisation noise, for example, is assumed to be uniformly distributed (see section 2.5.5).

Gaussian or Normal PDF

A Gaussian or normal random variable X obeys the following PDF,

$$f_X(x) = \frac{1}{\sqrt{2\pi}\sigma_X} \exp\left\{ -\frac{(x - \mu_X)^2}{2\sigma_X^2} \right\} \tag{2.120}$$

where μ_X and σ_X^2 denote the mean and variance of the distribution respectively. The Gaussian model is accurate for a wide variety of physical situations and it has numerous convenient mathematical properties.

The central limit theorem provides the mathematical justification for using a Gaussian process as a model for a large number of different physical phenomena in which the observed random variable, at a particular instant of time, is the result of a large number of individual random events [71]. Let X_i, $i = 1, 2, \ldots N$ be a set of statistically independent random variables, having arbitrary probability distributions with means $\mu_1, \ldots \mu_N$ and variances $\sigma_1^2, \ldots \sigma_N^2$. Let Z be a random variable, where

$$Z = \frac{1}{\sqrt{N}} \sum_{i=1}^{N} \frac{X_i - \mu_i}{\sigma_i}. \tag{2.121}$$

The central limit theorem states that as $N \to \infty$, the PDF for Z approaches a Gaussian PDF.

Poisson PDF

A Poisson random variable X is described by the following PDF [22]

$$f_X(x) = \sum_{k=0}^{\infty} \frac{\mu_X^k \exp(-\mu_X)}{k!} \delta(x-k) \tag{2.122}$$

where μ_X represents both the mean and the variance. The Poisson PDF is commonly used in astronomical imaging applications where it models the photon nature of light.

2.6.3 Moments

The description of properties of random variable PDFs can often be accomplished by use of a few parameters, namely the moments of the random variables. The PDF of a Gaussian random variable is completely defined by the first two moments, whereas, the Poisson PDF requires only the first moment.

The kth moment of a random variable X is defined as

$$\mu_{X^k} = E[X^k] = \left\langle X^k \right\rangle = \int_{-\infty}^{\infty} x^k f_X(x) dx, \tag{2.123}$$

where E denotes the statistical expectation operator and $\langle\rangle$ represents an ensemble average. An ensemble describes a collection of similar statistical processes. Hence, an ensemble average is obtained by averaging across many statistically similar signals.

The most important moments are the first two moments, μ_X and μ_{X^2},

$$\mu_X = E[X] = \langle X \rangle = \int_{-\infty}^{\infty} x f_X(x) dx \tag{2.124}$$

and

$$\mu_{X^2} = E[X^2] = \left\langle X^2 \right\rangle = \int_{-\infty}^{\infty} x^2 f_X(x) dx. \tag{2.125}$$

The first moment or mean value is often referred to as the expected value of the random variable X, whereas the second moment is the mean square value.

The central moments are used to describe the fluctuations of a random variable around its mean. The kth central moment is given by

$$E[(X-\mu_X)^k] = \int_{-\infty}^{\infty} (x-\mu_X)^k f_X(x) dx. \tag{2.126}$$

An important central moment is the second central moment, or variance, generally denoted by σ_X^2, where

$$\sigma_X^2 = \int_{-\infty}^{\infty} (x - \mu_X)^2 f_X(x) dx. \tag{2.127}$$

In fact,

$$\sigma_X^2 = \mu_{X^2} - (\mu_X)^2. \tag{2.128}$$

The square root of the variance, σ_X, is called the standard deviation of the random variable X.

In many cases the outcome of a random experiment requires more than one random variable for its description. The statistics of two or more random variables are described by their joint statistics. The joint distribution function of two random variables, X and Y, describes the probability that a point (X, Y) lies in a specific quadrant in the (x, y) plane, i.e.

$$F_{XY}(x, y) = P\{X \leq x, Y \leq y\}. \tag{2.129}$$

The joint PDF of X and Y, $f_{XY}(x, y)$, is equal to the partial derivative of $F_{XY}(x, y)$,

$$f_{XY}(x, y) = \frac{\partial^2 F_{XY}(x, y)}{\partial x \partial y}. \tag{2.130}$$

This has equivalent properties to PDFs for single random variables. That is, it is a monotonically increasing function of x and y, is always non-negative and has a total volume of unity.

Two random variables X and Y are statistically independent if knowledge of the outcome of X in no way affects the outcome of Y. This occurs if and only if

$$P\{XY\} = P\{X\}P\{Y\}. \tag{2.131}$$

If Eq. (2.131) holds, then

$$F_{XY}(x, y) = F_X(x) F_Y(y) \tag{2.132}$$

and

$$f_{XY}(x, y) = f_X(x) f_Y(y). \tag{2.133}$$

The expected value of the product of two random variables is termed the correlation of X and Y, denoted by R_{XY}, where

$$R_{XY} = E[XY] = \int_{-\infty}^{\infty}\int_{-\infty}^{\infty} xyf_{XY}(x,y)dxdy. \tag{2.134}$$

The correlation of a random variable with itself is termed *autocorrelation.* The joint moment of centred random variables X and Y, is the covariance of X and Y, C_{XY}, where

$$\begin{aligned} C_{XY} &= E[(X-\mu_X)(Y-\mu_Y)] &(2.135)\\ &= \int_{-\infty}^{\infty}\int_{-\infty}^{\infty}(x-\mu_X)(y-\mu_Y)f_{XY}(x,y)dxdy. &(2.136)\end{aligned}$$

The covariance of a random variable with itself is termed *autocovariance*, and is equal to the variance of the random variable. The covariance and correlation of two variables are related by

$$C_{XY} = R_{XY} - \mu_X\mu_Y. \tag{2.137}$$

2.6.4 Random processes

In many cases one may wish to analyse or characterise random time and/or space varying signals or data, e.g. wavefronts passing through a turbulent medium. A collection, often referred to as an ensemble, of all realisations of random time/space varying signals is a random or stochastic process. The random process can be considered to be a generalisation of the concept of a random variable. It is again necessary to define a sample space, $\mathcal{S}$, containing all the possible outcomes of a random experiment. However, each possible outcome is now a function of time (or space). The random variable corresponding to an event A is $X(A)$, often denoted by X. The random process associated with an event A is $X(A,t)$, often denoted by $X(t)$. Therefore, the theory of random processes describes functions of time or space that cannot be predicted in advance. An ensemble of sample time functions is illustrated in Fig. 2.20.

A random process requires a different random variable to describe its statistics at each point in time. Let $X(t_1), X(t_2), \ldots\ X(t_n)$ denote the random variables obtained by observing $X(t)$ at $t = t_1, t_2, \ldots\ t_n$. Each random variable can be described by its corresponding CDF and

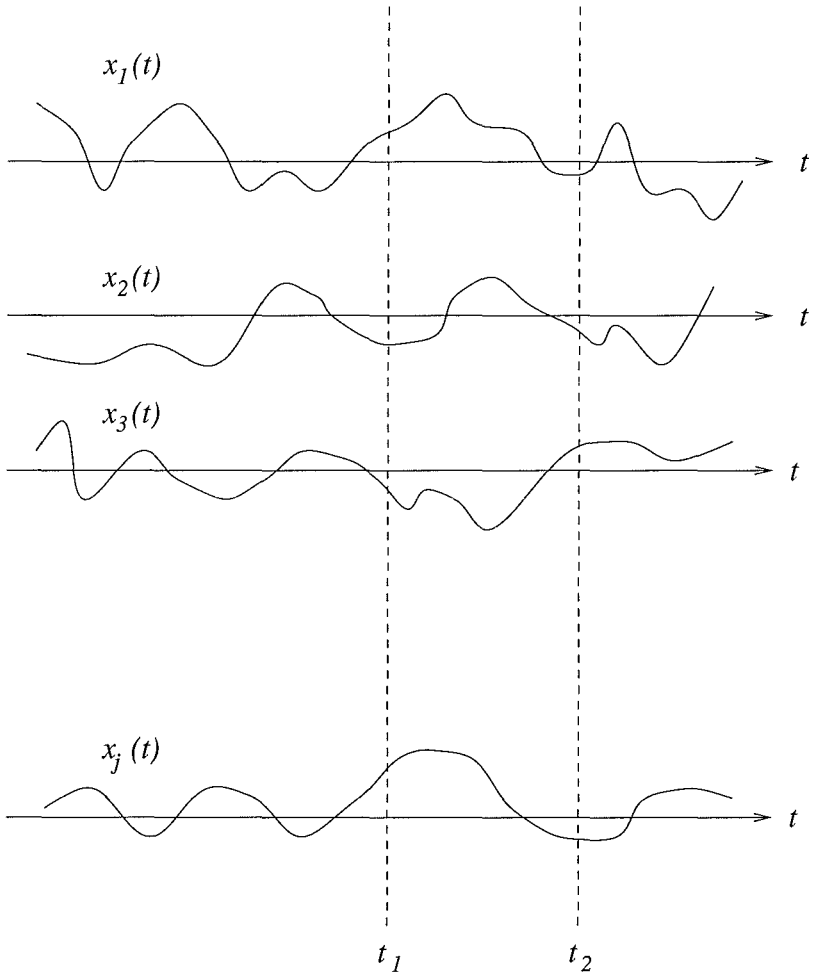

(a)

Figure 2.20: *An ensemble of sample functions, where t_1 and t_2 are the parameter values for which the joint density function $f_{X(t_1)X(t_2)}(x_1, x_2)$ is specified.*

PDF, $F_{X(t_1)}, F_{X(t_2)}, \cdots F_{X(t_n)}$ and $f_{X(t_1)}, f_{X(t_2)}, \cdots f_{X(t_n)}$ respectively. $F_X(t)$ is called the first order distribution function of $X(t)$ and $f_X(t)$ the first order density function of $X(t)$.

The second order density function is the joint density function of the random variables $X(t_1)$ and $X(t_2)$, given by

$$F_{X(t_1)X(t_2)}(x_1, x_2) = P\{X(t_1) \leq x_1, X(t_2) \leq x_2\} \tag{2.138}$$

and

$$f_{X(t_1)X(t_2)}(x_1, x_2) = \frac{\partial^2 F_{X(t_1)X(t_2)}(x_1, x_2)}{\partial x_1 \partial x_2}. \tag{2.139}$$

This can also be extended to the nth order joint density function of $X(t_1), X(t_2), \ldots X(t_n)$,

$$f_{X(t_1)X(t_2)\ \ldots\ X(t_n)}(x_1, x_2, \ \ldots\ , x_n) = \frac{\partial^n F_{X(t_1)X(t_2)\ \ldots\ X(t_n)}(x_1, x_2, \ \ldots\ , x_n)}{\partial x_1 \partial x_2 \ \ldots\ \partial x_n}. \tag{2.140}$$

A random process is called *strictly stationary* if the following condition holds,

$$F_{X(t_1+\tau)\ \ldots\ X(t_n+\tau)}(x_1, x_2, \ \ldots\ , \ x_n) = F_{X(t_1)X(t_2)\ \ldots\ X(t_n)}(x_1, x_2, \ \ldots\ , \ x_n), \tag{2.141}$$

or equivalently,

$$f_{X(t_1+\tau)\ \ldots\ X(t_n+\tau)}(x_1, x_2, \ \ldots\ , \ x_n) = f_{X(t_1)X(t_2)\ \ldots\ X(t_n)}(x_1, x_2, \ \ldots\ , \ x_n), \tag{2.142}$$

for all arbitrary time shifts τ, and orders n. In other words, the statistics are independent of the choice of the origin, $t = 0$. This leads to two situations of special interest.

1. If $n = 1$,

$$F_{X(t)}(x) = F_{X(t+\tau)}(x) = F_X(x). \tag{2.143}$$

   This result indicates that the first order distribution function of a stationary random process is time independent.

2. If $n = 2$ and $\tau = -t_1$,

$$F_{X(t_1)X(t_2)}(x_1, x_2) = F_{X(0)X(t_2-t_1)}(x_1, x_2). \tag{2.144}$$

   Hence, the second order distribution function of a stationary random process depends only on the time difference between observations.

A *wide sense stationary* process has a mean that is independent of time and an autocorrelation, $R_{X(t_1)X(t_2)}(x_1, x_2)$ which depends only on the time difference, $\tau = t_1 - t_2$. Hence, a strictly stationary process is also wide sense stationary, but the converse is generally not true. Most practical signals can be considered to be wide sense stationary only.

The averages calculated so far have been across a collection, or ensemble, of random variables. However, it is useful when dealing with random processes to investigate time averages. Time averages describe the properties of an individual sample function as it evolves in time, or in other words an average along the process. It is useful to relate time averages to ensemble averages, as time averages represent a practical means for the estimation of ensemble averages of a random process [71].

Recall that the ensemble or statistical average of a wide sense stationary random process is given by (c.f. Eq. (2.124)),

$$\mu_{X(t)} = E[X(t)] = \langle X(t) \rangle = \int_{-\infty}^{\infty} X(t) f_{X(t)}(x) dx. \tag{2.145}$$

The time average of a sample function $x(t)$ of a signal defined on $-T < t < T$ is given by

$$\mu_x(T) = \frac{1}{2T} \int_{-T}^{T} x(t) dt, \tag{2.146}$$

where $\mu_x(T)$ is itself a random variable. It depends on the observation interval and the sample function of $X(t)$ that is used for its calculation, with the property that

$$E[\mu_x(T)] = \mu_X, \tag{2.147}$$

where μ_X is the mean of the process $X(t)$. A stochastic process $X(t)$ is called *ergodic* in the mean if its time average can be substituted for its ensemble average. This occurs if the following two conditions are satisfied [71]:

$$\lim_{T \to \infty} \mu_x(T) = \mu_X \quad \text{and} \tag{2.148}$$

$$\lim_{T \to \infty} \text{var}\,[\mu_x(T)] = 0. \tag{2.149}$$

The time averaged autocorrelation function of a sample function $x(t)$ is

$$R_x(\tau, T) = \frac{1}{2T} \int_{-T}^{T} x(t+\tau) x(t) dt. \tag{2.150}$$

A stochastic process is ergodic in the autocorrelation function if the following two conditions are satisfied [71]:

$$\lim_{T \to \infty} R_x(\tau, T) = R_X(\tau) \quad \text{and} \tag{2.151}$$

$$\lim_{T\to\infty} \text{var}\left[R_x(\tau, T)\right] = 0. \tag{2.152}$$

Therefore, the most restrictive class of random processes is the class of ergodic random processes. For a random process to be ergodic it must be a strictly stationary process. As a result there is a hierarchy belonging to random processes, which is summarised in Fig. 2.21.

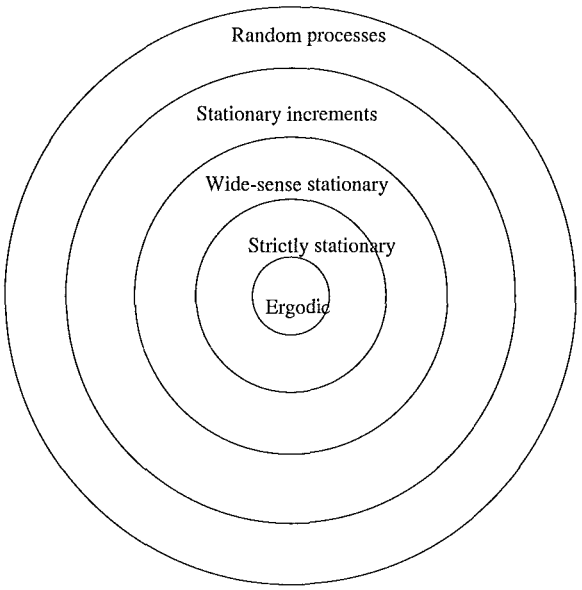

(a)

Figure 2.21: *The hierarchy of classes of random processes.*

Probability theory plays a key role in imaging through turbulence as well as in the understanding of incoherent imaging (introduced in chapter 3). For example, atmospheric turbulence is a random process where turbulence induced perturbations are often assumed to be wide sense stationary [139]. In addition, signal dependent photon noise and signal independent CCD readout noise must also be properly analysed to accurately model the random degradations of a real optical system.

2.7 Information theory

Information theory has made contributions to communications, statistical inference, probability, statistics and engineering and deals with mathematical modelling and analysis [71]. The key concepts of information, uncertainty and entropy are of particular interest and are outlined below.

The probability of an event A, $P\{A\}$, provides some measure of how certain or uncertain the occurrence of event A is. If $P\{A\} = 1$, there is no uncertainty associated with the event A, and therefore no new information is gained when event A occurs. The more uncertainty there is about an event, the more information is gained if it occurs. The amount of information gained after observing the occurrence of an event A, which has a probability $P\{A\}$ associated with it, is $I(A)$, where

$$I(A) = \log_2\left(\frac{1}{P\{A\}}\right) \tag{2.153}$$

$$= -\log_2(P\{A\}). \tag{2.154}$$

Hence, if $P\{A\} = 1$, the outcome of the experiment will be A, so $I(A) = 0$ as no information is gained.

It is now useful to introduce the concept of entropy. $I(s_k)$ is a discrete random variable that takes on the values $I(s_0), I(s_1), \ldots, I(s_{N-1})$ with probabilities $P\{s_0\}, P\{s_1\}, \ldots P\{s_{N-1}\}$. The average amount of information contained in the occurrence of an event over the entire set of possible events is termed the entropy, h, where

$$h = E\left[I(s_k)\right]$$

$$h = -\sum_{k=0}^{N-1} P\{s_k\}\log_2(P\{s_k\}). \tag{2.155}$$

The concept of entropy is utilised in chapters 5 and 7 as a criterion of optimality when reconstructing degraded images and during the inversion of scintillation covariances to estimate $C_N^2(h)$ profiles.

Chapter 3

Imaging through Turbulence

Optics deals with the study of light, where light is considered to be radiation that can be sensed by the eye. There exist a number of different light models each making up an entirely separate branch of optics; geometrical optics, physical optics and quantum optics [46]. This chapter introduces the geometrical and physical optics theory necessary for the understanding of later chapters of this thesis.

Geometrical optics provides a simplistic model for the understanding and investigation of light propagation. Light is considered to be a form of energy that travels in straight lines. Hence, light propagation can be computed using simple geometry. Geometrical optics is useful for the introduction of basic optics theory and is essential for some aspects of the design and use of almost any optical system [174], including telescopes, adaptive optics and SCIDAR systems.

Fourier optics provides a more in-depth study of the properties of light propagation. It is a study of the wave nature of light, which came about after Maxwell showed light to be a form of electromagnetic wave. The wave nature of light is used here to introduce the key concept of diffraction which does not fit into the realm of geometrical optics. Diffraction

arises due to the non-penetrating nature of visible light. It plays an important role in the understanding and modelling of optical imaging systems as it describes many situations in which the behaviour of an optical wavefront departs from the ideal performance predicted by geometrical optics. Therefore, a thorough introduction to the mathematics and assumptions behind the diffraction phenomenon is presented in section 3.2.1. The use of various mathematical approximations, resulting in the well-known Fresnel and Fraunhofer diffraction theories, are presented in sections 3.2.2 and 3.2.3. Fresnel diffraction theory, valid for short propagation distances, provides a parabolic approximation to the ideal spherical wavefronts. It models the propagation of light between turbulent layers, and as a result is used extensively in the modelling and simulation of wave propagation through atmospheric turbulence presented in chapter 4. In Fraunhofer diffraction theory, valid for long propagation distances, the parabolic wavefronts are replaced with planar wavefronts. Fraunhofer diffraction is valid for most practical optical imaging systems as the objects of interest, stars, are separated from the imaging system by light years. The resolution limits imposed by diffraction are investigated in section 3.2.5. Finally, diffraction theory is extended to two types of non-monochromatic illumination; coherent and incoherent illumination, in section 3.2.6.

The departure of real optical systems from the formation of a point image in response to a point object is due not only to diffraction but also to aberrations, introduced in section 3.3. Sources of aberrations include imperfections in the optical components of a system and external effects such as atmospheric turbulence. The basic aberrations of conventional optical systems, for example coma and spherical aberration, are shown to correspond to the low order Zernike polynomials, which can be used to represent both fixed aberrations and atmospheric turbulence.

Section 3.4 looks in-depth at imaging through atmospheric turbulence and how it affects optical imaging systems. The height, strength and number of turbulence layers all contribute to the distortion of the images formed in the telescope. The image degradation can be described by the PSF which is also a function of the turbulence distribution, with static low altitude turbulence and time varying high altitude turbulence corresponding to significantly

different distortions. Further, the information available for image formation depends on the size of the telescope aperture through which it is viewed and the exposure time of the images captured. A good understanding of the interaction between these variables is necessary for the compensation of the atmosphere and is made possible by its simulation outlined in chapter 4.

This chapter concludes with a brief introduction, in section 3.5, to the latest adaptive optics technologies for compensating for the effects of imaging through atmospheric turbulence. The compensation achieved by a conventional AO system is limited by a number of factors. The restrictions imposed by the lack of bright natural stars for accurate wavefront sensing led to the development of the laser guide, which in turn created an entirely new set of problems. However, even with a bright source a major limitation is the small field of view over which compensation can be achieved, with many objects of interest exceeding this region. Suggestions to overcome these problems include multiconjugate adaptive optics systems and the use of multiple laser guide stars discussed in sections 3.5.1 and 3.5.2 respectively.

3.1 Geometrical optics

Geometrical optics is the oldest branch of optics and deals with the study of light using a few simple geometrical relationships, known as the laws of geometrical optics [46]. These are the laws of rectilinear propagation, reflection, refraction and reversibility. However, it is first necessary to introduce the concept of a light ray. A straight line with an arrowhead is used to represent a light ray, with the arrowhead pointing in the direction of propagation. In a uniform or homogeneous medium, where the physical properties are constant, light travels in straight lines and the possible paths it can take are referred to as rays (see Fig. 3.1).

3.1.1 The laws of geometrical optics

The law of rectilinear propagation describes the assumption that light travels in straight lines. This is observed in everyday life by the existence of shadows (see Fig. 3.2). At a

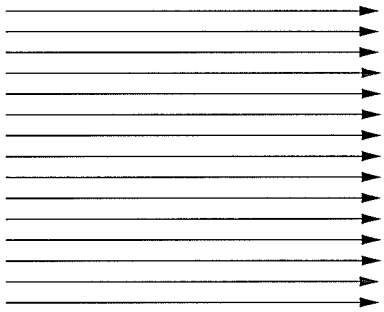

Figure 3.1: *Light rays in a homogeneous medium.*

boundary or interface between two media, light propagation is altered; it can be reflected or refracted. *Reflection* occurs when light bounces off the interface between the two media as illustrated in Fig. 3.3. The reflected ray lies in the same plane as the incident ray and the angle of incidence, θ_1, is equal to the angle of reflection, θ_2.

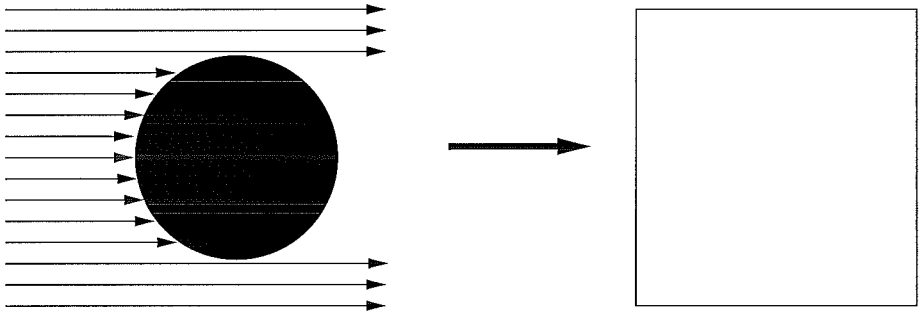

Figure 3.2: *The formation of a shadow.*

Refraction, however, describes the transmission of light through the second medium encountered at an interface. Light travels at different speeds in different media, and more slowly in media than in a vacuum. The ratio of the speed of light in a vacuum, c, to the speed of light in some arbitrary medium, v, is known as the refractive index, n, where

$$n = \frac{c}{v} = \sqrt{\epsilon\mu}. \tag{3.1}$$

Here ϵ is the dielectric constant of the medium and μ the magnetic permeability of the medium. It should be noted that n is always greater than 1. If a transparent medium, such as a piece of glass or a lens, is placed between a light source and your eye, the source is dis-

placed. This is due to refraction and can be described by Snell's law which states that when a beam of light passes through a boundary separating media of different refractive indices, the change in velocity results in a change in the direction of propagation. Mathematically this is represented as,

$$\frac{v_1}{v_2} = \frac{n_2}{n_1} = \frac{\sin(\theta_1)}{\sin(\theta_2)}, \tag{3.2}$$

where v_1 and v_2 are the velocities through the different media, n_1 and n_2 are the refractive indices of the media and θ_1 and θ_2 are the angles of incidence and refraction respectively.

The law of reversibility states that if the direction of a ray is reversed it follows exactly the same path in reverse. This becomes apparent when considering the reflected and refracted rays illustrated in Figs. 3.3 and 3.4. Clearly, if the roles of the incident and reflected/refracted rays are reversed the paths mapped out correspond to the original paths but in reverse.

The laws of geometrical optics can all be derived from Fermat's principle, which is based on the *optical path length*, describing the distance travelled by a light ray between two points. The optical path length between points A and B is denoted by $[AB]$ and is expressed mathematically as

$$[AB] = \int_A^B n \cdot ds, \tag{3.3}$$

where n is the refractive index of the medium and ds is a differential element of length along any one of the paths from A to B. Fermat's principle states that if a ray of light

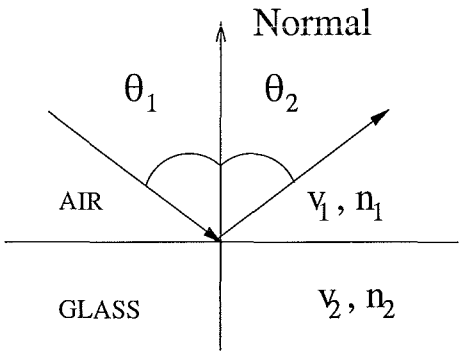

Figure 3.3: *The reflection of light at an interface between two media.*

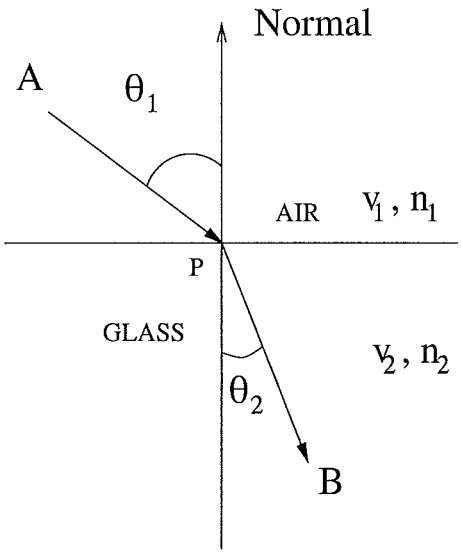

Figure 3.4: *The refraction of light at an interface between two media.*

passes from one point to another, undergoing reflections and refractions, the path taken is such that the time occupied over it is stationary (i.e. a maximum or a minimum) [51]. This applies to arbitrary points A and B. However, if A and B are close enough so that there is no real focus between them [173], then the path taken will be the shortest or minimum time path. Consequently Fermat's principle is often termed the *principle of least time.*

Using the optical path it is possible to introduce the concept of a *wavefront.* Wavefronts, like light rays, are used to model light. A wavefront is considered to be a surface of constant optical path length from the source or alternatively the surface orthogonal or normal to the rays emitted from the source. The concept of a wavefront is illustrated in Fig. 3.5. Wavefronts are very useful in modelling the aberrations suffered by real optical systems.

3.1.2 Lenses

Lenses play important roles in many optical systems. A lens does two things; it magnifies and inverts the image of an object [22]. An ideal lens, as with any ideal optical system, maps a point object to a point image as illustrated in Fig. 3.6. An ideal lens can also be viewed as changing the radius of curvature of a spherical wavefront. A real lens, however,

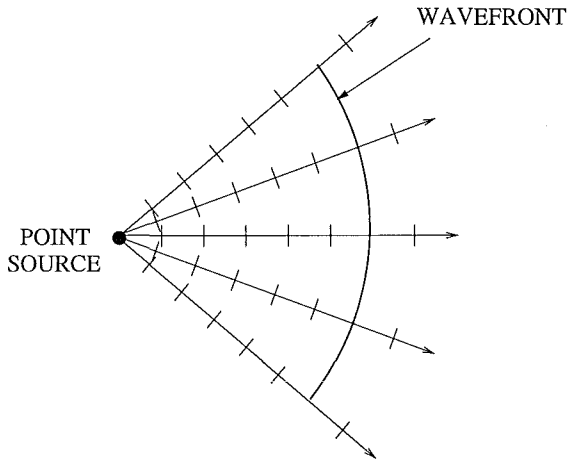

Figure 3.5: *A wavefront is a surface of constant optical path from the source or a surface orthogonal to the light rays emitted from a source.*

cannot convert an incident spherical wavefront into another spherical wavefront perfectly, due to inhomogenities introduced in the lens fabrication process.

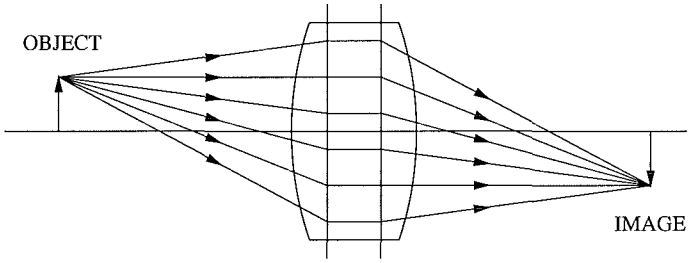

Figure 3.6: *An ideal lens: The formation of an ideal image point from an ideal object point.*

The physical properties of the lens can be combined into a single number, f, called the *focal length*, and defined as [66]

$$\frac{1}{f} = (n-1)\left(\frac{1}{R_1} - \frac{1}{R_2}\right) \tag{3.4}$$

where n is the refractive index of the lens, R_1 the radius of curvature of the left hand surface and R_2 the radius of curvature of the right hand surface.

A lens with useful properties is the thin lens, for which the separation of the opposite surfaces is small enough to be negligible. A good example of a thin lens is a pair of spectacles. More

complicated optical systems, for example telescopes can also sometimes be modelled as a thin lens. The distance behind the lens, d_o, where the rays emanating from a single point will again cross in an image point, a distance d_i in front of the lens, for a thin lens (see Fig. 3.7) is expressed mathematically as [66]

$$\frac{1}{d_o} + \frac{1}{d_i} - \frac{1}{f} = 0, \tag{3.5}$$

where f is the focal length defined in Eq. (3.4). Eq. (3.5) is referred to as the *thin lens equation* or the *lens law*. An equivalent form of this relationship is

$$f = \frac{m}{m+1} d_o, \tag{3.6}$$

where $m = \frac{d_i}{d_o}$ is the magnification performed by the lens.

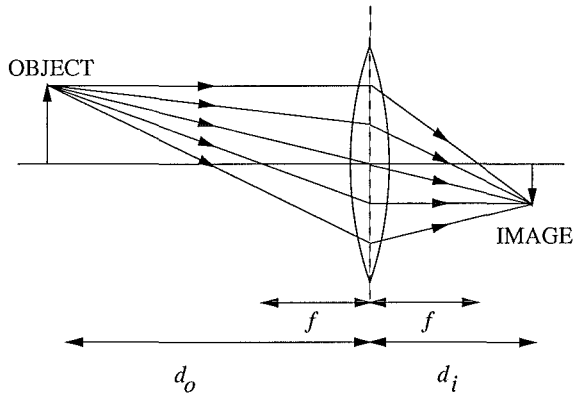

Figure 3.7: *Image formation through a thin lens, where f is the focal length of the lens and d_o and d_i are the distances from the object and image respectively.*

3.1.3 Aperture stops, entrance and exit pupils

The amount of light that reaches the imaging element depends not only on the brightness of the object but also on the dimensions of the optical elements, which limit how much light is seen by the system. This limit could be due to the finite aperture of an individual system component or a stop, a hole in an opaque screen purposely designed to limit light into the system. The limiting component is termed the *aperture stop*. The *entrance pupil*, defined as the image of the aperture stop as viewed from object space, is formed by all of the optical

elements preceding the aperture stop. The *exit pupil* is the image of the aperture stop, as seen looking back from image space, and is formed by all the optical elements following it.

3.2 Fourier optics

The simple geometrical model is often inadequate, as there are many situations in which the behaviour of an optical wavefront does not fit within the realm of geometrical optics. This is due to diffraction, inherent to all optical systems. Where geometrical optics predicts a single point the light is actually spread over a small region around that point. Hence, the aim becomes to reach the limit imposed by diffraction instead of the ideal geometrical performance predicted in section 3.1. Fourier or physical optics theory can be used to describe many of these situations and can be considered to be a study of the wave nature of light.

3.2.1 Diffraction

Let $u(P,t)$ be a scalar function representing the optical field due to a monochromatic wave at a position P and time t. The field for a monochromatic wave can be written as [66]

$$u(P,t) = \mathrm{Re}\left[U(P)\exp(-j2\pi vt)\right] \tag{3.7}$$

where v is the optical frequency. If $u(P,t)$ is an optical wave it must obey the scalar wave equation, defined as

$$\nabla^2 u - \frac{1}{c^2}\frac{\partial^2 u}{\partial t^2} = 0, \tag{3.8}$$

where $\nabla^2 = \frac{\partial^2}{\partial x^2} + \frac{\partial^2}{\partial y^2} + \frac{\partial^2}{\partial z^2}$ and c is the speed of light in a vacuum, $3\times10^8\mathrm{ms}^{-1}$. This can be simplified to the time independent wave equation, known as the Helmholtz equation, by substitution of Eq. (3.7) into Eq. (3.8), to give [66]

$$(\nabla^2 + k^2)U = 0, \tag{3.9}$$

where $k = \frac{2\pi}{\lambda}$ is known as the wavenumber and λ is the wavelength of light.

Given a complex wavefront or disturbance U, the aim is to determine its value at some arbitrary observation point (x_1, y_1) in image space. This is known as the diffraction problem,

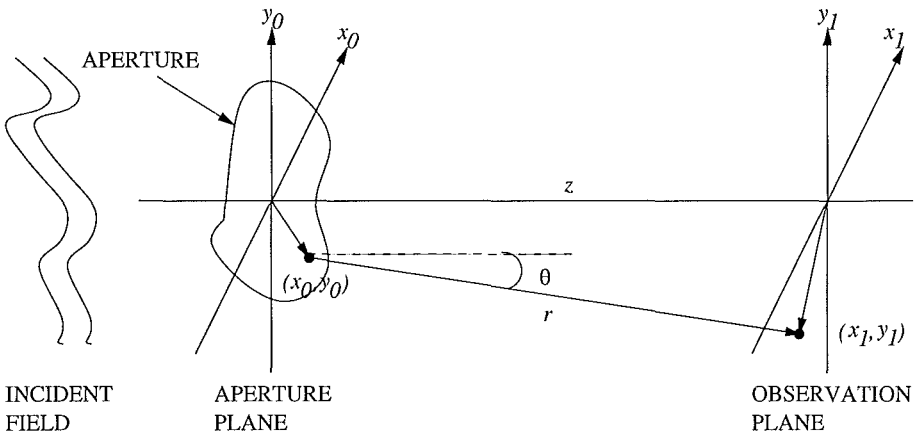

Figure 3.8: *The diffraction problem. What is the optical field at (x_1, y_1) in the observation plane due to an optical field incident on the aperture at (x_0, y_0)?*

where the geometry of the problem is illustrated in Fig. 3.8. An optical field incident on the aperture in the aperture plane, is propagated to the observation plane, with the distance between the aperture and observation planes given by z. The distance joining arbitrary points (x_0, y_0) and (x_1, y_1) is denoted by r. Application of the Helmholtz wave equation to this problem and the use of Green's theorem leads to the Rayleigh-Sommerfeld formula [139],

$$U(x_1, y_1) = \frac{1}{j\lambda} \int_{-\infty}^{\infty} \int_{-\infty}^{\infty} U(x_0, y_0) \frac{\exp(jkr)}{r} \cos(\theta) dx_0 dy_0, \tag{3.10}$$

where θ denotes the angle between z and r. Eq. (3.10) can be rewritten as

$$U(x_1, y_1) = \int_{-\infty}^{\infty} \int_{-\infty}^{\infty} U(x_0, y_0) h(x_1, y_1; x_0, y_0) dx_0 dy_0, \tag{3.11}$$

where

$$h(x_1, y_1; x_0, y_0) = \frac{1}{j\lambda} \frac{\exp(jkr)}{r} \cos(\theta). \tag{3.12}$$

Eq. (3.11) is a mathematical equivalent of the Huygens-Fresnel principle which states that every point on the aperture can be considered to be a point source that serves as a source for spherical waves. The optical field at any point beyond the aperture is simply the superposition of all spherical waves reaching that point.

The Rayleigh-Sommerfeld diffraction formula can be very difficult to use. However, use of various approximations leads to some well-known special cases of it. Firstly, it is assumed

that z is much greater than the extent of the region of observation, hence $\cos(\theta) \approx 1$. Therefore, r is approximately equal to z and Eq. (3.13) becomes

$$h = \frac{1}{j\lambda z}\exp(jkr). \tag{3.13}$$

It should be noted that r still features in the exponential, since a small percentage error in r represents a significant phase change. In order to avoid the introduction of phase errors the more accurate Fresnel and Fraunhofer approximations for r are used.

3.2.2 Fresnel diffraction

The Fresnel approximation is obtained by approximating r, the distance between the object and image points. The exact form for r is

$$r = \sqrt{z^2 + (x_0 - x_1)^2 + (y_0 - y_1)^2} \tag{3.14}$$

$$= z\sqrt{1 + \left(\frac{x_0 - x_1}{z}\right)^2 + \left(\frac{y_0 - y_1}{z}\right)^2}. \tag{3.15}$$

The binomial expansion of a square root is given as

$$\sqrt{1+b} = 1 + \frac{1}{2}b - \frac{1}{8}b^2 + \ldots, \tag{3.16}$$

however, it is often adequately approximated by the first two terms, i.e.

$$\sqrt{1+b} \approx 1 + \frac{1}{2}b. \tag{3.17}$$

Combining Eqs. (3.15) and (3.17) gives

$$r = z\left[1 + \frac{1}{2}\left(\frac{x_0 - x_1}{z}\right)^2 + \frac{1}{2}\left(\frac{y_0 - y_1}{z}\right)^2\right] \tag{3.18}$$

and, therefore, Eq. (3.13) becomes

$$h(x_1, y_1; x_0, y_0) = \frac{\exp(jkz)}{j\lambda z}\exp\left\{j\frac{k}{2z}\left[(x_0 - x_1)^2 + (y_0 - y_1)^2\right]\right\}. \tag{3.19}$$

A comparison of Eqs. (3.13) and (3.19) shows that the spherical wavefronts have been approximated by quadratic wavefronts. This approximation, resulting in Fresnel diffraction, is only valid when close to the aperture so is often referred to as *near-field* diffraction.

The substitution of Eq. (3.19) into Eq. (3.11), gives the optical field in the observation plane for Fresnel diffraction as

$$\begin{aligned} U(x_1,y_1) &= \frac{\exp(jkz)}{j\lambda z}\int_{-\infty}^{\infty}\int_{-\infty}^{\infty} U(x_0,y_0) \\ &\times \exp\left\{j\frac{k}{2z}\left[(x_0-x_1)^2+(y_0-y_1)^2\right]\right\} dx_0dy_0 \qquad (3.20) \\ &= \frac{\exp(jkz)}{j\lambda z}\exp\left\{j\frac{k}{2z}(x_1^2+y_1^2)\right\}\int_{-\infty}^{\infty}\int_{-\infty}^{\infty}\left\{U(x_0,y_0)\exp\left[j\frac{k}{2z}(x_0^2+y_0^2)\right]\right\} \\ &\times \exp\left[-j\frac{k}{z}(x_0x_1+y_0y_1)\right] dx_0dy_0. \qquad (3.21) \end{aligned}$$

The second representation of $U(x_1,y_1)$, Eq. (3.21), shows that the optical field $U(x_1,y_1)$ is simply the Fourier transform of $U(x_0,y_0)\exp\left[j\frac{k}{2z}(x_0^2+y_0^2)\right]$ evaluated at $(\frac{x_1}{\lambda z},\frac{y_1}{\lambda z})$.

3.2.3 Fraunhofer diffraction

The Fraunhofer approximation further simplifies the Rayleigh-Sommerfeld diffraction formula. When the Fraunhofer assumption [66]

$$z >> \frac{k(x_0^2+y_0^2)_{\max}}{2} \qquad (3.22)$$

is used the quadratic phase term $\exp\left(j\frac{k}{2z}(x_0^2+y_0^2)\right)$ in Eq. (3.21) is approximately unity. The Fraunhofer approximation, therefore, replaces the quadratic wavelets of the Fresnel approximation with plane waves to give

$$\begin{aligned} U(x_1,y_1) &= \frac{\exp(jkz)}{j\lambda z}\exp\left\{j\frac{k}{2z}(x_1^2+y_1^2)\right\} \\ &\times \int_{-\infty}^{\infty}\int_{-\infty}^{\infty} U(x_0,y_0)\exp\left[-j\frac{2\pi}{\lambda z}(x_0x_1+y_0y_1)\right] dx_0dy_0 \qquad (3.23) \\ &= \frac{\exp(jkz)}{j\lambda z}\exp\left\{j\frac{k}{2z}(x_1^2+y_1^2)\right\}\mathcal{F}\left\{U(x_0,y_0)\right\}_{|(\frac{x_1}{\lambda z},\frac{y_1}{\lambda z})}. \qquad (3.24) \end{aligned}$$

$U(x_1,y_1)$ is now found as the Fourier transform of the optical field in the aperture evaluated at $(\frac{x_1}{\lambda z},\frac{y_1}{\lambda z})$. Fraunhofer diffraction is only valid a long distance from the aperture, as indicated by Eq. (3.22), and as a result is termed *far-field* diffraction. It is simply the limiting case of the Fresnel approximation as illustrated by Fig. 3.9. The Fraunhofer approximation is valid for most astronomical applications, for example at a wavelength of 589×10^{-9}m (visible light) and a 1m aperture, the observation distance z must satisfy

$$z >> 2600 \text{ km}. \qquad (3.25)$$

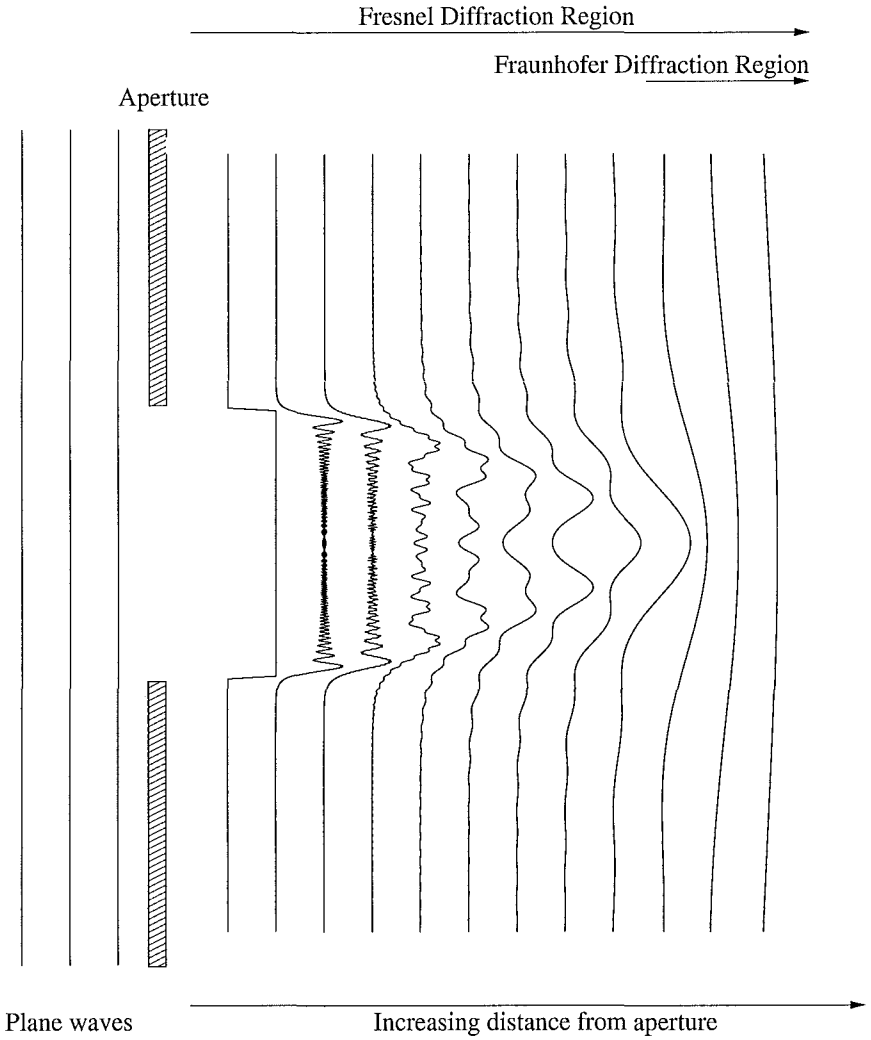

Figure 3.9: *The regions of diffraction and typical diffraction patterns observed within these regions for a square aperture. As the distance from the aperture is increased the similarity between the diffraction pattern and the aperture gradually disappears. Note that the distance from the aperture is not to scale. The physical distance between each of the diffraction patterns increases as the distance from the aperture increases.*

3.2.4 Diffraction from an aperture

The repeated application of diffraction formulae allows for the investigation of complex optical systems, for instance a system made up of a combination of optical elements. Alternatively, diffraction effects can be grouped and assumed to occur during the propagation from object to entrance pupil and exit pupil to image. The propagation of light through

the optical system is then adequately described by geometrical optics [66]. It is however possible to go a step further and associate all the diffraction effects with either of the above propagation paths, for example it is common to view diffraction effects as resulting from aberrations in the exit pupil [66]. This requires the introduction of the generalised pupil function, $\mathcal{P}(x,y)$, which represents the wavefront in the exit pupil, and is defined as

$$\mathcal{P}(x,y) = \begin{cases} P(x,y)\exp[j\phi(x,y)] & \text{inside aperture} \\ 0 & \text{outside aperture} \end{cases}, \tag{3.26}$$

where $P(x,y)$ represents the pupil function for a diffraction-limited system,

$$P(x,y) = \begin{cases} 1 & \text{inside aperture} \\ 0 & \text{outside aperture} \end{cases}. \tag{3.27}$$

The pupil phase, a measure of the phase aberrations, is given by $\phi(x,y)$ and can be expressed as a function of the overall wavefront aberration $W(x,y)$, defined in section 3.3, by

$$\phi(x,y) = \frac{2\pi}{\lambda} W(x,y). \tag{3.28}$$

The relationship between the object and image planes for the generalised framework, illustrated in Fig. 3.10, is given as [139]

$$U(x_1,y_1) = U(x_0,y_0) \odot h(x_1,y_1;x_0,y_0) \tag{3.29}$$

where $h(x_1,y_1;x_0,y_0)$ is the imaging system response. In the absence of aberrations, an analysis of the simplest possible imaging system, a single thin lens, gives [66]

$$h(x_1,y_1;x_0,y_0) = K\int_{-\infty}^{\infty}\int_{-\infty}^{\infty} P(x,y)\exp\left\{-j\frac{2\pi}{\lambda z}[(x_1-x_0)x+(y_1-y_0)y]\right\}dxdy, \tag{3.30}$$

where z represents the distance from the exit pupil to the observation plane (see Fig. 3.10). Eq. (3.30) corresponds to the Fraunhofer diffraction pattern of the exit pupil centred on the ideal image point ($x_1 = x_0, y_1 = y_0$). With the following change of variables,

$$u = \frac{x}{\lambda z} \text{ and} \tag{3.31}$$

$$v = \frac{y}{\lambda z}, \tag{3.32}$$

Eq. (3.30) becomes

$$h(x_1 - x_0, y_1 - y_0) = K' \int_{-\infty}^{\infty} \int_{-\infty}^{\infty} P(\lambda z u, \lambda z v) \exp\left\{-j2\pi \left[(x_1 - x_0)u + (y_1 - y_0)v\right]\right\} du dv. \tag{3.33}$$

Now setting $x = (x_1 - x_0)$, $y = (y_1 - y_0)$ and ignoring the constant gives an exact Fourier transform relationship

$$h(x, y) = \int_{-\infty}^{\infty} \int_{-\infty}^{\infty} P(\lambda z u, \lambda z v) \exp\left\{-j2\pi(ux + vy)\right\} du dv \tag{3.34}$$

$$= \mathcal{F}\left\{P(\lambda z u, \lambda z v)\right\}. \tag{3.35}$$

In this case the image can be considered to be a convolution of the image predicted by geometrical optics with an impulse response determined by the exit pupil of the system. For a system with aberrations the ideal pupil function $P(x, y)$ is replaced by $\mathcal{P}(x, y)$.

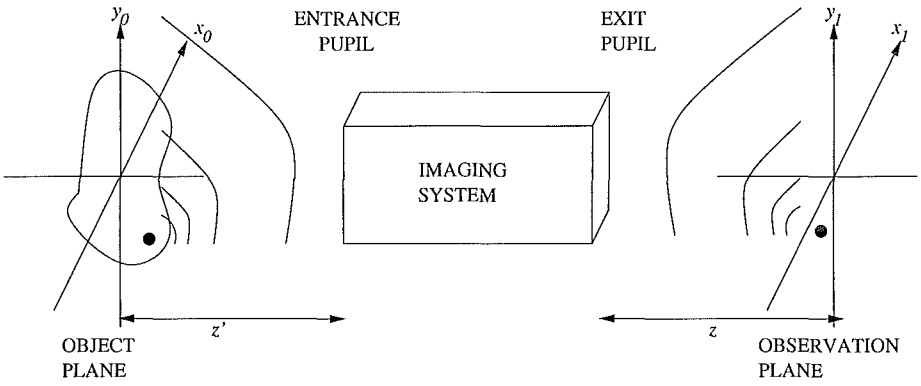

Figure 3.10: *Generalised imaging system.*

3.2.5 Resolution limits

In aberration-free imaging, diffraction provides the only limit to system resolution. Since diffraction effects are inherent to real images and cannot be removed, the aim becomes to minimise the wavefront aberration, $W(x, y)$, and hence to achieve as close to diffraction-limited imaging as possible.

As mentioned previously, most astronomical problems can be described by Fraunhofer diffraction. Since the apertures of most optical systems, for instance telescopes and micro-

scopes, are circular the Fraunhofer diffraction pattern of a circular aperture is an important result. The pupil function for an aberration-free circular aperture is

$$P(x,y) = \begin{cases} 1 & x^2+y^2 \leq a^2 \\ 0 & x^2+y^2 > a^2 \end{cases} \tag{3.36}$$

$$= \text{circ}\left(\frac{r}{a}\right) \tag{3.37}$$

where a is the radius of the aperture. Substitution of Eq. (3.37) into Eq. (3.35) gives

$$h(x,y) = \mathcal{H}\left\{\text{circ}\left(\frac{r}{a}\right)\right\}_{|\frac{r}{\lambda z}} . \tag{3.38}$$

The Hankel transform can be used since the aperture in this case is circularly symmetric. This gives

$$h(x,y) = \frac{2J_1(w)}{w} \tag{3.39}$$

where

$$w = \frac{2\pi}{\lambda}\frac{a}{z}\sqrt{x^2+y^2} \tag{3.40}$$

and $J_1(w)$ is a first order Bessel function of the first kind. The intensity is given by

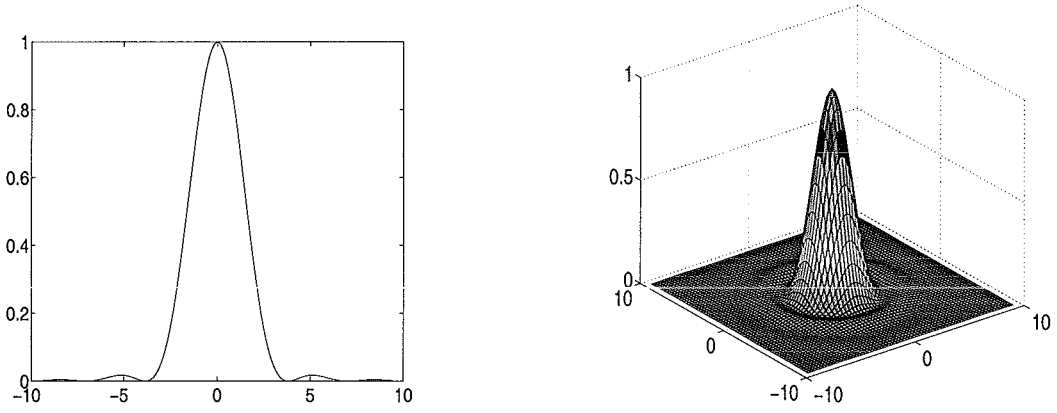

(a) (b)

Figure 3.11: *The Airy disk pattern in (a) 1D and (b) 2D.*

$$|h(x,y)|^2 = \left(\frac{2J_1(w)}{w}\right)^2 \tag{3.41}$$

and is shown in Fig. 3.11. This function is called the Airy disk function or pattern. It has a similar form to the sinc function, described by Eq. (2.34), with one major difference. The zero crossings of the sinc function are equal distances apart, whereas the distance between zero crossings for the Airy disk function decrease as the distance from the origin increases as indicated by Table 3.1.

w	$\left(\frac{2J_1(w)}{w}\right)^2$	
0	1	Max
3.833	0	Min
5.136	0.0175	Max
7.016	0	Min
8.417	0.0042	Max
10.174	0	Min

Table 3.1: *The first few maxima and minima of the Airy disk function*

The resolution of an imaging system is generally regarded as a measure of its ability to distinguish between two closely spaced point sources [60]. This would indicate that the resolution is determined by the impulse response of the imaging system. A system with an impulse response that closely represents a delta function has a much better resolution than a system with a more spread impulse response. Diffraction determines the PSF for aberration-free imaging and thus places a fundamental limit on how close two points can be and still be distinguished.

Consider again the Fraunhofer diffraction pattern corresponding to aberration-free imaging using a circular aperture. The image corresponding to two separated point sources is the sum of two shifted Airy disk patterns, as illustrated in Fig. 3.12. According to Rayleigh's criterion for resolution [66], two point sources of equal strengths are just resolved if the centre of the Airy disk due to one source falls on the first zero crossing of the Airy disk pattern due to the second source. Let $r_{\min}$ denote the minimum distance of separation

necessary to enable two point sources to be resolved, where

$$r_{\min} = \sqrt{x^2 + y^2}. \tag{3.42}$$

Inspection of Table 3.1 indicates that the first zero crossing occurs at 3.833, hence

$$3.833 = \frac{2\pi}{\lambda}\frac{a}{z} r_{\min}. \tag{3.43}$$

Manipulation of Eq. (3.43) gives

$$r_{\min} = 1.22\lambda\left(\frac{z}{2a}\right) \tag{3.44}$$

$$= 1.22\lambda F \tag{3.45}$$

where $F = \frac{z}{2a}$ is the F number of a system. The resolution can also be specified in terms of an angle between two objects and is preferable for astronomical applications. The minimum angle of separation to enable the detection of two stars is

$$\alpha_{\min} = 1.22\frac{\lambda}{D} \tag{3.46}$$

where D is the telescope diameter.

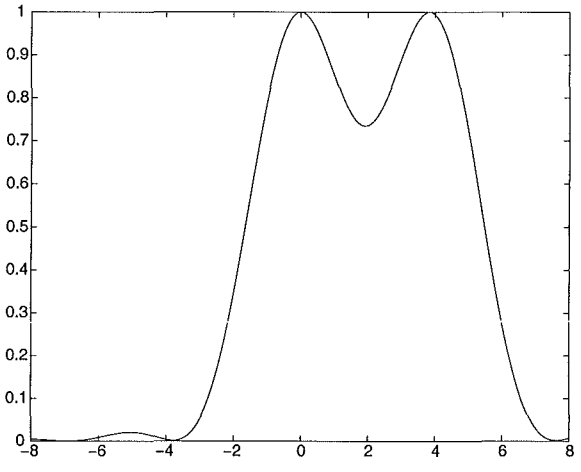

Figure 3.12: *Intensity pattern for two point sources separated by the Rayleigh resolution distance.*

Consider now an aberrated optical system. The PSF corresponding to an aberrated optical system is always more spread than that of the same system with no aberrations. The

spreading of the PSF results in a decrease in the corresponding peak height as area is preserved. A useful measure of the performance or quality of a system is the ratio of the peak PSF values for the same system, with and without aberrations. This measure, known as the *Strehl Ratio*, S, is described mathematically as

$$S = \frac{(|h(x,y)|^2_{\max})_{\text{actual}}}{(|h(x,y)|^2_{\max})_{\text{diffraction-limited}}}. \tag{3.47}$$

This concept is illustrated in Fig. 3.13. The values of S can lie only in the interval 0 to 1. It should be noted that a tip or tilt of the wavefront incident on the imaging system merely shifts the centre of the image without affecting the image or altering the corresponding Strehl ratio.

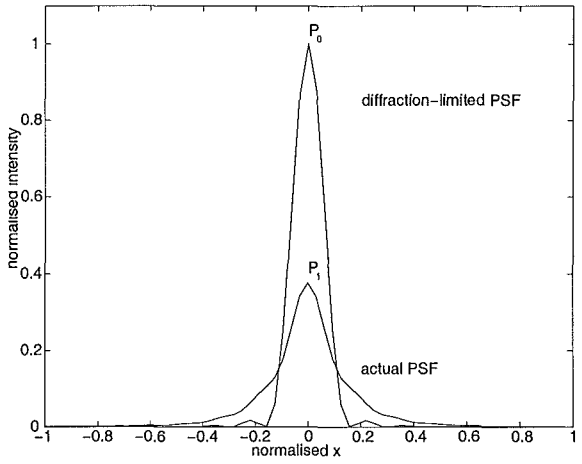

Figure 3.13: *The Strehl ratio is defined as the ratio of the peak of a system with aberrations and the peak of the same system free from aberrations.*

In astronomical imaging, atmospheric turbulence produces random aberrations (see section 3.4) and therefore it is important to relate the Strehl to these phase distortions. An alternative expression for S is [162]

$$S = \frac{1}{\pi^2}\left|\int_0^1\int_0^{2\pi} \exp\left\{-j\frac{2\pi}{\lambda}W(\rho,\theta)\right\}\rho d\rho d\theta\right|^2. \tag{3.48}$$

For small aberrations,

$$\exp\left\{-j\frac{2\pi}{\lambda}W(\rho,\theta)\right\} \approx 1 - j\frac{2\pi}{\lambda}W(\rho,\theta) - \frac{1}{2}\left(\frac{2\pi}{\lambda}\right)^2 W(\rho,\theta)^2. \tag{3.49}$$

Substitution of this result into Eq. (3.48) and integrating gives

$$S = 1 - \left(\frac{2\pi}{\lambda}\right)^2 \sigma_W^2 \tag{3.50}$$

$$= 1 - \sigma_\phi^2 \tag{3.51}$$

where σ_W^2 is the wavefront variance and σ_ϕ^2 represents the variance of the phase aberration. This expression indicates that S is independent of the form of aberration provided $\sigma_\phi^2 << 1$.

It is not possible to obtain a Strehl ratio of 1 for real optical systems. However, a system is said to be effectively diffraction-limited if $\sigma_\phi^2 < 0.2$ or $S \geq 0.8$. This is known as *Marechal's criterion.*

3.2.6 Coherent and incoherent imaging

To fully understand the forward problem in relation to optical imaging and imaging through turbulence it is necessary to know the properties of the light illuminating or being illuminated by the object, as these properties influence the image that is observed [67]. The assumption of strictly monochromatic light made previously is an idealistic assumption. The illumination generated by real sources is never perfectly monochromatic [66]. Furthermore, neither a perfectly coherent nor completely incoherent wave can exist, hence light does not fit into either category and is generally considered to be partially coherent. In this section the extreme cases of spatially coherent and spatially incoherent forms of illumination, referred to as coherent and incoherent illumination respectively, are discussed. These are of particular relevance since the spatial coherence properties of an optical field determine the performance limit of a system when imaging through the atmosphere.

Coherent illumination implies that the optical field is perfectly correlated or deterministic. Here all object points are assumed to have a fixed phase relationship, that is they must all be at the same frequency, and vary in unison. An example of a coherent radiation source is a laser. The nature of coherent illumination allows the responses of each object point to be added on a complex amplitude basis. It is therefore said to be linear in complex amplitude.

Recall the generalised imaging problem where the relationship between the input and output can be modelled as a convolution. The relationship between the object field $u_{\text{in}}(x, y)$ and the image field $u_{\text{out}}(x, y)$ is given as [139]

$$u_{\text{out}}(x, y) = u_{\text{in}}(x, y) \odot h(x, y), \tag{3.52}$$

where $h(x, y)$ represents the system impulse response. Application of the Fourier transform converts this to a multiplication,

$$U_{\text{out}}(u, v) = U_{\text{in}}(u, v)H(u, v) \tag{3.53}$$

where an uppercase quantity represents the Fourier transform of the corresponding lowercase quantity. The PSF of the generalised imaging system is given by Eq. (3.35). Hence the transfer function is obtained by Fourier transforming this to give

$$\begin{aligned} H(u, v) &= \mathcal{F}\{h(x, y)\} \\ &= \mathcal{F}\{\mathcal{F}\{P(\lambda z u, \lambda z v)\}\} \\ &= P(-\lambda z u, -\lambda z v). \end{aligned} \tag{3.54}$$

Therefore, the coherent transfer function is simply equal to the rotated pupil function. The coherent transfer functions and PSFs for square and circular apertures are illustrated in Fig. 3.14.

In incoherent illumination each object point is assumed to be statistically independent of all other object points. Incoherent imaging refers to the imaging of many types of objects, for example those that are self-luminous, illuminated by thermal light and astronomical objects, so it includes astronomical imaging. The independence of the responses to the object points requires that they are added on an intensity basis and, therefore, incoherent illumination is considered to be linear in intensity.

In the case of incoherent imaging the relationship between the input and output can be represented as [139]

$$i_{\text{out}}(x, y) = i_{\text{in}}(x, y) \odot |h(x, y)|^2. \tag{3.55}$$

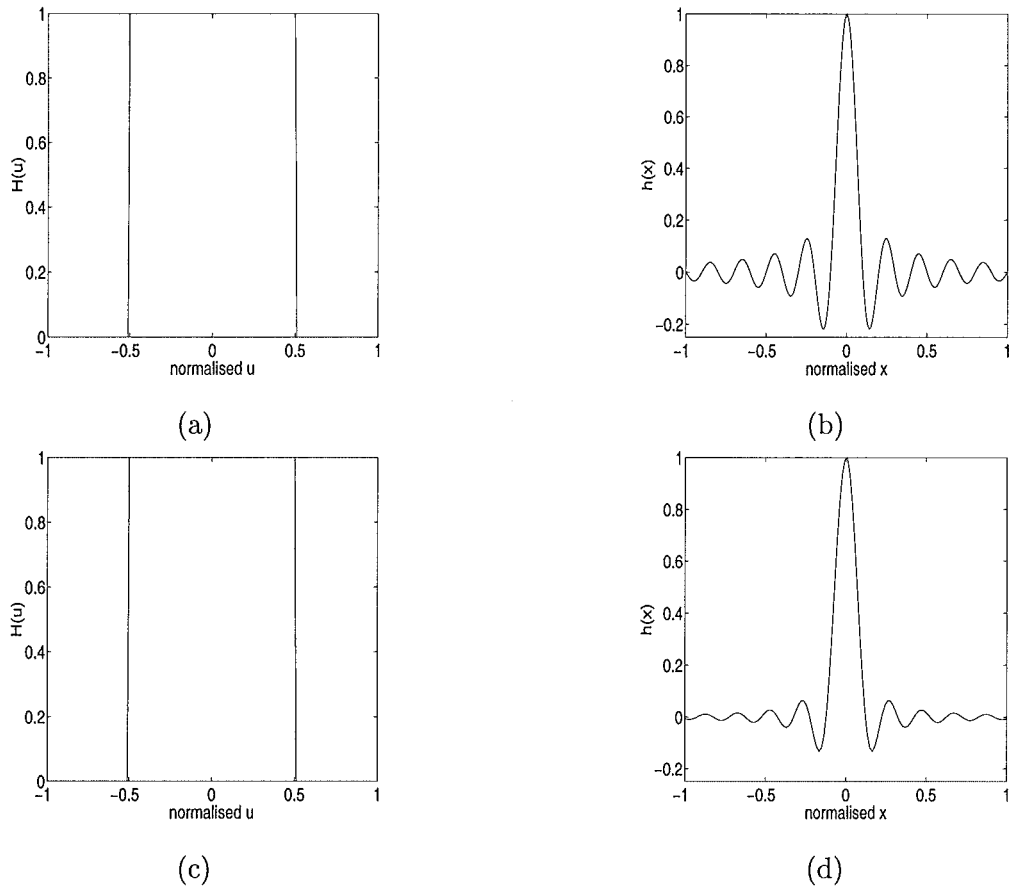

Figure 3.14: *Cross sections of the (a) Coherent transfer function for a square aperture (b) Coherent PSF for a square aperture (c) Coherent transfer function for a circular aperture and (d) Coherent PSF for a circular aperture.*

Application of the Fourier transform gives

$$I_{\text{out}}(u,v) = I_{\text{in}}(u,v)\mathcal{H}(u,v) \tag{3.56}$$

where an uppercase I corresponds to the Fourier transform of the corresponding lower case quantity and $\mathcal{H}(u,v)$ represents the incoherent transfer function, termed the optical transfer function (OTF). Using Eqs. (3.35), (3.55), (3.56) and the autocorrelation theorem, the incoherent transfer function is

$$\begin{aligned}\mathcal{H}(u,v) &= \mathcal{F}\left\{|h(x,y)|^2\right\} \\ &= \int\int P(\lambda z u', \lambda z v')P(\lambda z u' + \lambda z u, \lambda z v' + \lambda z v)dv'du' \\ &= P(\lambda z u, \lambda z v) * P(\lambda z u, \lambda z v).\end{aligned} \tag{3.57}$$

Therefore, the transfer function of an incoherent imaging system is simply the autocorrelation of the pupil function, as illustrated in Fig. 3.15.

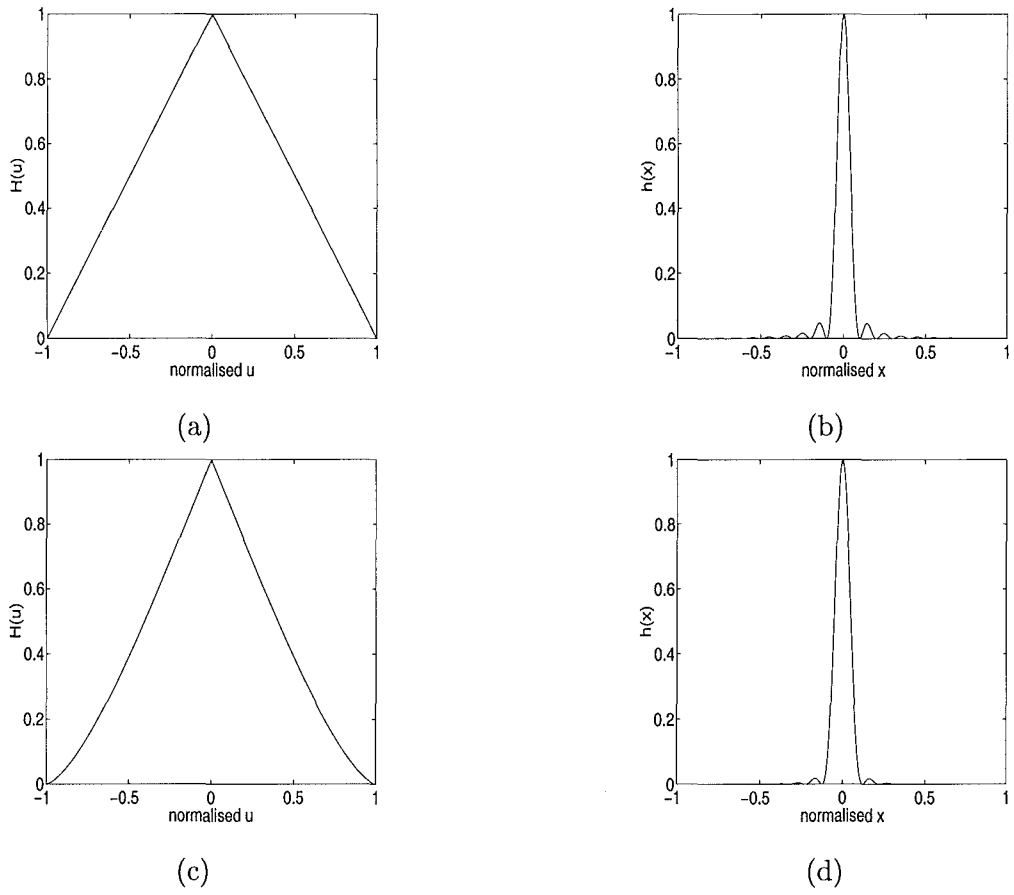

Figure 3.15: *Cross-sections of the (a) OTF for a square aperture (b) PSF for a square aperture (c) OTF for a circular aperture and (d) PSF for a circular aperture.*

3.3 Ideal and aberrated optical systems

All optical systems investigated so far have been considered to be ideal or diffraction-limited. An ideal system maps a point object to a point image at the correct location as in Fig. 3.6, whereas in a diffraction-limited system the image is no longer a point, the light is instead spread over a small area around the point. Real optical systems may fall short of this ideal behaviour as aberrations, which cause non-ideal images to be formed, may be encountered. In practice, image quality is degraded by imperfections in the image forming components

of a system, e.g. optical manufacturing and misalignments, non-linear behaviour due to the thermal and fluid properties of the system components and external random spatially and temporally varying wavefront perturbations such as atmospheric turbulence.

Ignoring external and non-linear aberrations (atmospheric turbulence is dealt with in section 3.4), the remaining aberrations can be divided into two general categories; those that are wavelength dependent, referred to as *chromatic aberrations* and those that are wavelength independent, known as *monochromatic aberrations.* Chromatic aberrations arise from the change in refractive index with changing wavelength, a phenomenon known as *dispersion.* It is the monochromatic aberrations, however, that are of interest in this thesis.

Consider the optical system represented in Fig. 3.16. The ideal spherical wavefront is denoted by S. In the absence of aberrations, the real wavefront is identical to S and an object point P_o is mapped to an image point P_i^*. In the presence of aberrations the real wavefront is distorted. A sample distorted wavefront is illustrated in Fig. 3.16 and denoted by S'. The aberrated wavefront maps point P_o to point P_i. The distance between P_i^* and P_i is termed the *ray aberration.* The path length between Q and $\bar{Q}$, points on the ideal and aberrated wavefronts respectively, is called the *wavefront aberration* and denoted by $W(x,y)$. Therefore, $W(x,y)$ represents the deformation of the wavefront from the ideal spherical shape of S, which causes the change in optical path length between Q and $\bar{Q}$.

All wavefront aberrations, those due to the system and external to the system, can be described by $W(x,y)$ which is termed the overall wavefront aberration. It is often expressed in polar coordinates, $W(\rho,\theta)$, with

$$\rho = \sqrt{x^2+y^2} \quad \text{and} \tag{3.58}$$

$$\theta = \tan^{-1}\left(\frac{y}{x}\right). \tag{3.59}$$

The expression for the wavefront aberration in polar coordinates can be expanded in a power series in terms of ρ, θ and y, where y is the position of the object in the field of view. This gives,

$$W(\rho^2, \rho y\cos(\theta), y^2) = a_1\rho^2 + a_2\rho y\cos(\theta)$$

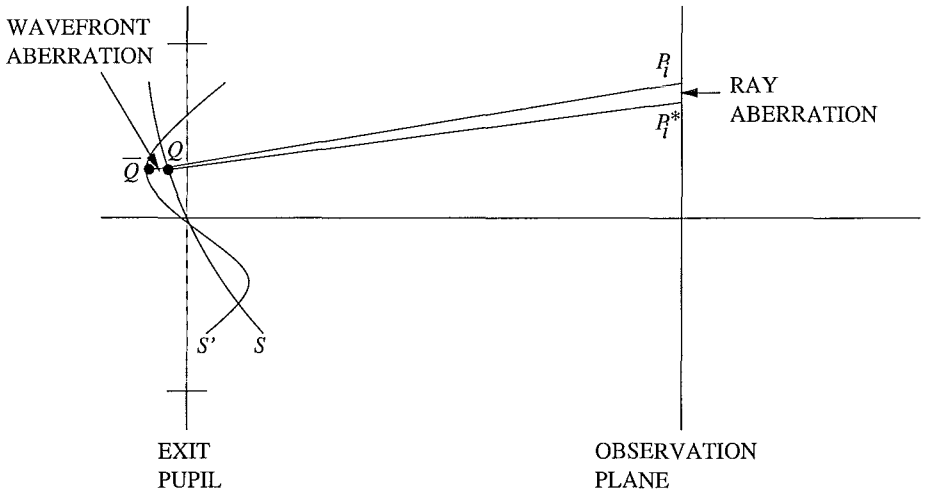

Figure 3.16: *Ray and wave aberrations. The displacement of the real image point P_i from the ideal image point P_i^* corresponding to an object at point P_o in the object plane describes the ray aberration. The deviation of the point $\bar{Q}$ on the real wavefront from the point Q on the ideal wavefront is termed the wave aberration.*

$$
\begin{aligned}
&+ \; b_1\rho^4 && \text{spherical aberration} \\
&+ \; b_2\rho^3 y\cos(\theta) && \text{coma} \\
&+ \; b_3\rho^2 y^2\cos^2(\theta) && \text{astigmatism} \\
&+ \; b_4\rho^2 y^2 && \text{field curvature} \\
&+ \; b_5\rho y^3\cos(\theta) && \text{distortion} \\
&+ \; \text{other higher order terms.} && (3.60)
\end{aligned}
$$

Terms 3 to 7 of Eq. (3.60) represent the most common monochromatic aberrations, known as the Seidal aberrations; spherical aberration, coma, astigmatism, field curvature and distortion. Each term represents a particular type of departure of the wavefront from the ideal spherical form.

The spherical aberration term in Eq. (3.60) is independent of y and hence affects both the off-axis and on-axis images. In the presence of spherical aberration there is no real focus, rays near the optical axis are brought to focus in a different location than those passing near the edge of the lens. The remaining Seidal aberrations contain a y^k term, where $k \geq 1$, indicating off-axis aberrations only. The first aberration to appear off-axis is

coma, followed by astigmatism, field curvature and distortion. Coma produces a cometlike asymmetric blurring of an image. Astigmatism arises when object rays lying in different planes are brought to focus at different distances from the lens. These three aberrations tend to blur or smear the image and prevent the formation of ideal point images.

Field curvature and distortion, on the other hand, allow the formation of ideal point images, but they deform the image. Field curvature produces ideal point images for each point object. These points, however, do not lie in a straight line so the position of the ideal point images is affected. When distortion is present the image of any straight line in the object plane which meets the axis is itself a straight line, but the image of any other straight line is curved.

3.3.1 Zernike polynomials

The Zernike polynomials are a set of polynomials defined on the unit circle [121] and are orthogonal over it. They have long been used to describe the aberrations of optical wavefronts due to external atmospheric turbulence and the fixed aberrations within optical systems themselves. Optical wavefronts can be described in terms of simple wavefront aberrations such as tip, tilt, defocus, astigmatism, coma and spherical aberration which correspond to the low order Zernike polynomials. Although many other sets of polynomials can also be used, the Zernike polynomials have several useful properties. They are generally defined in polar coordinates as the product of radial and angular terms. Using the ordering scheme of Noll [121] the Zernike polynomials are defined as

$$Z_{\text{even}j}(\rho,\theta) = \sqrt{n+1}R_n^m(\rho)\sqrt{2}\cos(m\theta), \quad m \neq 0 \tag{3.61}$$

$$Z_{\text{odd}j}(\rho,\theta) = \sqrt{n+1}R_n^m(\rho)\sqrt{2}\sin(m\theta), \quad m \neq 0 \tag{3.62}$$

$$Z_j(\rho) = R_n^0(\rho), \quad m = 0, \tag{3.63}$$

where,

$$R_n^m(\rho) = \sum_{s=0}^{(n-m)/2} \frac{(-1)^s(n-s)!}{s![(n+m)/2-s]![(n-m)/2-s]!}\rho^{n-2s}. \tag{3.64}$$

Here n is the radial degree or order and m is the azimuthal frequency or order and m and n are non-negative integers such that $m \leq n$ and $n - m =$ even. The index j is a mode

ordering number and is a function of n and m.

As mentioned above, Zernike polynomials are useful for expanding aberrated wavefronts in terms of the standard wavefront aberrations. The expansion of an arbitrary wavefront, $\phi(\rho,\theta)$, as a polynomial expansion over a circle of radius R is given by

$$\phi(R\rho,\theta) = \sum_j a_j Z_j(\rho,\theta). \tag{3.65}$$

The Zernike coefficients, a_j, are defined as

$$a_j = \int_0^1 \int_0^{2\pi} \mathcal{W}(\rho)\phi(R\rho,\theta)Z_j(\rho,\theta)d\rho \tag{3.66}$$

where $\mathcal{W}(\rho)$ is a unit volume weighting function,

$$\mathcal{W}(\rho,\theta) = \begin{cases} \frac{1}{\pi} & \rho \leq 1 \\ 0 & \rho > 1 \end{cases}. \tag{3.67}$$

Zernike polynomials are used in the design of "static" optical systems because of their useful aberration balancing properties [70], where balancing refers to the combining of different aberrations in order to obtain the best image. For example, a system suffering from a small amount of sixth-order spherical aberration (ρ^6) can be compensated by the introduction of a controlled amount of fourth-order spherical aberration (ρ^4) and defocus (ρ^2) [23]. Although Zernike polynomials have been widely used to represent fixed aberrations in optical systems [139], they can also be used to represent atmospheric turbulence as outlined in chapter 4.

3.4 Imaging through atmospheric turbulence

Atmospheric turbulence makes a significant contribution to wavefront aberrations. The refractive index fluctuations inherent to atmospheric turbulence affect all optical systems that use light which has propagated through long atmospheric paths [139]. Atmospheric turbulence was first introduced in chapter 1, as the measurement, compensation and elimination of its effects are the motivation for much of the work in this thesis. A short review of its effects is included in section 3.4.1 as well as an introduction to the phase structure function which is often used for its description.

The simulation of atmospherically distorted wavefronts is an important tool for studying light propagation and imaging and corresponds to one aspect of the forward problem for many of the inverse problems investigated in the later chapters of this thesis. Accurate simulations can be used to predict the performance of adaptive optics systems and test post processing algorithms under a wide variety of conditions. The ultimate aim, is to develop efficient and effective methods for imaging astronomical objects through the turbulent atmosphere.

The effect of the atmosphere is not deterministic and must be modelled using statistics. Most simulation techniques assume that atmospheric turbulence can be modelled with Kolmogorov statistics. As a result a large number of approaches have been used to generate phase screens with Kolmogorov statistics, many of which are detailed in chapter 4, including spectral methods, modal expansions as well as existing and new techniques using the fractal property of Kolmogorov turbulence. However, the Kolmogorov model is limited by its unrealistic inner and outer scale assumptions as a non-zero inner scale is imposed during the simulation of atmospheric turbulence. Simulation of other turbulence types is also important as deviation from the assumed Kolmogorov statistics has been measured [153]. The extension of the new turbulence simulation method to non-Kolmogorov statistics is straightforward as demonstrated in chapter 4.

Section 3.4.2 deals with long and short exposure imaging. The exposure time of optical imaging apparatus has a large effect on the statistics of the problem. Long exposure imaging captures average information, whereas short exposure imaging freezes the instantaneous effects of the atmosphere.

Perhaps the most familiar manifestation of atmospheric turbulence is in the twinkling of the stars. This effect, which results from the propagation of phase distorted wavefronts, is known as stellar scintillation and provides the basis for the SCIDAR technique discussed later in this thesis. The theory of wave propagation through atmospheric turbulence is outlined in section 3.4.3, with its simulation detailed in chapter 4.

3.4.1 Review of atmospheric turbulence and its properties

The atmosphere, heated by the sun during the day and cooled by radiation at night is in unceasing turmoil [16]. Optically the atmosphere acts like a collection of lenses of varying refractive indices. The effects of atmospheric turbulence manifest themselves in a number of ways; random image motion, image spreading and the twinkling of the stars. The atmospheric effects on an image depend not only on the atmosphere but also on the size of the telescope aperture through which it is viewed. Random image motion is observed with small apertures, whereas image spreading and blurring result from the use of large apertures. When a short exposure time is used to effectively freeze the atmosphere an image with a speckled appearance results. By contrast long exposure times tend to broaden and smooth the PSF, spreading the images.

Atmospheric turbulence is often modelled by Kolmogorov statistics, named after A. N. Kolmogorov who made key contributions to the mathematics of turbulent air motion [87]. The extension of Kolmogorov's results to include the statistics of refractive index fluctuations was made by Tatarskii [156]. A key quantity in describing turbulence is the refractive index structure function, $D_n(\mathbf{r}')$, which arises naturally in the analysis of the average optical transfer function of a telescope looking through turbulence [139]. It is simply the mean square difference of two random processes, defined as

$$D_n(\mathbf{r}') = \left\langle |n(\mathbf{r}) - n(\mathbf{r}+\mathbf{r}')|^2 \right\rangle, \tag{3.68}$$

where $n(\mathbf{r})$ represents the random refractive index fluctuations. This can be related to the covariance of the random process by

$$D_n(\mathbf{r}') = 2[C_n(0) - C_n(\mathbf{r}')]. \tag{3.69}$$

Consider now a plane wave entering the atmosphere. It undergoes phase and amplitude distortions due to optical path fluctuations resulting from the refractive index fluctuations inherent to atmospheric turbulence. The phase shift, $\phi(\mathbf{r})$, introduced by the random refractive index fluctuations is given by

$$\phi(\mathbf{r}) = k \int_h^{h+\delta h} n(\mathbf{r}, z) dz. \tag{3.70}$$

As in the case of refractive index fluctuations, it is possible to describe these phase fluctuations in terms of the phase structure function, $D_\phi(\mathbf{r}')$, which describes the variance of the difference of the phase at point $\mathbf{r}$ and a nearby point $\mathbf{r}+\mathbf{r}'$. Mathematically,

$$D_\phi(\mathbf{r}') = \left\langle |\phi(\mathbf{r}) - \phi(\mathbf{r}+\mathbf{r}')|^2 \right\rangle. \tag{3.71}$$

The phase structure function of a wave that has propagated through Kolmogorov turbulence is [136]

$$D_\phi(\mathbf{r}') = 2.91k^2(\cos\zeta)^{-1}|\mathbf{r}'|^{5/3}\int_0^\infty C_N^2(z)\mathrm{d}z \tag{3.72}$$

$$= 6.88\left(\frac{|\mathbf{r}'|}{r_0}\right)^{5/3}, \tag{3.73}$$

where r_0 is the turbulence coherence length or Fried's parameter defined by Eq. (1.13) and ζ is angle from the zenith or vertical, termed the zenith angle.

3.4.2 Diffraction-limited, short and long exposure imaging

Fig. 3.17 illustrates diffraction-limited, and sample short exposure and long exposure images for a circular aperture and $D/r_0 = 10$. The diffraction-limited image is simply the Fraunhofer diffraction pattern of the aperture and shows the diffraction effects of a finite aperture. An exposure time in the order of milliseconds produces the short exposure image illustrated in Fig. 3.17(b), which is speckled in appearance. Note that many of the individual speckles are the same size as the diffraction-limited image. A speckle image is considered to capture instantaneous atmospheric perturbations. The final image illustrated in Fig. 3.17 is a sample long exposure image obtained by summing 1000 short exposure images. Since the atmosphere is continually changing, the individual short exposure images are continually evolving and changing producing the average image illustrated.

Figs. 3.18 and 3.19 contain the diffraction-limited, short exposure and long exposure OTFs and PSFs for square and circular apertures respectively. The short and long exposure results are plotted for D/r_0 values of 0.1, 1, 2 and 10 and the diffraction-limited results are reproduced from Fig. 3.15 for comparison purposes. The quality of short exposure images is not affected by the wavefront tilt. Hence, the short exposure OTFs generated from an ensemble

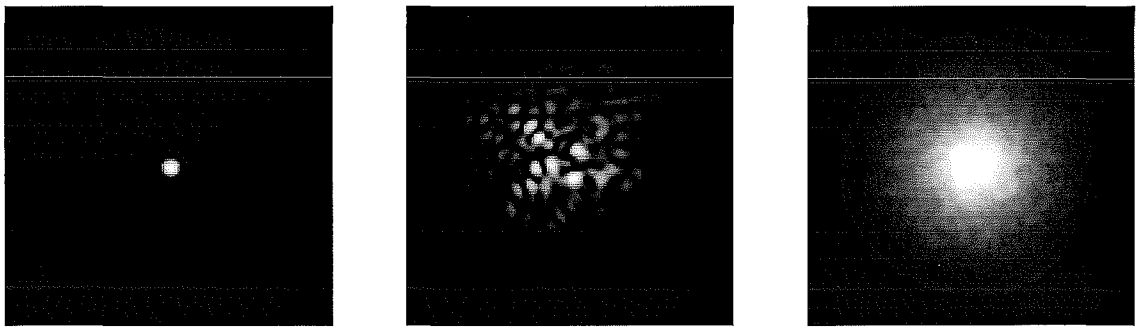

(a) (b) (c)

Figure 3.17: *Simulated single star images. (a) Diffraction-limited image, (b) short exposure image and (c) long exposure image.*

of centroided speckle images contain a considerable amount of high frequency information, particularly for low D/r_0. The corresponding PSFs are, therefore, relatively narrow and not far from the diffraction-limited result. As the turbulence increases in severity, the speckling becomes more severe resulting in a narrower transfer function and a broader PSF. The long exposure image is an average quantity. This is seen clearly as an attenuation of the high frequencies in the OTFs, even for low values of D/r_0. As a result the corresponding PSFs quickly diverge from the diffraction-limited result to smoother and broader functions.

Atmospheric turbulence is continually changing and evolving with time, but can be considered static when exposure times of the order of milliseconds are employed. Exposure times which exceed this significantly are known as long exposure images, where the long exposure image is an ensemble average. This quantity is denoted by $\langle d_{\mathrm{LE}}(x,y)\rangle$, where

$$\langle d_{\mathrm{LE}}(x,y)\rangle = f(x,y) \odot \langle h_{\mathrm{LE}}(x,y)\rangle + \langle n(x,y)\rangle\,. \tag{3.74}$$

Here $\langle h_{\mathrm{LE}}(x,y)\rangle$ denotes the average image of a point source, $f(x,y)$ the object and $\langle n(x,y)\rangle$ the average image noise. The incoherent imaging of objects is of interest in this thesis, therefore, Fourier transforming Eq. (3.74) gives

$$\langle D_{\mathrm{LE}}(u,v)\rangle = F(u,v)\,\langle \mathcal{H}_{\mathrm{LE}}(u,v)\rangle + \langle N(u,v)\rangle\,, \tag{3.75}$$

where the transfer function corresponding to this form of illumination, $\mathcal{H}_{LE}(u,v)$, is described by Eq. (3.57). In the non-ideal case the generalised pupil function defined in Eq.

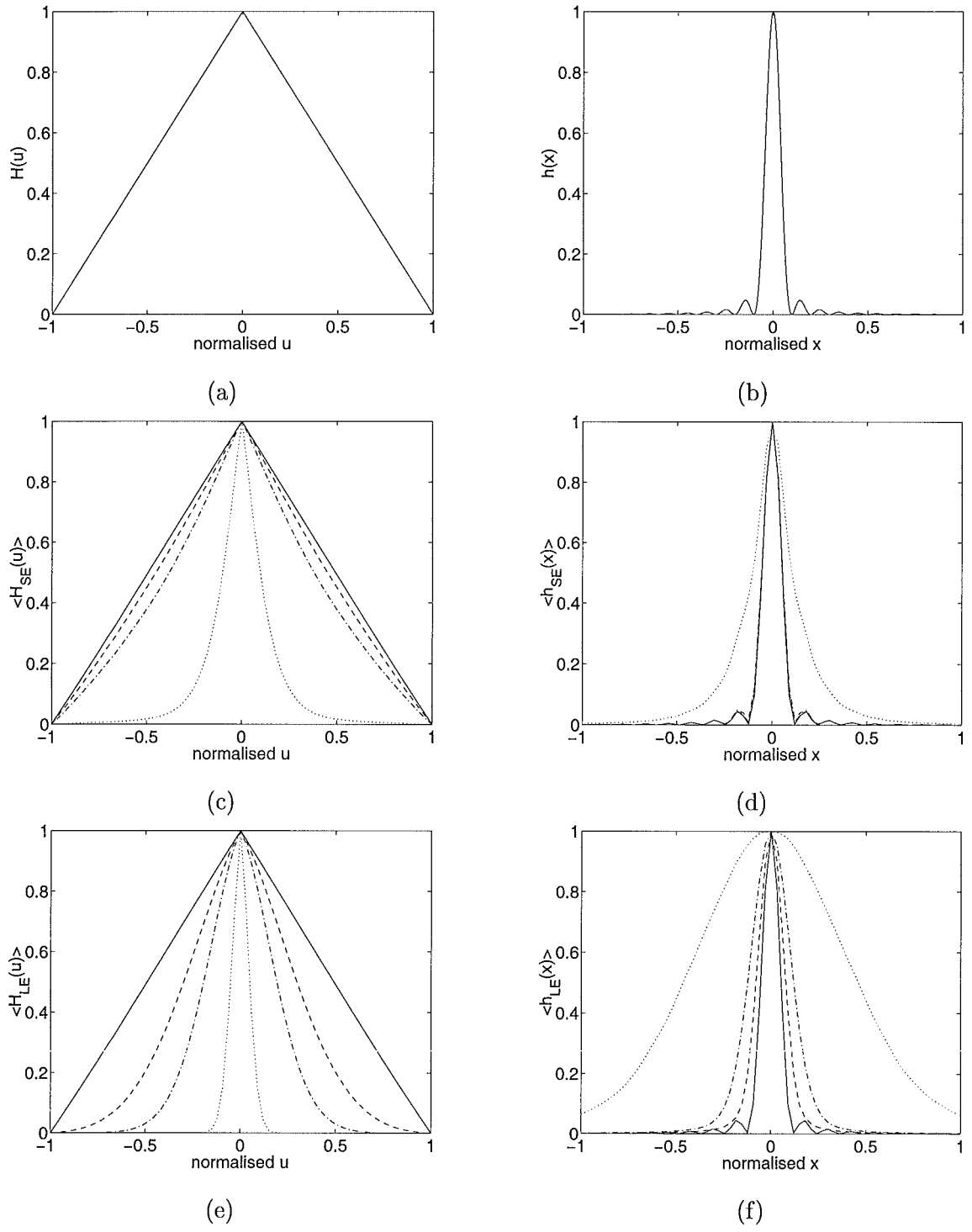

Figure 3.18: *Typical OTFs and PSFs for a square aperture. (a) Diffraction-limited OTF, (b) diffraction-limited PSF, (c) family of short exposure OTFs, (d) family of short exposure PSFs, (e) family of long exposure OTFs and (f) family of long exposure PSFs. The family of curves correspond to $D/r_0 = 0.1$ (solid), 1 (dashed), 2 (dashed-dotted) and 10 (dotted).*

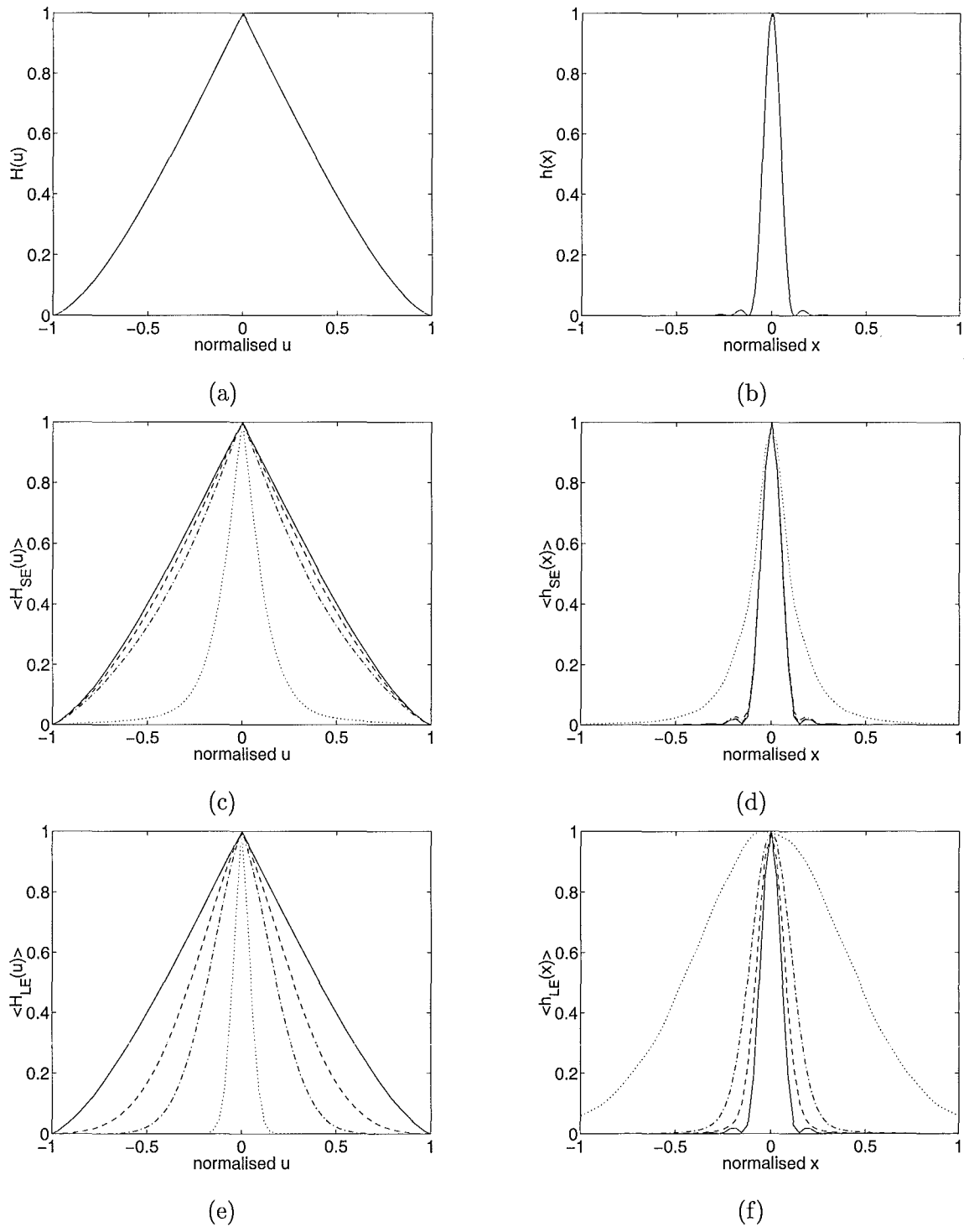

Figure 3.19: *Typical OTFs and PSFs for a circular aperture. (a) Diffraction-limited OTF, (b) diffraction-limited PSF, (c) family of short exposure OTFs, (d) family of short exposure PSFs, (e) family of long exposure OTFs and (f) family of long exposure PSFs. The family of curves correspond to $D/r_0 = 0.1$ (solid), 1 (dashed), 2 (dashed-dotted) and 10 (dotted).*

(3.26) is used in place of the diffraction-limited pupil function in Eq. (3.57) giving

$$\begin{aligned}\langle \mathcal{H}_{\mathrm{LE}}(u,v)\rangle &= \left\langle \int\int \mathcal{P}^*(\lambda z u', \lambda z v')\mathcal{P}(\lambda z u' + \lambda z u, \lambda z v' + \lambda z v)du'dv' \right\rangle \\ &= \langle \int\int P^*(\lambda z u', \lambda z v')\exp\{j\phi(\lambda z u', \lambda z v')\} \\ &\times \; P(\lambda z u' + \lambda z u, \lambda z v' + \lambda z v)\exp\{j\phi(\lambda z u' + \lambda z u, \lambda z v' + \lambda z v)\}\,\mathrm{d}u'\mathrm{d}v'\rangle \\ &= C_U(\lambda z u, \lambda z v)T(u,v) \end{aligned} \tag{3.76}$$

where $C_U(\mathbf{u})$ is the atmospheric transfer function,

$$C_U(\mathbf{u}) = \exp[-\frac{1}{2}D_\phi(\mathbf{u})], \tag{3.77}$$

and $T(u,v)$ is the telescope transfer function, given as

$$T(u,v) = \int\int P^*(\lambda z u', \lambda z v')P(\lambda z u' + \lambda z u, \lambda z v' + \lambda z v)\mathrm{d}u'\mathrm{d}v'. \tag{3.78}$$

Combining Eqs. (3.73), (3.77) and (3.78) gives the following expression for the long exposure transfer function,

$$\langle \mathcal{H}_{\mathrm{LE}}(u,v)\rangle = T(u,v)\exp\left[-3.44\left(\frac{\lambda z|\mathbf{u}|}{r_0}\right)^{5/3}\right]. \tag{3.79}$$

For long exposure times the OTF of the entire system is the product of the transfer function of the telescope with an atmospheric transfer function. The resolving power is limited by the telescope when $D < r_0$ and by the atmosphere when $D > r_0$ [134].

When the exposure time is short enough to freeze the effects of the atmosphere, a short exposure image is obtained. Short exposure astronomical images are highly structured and are made up of a collection of discrete segments that produce a speckled appearance as illustrated in Fig. 3.17(b), hence the name speckle images. A dominant effect of the atmosphere is a random wavefront tilt in the pupil [139]. This is clearly illustrated by the sample phase screen in Fig. 3.20. In fact Fried [54] calculated that approximately 90% of the degradation is due to the tilt of the wavefront. The tip and tilt components of atmospheric turbulence produce random motion of the images in the image plane, that shift the short exposure image without introducing additional distortion. The distortion present in the short exposure image is due instead to higher spatial perturbations.

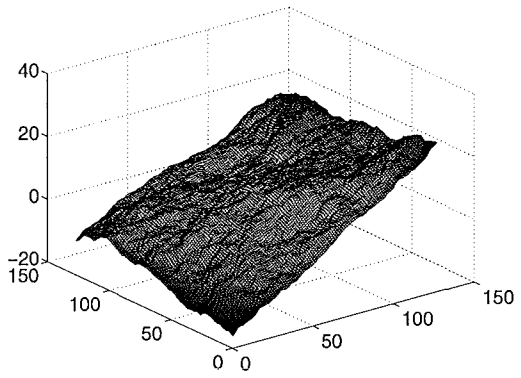

Figure 3.20: *A sample phase screen showing the dominant tilt effect.*

Since the quality of the short exposure image is unaffected by the dominant tip and tilt distortions, that broaden the long exposure PSFs and OTFs, the Strehl of a short exposure image is much better than that of a long exposure image. An alternative measure of image quality is given by the resolution, $\mathcal{R}$, defined as [55]

$$\mathcal{R} = \int_{-\infty}^{\infty} \langle \mathcal{H}(\mathbf{u}) \rangle \, d\mathbf{u}. \tag{3.80}$$

The resolution can be normalised by the limiting resolution $\mathcal{R}_{\max}$, the limiting value of the long exposure resolution as the aperture becomes arbitrarily large. The normalised short and long exposure resolutions are illustrated in Fig. 3.21. The results in Fig. 3.21 show the long exposure resolution tending to the limiting resolution $\mathcal{R}_{\max}$, as D/r_0 tends to infinity. This limiting aperture imposed by the atmosphere corresponds to the same resolution as diffraction-limited imaging with a lens of diameter r_0. The second curve in Fig. 3.21, however, shows a significant improvement in resolution may be obtained with short exposure times.

There are a number of ways that the wavefront tilt can be removed to improve the performance of the imaging system. The image can be compensated in real-time using a tilt correction mirror or a long term image can be formed by summing short exposure frames. This process is equivalent to the long exposure imaging of a tilt compensated system.

The transfer function for a short exposure image assuming incoherent illumination, the

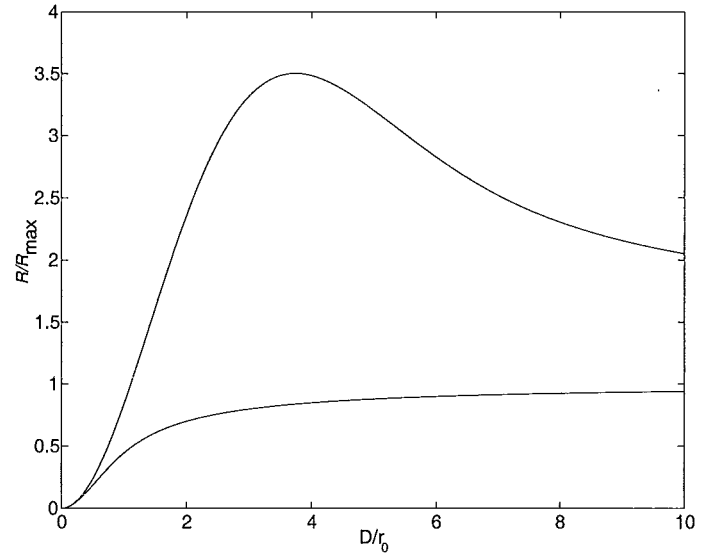

Figure 3.21: *The resolution $\mathcal{R}$ normalized by $\mathcal{R}_{\max}$ for long-exposure (lower curve) and short-exposure (upper curve) imaging.*

short exposure OTF, is given by [139]

$$\mathcal{H}_{\mathrm{SE}}(u,v) = T(u,v)\exp\left\{-3.44\left(\frac{\lambda z|\mathbf{u}|}{r_0}\right)^{5/3}\left[1-\alpha\left(\frac{\lambda z|\mathbf{u}|}{D}\right)^{1/3}\right]\right\}. \tag{3.81}$$

The difference between the long and short exposure results is the term

$$\left[1-\alpha\left(\frac{\lambda z|\mathbf{u}|}{D}\right)^{1/3}\right]. \tag{3.82}$$

In contrast to the long exposure OTF, the short exposure OTF is no longer simply the product of a telescope term with an atmospheric term. The atmospheric term now has a telescope dependence as indicated by Eq. (3.82). In long exposure imaging this term is equal to 1, i.e. $\alpha = 0$, whereas in short exposure imaging it is non-zero and the effect of the extra term varies with z. For small z the original exponential term dominates indicating the blur is mainly due to phase effects. For large z the second term becomes more significant, indicating contributions from phase and amplitude perturbations.

3.4.3 Wave propagation through Kolmogorov turbulence

Consider the propagation of a plane wave through atmospheric turbulence as illustrated in Fig. 3.22. The atmosphere is assumed to be homogeneous, except for a layer between the

altitudes of h and $h + \delta h$, which has an increased but constant C_N^2. A plane wave incident on the top of the layer at $h + \delta h$ suffers only a phase shift $\phi(x, y)$ as it passes through the layer. Since the layer is assumed to be so thin, diffraction effects can be neglected as there is no distance in which they can evolve. The effect of the layer on the wavefront is given by

$$U_h(x, y) = \exp\{j\phi(x, y)\} \tag{3.83}$$

where

$$\phi(x, y) = \frac{2\pi}{\lambda} W(x, y). \tag{3.84}$$

Alternatively, Eq. (3.83) can be written in polar coordinates as

$$U_h(\mathbf{r}) = \exp\{j\phi(\mathbf{r})\}. \tag{3.85}$$

Propagation through turbulence alters the correlation properties of the optical field. The correlation, which in this case is equivalent to the covariance since the process is zero mean, of the complex amplitude of a wave that has propagated through atmospheric turbulence is

$$\begin{aligned} C_h(\mathbf{r}') &= \langle U_h(\mathbf{r}) U_h^*(\mathbf{r} + \mathbf{r}') \rangle \\ &= \langle \exp\{j\left[\phi(\mathbf{r}) - \phi(\mathbf{r} + \mathbf{r}')\right]\} \rangle \\ &= \exp\left\{-\frac{1}{2} D_\phi(\mathbf{r}')\right\} \end{aligned} \tag{3.86}$$

where $D_\phi(\mathbf{r}')$ is the phase structure function as defined in Eq. (3.71).

Eq. (3.86) provides an expression for the correlation of the optical field at a height h, however, correlation at the pupil, $h = 0$, is of more practical interest as this is where measurements are made. Propagation of the optical field $U_h(\mathbf{r})$ from the output of the turbulence layer to the pupil gives rise to diffraction effects which in turn lead to amplitude fluctuations or scintillation. Optical wavelengths are generally much smaller than the scale of the observed wavefront perturbations, hence the Fresnel diffraction approximation can be used to obtain an expression for the complex field, $U_0(\mathbf{r})$, at ground level,

$$U_0(\mathbf{r}) = U_h(\mathbf{r}) \odot \left[\frac{\exp(jkz)}{j\lambda z} \exp\left(j\frac{k\mathbf{r}^2}{2z}\right)\right]. \tag{3.87}$$

It should be noted that this expression for evaluating the complex field at ground level is in terms of the linear convolution operation. This property of linearity is utilised in chapter

4 in the simulation of wave propagation through atmospheric turbulence. The accurate simulation of the propagation of an optical field using Eq. (3.87) requires the consideration of sampling issues which are discussed in detail in chapter 4.

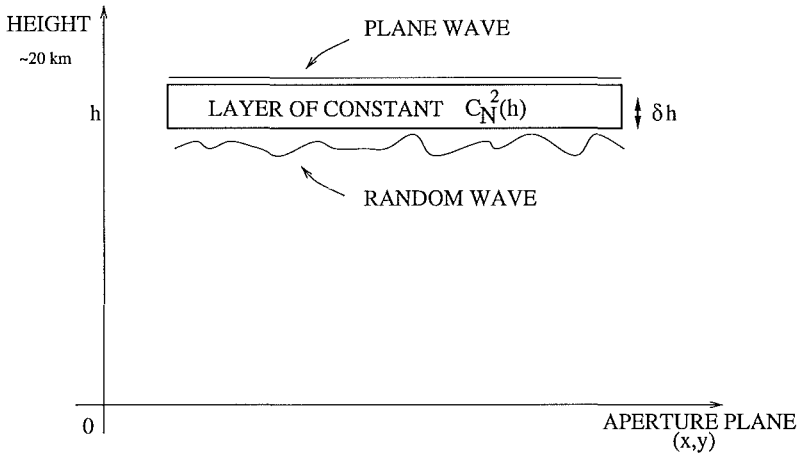

Figure 3.22: *Propagation of a planar wave through a single turbulent layer at an altitude of hkm.*

The field correlation of the complex amplitude at ground level is equal to the field correlation of the complex amplitude at the output of the layer, i.e.

$$\begin{aligned} C_0(\mathbf{r}') &= \langle U_0(\mathbf{r}) U_0^*(\mathbf{r}+\mathbf{r}') \rangle \\ &= C_h(\mathbf{r}'). \end{aligned} \tag{3.88}$$

In other words, the field correlation of the propagated optical field is invariant with free space propagation [139]. This result is useful when considering the effects of turbulence on an incoherent imaging system.

3.5 Adaptive optics technologies

Adaptive optics (AO) is a means for ground-based real-time compensation of the degradations introduced by the turbulent nature of the earth's atmosphere. An ideal AO system perfectly senses and compensates for atmospherically distorted wavefronts. However, this ideal performance is not achieved due to a number of limiting factors [139]; finite light lev-

els, anisoplanatism, fundamental limits of the system components and the finite temporal response.

The problem of the low light levels available for wavefront sensing is a significant limiting factor in AO systems. Astronomers are often interested in astronomical objects that are very dim, and hence the object itself cannot be used for wavefront sensing. Therefore, a nearby reference star must be used to obtain a measurement of the atmospheric distortion. However, this leads to anisoplanatism effects, which arise due to light from the reference star and the object of interest propagating through different regions of the atmosphere and hence seeing different distortions (see Fig. 3.23). The error introduced by the different perturbations the object and natural reference star see is termed *angular anisoplanatism* and is one of the major limitations to astronomical AO [70]. The difference in distortion is considered trivial if the two objects are separated by no more than the isoplanatic angle θ_o, which is a function of the vertical turbulence distribution. An additional limiting factor when considering visible wavelengths, is that only a fraction of the sky is within suitable distance of natural guide stars.

A solution to this problem was proposed in 1982 by Feinleib and again independently by Foy and Labeyrie [52] in the form of an artificial or laser guide star, providing enough light to accurately measure the atmospheric distortion at any point in the sky. However, the use of artificial guide stars introduces an entirely different set of problems in the form of *focal anisoplanatism* effects. Focal anisoplanatism results from light from the object and guide star travelling through different regions of high altitude turbulence, see Fig. 3.23(b). The resulting distortion is termed the *cone effect* as only a cone shaped volume of turbulence is measured, with turbulence above the beacon not being measured at all. Focal anisoplanatism is characterised by d_0, the effective diameter of the AO imaging system when a single artificial guide star is used, and is given by [56]

$$d_0 \approx \left[k^2 \cos^{-1}(\zeta) \int_0^H C_N^2(h)(h/H)^{5/3} dh\right]^{-3/5}, \tag{3.89}$$

where H is the altitude of the artificial star.

Focal anisoplanatism effects can be reduced by using backscattered light from a higher altitude, for example sodium beacons, which result from the excitation of sodium atoms in the sodium layer 90km above ground level and well above any turbulence of interest. The use of multiple artificial beacons has also been suggested to improve focal anisoplanatism and is discussed in section 3.5.2.

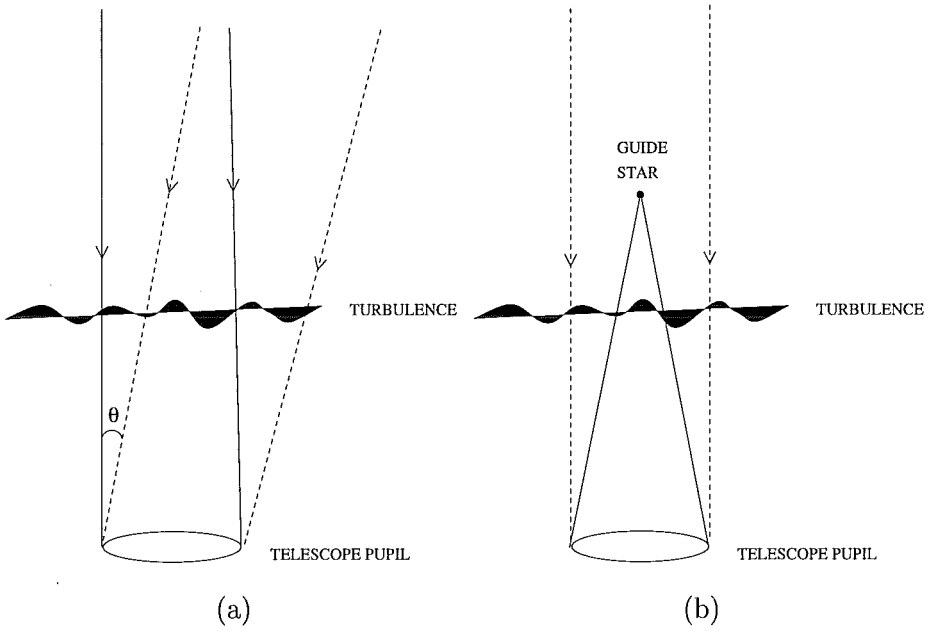

Figure 3.23: *(a) Angular anisoplanatism and (b) Focal Anisoplanatism, referred to as the cone effect.*

The fundamental limits of system components, for example the finite sampling of the wavefront sensor and the finite number of degrees of freedom of the deformable mirror, also prevent AO systems from achieving their ideal performance. Another limiting factor relates to the finite temporal response of the system. Errors introduced by changes in the atmosphere between measuring the turbulence and correcting for it lead to *temporal anisoplanatism.* As a result the systems ability to sense and compensate for the high spatial frequencies of the wavefront deformations is diminished [139]. These effects can be reduced by using wavefront sensors with higher spatial sampling rates and deformable mirrors with larger numbers of actuators corresponding to more degrees of freedom. However, these options are expensive and result in an increase in complexity. Less expensive and simpler

options include partially compensating and hybrid systems. Since 87% of the aberration is due to wavefront tilt, considerable compensation can be achieved with a simple tip-tilt system [62]. It essentially becomes a compromise between the cost and the compensation achieved. In addition, an AO system cannot completely remove atmospheric distortions, so some post processing may be required.

Many point objects such as stars and binary stars for example have been imaged at high resolutions using adaptive optics technologies. The same resolution images of extended objects, however, have not been seen. This is because the compensation performed by an AO system is only over a region of space known as the isoplanatic patch, with the size of extended objects such as planets, galaxies and nebulae, exceeding this region. A number of approaches have been suggested to improve the field of view of an adaptive optical telescope. These include single and multiple conjugate adaptive optics discussed in section 3.5.1 and the use of multiple laser guide stars discussed in section 3.5.2, which was also suggested as a means for reducing focal anisoplanatism. An additional benefit of a multiconjugate adaptive optics system is the reduction of the amplitude variations [15], that cannot be compensated for with a mirror.

3.5.1 Multiconjugate adaptive optics (MCAO)

The angular extent of many objects of interest exceeds the isoplanatic angle, so compensation over a wide field of view is a major goal for astronomical AO. In a conventional AO system the deformable mirror (DM) is conjugated to the telescope entrance pupil [129] and provides compensation only over the isoplanatic angle θ_0, typically 2-3 arcseconds for visible wavelengths. This corresponds to the optimal placement of the DM only if the boundary layer turbulence is dominant. A significant increase in the field of view (FOV) can be achieved by conjugating the deformable mirror to the average seeing layer. Racine *et al* [129] report an increase in the FOV by a factor of two when using this approach.

The conjugation of the DM to the average seeing layer is only optimal when the turbulence is confined to a single layer. However, atmospheric turbulence is known to consist of several

layers, for example the presence of more than one dominant layer has been reported by Kluckers *et al* [85]. Therefore, to achieve compensation over wide FOVs, it is necessary to employ three-dimensional wavefront compensation [70], to account for the three-dimensional structure of the atmosphere.

The possibility of increasing the isoplanatic patch by using multiple DMs, each imaged on a specific atmospheric layer has been proposed by a large number of authors [52,81,154], and is referred to as multiconjugate adaptive optics (MCAO). More complete reference lists for this area can be found in Beckers [15] and Hardy [70]. Ideally the DM positions correspond to the turbulent layers as illustrated for a two layer system in Fig. 3.24, although the general problem of fewer DMs than turbulent layers has been investigated by Fusco *et al* [59]. The placement of the DMs requires knowledge of the vertical structure of the atmosphere, or at least knowledge of the heights of the turbulent layers. This can be achieved using atmospheric tomography techniques or SCIDAR and related techniques investigated in some detail in chapters 7 and 8.

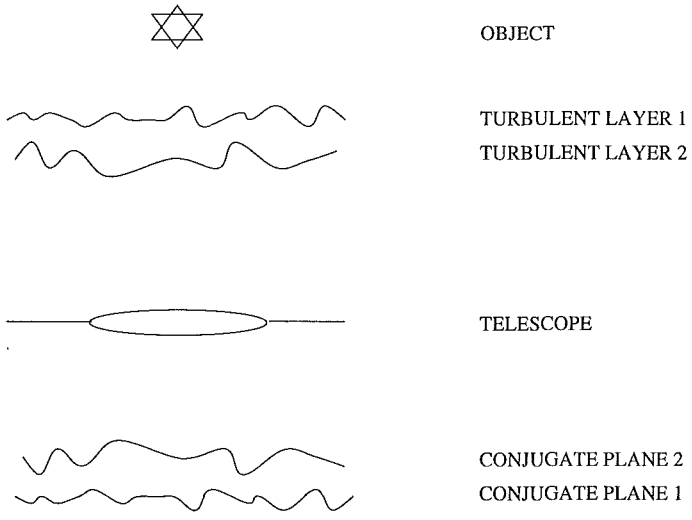

Figure 3.24: *A multiple conjugate system with two deformable mirrors.*

3.5.2 Multiple laser guide stars

The use of multiple laser guide stars, suggested by Foy and Labeyrie [52], has been proposed as a means for reducing focal anisoplanatism effects and increasing the field of view over which compensation can be achieved. The idea being that each laser guide star is used to image part of the atmosphere with the combined responses completely illuminating the region of interest.

The mean square wavefront distortion due to focal anisoplanatism is [136]

$$\sigma_{\mathrm{FA}}^2 = \left(\frac{D}{d_0}\right)^{5/3}, \tag{3.90}$$

where d_0 is given by Eq. (3.89). In the case of multiple guide stars this becomes [136]

$$\sigma_{\mathrm{FA}}^2 = \left(\frac{s}{d_0}\right)^{5/3}, \tag{3.91}$$

where the area of illumination of each beacon corresponds to a subsection of the telescope aperture with an area of s^2. When a large number of guide stars are used to probe the same region σ_{FA}^2 is considerably reduced. The aperture dimension serviced by each beacon is reduced to a dimension comparable to d_0, minimising the error due to focal anisoplanatism [70].

However, the practical implementation of a multiple laser guide star system is not trivial. Multiple guide stars introduce a host of technical problems, as well as being additional sources of wavefront error [70]. For example, the wavefront measurements from each beacon must have a unique identifying characteristic to ensure that each is processed correctly and must be combined with the measurements from the other beacons to provide an estimate of the overall wavefront distortion.

There are three ways that the distorted wavefront measurements can be combined; butting, stitching and merging [160] as illustrated in Fig. 3.25. Butting is a technique in which the data from each guide star is used to estimate the wavefront distortion directly under that star. Stitching involves combining data from regions where the guide stars overlap. Stitching error arises from the need to combine measurements from sources whose relative

positions cannot be precisely controlled, as is the case with laser guide stars as they can be subject to random beacon wander. The final technique is that of merging. In this case each subaperture views all laser guide stars and filtering techniques are used to combine the data and obtain an estimate of the distorted wavefront.

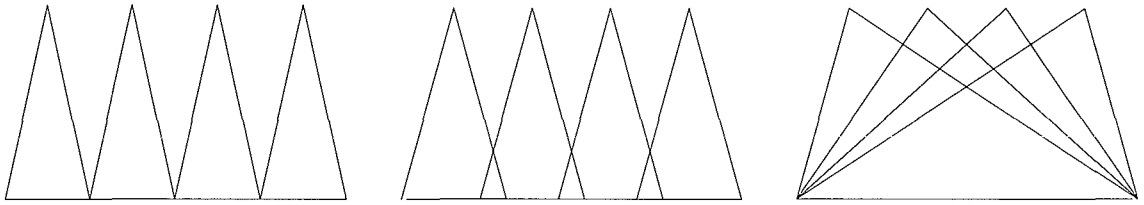

Figure 3.25: *Three methods of combining multiple wavefronts to reduce the impact of focal anisoplanatism (a) Butting, (b) Stitching and (c) Merging.*

Preliminary work has been carried out using multiple laser guide stars to extend the FOV of an AO system, by probing the turbulence to estimate the phase of each turbulent layer, combined with multiconjugate adaptive optics to increase the isoplanatic angle [136]. However, at this stage multiple laser guide star systems have not progressed much past the conceptual stage.

Chapter 4

Simulation of Atmospheric Turbulence

The simulation of atmospherically distorted wavefronts is an important tool for studying light propagation and imaging, although the final measure is always on real data. The lack of ground truth measurements and the desire to develop adaptive optics systems and data processing algorithms, provides the motivation for developing effective design tools. For example, the success of an AO system to compensate for wavefront perturbations is a complicated function of the components of the system, atmospheric conditions and light levels [139]. Accurate simulations can provide insight into how a system will perform, exposing problem areas and exploring possible solutions all at the design stage. The development of existing and new deconvolution, blind deconvolution and phase retrieval algorithms also benefit from simulation. Post processing techniques need to be tested in a controlled manner and under a wide variety of conditions, requiring the generation of ensembles of speckle images consistent with actual physical processes. An ideal simulation is one which matches the real world exactly, hence considerable effort is directed towards improving the simulation of real world quantities to achieve this.

The atmosphere is a weak, inhomogeneous extended random medium that manifests itself in discrete layers [170]. As a result it is often modelled as free space containing a series of thin layers or phase screens. In the case of static turbulence an adequate approximation is often a single phase screen located at the entrance pupil of the optical system, although this cannot account for non-isoplanatic effects [139]. The propagation of distorted light output from a single layer to the input of the next layer is modelled by a Fresnel propagation. This process is then repeated for the remaining turbulent layers with the propagation of the distorted wavefront output from the final layer to the telescope aperture also modelled by a Fresnel propagation. Therefore, the simulation of atmospherically distorted wavefronts at the telescope aperture requires the simulation of random phase screens and the propagation of light between these phase screens. The simulation of atmospheric turbulence is investigated in section 4.1, along with the introduction of an improved technique for its simulation. An improved method for the simulation of wavefront propagation through random media is presented in section 4.2.

4.1 Simulation of Kolmogorov turbulence

The starting point for nearly all the analysis of atmospheric turbulence has been the assumption that atmospheric turbulence follows a Kolmogorov spectrum [134], as outlined in section 3.4. Kolmogorov turbulence can be described statistically by its power spectrum of refractive index fluctuations, given in Eq. (1.8) and reproduced here for convenience,

$$\Phi_N(\kappa) = 0.033 C_N^2 \kappa^{-11/3}, \tag{4.1}$$

where κ denotes the scalar-wavenumber vector $(\kappa_x, \kappa_y, \kappa_z)$, and C_N^2 is the structure constant of refractive index fluctuations. The corresponding power spectrum of phase fluctuations is [134]

$$\begin{aligned} W_\phi(\mathbf{f}) &= 9.7 \times 10^{-3} k^2 |\mathbf{f}|^{-11/3} C_N^2(h) \delta h & (4.2) \\ &= \frac{0.023}{r_0^{5/3}} |\mathbf{f}|^{-11/3}, & (4.3) \end{aligned}$$

where $k = \frac{2\pi}{\lambda}$ is the wavenumber, δh corresponds to the turbulence layer thickness and r_0 is Fried's parameter.

Simulation of atmospheric turbulence is performed by generating phase screens, where a phase screen provides a single realisation of the phase distortion introduced by the atmosphere. An accurate turbulence simulation should not only produce a speckled distortion of the image, it should also shift the centroid of the image formed. The low frequencies in the Kolmogorov spectrum, contributing significantly to the tip and tilt components of the distortion, discussed in sections 3.2.5 and 3.3.2, account for the centroid motion. As a result it is important that these are accurately modelled. Furthermore, simulation of atmospheric turbulence is not restricted to Kolmogorov statistics, other power laws can also be modelled and this is investigated in section 4.1.8.

The phase screen is related to the spectrum of phase fluctuations, $P(k,l)$, by the Fourier transform pair [24]

$$P(k,l) = \int_{-\infty}^{+\infty}\int_{-\infty}^{+\infty} \psi(u,v)\exp(-i2\pi(uk+vl))dudv \tag{4.4}$$

and

$$\psi(u,v) = \int_{-\infty}^{+\infty}\int_{-\infty}^{+\infty} P(k,l)\exp(i2\pi(uk+vl))dkdl. \tag{4.5}$$

The notation $\psi(u,v)$ is used to represent a two-dimensional phase screen in the aperture of the telescope, where (u,v) are the coordinates in this aperture. One important property of the phase screens which are generated by assuming a pure Kolmogorov spectrum is that, although they are not statistically stationary, they have stationary increments. It is thus necessary to describe their statistics in terms of the phase structure function

$$\begin{aligned} D_p(u_1,v_1,u_2,v_2) &= D_p(u_1-u_2,v_1-v_2) && (4.6)\\ &= \left\langle (\psi(u_1,v_1)-\psi(u_2,v_2))^2 \right\rangle && (4.7)\\ &= 6.88\left(\frac{|(u_1-u_2,v_1-v_2)|}{r_0}\right)^{5/3} && (4.8) \end{aligned}$$

where r_0 is Fried's parameter [54] and $\langle\rangle$ is used to denote averaging over the ensemble of phase screens. It is important to note that the structure function is solely dependent on r_0 and the magnitude of the vector (u_1-u_2,v_1-v_2). Note also that in this thesis both D_p and D_ϕ are used to represent the phase structure function.

It is impossible to define a covariance function for points in a Kolmogorov phase screen

directly, since the covariance of the DC term is infinite. It is, however, possible to define a phase covariance for the phase screen over a finite region when the mean is removed [121,171]. Therefore, a new phase screen is generated by removing the mean component to give

$$\phi(u,v) = \psi(u,v) - \int W_A(u',v')\psi(u',v')du'dv', \tag{4.9}$$

where $W_A(u,v)$ is an aperture function which defines the region over which the phase is to be simulated. The aperture function has the property that

$$W_A(u,v) = \begin{cases} c & \text{over the region of simulation} \\ 0 & \text{outside the region of simulation} \end{cases} \tag{4.10}$$

where the constant, c, is chosen so that

$$\int W_A(u,v)dudv = 1. \tag{4.11}$$

The simplest simulation techniques use FFT methods of filtering white Gaussian noise. These techniques although straightforward to implement suffer from a lack of low frequency information since by definition the FFT is periodic and the Kolmogorov spectrum is not. As a result these techniques do not accurately simulate the random centroid motion resulting from propagation through atmospheric turbulence. Solutions to this problem include a variety of modifications to the original spectral technique, investigated in section 4.1.1. Modal expansions, a completely different simulation approach, involve combining appropriately weighted Zernike polynomials to generate Kolmogorov turbulence and are outlined in section 4.1.2. An exact, but intensive, direct simulation method is outlined in section 4.1.3. More recent approaches exploit the fractal nature of Kolmogorov turbulence and utilise algorithms created for generating fractal surfaces, namely the random midpoint displacement and successive random additions algorithms presented in section 4.1.4.

The random midpoint displacement method provides a reasonably accurate and fast method for simulating Kolmogorov turbulence [94]. However, the theory behind the method was not properly explained. Section 4.1.5 contains a theoretical justification of the approach taken in a previous study and extends it to improve the overall accuracy of the simulation by simulating the phase screen in a two stage process.

4.1.1 Spectral methods

Spectral methods, as they are termed throughout this thesis, are the simplest approach to generating phase screens. An array of uncorrelated random numbers is multiplied by a sampled approximation to the Kolmogorov power spectrum [94],

$$W(i,j) = 0.023 \left(\frac{2D}{r_0}\right)^{5/3} \sqrt{(i^2+j^2)^{-11/3}} \tag{4.12}$$

where i and j are the sample indices. The product is then Fourier transformed, with the resulting real and imaginary components each representing independent phase screens as illustrated in Fig. 4.1.

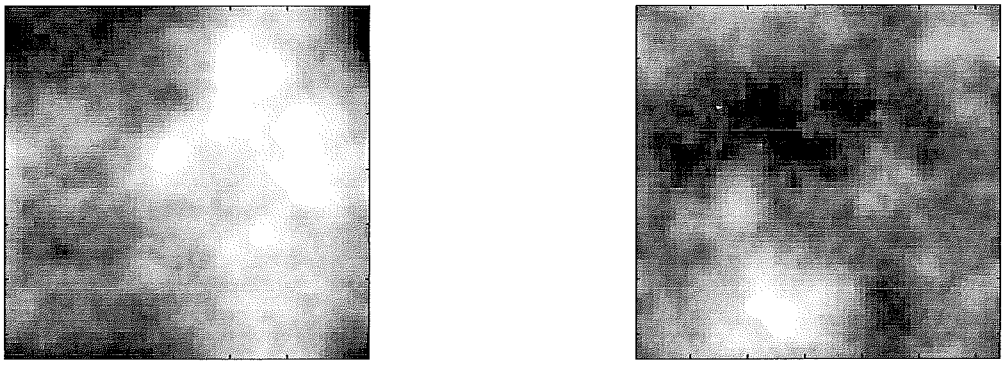

(a) (b)

Figure 4.1: *Typical phase screens simulated using the basic speckle method. (a) Real phase screen and (b) imaginary phase screen.*

For an accurate simulation the dimension of the simulation must be in the order of the outer scale, while at the same time the sampling interval must adequately sample the fine structure which is in the order of the inner scale of the turbulence. Hence for $l_0 = 1$mm and $L_0 = 50$m, the simulation dimension N must be at least 50000. If the simulation is of dimension L, no frequencies lower than $1/L$ exist in the Fourier transform, since frequencies with a period greater than the imposed aperture are not represented. This is a direct consequence of the periodicity assumption of the FFT, which by definition produces a result with a zero mean slope. The inaccurate modelling of the low frequency terms means that the tip and the tilt of the wavefront, which account for the centroid motion, are underrepresented. Consequently, this technique although simple does not provide an accurate approximation

to Kolmogorov statistics. Typical speckle patterns generated by this technique are shown in Fig. 4.2 and illustrate how the speckle centroid is not shifted significantly from the image centre.

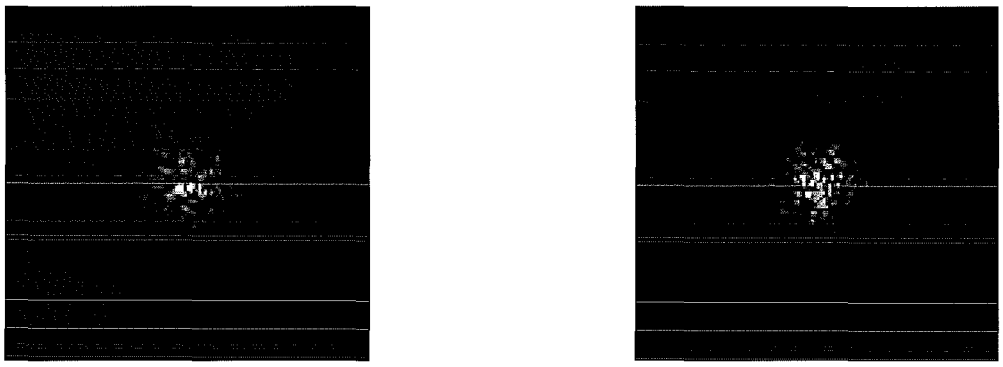

(a) (b)

Figure 4.2: *Typical speckle patterns for $D/r_0 = 10$ simulated from the phase screens in Figs. 4.1 (a) and (b).*

The accuracy of the spectral approach can be determined by a comparison of the phase structure function of the simulated phase screens with the ideal result given by Eq. (4.8), and illustrated in Fig. 4.3. Figs. 4.1 and 4.3 show that the phase screens and hence the corresponding structure function generated using the spectral technique are periodic. The ideal structure function, however, is not. This is a result of the sampling process and leads to large deviations from the desired statistics. The computation required to perform an $N \times N$ Fourier transform is $N^2 \log_2 N^2$ operations.

The effective simulation of the atmosphere was started by McGlamery [114] who simulated turbulence over an area 16 times larger than the aperture, using the spectral approach outlined above, to give a result of dimensions $4L \times 4L$. The resulting phase screen was the central $L \times L$ portion of this (see Fig. 4.4). The accuracy of this approach is illustrated by a comparison of ideal and simulated phase structure functions in Fig. 4.5. McGlamery's method produces a considerable improvement in the estimated phase structure function statistics. However, it is at a considerable increase in the computational cost of the original

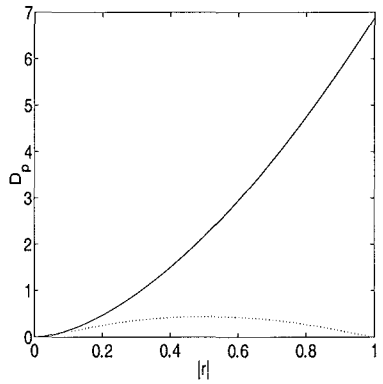

Figure 4.3: *Ideal (solid) and simulated (dotted) phase structure functions calculated over an ensemble of 10000 phase screens for the basic spectral method.*

technique and again is only adequate for applications where the overall tilt across the pupil is of no concern.

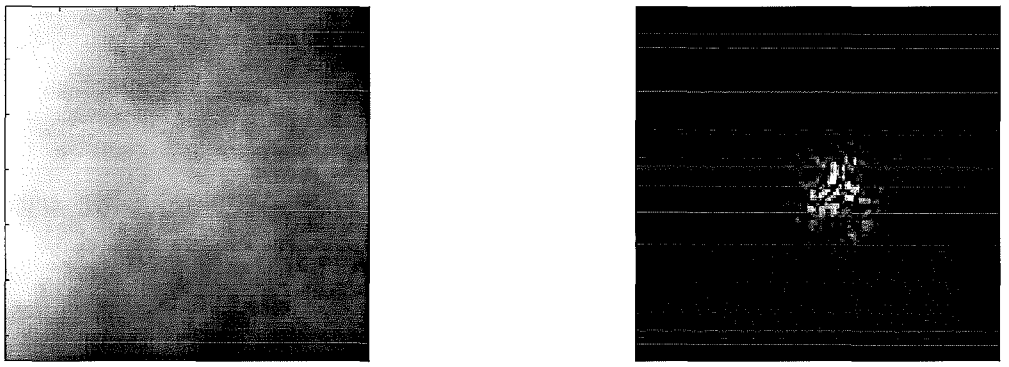

(a) (b)

Figure 4.4: *(a) Phase screen generated using McGlamery's method. (b) Corresponding speckle pattern for $D/r_0 = 10$.*

Various techniques were proposed for dealing with the inadequate low frequency modelling of the FFT based approaches, either by the artificial addition of lower frequency information to the spectrum or by the compensation of centroid motion after speckle image generation. A simple technique for modelling the effects of these lower frequencies is to generate additional random frequencies and add their effects to the sampled frequencies obtained from Eq. (4.12). Lane *et al* [94] achieve this by the addition of subharmonics. The sample at the

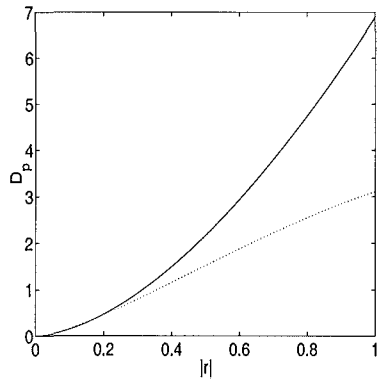

Figure 4.5: *Ideal (solid) and simulated (dotted) phase structure functions calculated over an ensemble of 10000 phase screens for McGlamery's method.*

origin of the spectrum is divided into nine samples, each $1/9th$ the area and weight of the original sample, where these additional frequencies are known as *subharmonics*. Additional subharmonic sets can be generated by further division of the remaining area around the origin, until the desired outer scale of turbulence is reached. This technique requires less computation than the technique of McGlamery and produces more accurate phase screens. Adcock and Jones [1] generated low frequencies in the simulated phase screen, by starting with a phase screen of size $N \times N$ and of dimensions $L \times L$. A central 2×2 piece of the phase screen is extracted and interpolated to $N \times N$ pixels. A second phase screen generated over this new area contains the higher frequencies absent from the first. These are then combined and the process repeated until the required phase screen scale results.

An approach proposed by Shaklan as outlined in Lane *et al* [94] is to generate a phase screen of dimensions $2D \times 2D$, where D represents the desired aperture dimensions, and extract the central $D \times D$ portion. The centroid of the resulting speckle pattern is then manually shifted. This gives an improvement in accuracy over the basic spectral technique, but it does not take into account all the information present at the lower frequencies [94]. For example, centroid motion is not purely a function of the tip and tilt distortions, higher order terms like coma can also move the centroid of a speckle image. Therefore, the manual shifting of the centroid does not ensure the correct relationship between the tip/tilt and higher order terms.

4.1.2 Modal expansions

An alternative approach to the simulation of atmospheric turbulence is to expand the turbulence induced phase aberrations in terms of a set of orthogonal basis functions, i.e.

$$\psi(u,v) = \sum_{j=1}^{\infty} a_j \varphi_j(u,v) \tag{4.13}$$

where $\psi(u,v)$ represents the phase of the aberrated wavefront, $\varphi_j(u,v)$ the jth basis function and a_j the coefficient of the jth basis function. The expansion can be performed using Zernike polynomials, however, it is not optimal as the coefficients in the Zernike expansion are not statistically independent. N. Roddier [137] performed the expansion in terms of randomly weighted Karhunen-Loève functions, where the Karhunen-Loève functions are a unique set of orthogonal functions which have statistically independent weights. Although these functions do not have an analytic formula, they can be expanded in terms of the Zernike polynomials.

The aberrated wavefront phase, using the Zernike expansion of Noll [121], is defined in polar coordinates as

$$\phi(R\rho,\theta) = \sum_{j=2}^{\infty} a_j Z_j(\rho,\theta), \tag{4.14}$$

where the Z_j represent the Zernike polynomials, R the radius of the aperture, $\phi(R\rho,\theta)$ the piston removed phase and the coefficients a_j of the expansion are given by [136]

$$a_j = \int_0^{2\pi} \int_0^{\infty} \mathcal{W}(\rho,\theta) Z_j(\rho,\theta) \phi(R\rho,\theta) \rho d\rho d\theta. \tag{4.15}$$

Here $\mathcal{W}(\rho,\theta)$ represents the aperture weighting function. Note that because of the underlying Gaussian distributed nature of $\phi(R\rho,\theta)$, the a_j are also Gaussian distributed [139]. The covariance of two Zernike polynomial coefficients a_j and a_k, corresponding to Zernike polynomials Z_j and Z_k, is given as [136]

$$\begin{aligned}
\langle a_j a_k \rangle &= \left\langle \int \mathcal{W}(\underline{\rho}) Z_j(\underline{\rho}) \phi(R\underline{\rho}) d\underline{\rho} \int \mathcal{W}(\underline{\rho}') Z_j(\underline{\rho}') \phi(R\underline{\rho}') d\underline{\rho}' \right\rangle \\
&= \int \left\langle \phi(R\underline{\rho}) \phi(R\underline{\rho}') \right\rangle \int \mathcal{W}(\underline{\rho}) \mathcal{W}(\underline{\rho}') Z_j(\underline{\rho}) Z_k(\underline{\rho}') d\underline{\rho} d\underline{\rho}' \\
&= \int \int C_\phi(R\underline{\rho}, R\underline{\rho}') \mathcal{W}(\underline{\rho}) \mathcal{W}(\underline{\rho}) Z_j(\underline{\rho}) Z_k(\underline{\rho}') d\underline{\rho} d\underline{\rho}'
\end{aligned} \tag{4.16}$$

where $\phi(R\underline{\rho})$ is the phase of the aberrated wavefront, $C_\phi(R\underline{\rho}, R\underline{\rho}')$ is the phase covariance function and $\underline{\rho} = (\rho, \theta)$. Since the a_j are zero mean Gaussian random variables the covariance is equivalent to the correlation of the a_j. Eq. (4.16) can be evaluated to give

$$\langle a_j a_k \rangle = c_{jk}(D/r_0)^{5/3} \tag{4.17}$$

where [136]

$$\begin{aligned} c_{jk} &= 7.2 \times 10^{-3}\sqrt{(n+1)(n'+1)}(-1)^{(n+n'-2m)/2}\pi^{8/3} \\ &\times \frac{\Gamma(14/3)\Gamma\left[(n+n'-5/3)/2\right]}{\Gamma\left[(n-n'+17/3)/2\right]\Gamma\left[(n'-n+17/3)/2\right]\Gamma\left[(n+n'+23/3)/2\right]}. \end{aligned} \tag{4.18}$$

The covariance values for a_2 to a_{10} are given in Table 4.1 and show that the coefficients corresponding to Zernike polynomials Z_2, Z_8 and Z_3, Z_7 are correlated. This indicates that a simple Zernike expansion is not optimal, since an optimal expansion would be given by uncorrelated coefficients.

	2	3	4	5	6	7	8	9	10
2	0.448	0	0	0	0	0	-0.0141	0	0
3	0	0.448	0	0	0	-0.0141	0	0	0
4	0	0	0.0232	0	0	0	0	0	0
5	0	0	0	0.0232	0	0	0	0	0
6	0	0	0	0	0.0232	0	0	0	0
7	0	-0.0141	0	0	0	0.00618	0	0	0
8	-0.0141	0	0	0	0	0	0.00618	0	0
9	0	0	0	0	0	0	0	0.00618	0
10	0	0	0	0	0	0	0	0	0.00618

Table 4.1: *Covariance matrix (c_{jk}) for a_2 to a_{10}.*

The Karhunen-Loève functions form a set of statistically independent basis functions and are therefore a better choice of basis functions for high order simulations than the weakly correlated Zernike functions. Although, they have no analytic formula they can be expressed

in terms of the Zernike polynomials. The Karhunen-Loève expansion is given by

$$\phi(R\rho,\theta) = \sum_{i=2}^{\infty} b_i K_i(\rho,\theta) \tag{4.19}$$

where the b_i are the coefficients of the Karhunen-Loève expansion and the $K_i(\rho,\theta)$ are the Karhunen-Loève functions.

The general technique for performing a Karhunen-Loève expansion is to compute the independent Karhunen-Loève coefficients, convert these to the corresponding Zernike coefficients and evaluate the phase screen as a sum of Zernike polynomials [137]. The process starts by defining the vector $\mathbf{a}$, where

$$\mathbf{a} = \begin{bmatrix} a_2 \\ \vdots \\ a_N \end{bmatrix} \tag{4.20}$$

is a matrix of $(N-1)$ Zernike coefficients, note that piston is not included. The covariance of the Zernike coefficients, $\mathbf{C_a}$, is computed from

$$\mathbf{C_a} = \left\langle \mathbf{a}\mathbf{a}^T \right\rangle = \begin{bmatrix} \langle a_2 a_2 \rangle & \langle a_2 a_3 \rangle & \dots \\ \langle a_3 a_2 \rangle & \langle a_3 a_3 \rangle & \dots \\ \vdots & \vdots & \ddots \\ & & \end{bmatrix} \tag{4.21}$$

where the components $\langle a_j a_k \rangle$ can be calculated using Eq. (4.17). $\mathbf{C_a}$ is a Hermitian matrix and can be decomposed via the singular value decomposition (SVD) to:

$$\mathbf{C_a} = \mathbf{U}\Lambda\mathbf{U}^T, \tag{4.22}$$

where Λ is a diagonal matrix containing positive eigenvalues and $\mathbf{U}$ contains the eigenvectors of $\mathbf{C_a}$. The covariance matrix $\mathbf{C_a}$ can be block diagonalised before the SVD is applied to accelerate the computation and improve the accuracy as outlined in N. Roddier [137].

Now consider the transformation of $\mathbf{a}$,

$$\mathbf{b} = \mathbf{U}^T\mathbf{a} \tag{4.23}$$

where $\mathbf{b}$ is a vector of Karhunen-Loève coefficients $(b_2, b_3, \ldots b_N)^T$. For the new coefficients to be statistically independent the corresponding covariance matrix must be diagonal. The covariance matrix of these new coefficients is given by

$$\begin{aligned} \left\langle \mathbf{b}\mathbf{b}^T \right\rangle &= \left\langle \mathbf{U}^T \mathbf{a}\mathbf{a}^T \mathbf{U} \right\rangle \\ &= \mathbf{U}^T \left\langle \mathbf{a}\mathbf{a}^T \right\rangle \mathbf{U} \\ &= \mathbf{U}^T \mathbf{C_a} \mathbf{U} \\ &= \Lambda. \end{aligned} \tag{4.24}$$

This result indicates that the coefficients in $\mathbf{b}$ are uncorrelated and statistically independent.

The corresponding Zernike coefficients are obtained by inverting Eq. (4.23) to give

$$\mathbf{a} = \mathbf{U}\mathbf{b}. \tag{4.25}$$

Combining Eqs. (4.14) and (4.25) gives the Karhunen-Loève expansion in terms of the Zernike polynomials

$$\begin{aligned} \phi(R\rho,\theta) &= \sum_{j=2}^{\infty} a_j Z_j(\rho,\theta) \\ &= \sum_{j=2}^{\infty} \left(\sum_{i=2}^{\infty} U_{ij} b_i \right) Z_j(\rho,\theta) \\ &= \sum_{i=2}^{\infty} b_i \left(\sum_{j=2}^{\infty} U_{ij} Z_j(\rho,\theta) \right) \\ &= \sum_{i=2}^{\infty} b_i K_i(\rho,\theta) \end{aligned} \tag{4.26}$$

where

$$K_i(\rho,\theta) = \sum_{i=2}^{\infty} U_{ij} Z_i(\rho,\theta). \tag{4.27}$$

One of the advantages of a Zernike based system is that it is often possible to estimate how many Zernike modes can be compensated by an AO system. Consider an AO system which compensates N Zernike modes. The remaining distortion must, therefore, be due to the uncompensated modes. The residual phase is

$$\phi_R(R\rho,\theta) = \phi(R\rho,\theta) - \phi_N(R\rho,\theta), \tag{4.28}$$

where $\phi_N(R\rho,\theta)$ is defined as

$$\phi_N(R\rho,\theta) = \sum_{i=2}^{N} a_i Z_i(\rho,\theta). \tag{4.29}$$

This can then be used to calculate the mean square residual phase error, $\sigma^2_{\phi_N}$, where

$$\begin{aligned}\sigma^2_{\phi_N} &= \int\int \mathcal{W}(\rho,\theta)\left\langle \phi^2_R(R\rho,\theta)\right\rangle \rho d\rho d\theta \\ &= \int\int \mathcal{W}(\rho,\theta)\left\langle (\phi(R\rho,\theta)-\phi_N(R\rho,\theta))^2\right\rangle \rho d\rho d\theta. \end{aligned}\tag{4.30}$$

In the case of a Zernike expansion, the mean square residual phase error is given by [121]

$$\sigma^2_{\phi_N}(Z) = \left\langle \phi^2\right\rangle - \sum_{j=1}^{N}\left\langle |a_j|^2\right\rangle \tag{4.31}$$

where $\langle\phi^2\rangle$ is the phase variance, which is infinite due to the piston mode. For large N this can be approximated by [121]

$$\sigma^2_{\phi_N}(Z) \approx 0.2944 N^{-\sqrt{3}/2}(D/r_0)^{5/3}. \tag{4.32}$$

The values of $\sigma^2_{\phi_N}(Z)$ for Zernike modes $N \leq 10$ are given in Table 4.2. Note that 86% of the total error is removed when the tip and tilt modes of turbulence, Z_2 and Z_3, are removed [139]. Considerable compensation is achieved by removal of the low order terms in the Zernike expansion as shown in Table 4.2. A further significant reduction in mean square residual phase error requires the removal of a large number of modes. For $N > 15$ the removal of a single Zernike mode corresponds only to a marginal reduction [139].

The mean square residual phase error remaining after the removal of N Karhunen-Loève modes is given as [139]

$$\sigma^2_{\phi_N}(KL) = 1.0299\left(\frac{D}{r_0}\right) - \sum_{i=1}^{N}(\bar{b}_i^2), \tag{4.33}$$

where a bar denotes a mean quantity. The values of $\sigma^2_{\phi_N}(KL)$ for Karhunen-Loève modes $N \leq 10$ are given in Table 4.3. The Karhunen-Loève expansion returns a slightly smaller mean square residual phase error than the Zernike expansion.

Fig. 4.6 shows a phase screen generated by summing 396 Zernike polynomials and the corresponding speckle pattern for $D/r_0 = 10$. The computational load for the technique of

Zernike mode	$\sigma^2_{\phi_N}(Z)$ $[(D/r_0)^{5/3}$ rad$^2]$
1	1.0299
2	0.582
3	0.134
4	0.111
5	0.0880
6	0.0648
7	0.0587
8	0.0525
9	0.0463
10	0.0401

Table 4.2: *$\sigma^2_{\phi_N}(Z)$ for the compensation of $N \leq 10$ Zernike modes.*

summing Zernike polynomials is proportional to αN^2 [94], where α is the number of Zernike polynomials used. For a 64×64 phase screen, α would need to be less than 9 to compare with the computation required for the basic spectral methods. However, the use of about 400 Zernike polynomials is suggested, and this will increase for higher values of D/r_0.

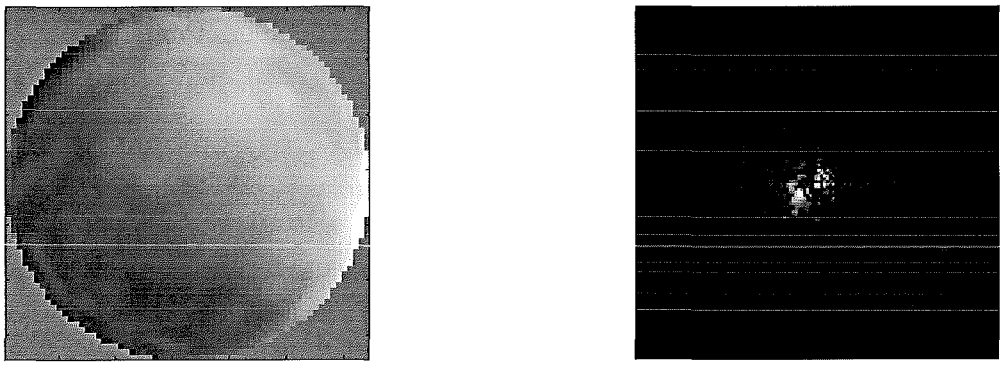

(a) (b)

Figure 4.6: *(a) Phase screen generated using an expansion of 396 Zernike polynomials. (b) Corresponding speckle pattern for $D/r_0 = 10$.*

Karhunen-Loève mode	$\sigma^2_{\phi_N}$(KL) $[(D/r_0)^{5/3}$ rad$^2]$
1	1.0299
2	0.581
3	0.133
4	0.109
5	0.0849
6	0.0617
7	0.0551
8	0.0485
9	0.0422
10	0.0360

Table 4.3: *$\sigma^2_{\phi_N}(KL)$ for the compensation of $N \leq 10$ Karhunen-Loève modes.*

4.1.3 Direct simulation of a phase screen

The covariance of the piston removed phase screen $\phi(u,v)$, defined in Eq. (4.9), is given by [171]

$$\begin{aligned} C(u_1,v_1,u_2,v_2) &= \langle \phi(u_1,v_1)\phi(u_2,v_2)\rangle \\ &= \Big\langle \int (\psi(u_1,v_1)-\psi(u_1',v_1'))W_A(u_1',v_1')du_1'dv_1' \\ &\times \quad \int (\psi(u_2,v_2)-\psi(u_2',v_2'))W_A(u_2',v_2')du_2'dv_2' \Big\rangle \\ &= \int\int \langle (\psi(u_1,v_1)-\psi(u_1',v_1'))(\psi(u_2,v_2)-\psi(u_2',v_2'))\rangle \\ &\qquad W_A(u_1',v_1')W_A(u_2',v_2')du_1'du_2'dv_1'dv_2'. \end{aligned} \tag{4.34}$$

Using

$$D_p(u_1,v_1,u_2,v_2) = \left\langle \psi(u_1,v_1)^2 - 2\psi(u_1,v_1)\psi(u_2,v_2) + \psi(u_2,v_2)^2 \right\rangle \tag{4.35}$$

and Eq. (4.8) it is possible to rearrange Eq. (4.34) to produce

$$\begin{aligned} C(u_1,v_1,u_2,v_2) &= -\frac{1}{2}D_p(u_1,v_1,u_2,v_2) \\ &+ \frac{1}{2}\int D_p(u_1',v_1',u_2,v_2)W_A(u_1',v_1')du_1'dv_1' \\ &+ \frac{1}{2}\int D_p(u_1,v_1,u_2',v_2')W_A(u_2',v_2')du_2'dv_2' \end{aligned}$$

$$- \frac{1}{2}\int\int D_p(u_1', v_1', u_2', v_2') W_A(u_1', v_1') W_A(u_2', v_2') du_1' dv_1' du_2' dv_2' \tag{4.36}$$

the result for a continuous phase screen. However, for computation purposes a sampled phase screen is required.

The covariance is now calculated as the outer product of the stacked phase screen,

$$\mathbf{C_S} = \left\langle \Phi\Phi^T \right\rangle, \tag{4.37}$$

where Φ is the original phase screen rearranged into a vector, by the stacking operator R, i.e.

$$\Phi(mN + n) = R[\phi(m\Delta u, n\Delta v)]. \tag{4.38}$$

Here N is the number of samples in the v direction, and Δu and Δv are the sample intervals in the u and v directions respectively. If the dimension of the starting screen is $N \times N$ then the dimension of $\mathbf{C_S}$ is $N^2 \times N^2$.

The direct simulation of a phase screen can now be achieved by the use of the eigensystem of $\mathbf{C_S}$ computed using a singular value decomposition (SVD):

$$\mathbf{C_S} = \mathbf{U}\Lambda\mathbf{U}^T, \tag{4.39}$$

where Λ is a diagonal matrix containing positive eigenvalues and $\mathbf{U} = (U_1, U_2, \ldots, U_{N^2})$, where the U_i are the eigenvectors of $\mathbf{C_S}$.

An exact stacked phase screen is then given by

$$\Phi = \mathbf{U}\mathbf{x} \tag{4.40}$$

where $\mathbf{x}$ is a random vector of independent elements. Each element has its variance given by the corresponding element on the leading diagonal of Λ. This matches the second order statistics of the Kolmogorov turbulence [134] which is sufficient to completely describe a Gaussian process. The unstacked phase screen is obtained by reversing the stacking operation in Eq. (4.38) to produce $\phi(m\Delta u, n\Delta v)$, a simulated phase screen with the desired

covariance statistics. The columns of $\mathbf{U}$ when unstacked give the Karhunen-Loève basis functions of the turbulence. Therefore, this approach differs to that of N. Roddier [137] only in a choice of basis functions. This direct phase screen simulation method was outlined in Goldring and Carlson [64].

The approach described here has the advantage that the coefficients generated by Eq. (4.40) can be used directly as the samples of the phase screen, without the need to sum weighted Zernike polynomials. A drawback of this technique is that the SVD factorisation of $\mathbf{C_S}$, although it only needs to be performed once for a given size of phase screen, requires a large amount of computation, in the order of N^6 operations for an array of N^2 points [151]. As a result 32×32 pixels is the practical computational limit for phase screens simulated directly. A phase screen and the corresponding $D/r_0 = 10$ speckle pattern simulated using the direct method are illustrated in Fig. 4.7.

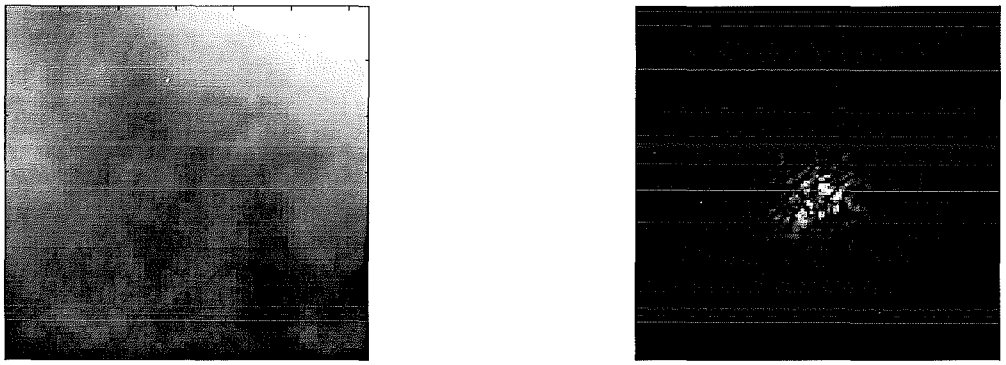

(a) (b)

Figure 4.7: *(a) Phase screen generated using the direct method. (b) Corresponding speckle pattern for $D/r_0 = 10$.*

4.1.4 Fractal methods

Fractal geometry is a relatively new branch of mathematics and was conceived and developed by Benoit Mandelbrot [124]. Fractal shapes are invariant to scale, that is they look similar regardless of the scale at which they are viewed, a property known as *self-similarity*. For Kolmogorov turbulence this means that changing the size of the aperture has no effect on

the shape of the phase structure function [94], i.e.

$$D_\phi(\alpha|\mathbf{r}|) = \alpha^{5/3} D_\phi(|\mathbf{r}|). \tag{4.41}$$

This fractal nature of Kolmogorov phase screens was noted by Lane *et al* [94] and later by Schwartz *et al* [144]. It is, therefore, possible to apply existing fractal generation algorithms to the simulation of Kolmogorov turbulence. Lane *et al* used the random midpoint displacement method, whereas Schwartz *et al* investigated the successive random additions method for simulating atmospheric turbulence.

It is necessary to introduce Brownian motion before further discussion of fractal generation algorithms. Brownian motion in one variable constitutes the simplest random fractal [124] and can be described in one dimension by the following power law

$$\Psi_b(k) = 1/k^2, \tag{4.42}$$

the spectrum of Brownian motion. It can also be described by its structure function,

$$D_b(r) = |r|. \tag{4.43}$$

Brownian motion can be generated by integrating white noise, where white noise is completely uncorrelated from point to point.

When the exponent of the power spectrum in Eq. (4.42) is not equal to 2 this defines fractional Brownian motion (fBm), a generalisation of Brownian motion. Fractional Brownian motion is a Gaussian random process characterised by,

$$D_b(r) \propto |r|^{2H}, \tag{4.44}$$

where $0 < H < 1$ and is known as the Hurst parameter. $H = 1/2$ corresponds to Brownian motion and indicates no correlation between the random variables. $H > 1/2$ indicates a positive correlation between the random variables and $H < 1/2$ a negative correlation.

Random midpoint displacement is a technique for simulating and increasing the resolution of fBm. The random midpoint displacement algorithm has mainly found application in the

computer generation of artificial landscapes, where it results in more natural landscapes than can be generated by other means. This process for 1D fBm starts with two independent zero mean Gaussian random variables, X_0 and X_1, with a variance equal to σ^2. For a unit length separation,

$$D_b(1) = \left\langle (X_0 - X_1)^2 \right\rangle = 2\sigma^2. \tag{4.45}$$

The algorithm uses the process of successive subdivision to increase the resolution of the fBm. The midpoint between the two original points, $X_{1/2}$, is calculated by interpolation and the addition of an independent random variable d_1, with variance $\triangle^2$, to give

$$X_{1/2} = \frac{X_0 + X_1}{2} + d_1. \tag{4.46}$$

The variance $\triangle^2$ is chosen so that

$$\left\langle (X_0 - X_{1/2})^2 \right\rangle = \sigma^2, \tag{4.47}$$

to give $\triangle^2 = \sigma^2/2$. This process is repeated to produce finer and finer resolution samples of fBm.

For Kolmogorov turbulence, midpoint displacement is a technique for increasing the sampling rate and consequently the number of samples of the initial phase screen in a manner consistent with the structure function statistics. The original midpoint displacement [94] was based on using bilinear interpolation between 4 existing points on the phase screen followed by a random displacement of the interpolated point, where the four starting points are samples of 2D Kolmogorov turbulence and hence correlated. This process is shown in Fig. 4.8 for a larger number of initial points. Peitgen [124] assumed the interpolation was between four uncorrelated Gaussian random variables, regardless of the power spectrum being simulated and as a result failed to produce phase screens with acceptable structure functions or speckle transfer functions [94].

The interpolation at each iteration consisted of three steps. In the first step, Fig. 4.8(a), the value of the centre point $\phi(u_i, v_i)$, shown by a $\bullet$, was given by

$$\phi(u_i, v_i) = \frac{1}{4}(\phi(u_1, v_1) + \phi(u_2, v_2) + \phi(u_3, v_3) + \phi(u_4, v_4)) + \epsilon_i. \tag{4.48}$$

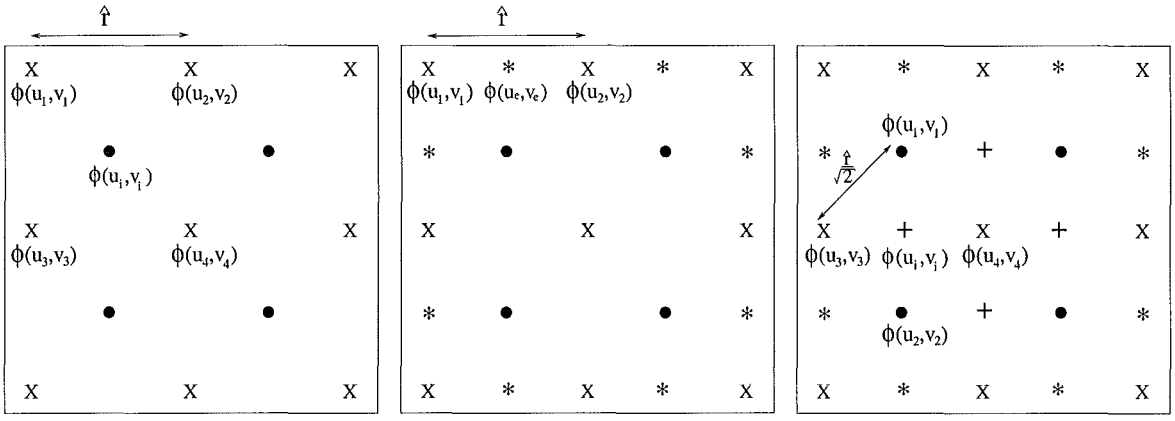

Figure 4.8: *The interpolation steps for generating a higher resolution phase screen where the known initial points are marked by X (a) First step of interpolation. The points determined at this stage are marked •. (b) Second step of interpolation. The points determined at this stage are marked ∗. (c) Third step of interpolation. The points determined are marked +. In this case $\hat{r}$ is reduced by a factor of $\sqrt{2}$ because the spacing is equivalently reduced.*

The first term on the right hand side is the bilinearly interpolated phase value. The random value, ϵ_i, follows a normal law with variance given by $0.6091(\hat{r})^{5/3}$. The steps for calculating ϵ_i are outlined in Lane *et al* [94]. The term $\hat{r}$ is the spacing between the points being interpolated, initially the original points (indicated by a cross in Fig. 4.8), whereupon $\hat{r} = 1$. This additional term is required to give the correct structure function between the phase at the central point and those at the corners, as predicted by Eq. (4.8). The second step established a value for the edge points, shown by $*$ in Fig. 4.8(b). These were calculated in a similar manner except that only the adjacent corner points were averaged:

$$\phi(u_e, v_e) = \frac{1}{2}(\phi(u_1, v_1) + \phi(u_2, v_2)) + \gamma_e \tag{4.49}$$

with the additional random displacement, γ_e, having a variance given by $0.4471(\hat{r})^{5/3}$. The final step, shown in Fig. 4.8(c), produced the + in the same way as the first step found the •, except that the $\hat{r}$ used to determine additional displacement, was reduced by a factor of $\sqrt{2}$ due to the reduced spacing of the four surrounding samples. These steps completed a higher resolution phase screen and the same steps could be repeated, with a value of $\hat{r}$ halved after each iteration, until the phase screen was as large as required.

The algorithm described in the original paper started from a 2×2 array but it is simpler to demonstrate all steps on a 3×3 initial phase screen (see Fig. 4.8). This original approach, whilst producing reasonable structure functions had three major limitations [94]. Firstly, the choice of the standard bilinear interpolator, whilst intuitively reasonable, did not have a rigorous theoretical basis. Secondly, the interpolation at the edges was clearly less accurate than the central pixel calculation. Thirdly, by starting with a 2×2 pixel array the operation had to be repeated many times to produce large phase screens. This allowed errors in the approximation to accumulate.

A sample phase screen generated using the midpoint displacement method from a 2×2 array is illustrated in Fig. 4.9 along with the corresponding $D/r_0 = 10$ speckle pattern. This technique has the advantage that only N operations are needed for an array of N points, a significant reduction in computation over the spectral, modal and direct methods.

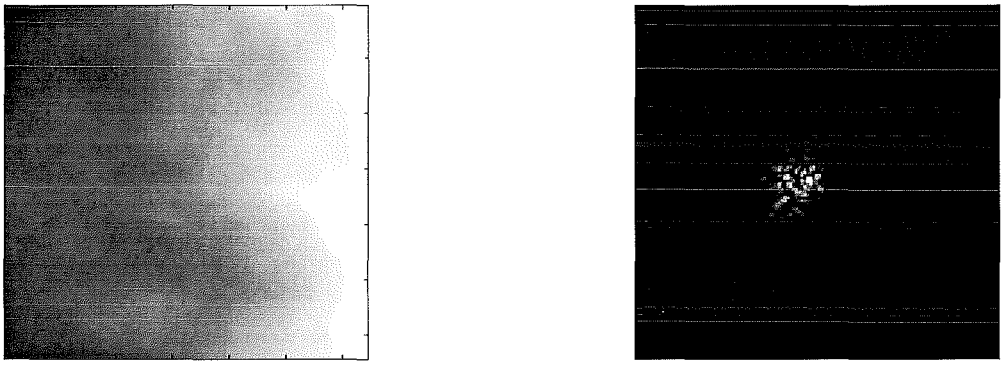

(a) (b)

Figure 4.9: *(a) Phase screen generated using the original midpoint method. (b) Corresponding speckle pattern for $D/r_0 = 10$.*

The method of successive random additions (SRA) is another technique for generating fBm and was used by Schwartz *et al* [144] for the simulation of Kolmogorov turbulence. The technique is very similar to that of the random midpoint displacement method with one major difference. In random midpoint displacement once a point has been determined, its value remains unchanged at all later stages. The SRA method adds randomness to all points

at each stage of the subdivision process. This technique also requires only N operations for an array of N points.

4.1.5 Derivation of the midpoint displacement algorithm

A more general technique for deriving the midpoint displacement process can be achieved by representing the phase over a finite region as a set of basis functions. The process is best explained by considering an $N \times N$ set of samples from a Kolmogorov phase screen. These existing samples are shown by an X in Fig. 4.10(a) and are denoted by $\Phi_l(u_i, v_i)$. The aim is to produce the optimal estimates of the additional points marked • and * in Fig. 4.10(a). Adding these new points doubles the sampling rate to produce a higher resolution phase screen, $\Phi_h(u, v)$, of dimensions $(2N-1) \times (2N-1)$.

This higher resolution phase screen, $\Phi_h(u, v)$, can be expressed in terms of basis functions by

$$\Phi_h = \sum_{k=0}^{M^2} a_k U'_k(u, v) \tag{4.50}$$

where $M = (2N-1)$, the a_k are the coefficients of the basis functions and the $U'_k(u, v)$ are the eigenvectors (or basis functions) computed from the covariance matrix of the high resolution samples. Each eigenvector has dimension $M^2 \times 1$ and can be unstacked to produce an $M \times M$ two-dimensional basis function. Note $U'_0(u, v)$, the eigenvector for the DC term, is included. Since the DC term is theoretically of infinite variance it is removed when the eigenvectors covariances are calculated. The DC term must, however be included when computing the interpolator over a small region of the phase screen since this subregion may have a non-zero mean. It is computationally sufficient to set the associated eigenvalue of this eigenvector to a very large number. To solve for the coefficients $\{a_i\}$, Φ and U' are converted into vectors using the stacking operation described in Eq. (4.38). This results in the system of equations

$$\Phi_h = \mathbf{U'A} \tag{4.51}$$

where $\mathbf{U'} = (U'_0(u, v), U'_1(u, v), \ \ldots \ U'_{M^2}(u, v))$ and $\mathbf{A} = (a_0, a_1, a_2 \ \ldots \ a_{M^2})^T$ are the coefficients of the basis functions.

A subset of the equations is obtained by selecting the rows of $\mathbf{U}'$ and Φ_h corresponding to the low resolution points whose values are known. In the 4×4 case, this would be rows (1, 3, 5, 7, 15, 17, 19 ... 49). This reduced set of equations is given by

$$\Phi_l = \Theta \mathbf{A} \tag{4.52}$$

where Θ is a submatrix of $\mathbf{U}'$ of dimension $N^2 \times (M^2+1)$ and $\mathbf{A}$ is as given for the previous equation.

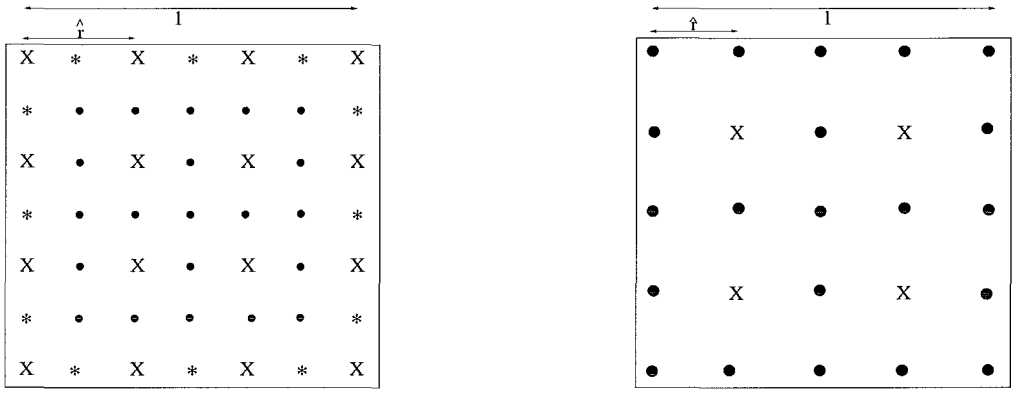

Figure 4.10: *The interpolation steps for generating a higher resolution phase screen where the initial low resolution points are marked by X. (a) • and ∗ are the interpolated points. (b) The effect of removing the edge points for a 2×2 interpolator and rescaling the phase screen.*

To interpolate the required high resolution points, Φ_h, it is first necessary to solve Eq. (4.52) for $\mathbf{A}$ and substitute this into Eq. (4.51). The difficulty in solving Eq. (4.52) is that there are only the original N^2 low resolution points and $(2N-1)^2+1$ coefficients to be estimated, an underdetermined problem. This system of equations can be solved by using *a priori* knowledge about the statistics of the coefficients to increase the number of equations. Using a Bayesian approach, or equivalently incorporating extra equations [99] for the unknowns, results in a weighted least squares estimator. This gives [99, 105]

$$\hat{\mathbf{A}} = \Lambda' \Theta^T (\Theta \Lambda' \Theta^T)^{-1} \Phi_l \tag{4.53}$$

where Θ and Φ_l are as defined above. Λ' corresponds to the eigenvalues computed from the covariance matrix of the high resolution samples, note that it contains an eigenvalue for the

DC term.

The interpolated higher resolution points can now be generated by a weighted sum of low resolution points. The higher resolution estimate, $\hat{\Phi}_h$, is generated from $\hat{\mathbf{A}}$ as described by Eq. (4.51). It should be noted that Eq. (4.53) can be used to generate all high resolution points, and the points corresponding to low resolution points are returned unchanged.

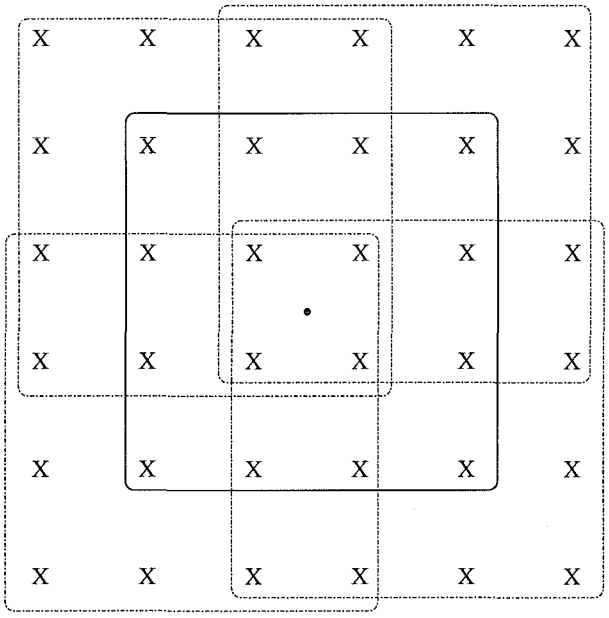

Figure 4.11: *Illustration of the possible choices of 4×4 regions of low resolution points, marked by X, capable of interpolating a high resolution point •. The choice marked by the solid line is used except when interpolating near edges.*

This process describes how it is possible to interpolate any high resolution sample throughout the region bounded by the original low resolution samples. When the interpolation is based on a region greater than the 2×2 low resolution points this leads to a choice of how to interpolate a high resolution point. Fig. 4.11 illustrates that using a 4×4 region of low resolution points there are 5 possible ways of interpolating the high resolution point marked by a •. Since the interpolation is expected to be the best at the centre of a patch of low resolution samples this interpolation is preferred, except when precluded from doing so by the edge of the low resolution phase screen. This has the advantage that the bulk of the

phase screen can be interpolated using a convolution, and also any blocking artifacts are minimised. The process described so far is the first stage in increasing the resolution of the phase screen, namely interpolating the low resolution samples. As with the method described in section 4.1.4, it is then necessary to displace the interpolated points randomly to ensure good agreement with the structure function. The amount of random displacement required is computed by considering the residual covariance between the true phase screen points, Ψ, and their estimated values. This yields

$$\begin{aligned} \text{Residual covariance} &= E\{(\Psi - \hat{\Psi})(\Psi - \hat{\Psi})^T\} && (4.54) \\ &= \mathbf{U}'\Lambda'\mathbf{U}'^T - 2\mathbf{U}'\Lambda'\Theta^T\Delta^T\mathbf{U}'^T + \mathbf{U}'\Delta\Theta\Lambda'\Theta^T\Delta^T\mathbf{U}'^T && (4.55) \end{aligned}$$

where $\Delta = \Lambda'\Theta^T[\Theta\Lambda'\Theta^T]^{-1}$.

The residual covariance, shown in Fig. 4.12, is zero at the low resolution points on the phase screen, as expected. It is also necessary that the added random displacements are uncorrelated with each other. This is the case as most of the cross-terms in the residual covariance are close to zero, the dominant values occurring on the diagonal. Although residual values can be determined corresponding to any interpolated point in the higher resolution grid, in general only the central point is needed and the window shifted accordingly. The variance of the random displacement required for an interpolated point is found on the diagonal of the residual covariance. This is then used to generate a random displacement, ϵ, in the manner discussed in Section 4.1.4. The optimal 2×2 interpolator and residual displacement with a variance of 0.6093 proved to be identical to the bilinear interpolator proposed in the original method. The 4×4 interpolator is more precise and consequently requires the addition of a random variable with a lower residual variance of 0.0844.

4.1.6 Implementation of interpolators

The interpolation process described in the previous section can also be viewed as a zero-filling operation to increase the sampling rate, followed by a filtering operation. The original

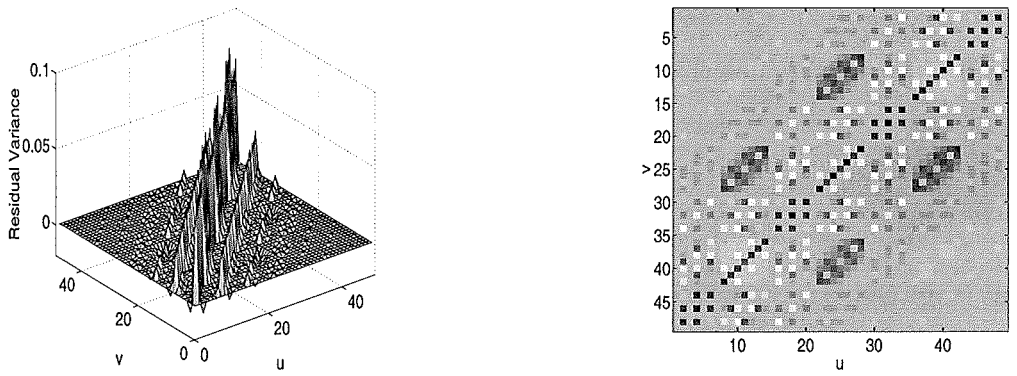

(a) (b)

Figure 4.12: *Different views of the residual variance on the estimated screen points for a 4×4 interpolator, $\hat{r} = 1$. The residual is zero at the initial screen points, since these are exact.*

bilinear interpolator then corresponds to a 3 × 3 interpolating filter:

$$I_{2\times 2} = \begin{bmatrix} 0.25 & 0 & 0.25 \\ 0 & 1 & 0 \\ 0.25 & 0 & 0.25 \end{bmatrix}. \tag{4.56}$$

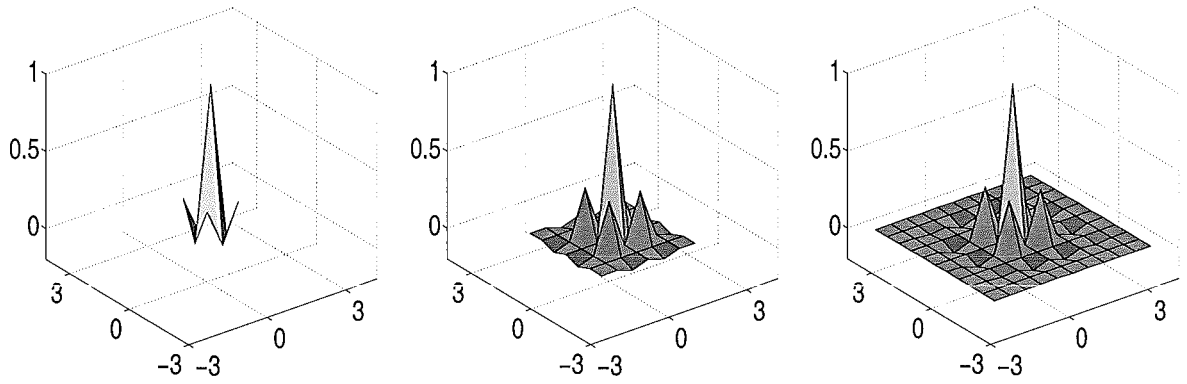

(a) (b) (c)

Figure 4.13: *The interpolators change as their size increases, however, after 4×4 they are very similar and little is to be gained by increasing past this size. (a) 2×2 interpolator, (b) 4×4 interpolator and (c) 6×6 interpolator.*

Derivation of the 4×4 interpolator by this method gives a significant change from the 2×2

coefficients:

$$I_{4\times4} = \begin{bmatrix} -0.0017 & 0 & -0.0341 & 0 & -0.0341 & 0 & -0.0017 \\ 0 & 0 & 0 & 0 & 0 & 0 & 0 \\ -0.0341 & 0 & 0.3198 & 0 & 0.3198 & 0 & -0.0341 \\ 0 & 0 & 0 & 1 & 0 & 0 & 0 \\ -0.0341 & 0 & 0.3198 & 0 & 0.3198 & 0 & -0.0341 \\ 0 & 0 & 0 & 0 & 0 & 0 & 0 \\ -0.0017 & 0 & -0.0341 & 0 & -0.0341 & 0 & -0.0017 \end{bmatrix} \tag{4.57}$$

but subsequent increases in interpolation size do not produce significant changes in the interpolator values, a point demonstrated graphically in Fig. 4.13.

The higher resolution screen is then generated by convolving the lower resolution screen that has been zero-filled and the interpolating filter followed by random displacement of the interpolated values. The interpolation of the central points is performed in two stages as discussed in relation to Fig. 4.8. As can be seen in Fig. 4.8(c) the interpolator is rotated by 45° in the second stage. The effect of rotating the 4×4 interpolator is shown in Fig. 4.14.

While in theory an interpolator larger than 4×4 would produce better results, there are two reasons to use this interpolator. Firstly as previously explained the coefficients of the interpolator change very little as its size increases past 4×4, and very little improvement in the structure function is observed past this size. Secondly, and perhaps more importantly, the number of points that can no longer be interpolated as the central point of a region of low resolution points increases. This makes interpolating edges of the phase screen more difficult as the size of the interpolator grows.

Computing the higher resolution points at the edge of the phase screen requires a different approach because not all their surrounding points exist. As the size of the interpolator increases, so do the number of affected edge points. Two techniques for dealing with this problem were investigated. For the first method interpolating filters specifically for the edge points were constructed and the appropriate residual determined. In the second method the edges were simply removed from the phase screen in the final step of each iteration and the

value of $\hat{r}$ adjusted so that the overall dimension of the phase screen is the same as it was in the first step. For example when a 2×2 interpolator is used the outer border of points in Fig. 4.10(a) are deleted to produce Fig. 4.10(b). This second method requires the initial phase screen to be larger than the interpolating filter, otherwise the phase screen does not grow at each iteration.

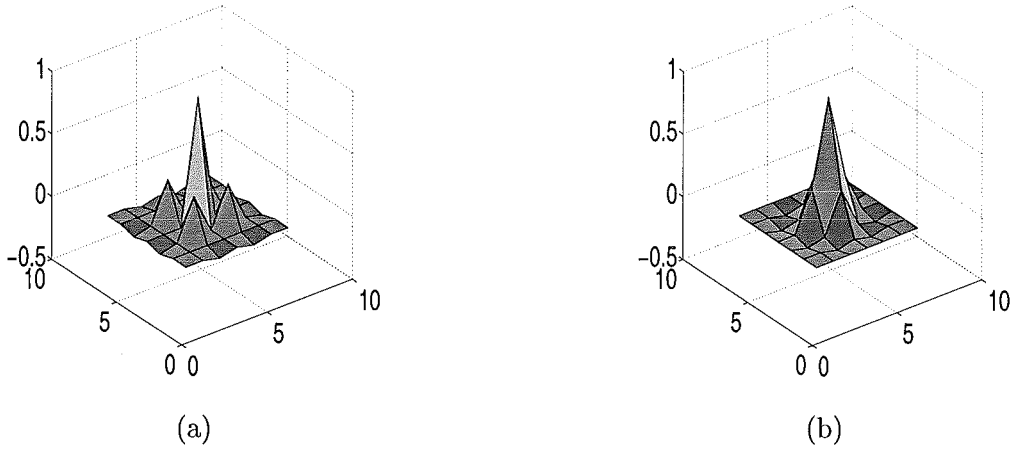

Figure 4.14: *The 4×4 interpolators used for the (a) 1st and (b) 2nd levels of interpolation. The structure of the filter depends on the spatial relationship between the known points and the point to be estimated as in Figs. 4.8(a) and 4.8(c).*

4.1.7 Simulation of Kolmogorov turbulence

The phase screens produced by the midpoint method can be increased in size by further iterations. Therefore increasing the number of iterations can produce a phase screen of the required resolution. Fig. 4.15 shows the effect of successive levels of iteration on the appearance of the phase screen. It appears that higher levels of iteration produce a 'smoother' phase screen, this is due however to a reduction in the aliasing artifact. Visually there is little difference in the phase screen's appearance between using a 2×2 interpolator and a 4×4 interpolator. As the phase screen resolution increases the extent of the speckle in the transform domain also increases due to oversampling, resulting in the corresponding speckle images at different phase screen resolutions shown in Fig. 4.16.

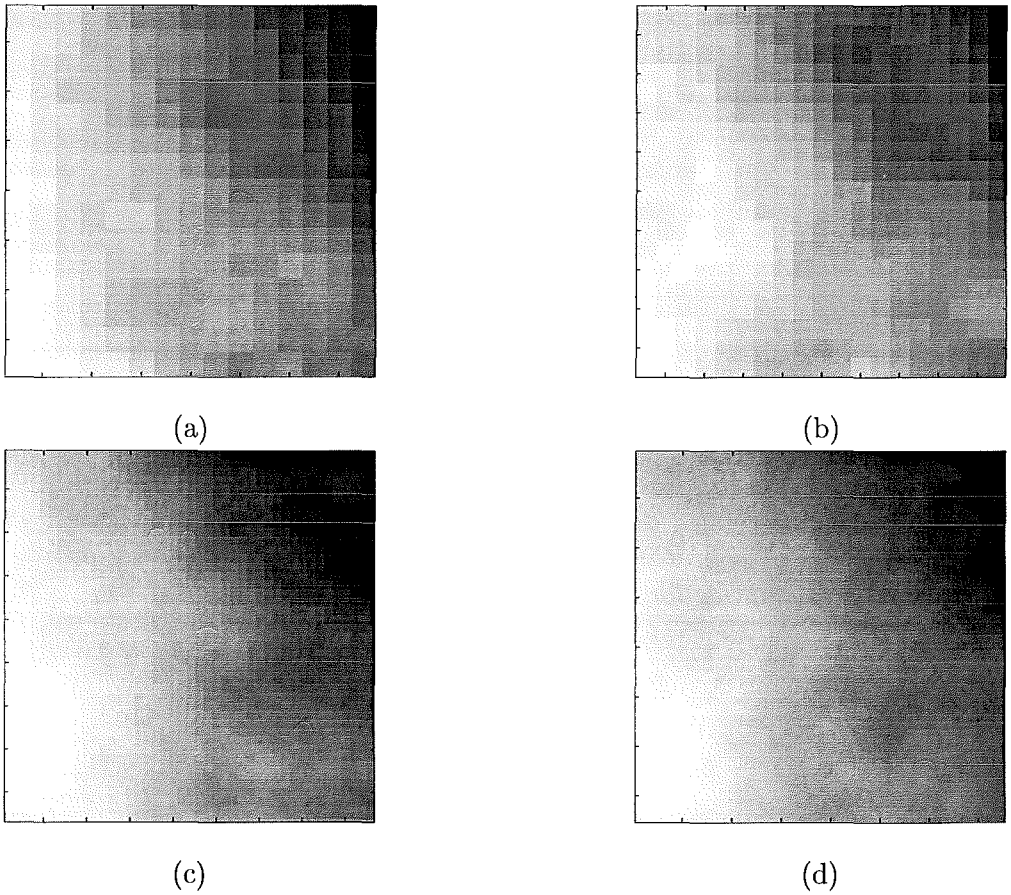

Figure 4.15: *The same initial phase screen as the number of successive iterations is increased. (a) The initial 15×15 exact screen, (b) 1 iteration, (c) 3 iterations and (d) 5 iterations.*

The accuracy of the phase screens is better determined by comparing their structure functions, over an appropriately sized ensemble, to the ideal structure function, described in Eq. (4.8). Fig. 4.17 shows these comparisons over an ensemble of 10,000 phase screens, each produced by iterating 4 times from the initial low resolution points. In order to quantitatively assess the performance of the method a statistical analysis of the structure function was also performed (see Fig. 4.17). Using $D_{p(i)}$ to denote the structure function computed from the ith phase screen,

$$\sigma(u,v) = \sqrt{\frac{1}{(N-1)}\sum(D_{p(i)}(u,v) - \frac{1}{N}D_{p(i)}(u,v))^2}. \tag{4.58}$$

This gives the standard deviation of the mean structure function generated by this technique. Fig. 4.18 shows a plot of the number of standard deviations between the average

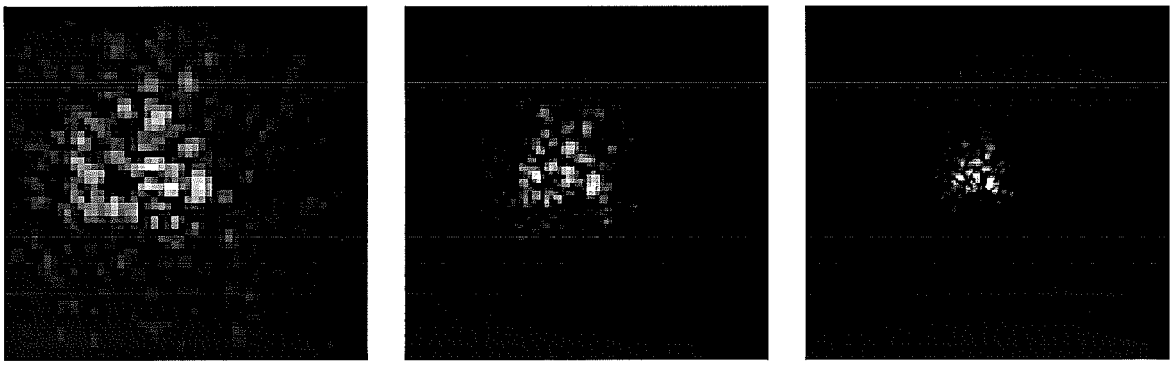

(a) (b) (c)

Figure 4.16: *For each speckle a D/r_0 of 10 was used, from a phase screen of (a) 2 iterations, (b) 3 iterations and (c) 4 iterations. In each case the detail is of approximately the same scale with the interpolation operation accounting for the increase in image size.*

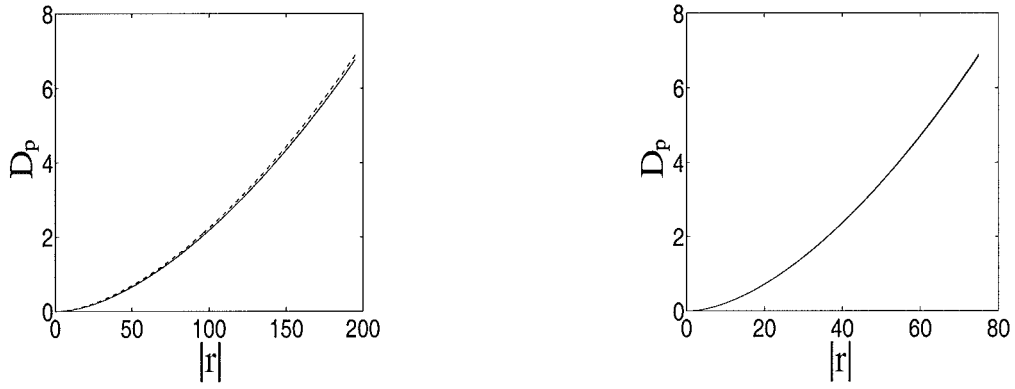

(a) (b)

Figure 4.17: *Phase structure functions for the phase screens generated (solid lines) are compared against the ideal phase structure function (dashed lines) as given by Eq. (4.8) (a) for the 2×2 interpolator and (b) for the 4×4 interpolator. In both cases edges are removed at each iteration.*

and ideal structure functions for both the 2×2 and 4×4 interpolators, i.e.

$$\frac{D_p(u,v) - (\frac{1}{N}\sum D_{p(i)}(u,v))}{\sigma(u,v)}. \tag{4.59}$$

The results for the 2×2 interpolator are statistically significant for an ensemble of 100, however for the 4×4 interpolator a statistically significant deviation is only reached for an ensemble size of 10,000. When comparing the two methods for dealing with edge points,

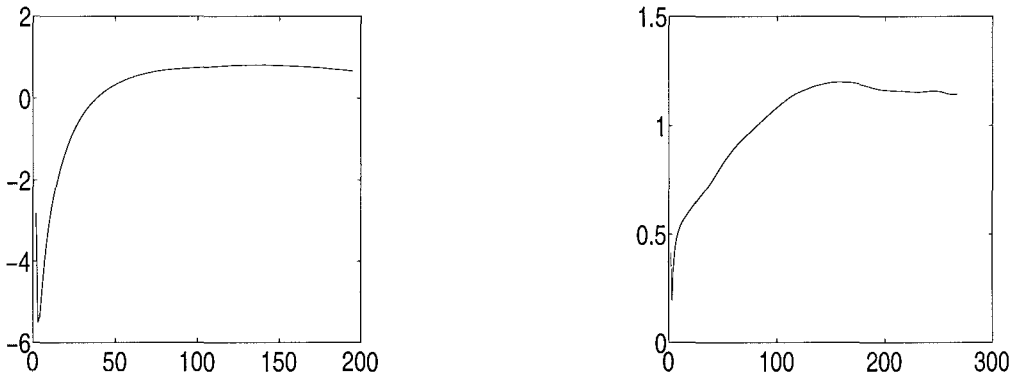

(a) (b)

Figure 4.18: *Number of standard deviations from ideal structure functions for structure functions generated from an ensemble of 100 for (a) a 2×2 interpolator and (b) a 4×4 interpolator. Note that the structure functions for the 4×4 interpolator were generated from an initial 15×15 phase screen with 6 iterations, whereas for the 2×2 interpolator only 4 iterations were used. This is due to the greater edge effects in the 4×4 case.*

the structure functions show that superior results are obtained by removing the edges of the phase screens rather than by interpolating them, Fig. 4.19.

Phase screens can be generated by this method very quickly. Fig. 4.20 shows the CPU time taken to produce a screen, against the number of samples produced. Initially the time taken is steep due to the overhead from direct computation of the initial exact phase screen, however as the size increases the relationship becomes linear. An initial 15×15 phase screen was used because the computational requirements are not huge and it provides a reasonable base for interpolation. Therefore, each iteration produces a screen of area approximately four times larger than the previous one and it should take four times longer to generate it. To produce a phase screen of 139×139 elements (5 iterations from an initial 15×15 screen, using a 4×4 interpolator with the edges removed) requires 2704697 floating point operations (flops) and takes 0.17 CPU seconds on a Sun Enterprise 450. This does not differ significantly from the computational requirements of the spectral methods [94], but the phase screen is substantially more accurate.

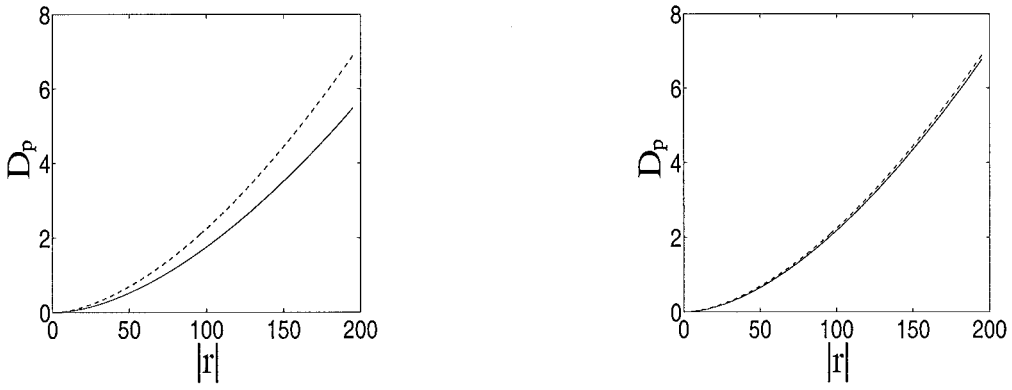

Figure 4.19: *Phase structure functions for the phase screens generated (solid lines) using different techniques for the edge points are compared against the ideal phase structure function (dashed lines) as given by Eq. (4.8). A 2×2 interpolator was used for these results. (a) Edge points are interpolated. (b) Edge points are removed.*

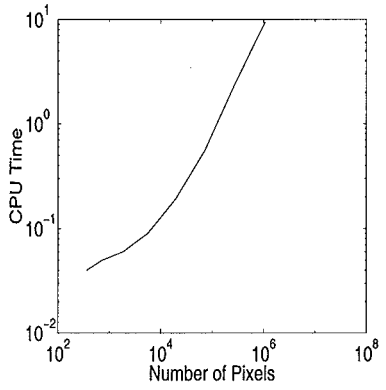

Figure 4.20: *CPU time to produce phase screens as the number of samples generated increases.*

4.1.8 Simulation of non-Kolmogorov turbulence

The simulation of atmospheric turbulence using the improved midpoint displacement method is not restricted to Kolmogorov statistics. Consider turbulence described by a more general power spectrum of phase fluctuations,

$$W_\phi(\mathbf{k}) \propto \mathbf{k}^{-\beta}, \tag{4.60}$$

where $\beta = 11/3$ corresponds to Kolmogorov statistics. The power spectrum and structure function of a random process are related by [139]

$$D_\phi(\mathbf{r}) = 2\int_{-\infty}^{\infty} W_\phi(\mathbf{k})[1 - \cos(2\pi\mathbf{rk})]d\mathbf{k}. \tag{4.61}$$

Since the structure function and power spectrum are both rotationally symmetric this can be written as a Hankel transform,

$$D_\phi(r) = 4\pi\int_0^{\infty} W_\phi(k)[1 - J_0(2\pi rk)]kdk, \tag{4.62}$$

where $r = |\mathbf{r}|$ and $k = |\mathbf{k}|$. Therefore, the structure function for the general power spectrum is

$$D_\phi(r) \propto 4\pi\int_0^{\infty} k^{1-\beta}[1 - J_0(2\pi rk)]dk. \tag{4.63}$$

This can be evaluated with [121]

$$\int_0^{\infty} x^{-p}\left[1 - J_0(bx)\right]dx = \frac{\pi b^{p-1}}{2^p\left[\Gamma\left(\frac{p+1}{2}\right)\right]^2\sin\left(\frac{\pi(p-1)}{2}\right)}, \tag{4.64}$$

to give

$$D_\phi(r) \propto r^{\beta-2} \tag{4.65}$$

for $2 < \beta < 4$. For $\beta = 11/3$ the well-known structure function for Kolmogorov statistics results (4.8). For $\beta = 10/3$ this gives

$$D_\phi(r) \propto r^{4/3} \tag{4.66}$$

and for $\beta = 9/3$,

$$D_\phi(r) \propto r. \tag{4.67}$$

Consider now

$$D_\phi(r) = \frac{6.88}{r_0^{5/3}}r^{\beta-2}, \tag{4.68}$$

for $\beta = 9/3$, $10/3$, $11/3$ and $12/3$. Although Eq. (4.64) does not converge for $\beta = 12/3$ it is assumed that $\beta = 12/3$ corresponds to $D_\phi(r) \propto r^2$ in the limit. Knowledge of the structure function allows the phase covariance to be calculated from Eq. (4.36). A SVD can now be performed to obtain the eigenvalues and eigenvectors. The direct simulation

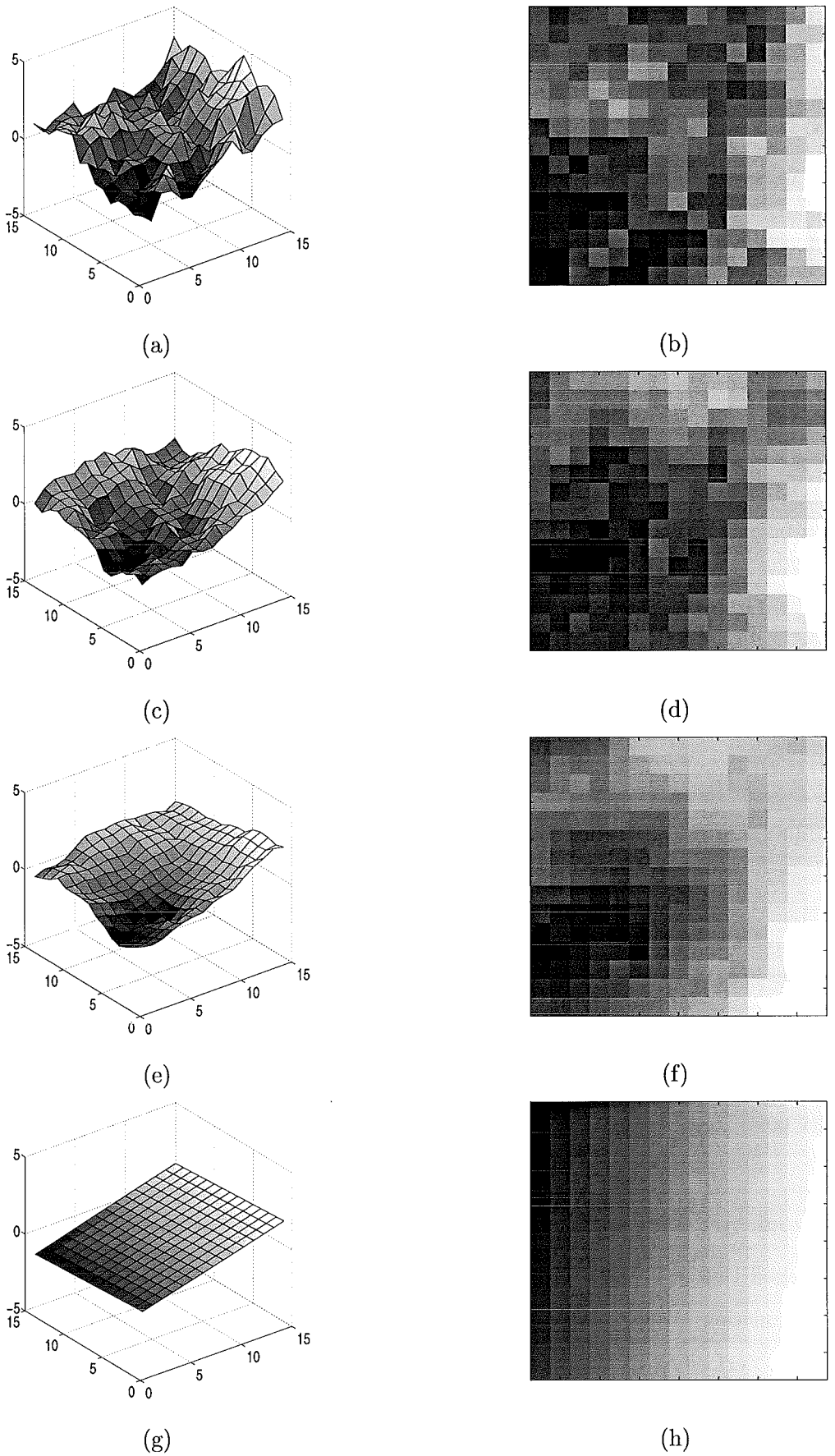

Figure 4.21: *Different views of phase screens generated by direct simulation for (a),(b) 9/3 (c),(d) 10/3 (e),(f) 11/3 and (g),(h) 12/3 power laws.*

of phase screens with these power laws is possible with sample phase screens illustrated in Fig. 4.21. As β is decreased from 11/3 a smaller percentage of the distortion is due to the tip-tilt components, whereas $\beta = 12/3$ corresponds to a completely tip-tilt distortion.

As with Kolmogorov turbulence, the optimal interpolators for the power laws presented here can be determined. An investigation of interpolators for $\beta = 9/3$ and 10/3 was carried out. For $\beta = 12/3$ interpolation is simple as the screen is determined exactly by its slope, hence standard bilinear interpolation produces an exact result. The 2×2 interpolators for $\beta = 9/3$ and 10/3 were identical to the interpolator calculated for Kolmogorov statistics. However, the necessary random displacements are larger, 1.9287 and 1.2490 respectively, reflecting the larger contribution of the higher order terms. The 4×4 interpolators have the same form but slightly different values, i.e.

$$I_{9/3(4\times4)} = \begin{bmatrix} -0.0122 & 0 & -0.0098 & 0 & -0.0098 & 0 & -0.0122 \\ 0 & 0 & 0 & 0 & 0 & 0 & 0 \\ -0.0098 & 0 & 0.2819 & 0 & 0.2819 & 0 & -0.0098 \\ 0 & 0 & 0 & 1 & 0 & 0 & 0 \\ -0.0098 & 0 & 0.2819 & 0 & 0.2819 & 0 & -0.0098 \\ 0 & 0 & 0 & 0 & 0 & 0 & 0 \\ -0.0122 & 0 & -0.0098 & 0 & -0.0098 & 0 & -0.0122 \end{bmatrix} \tag{4.69}$$

and

$$I_{10/3(4\times4)} = \begin{bmatrix} -0.0084 & 0 & -0.0233 & 0 & -0.0098 & 0 & -0.0233 \\ 0 & 0 & 0 & 0 & 0 & 0 & 0 \\ -0.0233 & 0 & 0.3050 & 0 & 0.3050 & 0 & -0.0233 \\ 0 & 0 & 0 & 1 & 0 & 0 & 0 \\ -0.0233 & 0 & 0.3050 & 0 & 0.3050 & 0 & -0.0233 \\ 0 & 0 & 0 & 0 & 0 & 0 & 0 \\ -0.0084 & 0 & -0.0233 & 0 & -0.0233 & 0 & -0.0084 \end{bmatrix} \tag{4.70}$$

and are illustrated in Fig. 4.22. Once again the required random displacements are larger than that required for $\beta = 11/3$, 0.6320 and 0.2701 respectively. Phase screens with different values of β simulated using the improved midpoint method are illustrated in Fig. 4.23.

The accuracy of the simulations can again be checked by comparison with the appropriate structure function (see Fig. 4.24).

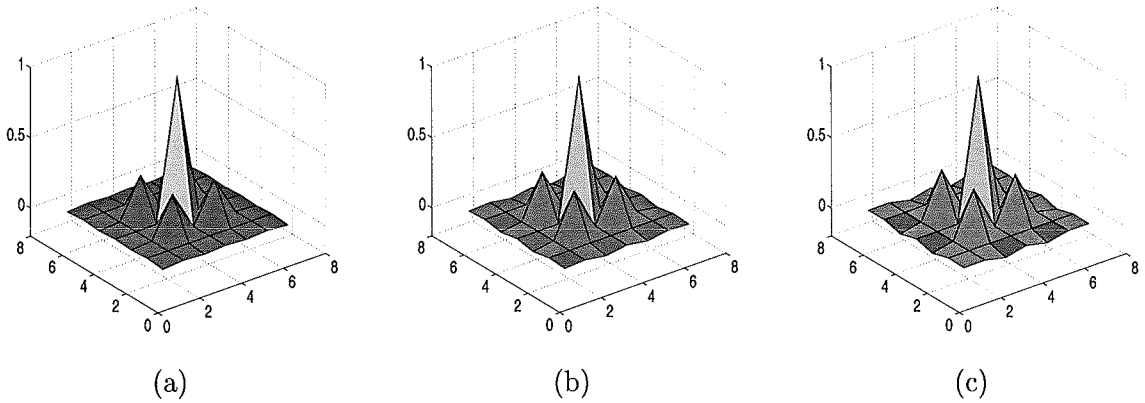

Figure 4.22: 4×4 *interpolators for (a) 9/3 (b) 10/3 and (c) 11/3 power laws*

4.2 Wave propagation through random media

This section outlines a technique for the accurate modelling and simulation of scintillation patterns due to various turbulence statistics without the need to assume periodic boundary conditions. The more physically justifiable assumption of smoothness results in a propagation kernel of finite extent. This allows the phase screen dimensions for an accurate simulation to be determined and truncation can then be used to eliminate the unwanted spectral leakage and diffraction effects usually inherent in the use of finite apertures. A detailed outline of the proposed technique and comparison of simulations with analytic results are presented.

Many different methods for simulating wavefront propagation have been published [1, 33, 50, 109, 110, 141, 164]. A common theme to these papers has been the assumption of periodic boundary conditions, originally proposed for laser propagation applications by Martin and Flatté [109]. This assumption is a consequence of using the basic spectral technique for simulating turbulence.

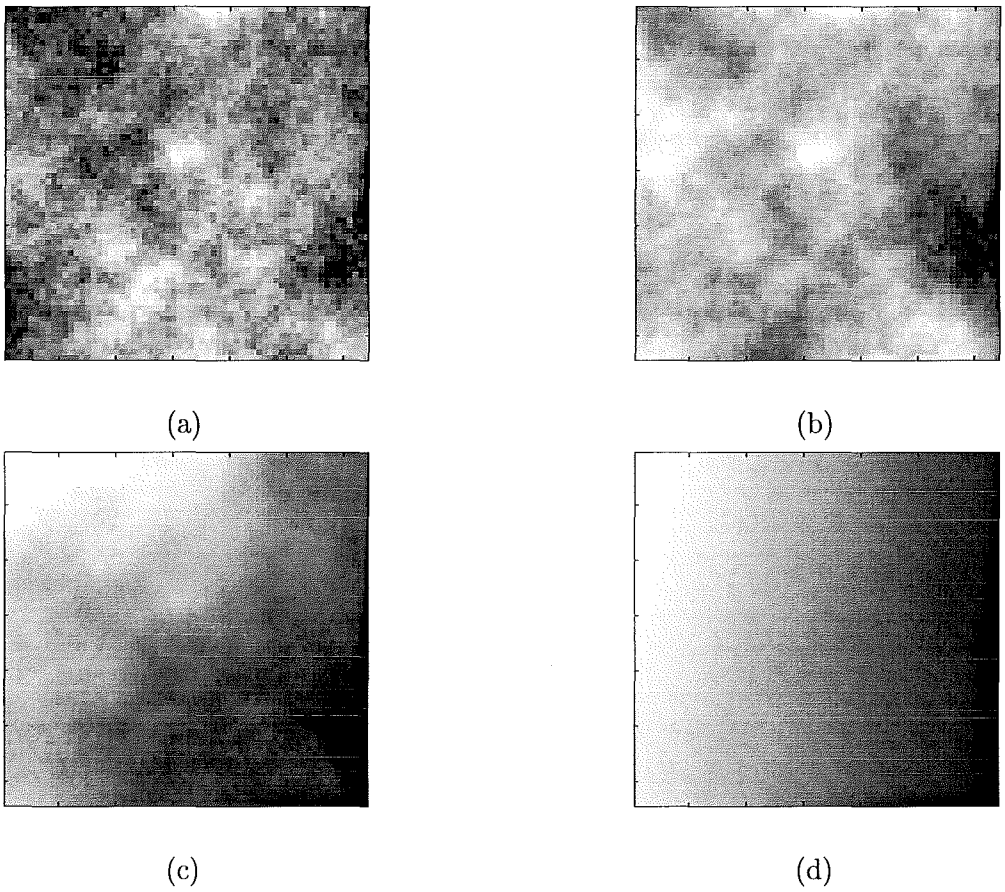

Figure 4.23: *Phase screens simulated using the improved midpoint method for (a) 9/3, (b) 10/3, (c) 11/3 and (d) 12/3 power laws.*

The assumption of periodic boundary conditions, as in Fig. 4.25, has no physical basis and can lead to a number of difficulties in simulating the effects of atmospheric turbulence. For example, periodic phase screens do not have a significant average slope [94] and as a result do not model the deflection of the wavefront caused by atmospheric turbulence. This causes problems when simulating wavefront sensors, where the estimation of the average slope is critical and also when modelling laser propagation when the deflection of the beam is an important issue. Another example where assumption of boundary conditions causes difficulties is the simulation of moving turbulence [63]. Although it can be argued that there are circumstances where the assumption of periodic boundary conditions does not affect the simulated results [33], this assumption is unnecessary and as a consequence it should not be used.

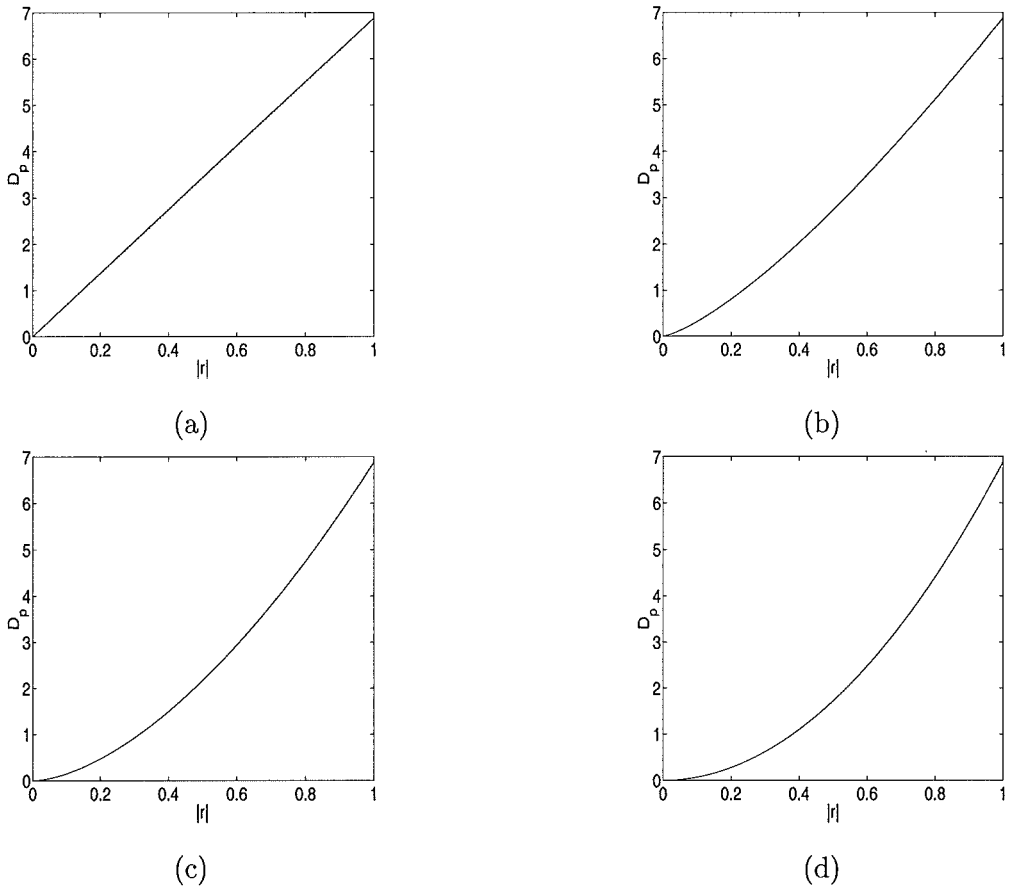

Figure 4.24: *Ideal (solid) and simulated (dotted) structure functions for (a) 9/3, (b) 10/3, (c) 11/3 and (d) 12/3 power laws. Plots in which there appears to be only a single solid line indicate a very good match between the simulated and ideal structure functions.*

An important feature of the proposed technique is that the errors introduced by aliasing and edge effects are both quantifiable and controllable. Since the Fresnel kernel and the phase screen are not bandlimited in either time or frequency, the ability to sample adequately in either domain is an important issue. Problems caused by the infinite size of both the atmosphere and the Fresnel propagation kernel can be avoided, by an appropriate regularisation of the problem.

4.2.1 Theory

The atmosphere is a weak, inhomogeneous random medium known to have a finite number of horizontal layers [170]. For simulation purposes it is considered to be free space containing a finite number of very thin phase screens, where the simplest case is a single phase layer situated a height z above the telescope aperture. The layer is assumed so thin, that only the phase of the incident wavefront is distorted when passing through the phase screen. The phase distorted wavefront, $\psi(x, y, z-)$, is given by [109]

$$\psi(x, y, z-) = \psi(x, y, z+)\exp(j\phi(x, y, z)), \tag{4.71}$$

where $\psi(x, y, z+)$ is incident on the phase layer $\phi(x, y, z)$ at a height z (see Fig. 4.25), as outlined in section 3.4.3. The atmosphere is modelled as a series of thin phase screens that obey a Kolmogorov power law [134]. These phase screens are simulated using the improved midpoint displacement technique outlined in section 4.1.5, which generates phase screens with accurate statistics. Propagation between the phase layers is obtained by evaluating the Fresnel diffraction over the distance between the phase screens. This is achieved by convolution of the incident wavefront with the Fresnel convolution kernel as outlined in section 3.4.3 or alternatively by use of the angular spectrum transfer function [139]. The existing methods for evaluating the propagation, outlined in section 4.2.2 below, differ in their treatment of edge effects and sampling considerations. A major limitation of these techniques is they make unrealistic assumptions. A more realistic method for the simulation of Fresnel propagation is outlined in sections 4.2.3 to 4.2.6, with the extension to propagation through non-Kolmogorov turbulence presented in section 4.2.7.

4.2.2 Existing techniques

Wave propagation can be simulated using the Fresnel diffraction integral [66],

$$U_p(x, y) = \int_{-\infty}^{\infty}\int_{-\infty}^{\infty} U_o(\xi, \eta)h(x - \xi, y - \eta)d\xi d\eta, \tag{4.72}$$

where $U_o(x, y)$ is the original wavefront and $U_p(x, y)$ the propagated wavefront. The basic procedure to propagate a wave through a single turbulence layer at a height of z above ground level is outlined below and corresponds to the technique outlined in Martin and

Flatté [109]:

Step 1 - Propagate through the phase layer represented by $\phi(x, y, z)$

$$\psi(x, y, z-) = \psi(x, y, z+)\exp(j\phi(x, y, z)) \tag{4.73}$$

Step 2 - Fourier transform the resulting wavefront

$$\Psi(u, v, z-) = \mathcal{F}\{\psi(x, y, z-)\}, \tag{4.74}$$

where

$$\mathcal{F}\{\psi(x, y, z-)\} = \int_{-\infty}^{+\infty}\int_{-\infty}^{+\infty} \psi(x, y, z-)\exp(j2\pi(ux + vy))dxdy. \tag{4.75}$$

Step 3 - Convolve with the Fresnel convolution kernel by multiplication in the Fourier domain

$$\Psi(u, v, 0) = \Psi(u, v, z-)H(u, v) \tag{4.76}$$

Step 4 - Take the inverse Fourier transform to obtain the propagated wavefront

$$\psi(x, y, 0) = \mathcal{F}^{-1}\{\Psi(u, v, 0)\} \tag{4.77}$$

Although straightforward in concept, a practical issue arises since both $h(x, y)$ and

$$H(u, v) = \exp(jkz)\exp\left(-j\frac{z}{2k}\left(u^2 + v^2\right)\right) \tag{4.78}$$

are infinite in extent. As a consequence aliasing causes significant differences between the discrete Fourier transform of $h(x, y)$ and $H(u, v)$ sampled from Eq. (4.78). One of the advantages of the proposed method is to theoretically relate the effective extent of the Fresnel kernel to the smoothness of $U_o(x, y)$.

Although both the atmosphere and the Fresnel kernel are in theory of infinite extent, only a finite piece of the atmosphere can be used for computational purposes. This effectively superimposes a limiting aperture on the atmosphere and edge diffraction effects are seen in the resulting scintillation patterns unless the atmosphere is assumed to be periodic, an approximation which has no physical basis (see Fig. 4.25(a)).

Scintillation simulated from a periodic phase screen is illustrated in Fig. 4.26(a) and is also periodic. By contrast, scintillation simulated from a non-periodic phase screen (see Fig. 4.26(b)) clearly suffers from edge effects. A solution used by Adcock and Jones [1] is to window the data with a Gaussian edged apodising mask as in Fig. 4.26(c). However, this reduces the dimension of accurate and useful simulation data and again is not a representation of the physical process. An alternative solution, which was an early attempt at producing useful simulation data from a non-periodic screen, involved using reflection at the edges of the screen (as in the DCT) to perform the propagation (see Fig. 4.26(d)). Although it enabled scintillation to be easily calculated from non-periodic phase screens, the assumption of reflection at the edges is again physically unjustified.

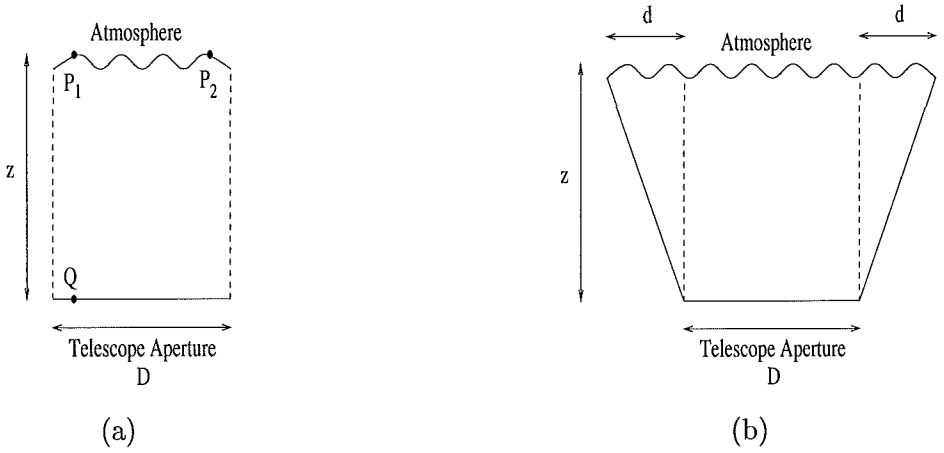

Figure 4.25: *(a) The periodic assumption. Note the propagated wavefront at Q depends equally on the initial wavefront at the points P_1 and P_2. (b) The use of an extended initial wavefront showing the extra screen dimensions required for an accurate scintillation simulation. A phase screen of dimension $(D+2d)m \times (D+2d)m$ is required for an accurate scintillation representation of $Dm \times Dm$ at the telescope aperture, after propagation over the height z.*

4.2.3 Scintillation from an aperiodic phase screen

An alternative is to employ a larger starting phase screen than required, to minimise edge effects, as illustrated in Fig. 4.25(b). Goodman [68] suggests that an extra dimension of $4\sqrt{\lambda z}$ is required, but this is an approximation computed for a sharp edge or finite aperture

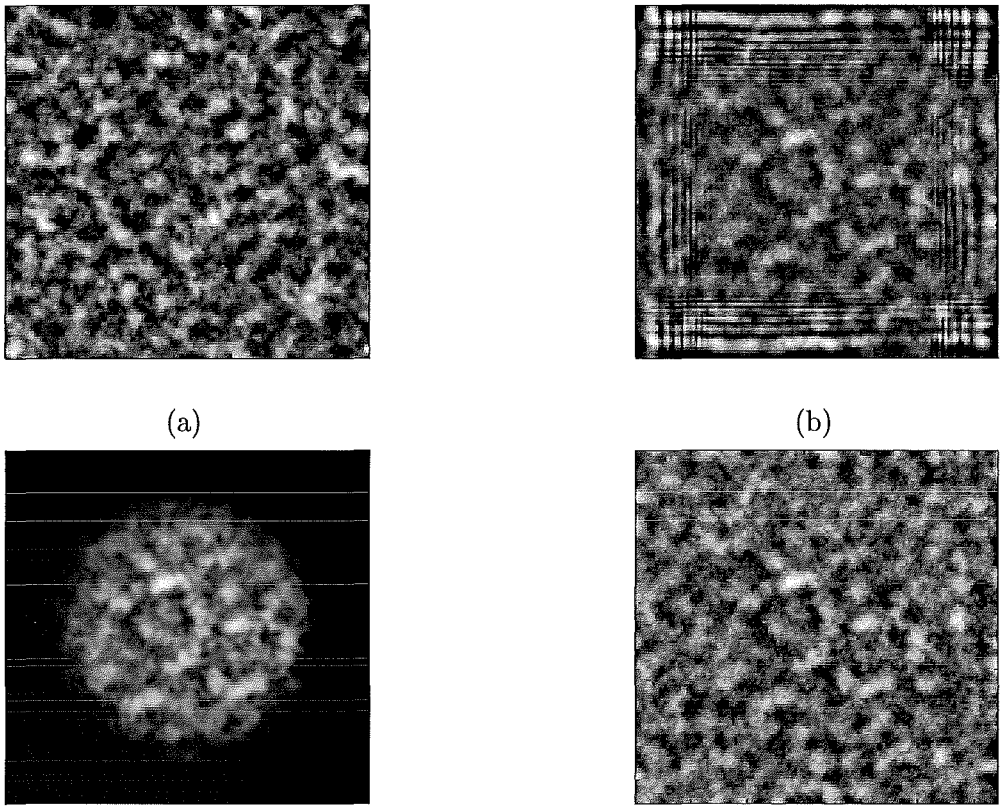

Figure 4.26: *Simulation of scintillation over a propagation distance of 5km from (a) a periodic phase screen, (b) a non-periodic phase screen, (c) a non-periodic phase screen with a Gaussian edged apodising mask and (d) a non-periodic phase screen with reflection at the edges.*

and is inappropriate for atmospheric turbulence. Instead, it is possible to use the statistics of the wavefront to determine the extra aperture dimension required.

The principle of stationary phase [23] is particularly relevant to this problem. Stationary phase is a technique for finding asymptotic values of integrals of the form

$$\int g(z)\exp(jkf(z))dz, \tag{4.79}$$

where $g(z)$ is slowly varying with respect to $kf(z)$. The Fresnel diffraction integral, Eq. (4.72), is of this form. Because the extreme parts of the kernel away from the saddle in the middle vary rapidly, they do not contribute significantly to the integral provided the envelope $g(z)$ is slowly varying [76]. Referring again to Fig. 4.25(b), this means that in

practice the extra distance required, $2d$, is finite. Since Kolmogorov phase screens are fractal [94, 144], an approximation that makes $g(z)$, in this case $U_o(x, y)$, slowly varying is required in order to apply stationary phase rigorously.

This is achieved by regularising $U_o(x, y)$ by convolution with a Gaussian

$$s(x, y) = \frac{1}{2\pi\sigma^2}\exp\left(-\frac{x^2 + y^2}{2\sigma^2}\right), \tag{4.80}$$

where σ is a user defined constant that defines the width of the Gaussian. The convolution with the Gaussian smooths the fractal detail of the phase screen, so that the principle of stationary phase can be applied. In the limit, as $\sigma \to 0$, $s(x, y)$ tends to a delta function and the smoothed solution tends to the unregularised solution. It is important to note that convolving with $s(x, y)$ introduces an error into the simulation, but it does however ensure that the problem is computable. Decreasing σ means that the solution is more accurate but requires more computing resources, and the choice of σ thus provides a mechanism for this tradeoff. The desired accuracy of the simulation can therefore be set by the user for a specific application.

The convolution of the data with the Gaussian smoothing term can be considered to be a low pass filtering of the angular spectrum or equivalently multiplication of the spatial spectrum of the phase by a Gaussian determined by the inner scale. This is known to restrict the required sampling rate of the simulation, but it also limits edge effects in the simulation procedure. This approach can also be viewed as a means of imposing a finite inner scale in a well controlled manner. The propagation of the wavefront can now be written as

$$U_p(x, y) = (U_o(x, y) \odot s(x, y)) \odot h(x, y). \tag{4.81}$$

Because convolution is a linear operation, the result is unchanged by the order of convolution. Hence it is possible to combine the Gaussian with the chirp and then convolve the modified chirp with the phase screen. The analytic expression for the smoothed chirp is

$$\begin{aligned} \hat{h}(x, y) &= h(x, y) \odot s(x, y) \\ &= K\exp(jkz)\exp\left(-\frac{x^2 + y^2}{2\sigma_w^2}\right)\exp\left(\frac{jk}{2z}\left(\frac{x^2 + y^2}{\beta}\right)\right), \end{aligned} \tag{4.82}$$

where

$$K = \frac{-jz + k\sigma^2}{\lambda(z^2 + k^2\sigma^4)}, \sigma_w^2 = \frac{(z^2 + k^2\sigma^4)}{k^2\sigma^2}, \beta = 1 + \frac{k^2\sigma^4}{z^2}, \tag{4.83}$$

are found using Eqs. (3.19) and (4.80). It should be noted that as $\sigma \to 0$, Eq. (4.82) tends to the original Fresnel kernel $h(x, y)$. In addition, regardless of the choice of σ it integrates to 1. Finally, it should be noted that when simulating turbulence in cases that σ can be chosen to limit the size of $s(x, y)$ to below the size of the inner scale there is a minimal effect on $U_o(x, y)$.

4.2.4 Determining the required screen size for simulation

The key advantage of using $\hat{h}(x, y)$ instead of $h(x, y)$ arises from the presence of the term $\exp\left(-\frac{x^2+y^2}{2\sigma_w^2}\right)$ which windows $h(x, y)$ as illustrated in Fig. 4.27. The effective width W of $\hat{h}(x, y)$ is defined by

$$1 - \frac{1}{2\pi\sigma_w^2} \int_{-W/2}^{W/2} \int_{-W/2}^{W/2} \exp\left(-\frac{x^2 + y^2}{2\sigma_w^2}\right) < X \tag{4.84}$$

where X is the acceptable error fraction. This in turn defines the extra size required in $U_o(x, y)$ to obtain the desired size of $U_p(x, y)$ as $d = W/2$. The results presented throughout this thesis have used $W = 6\sigma_w$ which corresponds to $X = 0.005$.

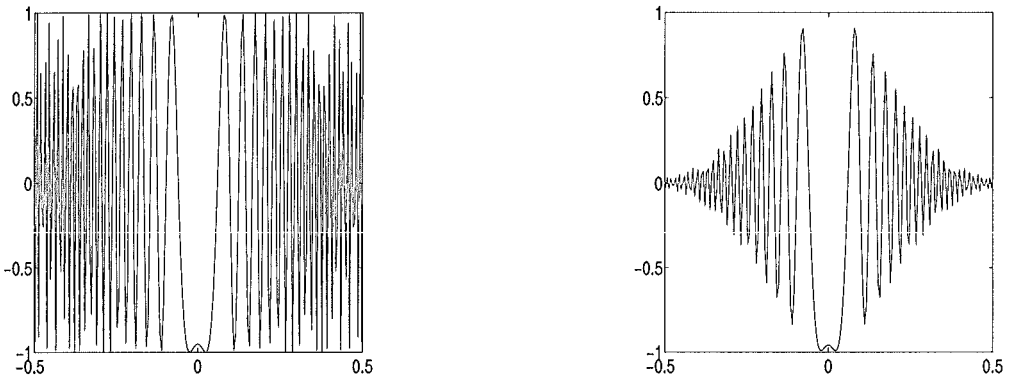

(a) (b)

Figure 4.27: *Comparison of the real parts of the original and smoothed Fresnel kernels. (a) Original kernel and (b) smoothed kernel.*

The extra aperture dimension required in the simulation is a function of two quantities.

Firstly, the amount of smoothing performed and secondly the distance propagated. Now the basic procedure for propagating a wave through a single turbulence layer at a height of z above ground level, outlined in section 4.2.2, requires two modifications. Firstly, the convolution kernel $H(u, v)$ in step 3 must be replaced with $\hat{H}(u, v)$ and secondly an extra step (step 5) is needed. In step 5 the resulting $(D + 2d) \times (D + 2d)$ phase screen must be truncated to dimensions of $D \times D$. Assuming a propagation distance of 10km, Fig. 4.28(a) shows how the extra distance required decreases as the smoothness increases. The tradeoff in accuracy is shown in Fig. 4.28(b) which illustrates the distortion of the original phase screen as a function of increasing smoothness. Finally, Fig. 4.28(c) illustrates how the effective width of $\hat{h}(x, y)$ and consequently the computational cost required by the convolution increases as the distance propagated increases.

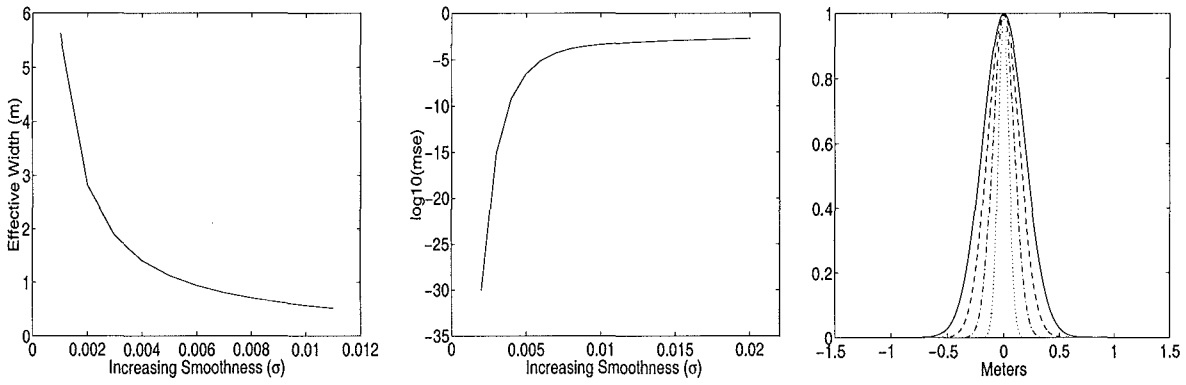

Figure 4.28: *Simulation parameters as a function of smoothing and propagation distance. (a) Extra distance required versus smoothness for z = 10km and $D/r_0 = 1$. (b) Phase screen distortion versus smoothness for z = 10km and $D/r_0 = 1$. (c) The envelope of the modified kernel as a function of the propagation distance (10km (solid), 7.5km (dashed), 5km (dashed-dotted) and 2.5km (dotted)) for $D/r_0 = 1$ and $\sigma = 0.005m$.*

Convolution of the Fresnel kernel with the Gaussian is almost equivalent to multiplying the chirp with a Gaussian window apart from the (usually small) alteration to the chirp phase. An alternative, suggested in Refs. [1] and [33] and illustrated in section 4.2.2, is to window the phase screen by multiplication with a suitable window. However, apodising techniques

have the effect of reducing the dimension of accurate and useful simulation data, requiring large starting screens to be used. More importantly the effect of apodising is very difficult to quantify on the final simulation, since the order of convolution and multiplication cannot be interchanged. By contrast, here the effect of the convolution by the Gaussian can be quantified as a distortion on the input or output, since the smoothing convolutions can be performed at any stage of the propagation process. For the purposes of analysis it is useful to consider convolving the Gaussian with the input phase screen or the output scintillation, while for computation purposes it is useful to combine it with the chirp and generate a kernel of finite extent. Fig. 4.29 demonstrates the relationship between the input phase screen and the output scintillation.

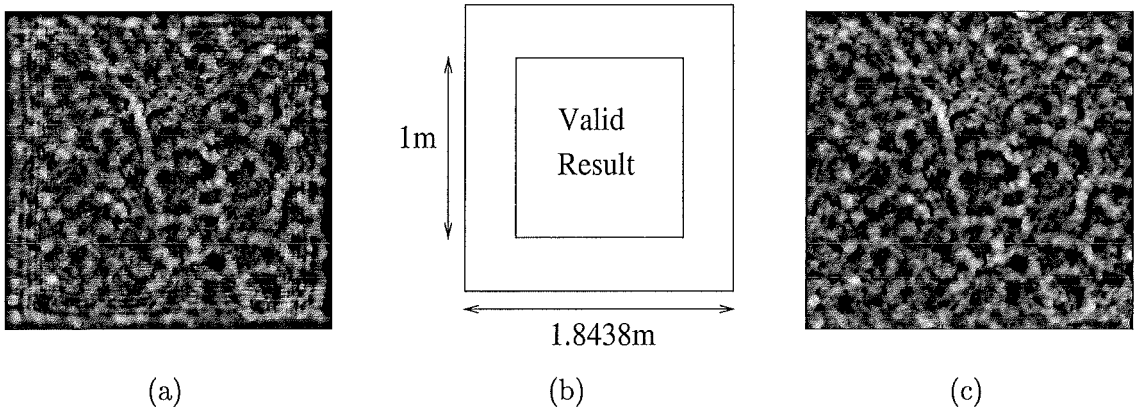

Figure 4.29: *Illustration of edge effects for an aperture of size 1m × 1m, propagation distance of 3km, r_0 of 10cm, $\sigma = 0.002$m and visible light. (a) The 1m × 1m scintillation pattern resulting from the convolution of a 1m × 1m non-periodic phase screen with the unmodified Fresnel kernel. Edge effects are apparent only close to the edges in the image however they extend across the entire result. (b) Use of the smoothed Fresnel kernel and a starting phase screen of size 1.8438m × 1.8438m is necessary to produce an undistorted 1m × 1m scintillation pattern. Although the introduced smoothing does not eliminate the edge effects it does guarantee that they do not extend into the valid result region. (c) The valid 1m × 1m portion of the scintillation from the 1.8438m × 1.8438m starting screen, which is clearly free from diffraction effects.*

4.2.5 Determining the required sampling rate

The Fourier transform of the regularised kernel, Eq. (4.82), is given by,

$$\hat{H}(u,v) = \exp(jkz)\exp\left(-\frac{u^2+v^2}{2\sigma_s^2}\right)\exp\left(-\frac{jz}{2k}(u^2+v^2)\right), \tag{4.85}$$

where $\sigma_s = 1/\sigma$. Convolution by the Gaussian smoothing term effectively bandlimits the chirp (Fig. 4.30), thus enabling adequate sampling in the frequency domain to be achieved.

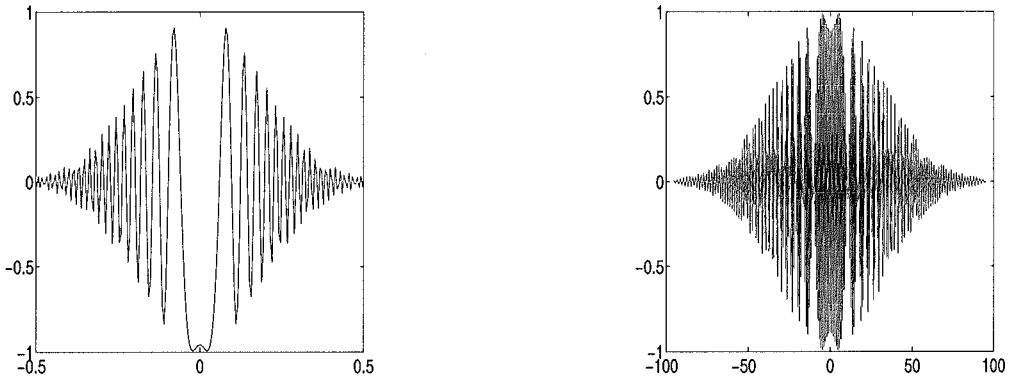

(a) (b)

Figure 4.30: *The real part of the regularised kernel in (a) the time domain, $\hat{h}(x,y)$, and (b) the frequency domain, $\hat{H}(u,v)$.*

It is essential that the phase screens, the Fresnel propagation kernel (or the angular spectrum transfer function) and the scintillation itself are sampled adequately so as to avoid aliasing and the resulting effects on the accuracy of the scintillation simulations. Using classical Nyquist theory, a signal is adequately sampled at twice the maximum frequency present. Since all signals here are of infinite bandwidth, a more practical alternative for sampling the phase screen is to ensure that for the chirp and the phase screen [1]

$$\frac{\phi(x) - \phi(x+\triangle x)}{\triangle x} \leq \pi, \tag{4.86}$$

where $\phi(x)$ is the instantaneous phase. The variance of the phase difference can be found from the structure function for Kolmogorov turbulence,

$$D_\phi(\triangle x) = E\{(\phi(x) - \phi(x+\triangle x))^2\} \tag{4.87}$$

$$= 6.88\left(\frac{\triangle x}{r_0}\right)^{5/3}, \tag{4.88}$$

where r_0 is the turbulence coherence length and can be described as the effective diameter of the telescope imposed by the atmosphere. The spatial sampling $\triangle x$ has been chosen as

$$\Delta x = \frac{r_0}{3} \tag{4.89}$$

which corresponds to the phase difference being less than π radians 99.7% of the time.

The scintillation must be adequately sampled so that the detail determined by the inner-scale cutoff can be seen. The size of the scintillation is approximately given by the Fresnel length,

$$r_f = \sqrt{\lambda z}. \tag{4.90}$$

As the propagation distance, z, is increased the scale of the scintillation also increases. In this case $\triangle x$ has been chosen to be less than half of the smallest scale of the scintillation,

$$\triangle x \leq \frac{\sqrt{\lambda z}}{2}. \tag{4.91}$$

The sampling of the Fresnel propagation kernel, however, now requires a different analysis. The continuous Fresnel propagation kernel, Eq. (3.19), is of infinite bandwidth and so cannot be adequately sampled. However, once convolved with a Gaussian, it is both of finite extent and bandlimited in frequency (see Fig. 4.30). Thus once d is determined it is sufficient to ensure that the adjacent pixels differ by less than π at the smaller distance of d. Since d is equal to $W/2$ (half the effective width of $\hat{h}(x,y)$), the sampling requirement imposed by the need to adequately sample the Fresnel kernel is thus

$$\Delta x \leq \frac{\lambda z \beta}{W}. \tag{4.92}$$

The overall sampling rate corresponds to the minimum individual sampling rate required, from Eqs. (4.89), (4.91) and (4.92). As an example, where z is 10km, $\lambda = 589 \times 10^{-9}$m the wavelength of visible light, $D = 1$m, $\sigma = 0.005$m and $r_0 = 25$cm, the regularised kernel requires a sampling interval of 0.0052m. This corresponds to a maximum frequency that can be recovered of 95.46 cycles m^{-1}. From Eq. (4.85) the envelope of the spectrum has fallen

to 0.0111, confirming that there is indeed minimal aliasing. A further test was carried out by extending the effective width of $\hat{h}(x,y)$ to $8\sigma_w$, corresponding to the regularised kernel requiring a sampling interval of 0.0039m. Although the envelope of the spectrum has now fallen to 3.4×10^{-4}, no further reduction in aliasing is gained for the required increase in sampling rate.

4.2.6 Simulation of Kolmogorov scintillation

A variety of tests of the proposed technique were performed, ranging from simple visual tests to comparisons of simulated and theoretical results. The comparison of theoretical and simulated variance and covariance results necessary for the development of the SCIDAR technique was the main focus. Theoretical covariance curves are the basis functions for the SCIDAR technique, so a simulation approach that closely approximates these was required. Although tests of scintillation statistics based on spectra are often used in evaluating propagation techniques [50,109,110], spectral leakage effects are difficult to address when calculating spectra from non-periodic data. Lane *et al* [94] illustrate that the power law computed from a non-periodic phase screen decays as $|k|^{-2}$, instead of the $|k|^{-11/3}$ expected for a Kolmogorov spectrum, an effect attributable to spectral leakage.

The phase screens used in the simulations were generated using the improved midpoint displacement technique (see sections 4.2.3 to 4.2.6) providing considerable improvement in accuracy over the periodic realisations used in many of the other simulation techniques. The scintillation patterns for propagation distances of 2.5km, 5km, 7.5km and 10km, for $D/r_0 = 4$, are displayed in Fig. 4.31. The scintillation patterns do increase in size as expected as the propagation distance increases. As expected, no significant edge effects are present in the simulations.

The scintillation index or mean normalised variance numerically describes the percentage scintillation present. Accurate simulations must generate the appropriate scintillation levels for different propagation distances and turbulence strengths. Experimentally, the scintilla-

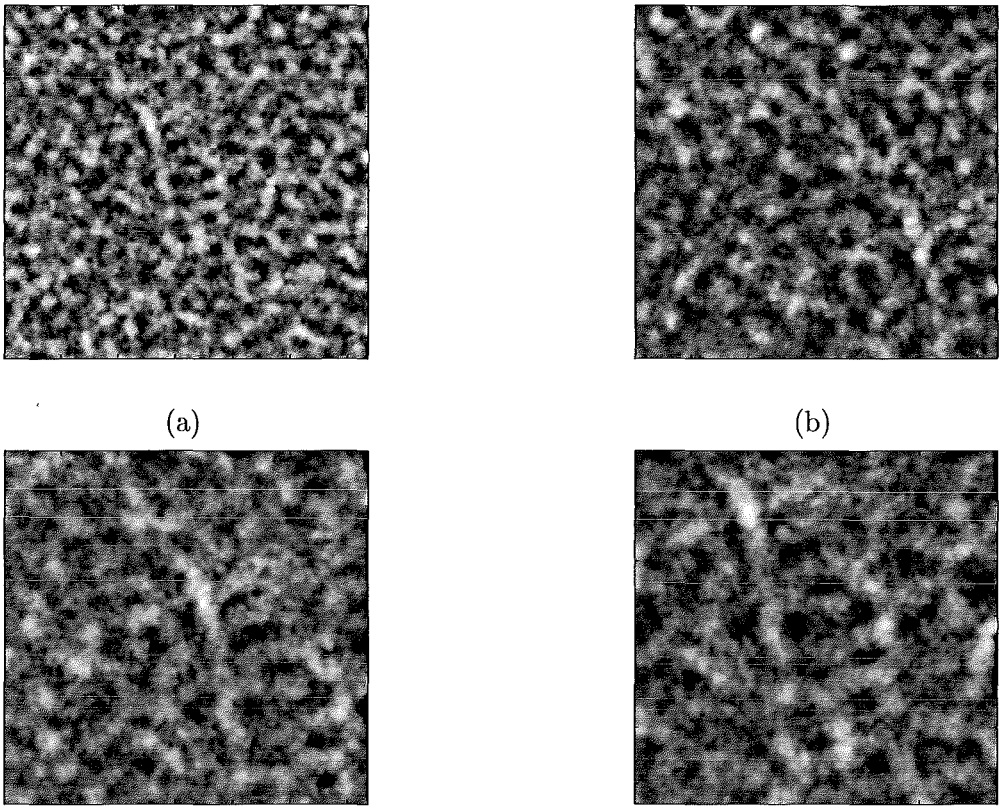

Figure 4.31: *Scintillation patterns for $\sigma = 0.003m$ and $D/r_0 = 4$ phase screens propagated over (a) 2.5km, (b) 5km, (c) 7.5km and (d) 10km.*

tion index can be calculated as

$$\sigma_I^2 = \frac{\langle I^2 \rangle - \langle I \rangle^2}{\langle I \rangle^2}, \tag{4.93}$$

where σ_I^2 is the mean normalised intensity variance [1] and I is the scintillation intensity. This can be compared to the analytic expression for the scintillation index, obtained by the Rytov approximation [1],

$$\sigma_I^2 = 19.12\lambda^{-7/6} \int_0^\infty h^{5/6} C_N^2(h) dh. \tag{4.94}$$

The Rytov approximation is valid for small perturbation theory only, that is for log normal variances of less than 0.3, and for $l_0 << \triangle x << L_0$, where l_0 and L_0 are the inner and outer scales of turbulence respectively. The convolution of the Fresnel propagation kernel with the Gaussian introduces discrepancies between the simulated and analytic σ_I^2 values. However,

as the user defined constant σ tends to zero, the Gaussian tends to a delta function and the modified convolution kernel tends to the original kernel. In addition, as σ is decreased, the sampling rate is increased and the simulated results tend towards the ideal results; the price being an increase in the computational processing required. A comparison of the simulated and analytic results is displayed in Fig. 4.32. These results confirm the effect of a non-zero Gaussian inner scale on the normalized scintillation variances as described by Davis and Walters [44].

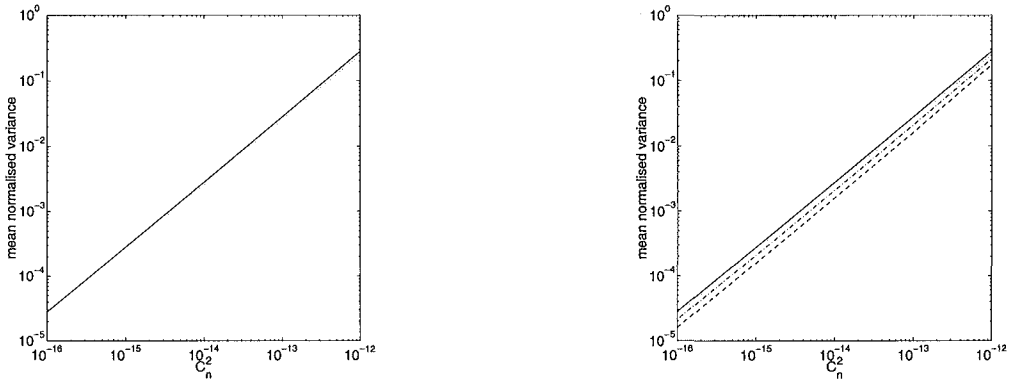

Figure 4.32: *Comparison of theoretical (solid) and simulated intensity variance results for propagation over 3km, $D = 1m$, $r_0 = 25cm$. (a) $\sigma = 0.002m$ (dotted). (b) $\sigma = 0.002m$ (dotted), $\sigma = 0.005m$ (dashed-dotted) and $\sigma = 0.008m$ (dashed).*

The final test performed was a comparison of the simulated and analytic covariance curves for single star scintillation. The covariance is given by the Fourier transform of the spatial power spectrum of the scintillation. The power spectrum in 1D is given by

$$W_S(f) = 0.039k^2 f^{-11/3} \int_0^\infty C_N^2(h)\sin^2(\pi\lambda h f^2)dh. \tag{4.95}$$

Fig. 4.33 shows a good match between the simulated and analytic results, provided σ is not too large. However, the errors introduced by smoothing can be modelled by convolving the true covariance with the autocorrelation of the smoothing kernel given in Eq. (4.80). This is shown in Fig. 4.34, which shows how smoothing improves the agreement between the theoretical and simulated results obtained at a considerably lower computational cost.

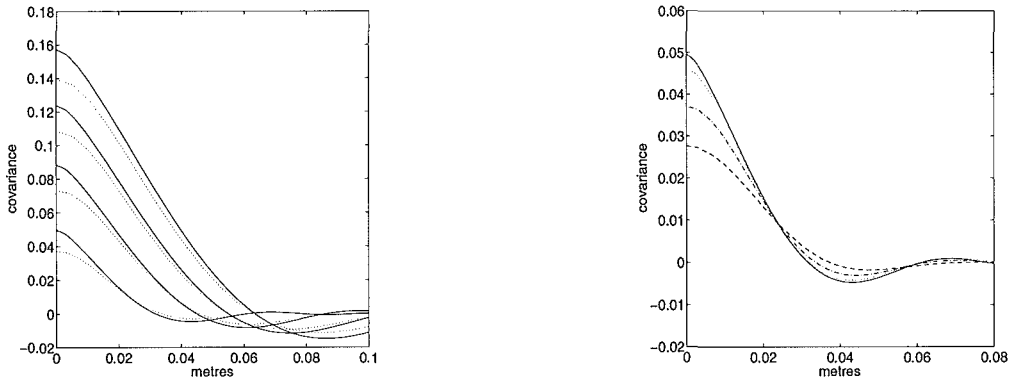

(a) (b)

Figure 4.33: *Comparison of theoretical (solid) and simulated covariance curves for $D = 1$m and $r_0 = 25$cm. (a) Propagation distances of 2.5km, 5km, 7.5km, 10km, $\sigma = 0.005$m (dotted, 2.5km lowest, 10km highest). (b) σ values of 0.002m (dotted), 0.005m (dashed-dotted), 0.008m (dashed) for a propagation distance of 2.5km.*

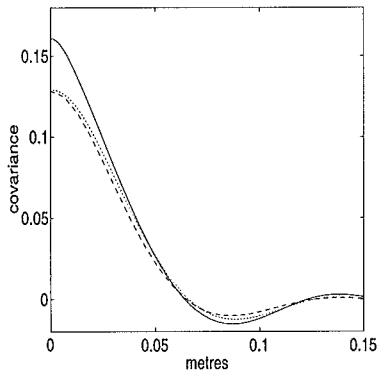

Figure 4.34: *Comparison of theoretical zero inner scale (solid), theoretical non-zero inner scale (dotted) and simulated covariance curves (dashed) for $D = 1$m, $r_0 = 25$cm, $\sigma = 0.008$ and a propagation distance of 10km. Note that the non-zero inner scale covariance is a smoothed version of the ideal result obtained by convolving the ideal result with the autocorrelation of the corresponding Gaussian smoothing term.*

4.2.7 Simulation of non-Kolmogorov scintillation

It is also possible to simulate scintillation with non-Kolmogorov statistics. The power spectrum of scintillation fluctuations is related to the power spectrum of phase fluctuations

by [134]

$$W_S(f) = 4W_\phi(f)\sin^2(\pi\lambda h f^2) \quad (4.96)$$

$$= 0.039k^2 f^{-\beta} \int_0^\infty C_N^2(h)\sin^2(\pi\lambda h f^2)dh, \quad (4.97)$$

where $\beta = 11/3$ once again corresponds to Kolmogorov statistics (see Eq. (4.95)). Hence,

$$W_\phi(f) \propto f^{-\beta} \quad (4.98)$$

corresponds to

$$W_S(f) \propto f^{-\beta}. \quad (4.99)$$

The scintillation covariances for β values of 9/3, 10/3, 11/3 and 12/3 were evaluated and are illustrated in Fig. 4.35 for $z = 5$km and $C_N^2 = 10^{-14}\text{m}^{-2/3}$. Although the general shape of the covariance curves is preserved as β is varied, the heights of the peaks differ considerably over the standard Kolmogorov statistics. Powers of 9/3 and 10/3 correspond to an increase in the peak heights, whereas a β of 12/3 produces a reduction.

One explanation for this difference is that the scintillation covariance is not a function of the tip-tilt component of the measured distortion. Phase distortions of equal strengths, but obeying different power laws contain different percentages of tip-tilt distortion. For example, 9/3 and 10/3 power laws contain a smaller percentage of tip-tilt distortion than Kolmogorov turbulence as illustrated in section 4.1.8. Whereas, a 12/3 power law defined in section 4.1.8 corresponds to a completely tip-tilt distortion. The scintillation covariance should, therefore, be zero as a wavefront passing through this type of distortion is shifted but not distorted. However, the evaluation of the Hankel transform of Eq. (4.97) for $\beta = 12/3$ indicates a non-zero covariance. Nevertheless, scintillation patterns corresponding to 9/3, 10/3 and 11/3 power laws, as illustrated in Fig. 4.36, clearly indicate a drop in scintillation with increasing β.

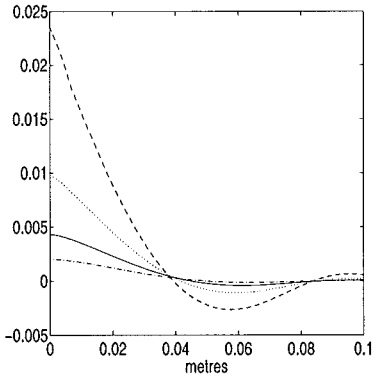

Figure 4.35: *Theoretical covariance spectra for β values of 9/3 (dashed), 10/3 (dotted), 11/3 (solid) and 12/3 (dashed-dotted).*

4.3 Summary

The simple spectral based techniques produced very inaccurate simulation results, whereas the more accurate technique of summing Karhunen-Loève functions proved to be very computationally expensive. The original midpoint method produced adequate phase structure function results, however the theory behind the method was not rigorous. A formal derivation of the original bilinear interpolator was presented as well as the extension to higher order interpolators. Another improvement over the original midpoint technique is the use of initial phase screens generated by expansion of the phase screen into basis functions.

The use of 4×4 interpolators and larger initial phase screens produced very accurate simulation results and as a result no advantage was gained in using interpolators past this size. No statistically significant deviations, from the ideal structure function for an ensemble of 10,000 screens, were seen with the 4×4 interpolator.

An investigation of existing propagation techniques was then needed to enable the improved phase screen simulations to be used to generate accurate scintillation. Many of the existing techniques used the physically unjustifiable assumption of the periodicity of the phase screen and the Fresnel kernel, a direct consequence of using spectral phase screen simulation techniques. The same approach applied to aperiodic phase screens, as simulated by the improved midpoint method, was limited by spectral leakage effects. The new technique of

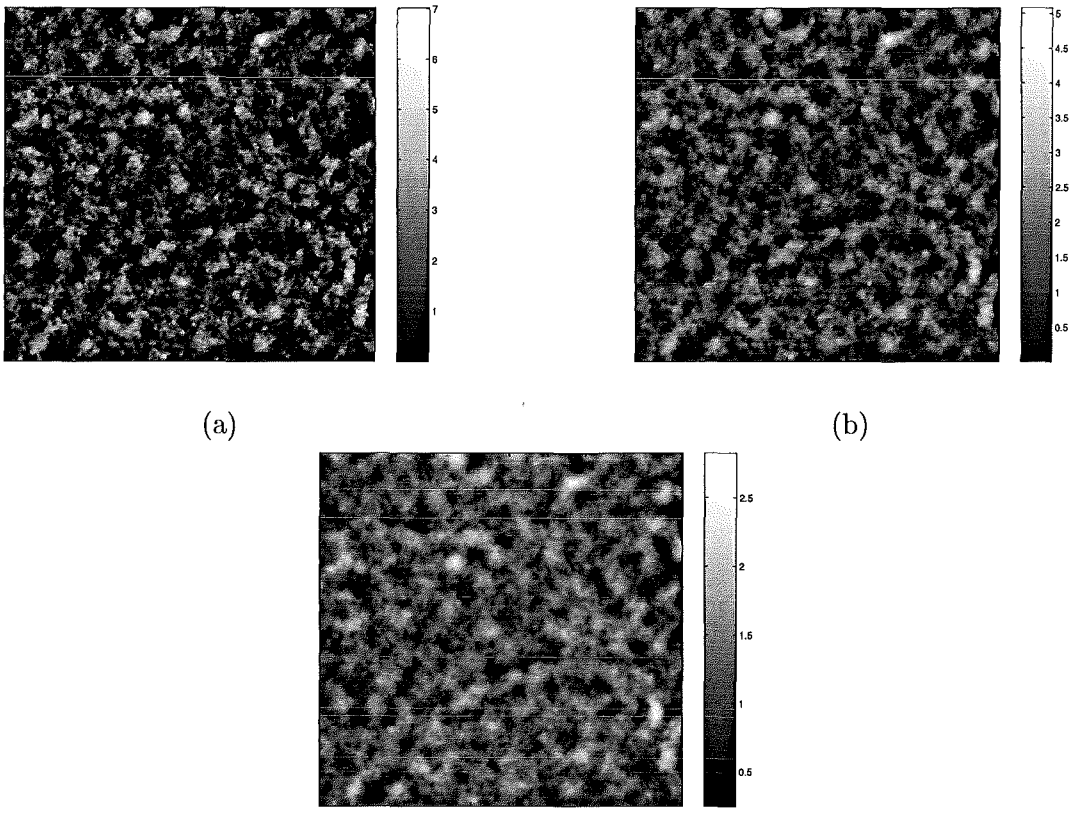

Figure 4.36: *Comparison of scintillation patterns for (a) 9/3, (b) 10/3 and (c) 11/3 power laws, corresponding to* $\sigma = 0.002$, $z = 5km$ *and* $D/r_0 = 4$.

convolving the Fresnel propagation kernel with the Gaussian was shown to produce accurate results from non-periodic phase screens, that were free from spectral leakage and unwanted edge diffraction effects.

The introduction of the Gaussian smoothing introduced some discrepancies between the simulated and theoretical results. However, the desired accuracy could be adjusted by altering the smoothing constant in the expression for the Gaussian term. This extra accuracy was at the expense of computational load since a decrease in σ led to a decrease in the spatial sampling, $\triangle x$, and a subsequent increase in N for a fixed aperture dimension, D. Although smoothing introduced a modelling error, the effect on the output was easily quantifiable since the smoothing and propagation were represented as a series of convolutions.

Finally, the new and improved techniques for the simulation of atmospheric turbulence and wavefront propagation through random media presented in this chapter produce simulations that accurately match the theory. The usefulness and accuracy of these techniques were confirmed by comparison of numerical simulation and analytic results. These results provide confidence in the generation of speckle and scintillation patterns to be used for testing and development of post processing and SCIDAR techniques presented in later chapters. In addition, these techniques can be easily extended to the simulation of non-Kolmogorov turbulence and scintillation.

Chapter 5

Enforcing Positivity in Deconvolution Problems

Real world images are often blurred or distorted in some way, for instance images captured by an out of focus camera or imaged through atmospheric turbulence. Even adaptive optics compensated images contain residual blurring. Deconvolution techniques attempt to remove the distortion when the blurring function, or an estimate of the blurring function, is available. Many techniques use *a priori* blur identification methods to estimate the blurring or PSF and then use conventional deconvolution to estimate the object. This chapter provides an introduction to the conventional deconvolution problem and its inversion to obtain positive reconstructions. When the blurring function is unknown, a blind deconvolution problem results. An introduction to the blind deconvolution problem and its solution is given in chapter 6.

Practically, the blurring process causes information to be lost. In this case it is necessary to incorporate additional information to enable the components of the problem to be estimated. In astronomical, or incoherent, imaging it is common to enforce positivity in an attempt to achieve the closest possible match to the actual object. This is because real intensities

cannot be negative, hence the components of the problem are positive, for example the incoherent PSF is the squared modulus of the coherent PSF. It is also necessary to regularise the deconvolution problem to enable its inversion in the presence of noise. Therefore, a variety of regularisation options are investigated. Deconvolution algorithms incorporating positivity and regularisation under the assumption of Gaussian, Poisson and mixed noise statistics are presented.

5.1 Introduction

Many problems in image processing can be represented by a linear convolution of the form

$$\begin{aligned} d(x,y) &= g(x,y) + n(x,y) \\ &= f(x,y) \odot h(x,y) + n(x,y) \end{aligned} \tag{5.1}$$

where $d(x,y)$ represents the observed data, $g(x,y)$ the noise free data, $f(x,y)$ the true image, $h(x,y)$ the space invariant point spread function, $n(x,y)$ the additive noise and $\odot$ the operation of convolution. Many astronomical imaging problems can be described by Eq. (5.1), where $f(x,y)$ represents a stellar object and $h(x,y)$ the space invariant or isoplanatic PSF which represents the instantaneous blurring introduced by the atmosphere. The deconvolution techniques presented here, however, are not restricted to astronomical problems, they find wide application as emphasised in later chapters of this thesis.

For practical purposes it is more convenient to consider a discretisation of Eq. (5.1), which can be represented in matrix form [3] as,

$$d = Hf + n \tag{5.2}$$

where the operation of convolution is implemented by a matrix multiplication with H, and f and d have been rasterised into vectors. In this matrix form $f(j)$ denotes a pixel within the image. Although this matrix form is used to illustrate the theory, in practice matrix multiplications such as Hf are more efficiently computed by the convolution of f and h using the FFT (see Appendix A).

When $d(x,y)$ and $h(x,y)$ are known, solving Eq. (5.1) for $\hat{f}(x,y)$ is considered a deconvolution problem. In practice the aim is to estimate $\hat{f}^{opt}$ when it is known to be both of a large, but finite, size and positive. Many solutions to this problem have been proposed. The simplest method for estimating $\hat{f}$ from d is that of inverse filtering, where the spectrum of $\hat{f}$ is given as [65]

$$\hat{F}(u,v) = \frac{D(u,v)}{H(u,v)}. \tag{5.3}$$

Note an uppercase quantity represents the Fourier transform of the corresponding lowercase quantity. However, this inversion is only possible in noiseless conditions since the solution breaks down for even a small amount of noise. As a result the Wiener filter was developed to take into account the noise, i.e. [65]

$$\hat{F}(u,v) = \frac{H^*(u,v)D(u,v)}{|H(u,v)|^2 + \frac{S_n(u,v)}{S_f(u,v)}}, \tag{5.4}$$

where $S_n(u,v)$ and $S_f(u,v)$ represent the power spectra of $n(x,y)$ and $f(x,y)$ respectively. Consequently the Wiener filter has a superior performance to the inverse filter, emphasising the need for the incorporation of *a priori* information relating to the problem. These simple Fourier domain based techniques, however, do not guarantee a positive solution and hence do not provide reconstructions which incorporate all available *a priori* information.

Due to the ill-posed nature of the deconvolution problem, the quality of the reconstruction depends on the assumed noise statistics and the available object prior information. When only the noise statistics of the problem are assumed, it becomes one of maximum-likelihood. In this case the resulting object estimate is the one which best fits the data according to the assumed noise model. For example, astronomical images suffer from image dependent photon noise modelled by Poisson statistics. In addition, digital images are corrupted by image independent sensor noise described by Gaussian statistics. Images that contain both forms of noise, and hence are not adequately described by either model, can be described by a mixed noise model. Whether $n(x,y)$ is modelled as resulting from a Gaussian, Poisson or mixed noise process has a significant effect on the resulting deconvolution algorithm, since it is noise that proves the major limitation to the ability to perform deconvolution. Generally knowledge of the noise model alone is not sufficient to produce a meaningful

solution. Extra prior information about the object is necessary to constrain the solution away from unrealistic and undesirable object estimates.

Common forms of prior information include positivity and energy constraints, and are incorporated into the algorithms presented here. Since enforcing positivity is particularly relevant in astronomical applications, many techniques have been proposed to achieve this. These existing methods, however, can lead to the introduction of local minima and non-convergence, both of which should be avoided. There are many possible approaches to this problem, but the aim is a technique that has guaranteed and rapid convergence. This led to an improved technique for enforcing positivity in deconvolution applications, based on quadratic programming. The resulting algorithms produce monotonically decreasing error functions and guaranteed convergence.

This improved technique for enforcing positivity is developed for the assumption of Gaussian noise statistics so algorithms such as the Richardson-Lucy which assume Poisson noise are inappropriate [49,143,157]. However, extension to Poisson and mixed noise statistics is also investigated (see section 5.6). The basic quadratic programming approach implemented for Poisson noise statistics is impractically slow. Acceleration of the Poisson noise algorithm led to the development of a modified Richardson-Lucy algorithm which is shown to overcome many of the problems associated with the well-established standard algorithm.

Another limitation of deconvolution techniques is the requirement of an accurate characterisation of the blurring function or PSF. An inaccurate or incorrect PSF prevents the desired compensation being achieved. The extension to blind deconvolution, the estimation of both the blurring and the object, is a solution to this problem and is investigated in chapter 6.

An introduction to prior information is provided in section 5.2 and includes detailed sections on the assumed noise statistics, regularisation and positivity. The quadratic programming formulation of the deconvolution problem under the assumption of Gaussian noise statistics is introduced in section 5.3. Section 5.4 investigates methods for accelerating the standard quadratic programming method resulting in a number of practical algorithms. The perfor-

mance of these algorithms is illustrated in section 5.5. The extension to Poisson and mixed noise statistics is given in section 5.6. A modified Richardson-Lucy algorithm is outlined in section 5.7 and demonstrated in section 5.8. Finally a summary is presented in section 5.9.

5.2 Prior information

The prior information relevant to deconvolution problems can be divided into two areas; the assumed noise statistics and the object prior information.

5.2.1 Noise statistics

The assumption of a statistical distribution for the noise requires the formulation of the deconvolution problem in terms of statistics. The maximum *a posteriori* (MAP) solution to the deconvolution problem described by Eq. (5.1) can be considered the estimation of the most likely object estimate, $\hat{f}(x,y)$, given the observed data, $d(x,y)$. Mathematically this can be expressed as

$$\max_{\hat{f}} P\{\hat{f}(x,y)|d(x,y)\} \tag{5.5}$$

where $P\{x\}$ denotes the probability of x and a circumflex indicates an estimated quantity. Using Bayes' rule (Eq. (2.115)),

$$P\{\hat{f}(x,y)|d(x,y)\} = \frac{P\{d(x,y)|\hat{f}(x,y)\}P\{\hat{f}(x,y)\}}{P\{d(x,y)\}}. \tag{5.6}$$

Taking the logarithms and discarding terms that are not a function of $\hat{f}(x,y)$ results in the log-likelihood equation

$$\ln[P\{\hat{f}(x,y)|d(x,y)\}] = \ln[P\{d(x,y)|\hat{f}(x,y)] + \ln[P\{\hat{f}(x,y)\}]. \tag{5.7}$$

The first term describes the fit to the assumed noise statistics and the second term describes the likelihood of the object according to the available prior information. If only the first term in Eq. (5.7) is maximised, i.e.

$$\max_{\hat{f}} \ln[P\{d(x,y)|\hat{f}(x,y)\}] \tag{5.8}$$

this becomes the maximum-likelihood (ML) solution and requires knowledge of the noise statistics only.

The log-likelihood corresponding to the assumption of Gaussian noise statistics is

$$ML_g = -\frac{1}{2}\sum_{(x,y)}\left[\frac{(d(x,y)-\hat{g}(x,y))^2}{\sigma^2}\right]. \tag{5.9}$$

The maximisation of ML_g is also equivalent to the minimisation of

$$E = \|d - \hat{f} \odot h\|^2 \tag{5.10}$$

where $\|x\|$ denotes the L_2 norm of x and Eq. (5.10) is known as the *least squares* solution. In vector-matrix form this becomes

$$E = \|d - H\hat{f}\|^2. \tag{5.11}$$

The assumption of Poisson noise statistics leads to the following log-likelihood function

$$ML_p = \sum_{(x,y)}\left[d(x,y)\ln\left[\hat{g}(x,y)\right] - \hat{g}(x,y)\right]. \tag{5.12}$$

Finally, the mixed noise statistics model is described by a log-likelihood ML_m defined as

$$ML_m = -\frac{1}{2}\sum_{(x,y)}\left[\frac{(d(x,y)-\hat{g}(x,y))^2}{\hat{g}(x,y)+\sigma^2}\right]. \tag{5.13}$$

In each case the theory defines a likelihood function to be maximised or an error function to be minimised. A variety of techniques exist for performing the required minimisations and maximisations. Steepest descent, optimal step length steepest descent, conjugate gradient and non-linear conjugate gradient methods are all used throughout this thesis. An outline of these techniques can be found in Appendix A.

These techniques for optimisation are based on calculating the ML gradients with respect to $\hat{f}(x,y)$:

$$\frac{\partial ML_g}{\partial \hat{f}(x,y)} = \sum_{(x,y)}\left(\frac{d(x,y)-\hat{g}(x,y)}{\sigma^2}\right) * h(x,y) = \sum_{(x,y)}\frac{\hat{n}(x,y)}{\sigma^2} * h(x,y) \tag{5.14}$$

$$\frac{\partial ML_p}{\partial \hat{f}(x,y)} = \sum_{(x,y)} \left(\frac{d(x,y) - \hat{g}(x,y)}{\hat{g}(x,y)} \right) * h(x,y) = \sum_{(x,y)} \frac{\hat{n}(x,y)}{\hat{g}(x,y)} * h(x,y) \quad (5.15)$$

$$\frac{\partial ML_m}{\partial \hat{f}(x,y)} = \sum_{(x,y)} \left(\frac{d(x,y) - \hat{g}(x,y)}{\hat{g}(x,y) + \sigma^2} \right) * h(x,y) = \sum_{(x,y)} \frac{\hat{n}(x,y)}{\hat{g}(x,y) + \sigma^2} * h(x,y) \quad (5.16)$$

where $\hat{n}(x,y) = d(x,y) - \hat{g}(x,y)$ represents the difference between the estimate of the observed data and the noise free data and thus corresponds to the current estimate of the noise. These gradients differ only in the denominator, which in each case represents the assumed noise variance. In the case of Gaussian noise the denominator is constant and hence well suited to image independent sensor noise. The choice of a Gaussian model enables a computationally efficient minimisation. The assumption of Poisson noise statistics accurately models the image dependent photon nature of light. This is reflected in the denominator which varies as the estimate varies. Although the Poisson noise model is often the best model of low light level imaging [143], it is less robust to modelling errors than a Gaussian noise model [91]. For example, if the sensor produces spurious noise far from the actual location of $g(x,y)$, then $\hat{g}(x,y)$ is forced to be non-zero, since a zero mean Poisson process is identically zero. This distortion of $\hat{g}$ causes significant errors in $\hat{f}$ and $\hat{h}$. A further problem with the Poisson noise model is that the noise variance varies with $\hat{g}(x,y)$, exacerbating the non-linearity of the problem. However, Poisson statistics can be modelled as a Gaussian process with a spatially differing variance. The mixed noise model incorporates both image dependent and independent noise and so seems well suited to astronomical imaging where images can suffer from both photon and sensor noise.

The matched filter, introduced in chapter 2, is designed for the optimum detection of a transmitted pulse in the presence of noise. It achieves this by maximising the output signal to noise (SNR), accentuating the signal and suppressing the noise, although other criteria such as maximum-likelihood will also yield the form of the matched filter [22]. In the context of image processing, the matched filter is a spatial filter that provides an output measure of the spatial correlation between an input image and a reference image [126]. The gradients in Eqs. (5.14) to (5.16) correspond to the division of the estimated noise by the noise variance and the subsequent correlation of this result with the PSF. This division gives a larger weighting to pixels in the correlation with less noise in a manner consistent with that

of a matched filter.

For large $\hat{n}(x,y)$, indicating the presence of large amounts of noise, the maximum-likelihood solutions are unstable. This inherent ill-conditioning of the deconvolution problem results in the possibility of noise induced fluctuations in $\hat{f}(x,y)$, introducing a tendency to move away from the solution. Hence, the resulting estimates are unsatisfactory and not uniquely defined [158]. This numerical instability of the inversion of Eq. (5.1) can be dealt with by incorporating regularisation, discussed in some detail in section 5.2.2 below, which converts the ill-posed problem to a well-posed problem that can be solved, with the advantage that the solution of the well-posed problem tends to the solution of the ill-posed problem as the noise tends to zero.

5.2.2 Regularisation

The blind deconvolution problem is inherently ill-conditioned [158] and as a result its inversion can lead to unacceptable noise amplification. In the presence of noise, the solution is very unstable. Small changes in the data can lead to a large change in the solution. These oscillations can be suppressed by early termination of the conjugate gradient iteration, use of Tikhonov-Miller regularisation or by application of a positivity constraint [35].

Regularisation, a prior statement of the energy or smoothness of the solution, is a practical solution to the ill-conditioning of the deconvolution problem. Incorporating regularisation alters the error function to be minimised to:

$$E = -ML_{(g,p,m)} + \gamma \|\hat{f} \odot c\|^2 \tag{5.17}$$

where c is the regularisation operator and γ the regularisation weighting which determines the tradeoff between the importance of the fit to the data and the regularisation. The addition of the extra term in Eq. (5.17) acts as a stabilising term, penalising deviations from the solution caused by noise, when it is desired to ensure the smoothness of the solution. The operator c is often chosen to be equivalent to convolving with a Laplacian [180]. An alternative used here is to define c as being equivalent to convolving with a delta function.

This results in standard Tikhonov-Miller regularisation, which defines an energy constraint on the problem. This is still sufficient to regularise the solution and is more consistent with point sources than the Laplacian.

In general, the solution can also suffer from null-objects. These are artifacts in the image that do not affect the observed data. For example, a null-object of f denoted here by k has the property that

$$k \odot h = 0. \tag{5.18}$$

Incorporating regularisation requires adding extra terms to the error function, e.g. $\gamma \| \hat{f} \odot c \|^2$ for conventional deconvolution. Addition of these terms effectively removes these artifacts since the presence of null-objects increases the $\gamma \| \hat{f} \odot c \|^2$ term without affecting how well the solution matches the observed data d. Hence a solution containing null-objects does not minimise the error. The regularisation parameter, γ, is often set equal to the noise to signal ratio for conventional deconvolution [82], i.e.

$$\gamma = \frac{\|n\|^2}{\|f\|^2} \tag{5.19}$$

where $\|n\|^2$ is the noise power and $\|f\|^2$ the signal power.

Another approach that can be used for the regularisation of Eq. (5.1) is the use of of maximum entropy (ME) techniques which not only regularise the problem but also guarantee a positive solution. The maximum entropy method works very well if the reconstruction is required to be peaky with a flat baseline [120] and is reported to produce positive solutions with very few artifacts. The most common form of entropy used for this type of inversion problem is Shannon's entropy, where the entropy term $-\hat{f} \ln \left[\hat{f} \right]$ is added to Eq. (5.10) to give

$$E = -ML_{(g,p,m)} - \gamma \hat{f} \ln \left[\hat{f} \right]. \tag{5.20}$$

Another common form of entropy is the $\ln \left[\hat{f} \right]$ formulation. However, as noted by Nityananda and Narayan [120], the choice of an entropy function can be viewed as a prior statement about the desired shape of the peaks in the reconstruction. They show that the entropy functions $-\hat{f} \ln \left[\hat{f} \right]$ and $\ln \left[\hat{f} \right]$ are members of a family of entropy functions, where $-\hat{f} \ln \left[\hat{f} \right]$

is considered a soft form of the entropy function producing positive reconstructions with flat baselines but relatively wide Gaussian shaped peaks. This result is characteristic of a soft function which only affects low-level features, leaving the peaks relatively unsharpened. The properties of this choice of entropy have resulted in the ME reconstructions being labelled as smooth and featureless.

5.2.3 Object prior information

Prior information is used to select a specific solution or subset of solutions from the sometimes infinite set of possible solutions. Prior information for the object can take many forms, however, care should be taken to ensure that only realistic assumptions are made to avoid fitting the prior information instead of the data.

Real intensities cannot be negative, therefore, it is reasonable to constrain the object reconstructions to be non-negative. This is essentially the same as imposing a lower bound on the reconstruction. Energy and smoothness constraints are also popular and are used to regularise the problem. Tikhonov-Miller regularisation provides a prior statement about the energy contained in the solution, whereas maximum entropy (ME) techniques can be used to produce smooth reconstructions. Other forms of object prior information include conservation of light energy, support constraints and upper bounds. It is easy to measure the total number of photons when imaging with a charge-coupled device (CCD), so conservation of light energy is a commonly used constraint, provided noise is taken into account. When the extent of an object is known a support constraint can be used, here the object is constrained to be within the known support. Although a powerful constraint, it can be difficult to determine in practice. Upper bounds on the object intensity can also be used to constrain the solution, just as positivity can be considered to be a lower bound on image intensity. Once again this information can be hard to obtain, but can sometimes be estimated from the illumination source and some crude knowledge of the object properties. There also exist many other ad-hoc priors that have been used to constrain the object, for example the penalty term of Schulz [143].

5.2.4 Existing methods for enforcing positivity

One of the common techniques for ensuring positivity of $\hat{f}$ in Eq. (5.11) is by reparameterisation, for example by using a square reparameterisation $\hat{f} = \hat{\phi}^2$ [157]. However, reparameterisation has the effect of distorting a parabolic error surface (see Fig. 5.1(a)) having a single well defined global minimum, to a more complicated surface which may have local minima (see Fig. 5.1(b)). In the case of a squared reparameterisation $\frac{\partial E}{\partial \hat{\phi}} = 2\hat{\phi}\frac{\partial E}{\partial \hat{f}}$, hence $\frac{\partial E}{\partial \hat{\phi}} = 0$ does not imply $\frac{\partial E}{\partial \hat{f}} = 0$. Monotonic reparameterisations are also possible, for example the exponential reparameterisation, $\hat{f} = \exp(\hat{\phi})$ (see Fig.5.1(c)) with $\frac{\partial E}{\partial \hat{\phi}} = \hat{f}\frac{\partial E}{\partial \hat{f}}$ [36]. It should be noted that for both the squared and exponential reparameterisations once a pixel value goes to zero it remains zero because the original gradient is multiplied by either $\hat{f}$ or $\hat{\phi}$. Figs. 5.1(b) and (c) illustrate that both the reparameterisations presented here have a zero derivative, or slope, for significant regions of the minimisation surface, which can make minimisation of the function difficult. As a consequence reparameterisation techniques have not been considered, since, although they have been used successfully, it is difficult to assure convergence.

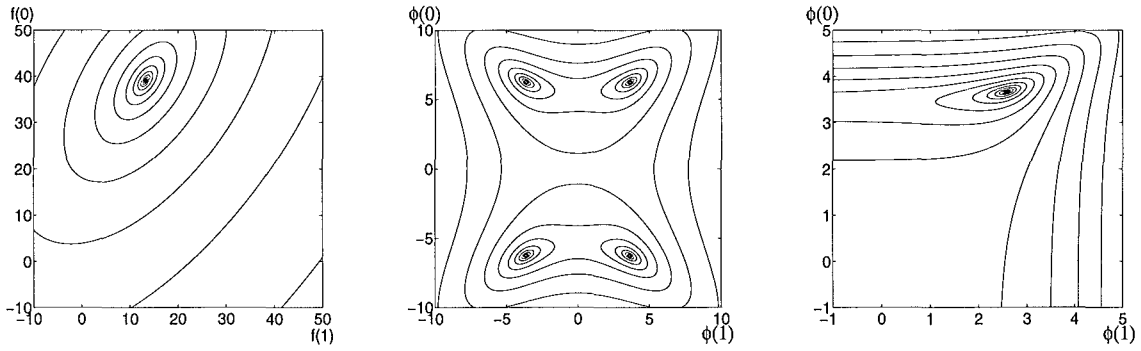

(a) (b) (c)

Figure 5.1: *Contour maps for two-pixel images. (a) Standard parabolic error surface. (b) Squared reparameterisation of surface in (a). (c) Exponential reparameterisation of surface in (a).*

5.3 Quadratic programming

The assumption of Gaussian noise on the observations leads to the minimisation of

$$E(\hat{f}) = ||d - H\hat{f}||^2 + \gamma||C\hat{f}||^2 \tag{5.21}$$

as a means for estimating $\hat{f}$. Here C is the rasterised form of the regularisation operator $c(x, y)$. The first term ensures that the estimate of the solution, $\hat{f}$, gives a good fit to the the observed data, d, while the second term is needed to regularise the solution [17]. Under the assumption of Gaussian noise statistics E defines a convex error surface, the minimum of which can be reached by using standard steepest descent or conjugate gradient routines.

The problem of minimising Eq. (5.21) is equivalent to the minimisation of

$$\frac{1}{2}\hat{f}^T Q\hat{f} - \hat{f}^T b \tag{5.22}$$

subject to

$$\begin{aligned} \hat{f}(j) &\geq 0, \quad \forall j \in S \\ \hat{f}(j) &= 0, \quad \forall j \notin S \end{aligned} \tag{5.23}$$

where S is the set of points for which $\hat{f}(j)$ may be non-zero, i.e. the support of f, $Q = H^T H + \gamma I$ when using Tikhonov-Miller regularisation and $b = H^T d$. When written this way, a positively constrained deconvolution becomes a quadratic programming problem. However standard solutions to such a problem need to be adapted to the specific problems of deconvolution.

Without constraints, minimisation of E with respect to $\hat{f}$ yields,

$$\hat{f}^{opt} = (H^T H + \gamma I)^{-1} H^T d. \tag{5.24}$$

It should be noted that the unconstrained problem described in Eq. (5.24) can be diagonalised into a discrete Fourier basis and therefore solved directly using a Wiener filter [78].

The correct approach to solving for $\hat{f}^{opt}$ when some pixels are known *a priori* to be zero is to solve the problem only on the subset of pixels that are known to be non-zero. Perhaps

surprisingly, this does not give the same solution as solving the unconstrained solution and setting the pixels to zero. To demonstrate this point, consider a hypothetical contour map for E for a two-pixel image (Fig. 5.2(a)). The point x in Fig. 5.2(a) corresponds to the optimal unconstrained solution, and the point y corresponds to the optimal solution if $\hat{f}(1)$ is known *a priori* to be equal to zero. The point z is the solution found by setting $\hat{f}(1)$ to zero in the optimal unconstrained solution.

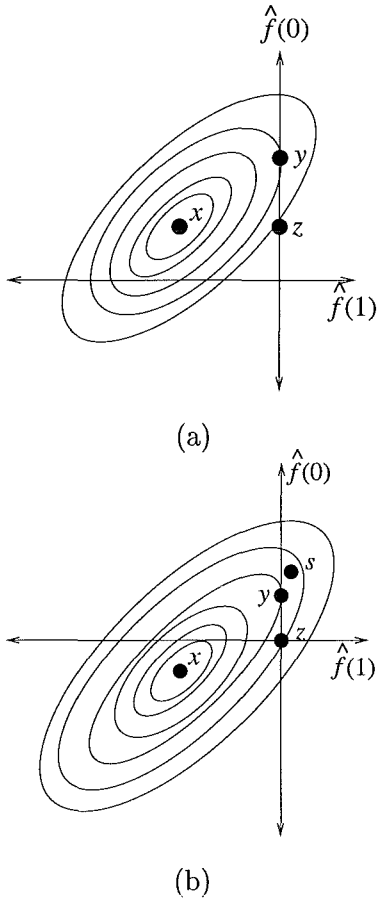

Figure 5.2: *Contour maps for two-pixel images. (a) The variable x represents the optimal unconstrained solution and y the optimal constrained solution, when $\hat{f}(1)$ is constrained a priori to be zero. Whereas, z corresponds to setting $\hat{f}(1) = 0$ in the unconstrained solution. (b) The variable x again represents the optimal unconstrained solution and y the optimal constrained solution. However, z is now the result of setting the negative pixels in the unconstrained solution to zero. Note that z returns a higher error value that the starting point, s.*

Mathematically this solution is achieved over the non-zero pixels of $\hat{f}$ by defining a vector $\hat{q}$ that comprises only the non-zero pixels of $\hat{f}$. These two vectors are related by the $N \times M$ matrix D, where N is the number of pixels in $\hat{f}$ and M is the number of pixels in $\hat{q}$. D is formed by deleting every column of an $N \times N$ identity matrix that would multiply an element of $\hat{f}$ that is known *a priori* to be zero. Thus $\hat{f} = D\hat{q}$ and $\hat{q} = D^T\hat{f}$. It is therefore necessary to minimise

$$E(\hat{q}) = ||d - HD\hat{q}||^2 + \gamma||D\hat{q}||^2, \tag{5.25}$$

and the corresponding optimal solution for $\hat{f}$ is given by

$$\hat{f}^{opt} = D(D^T(H^TH + \gamma I)D)^{-1}D^TH^Td. \tag{5.26}$$

Eq. (5.26) cannot be solved directly using a Wiener filter, but can still be solved using a conjugate gradient technique based on FFTs described in Appendix A.

When $\hat{f}$ is constrained to be positive, a solution where

$$\begin{aligned} \hat{f}^{opt}(j) &\geq 0 \ \ \forall j \\ \frac{\partial E}{\partial \hat{f}^{opt}} &= 0 \ \ \forall \hat{f}^{opt}(j) > 0 \\ \frac{\partial E}{\partial \hat{f}^{opt}} &\geq 0 \ \ \forall \hat{f}^{opt}(j) = 0 \end{aligned} \tag{5.27}$$

is required, with the gradient $\frac{\partial E}{\partial \hat{f}}$ given by

$$\frac{\partial E}{\partial \hat{f}} = 2((H^TH + \gamma I)\hat{f} - H^Td). \tag{5.28}$$

Thus every point $\hat{f}(j)$ must be either positive or zero. When it is positive the constraint is inactive and $\frac{\partial E}{\partial \hat{f}}$ must be zero. When $\hat{f}(j)$ is zero, $\frac{\partial E}{\partial \hat{f}}$ must be non-negative, so that if $\hat{f}(j)$ deviates from zero it either violates the positivity constraint or increases E.

The conventional way of dealing with inequality constraints in quadratic programming is by using the concept of an active set of pixels. This effectively partitions the inequality constraints into active constraints, for which it is assumed $\hat{f}(j) = 0$, and inactive constraints for which the constraint is ignored. Once a set of active constraints is assumed this defines a D matrix, enabling $\hat{f}^{opt}$ to be found by solving Eq. (5.26). The D matrix is defined by

removing the columns of an $N \times N$ identity matrix corresponding to the active set of pixels. The problem then becomes the determination of the correct active set. The advantage of this technique is that a pixel that has been set to zero can be reintroduced into the solution set. Consider the error surface for a two-pixel image illustrated in Fig. 5.3. Starting from point A, the minimum when the inactive set contains only pixel $\hat{f}(1)$ is at $\hat{f}(1) = 0$ and is denoted by B. If this pixel is removed from the inactive set and pixel $\hat{f}(0)$ added, the minimum over this set is at point C. Finally, when pixel $\hat{f}(1)$ is reintroduced to the inactive set, the global minimum at D is obtained.

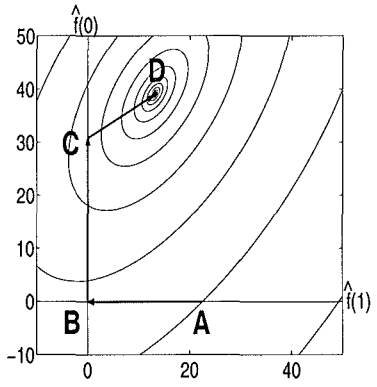

Figure 5.3: *Contour map for a two-pixel image. When the minimum is found using the active sets approach the path to the minimum is in the order A, B, C, D, illustrating that a pixel with a zero value can be reintroduced into the solution set.*

The following algorithm is guaranteed to find the correct active set and converge to the overall constrained optimum in a finite number of steps:

Step 1.

Start with an initial estimate $\hat{f}^{(k)}$, where $k = 0$. Define the initial active set to be all the pixels that are known *a priori* to be zero, that is all the pixels outside the support of f.

Step 2.

Using the current active set to define D, solve for $\tilde{f}^{(k)}$ using Eq. (5.26).

Step 3.

If any pixel of $\tilde{f}^{(k)}$ is negative, update $\hat{f}^{(k)}$ using

$$\hat{f}^{(k+1)} = \hat{f}^{(k)} + \alpha^{(k)}(\tilde{f}^{(k)} - \hat{f}^{(k)}) \tag{5.29}$$

where $\alpha^{(k)}$ is the largest value in the range $0 < \alpha^{(k)} \leq 1$ that ensures $\hat{f}^{(k+1)}$ is positive. Unless $\alpha^{(k)} = 1$ this results in one or more pixels of $\hat{f}^{(k+1)}$ becoming zero.

Step 4.

If $\alpha^{(k)} < 1$, in step 3, then add one of the pixels that has become zero to the active set. If $\alpha^{(k)} = 1$ evaluate $\frac{\partial E}{\partial \hat{f}}$ on the pixels that are in the active set but still inside the support of f. If for any of these pixels $\frac{\partial E}{\partial \hat{f}(j)} < 0$ the pixel with the most negative value of $\frac{\partial E}{\partial \hat{f}(j)}$ is deleted from the active set.

Step 5.

If the active set was not altered by step 4, set $\hat{f}^{(opt)} = \tilde{f}^{(k)}$ and finish, otherwise return to step 2.

The convergence of this algorithm is demonstrated in Luenberger [106], with the proof based on the fact that since the error decreases at every stage of the algorithm, it is impossible to return to a previous active set. Since there are only a finite number of possible active sets, and an unconstrained minimisation can be solved in a finite number of steps by the conjugate gradient algorithm, the overall problem can be solved in a finite number of steps.

The difficulty with this approach is that, although it guarantees convergence, it requires performing an unconstrained minimisation in order to change a single constraint in the active set. This approach has been implemented and the monotonic convergence confirmed, but for a realistic example an impractical number of iterations were required.

5.4 Accelerating the quadratic programming approach

The quadratic programming technique, although having the desirable property of assured convergence is too slow to be used in practice. There are two obvious ways that the convergence can be accelerated. First, it is advantageous to identify more than one change to the active constraint set at step 4, since although there is a finite number of possible active sets this number is very large for a realistic image. Second, it is desirable to reduce the computation involved in minimising E, in step 2, before moving to a new active set.

5.4.1 Improving the active set selection

One method for identifying a new active constraint set is by projection. Defining a projection operation by

$$P[\hat{f}(j)] = \begin{cases} \hat{f}(j) & \hat{f}(j) > 0 \\ 0 & \text{otherwise} \end{cases}, \tag{5.30}$$

one can simply update by projection at step 3, $\hat{f}^{(k+1)} = P[\tilde{f}^{(k)}]$. In step 4, the new active set is now defined by all points which are outside the support of $\hat{f}$ and all points in S for which $\frac{\partial E}{\partial \hat{f}(j)} > 0$.

Unfortunately, projecting $\tilde{f}^{(k)}$ can cause the error E to increase. How this arises is shown in Fig. 5.2(b), which gives the contour map for E for a two-pixel image. The point x corresponds to the optimal unconstrained solution, and the point y corresponds to the optimal solution if the image is known to be positive. The point z illustrates the solution found if negative values in the unconstrained solution for $\hat{f}$ are set to zero. The E corresponding to point z is in fact higher than the E corresponding to a possible starting point, s.

The algorithm of Nakamura *et al* [117] combines projection with the accelerated constraint selection outlined above. However, it does not guarantee that each new point strictly reduces the value of the error function. As a result it may oscillate between minimisation on two different sets of constraints, which may lead to an increase in E from one iteration to the next.

The fact that changing the active set can increase E means that the global convergence inherent in the quadratic programming technique is lost. However, if $\hat{f}^{(k+1)}$ is updated in step 3 using

$$\hat{f}^{(k+1)} = P\left[\hat{f}^{(k)} + \alpha^{(k)}\left(\tilde{f}^{(k)} - \hat{f}^{(k)}\right)\right], \tag{5.31}$$

where $\alpha^{(k)}$ is a step size parameter that is selected to ensure that $E(\hat{f}^{(k+1)}) < E(\hat{f}^{(k)})$, then the property of theoretical convergence remains assured, since the addition of the linesearch in Eq. (5.31) guarantees a monotonic decrease in E. Due to the non-linear nature of the projection step in Eq. (5.31), $\alpha^{(k)}$ must be found by a linesearch technique. Note that the $\hat{f}^{(k+1)}$ found by quadratic programming lies on the line defined by Eq. (5.31) when $\alpha^{(k)}$

is varied. As a consequence the $E(\hat{f}^{(k+1)})$ resulting from an accurate linesearch for $\alpha^{(k)}$ cannot be greater than the E corresponding to $\hat{f}^{(k+1)}$ calculated using the conventional quadratic programming approach.

5.4.2 Reducing computation in a single active set

In order to assure convergence in a finite number of steps quadratic programming requires that E be minimised on the current active set at step 2. Although it is known that the conjugate gradient approach will solve this problem in a finite number of iterations, in practice the most significant reduction in error occurs during the first iterations [106]. Therefore, a more practical approach is to terminate the conjugate gradient minimisation at $\mathcal{N}$ iterations, where $\mathcal{N}$ is considerably less than the N^2 iterations which guarantee the minimum.

Moving to a new constraint set before reaching the minimum on the current constraint set, makes it possible, although unlikely, for the algorithm to return to a previous constraint set. However, the repeated application of $\mathcal{N}$ conjugate gradient iterations on a given constraint set is equivalent to the partial conjugate gradient method which is known to be convergent [106], although not in a finite number of steps. This new approach guarantees only monotonic convergence as opposed to the finite convergence of the conjugate gradient method. In practice, however, not only does this approach converge much more quickly, but it does not return to a previous constraint set.

5.4.3 Practical algorithms

Four alternative techniques for performing deconvolution are considered. The first approach is to use steepest descent to reduce E, at step 2, i.e.

$$\tilde{f}^{(k)} = \hat{f}^{(k)} - \beta^{(k)} \frac{\partial E}{\partial \hat{f}^{(k)}}. \tag{5.32}$$

For projected steepest descent, provided $\beta^{(k)}$ is restricted such that

$$\beta^{(k)} < \frac{2}{\|Q\|}, \tag{5.33}$$

where $\|Q\|$ denotes the matrix norm of Q, then convergence can be assured [125] by minimising over all image pixels not a selected subset of pixels. Although convergence may be guaranteed using Eq. (5.33), faster convergence was obtained by choosing $\beta^{(k)}$ to minimise E again at the expense of assured convergence. This was achieved by using only a single conjugate gradient iteration at step 2, corresponding to optimal step length steepest descent, and use of projection to update $\hat{f}^{(k+1)}$ as outlined in Eq. (5.30). No additional linesearch is implemented in this method and if a pixel goes negative it is set to zero by the projection operation. This algorithm is referred to as projected optimal steepest descent, and it is representative of the speed that can be expected from steepest descent algorithms.

The second approach is to terminate the conjugate gradient minimisation, in step 2, at a fixed $\mathcal{N}$ iterations and again use projection to update $\hat{f}^{(k+1)}$. The minimisation is performed using the accelerated active set selection method. Here any problems that may occur when $\tilde{f}^{(k)}$ is projected are ignored. Although, the convergence of E may be erratic, there is no computational expense incurred in performing a linesearch. This technique is referred to as Nakamura's method after the original proposers of the matrix form of this algorithm.

Experience with Nakamura's algorithm indicates that, although the decrease in E cannot be guaranteed, in practice it usually both converges and identifies the active constraints quickly. Modification of this algorithm to provide assured convergence to enhance its utility is sought. Of particular interest are blind deconvolution algorithms, because these algorithms, discussed in chapter 6, often rely on alternating between estimating $\hat{f}$ and $\hat{h}$ as the solutions to linked conventional deconvolution problems [96,179]. Therefore, it is important that each stage of this process has reliable convergence and that pixels are not permanently removed from the solution set.

The third or weak linesearch approach also terminates the conjugate gradient minimisation at a fixed $\mathcal{N}$ iterations using the accelerated active set selection method and performs a linesearch at step 3 as in Eq. (5.31). The linesearch continues only until an $\alpha^{(k)}$ value that causes E to decrease is found. The emphasis in this technique is to proceed as rapidly as possible to a new, and potentially better, constraint set. This approach is implemented

by initially setting $\alpha^{(k)}$ to 1, and successively halving $\alpha^{(k)}$ until a reduction in the error is found. This technique is referred to as the bisection method, and it provides a reduction in E with the minimum of extra computations over Nakamura's method.

The fourth, or strong linesearch approach is similar to the third approach, however, it attempts to gain as much as possible from the current optimisation by locating $\alpha^{(k)}$ accurately. There are a variety of techniques available to optimise $\alpha^{(k)}$, but Brent's method [127] was found to be the most effective.

5.5 Performance of the Gaussian algorithms

The example chosen is superresolution of a binary object, since the solution is heavily dependent on the positivity constraint. The object chosen is shown in Fig. 5.4(a), with the corresponding bandlimited image shown in Fig. 5.4(b). The bandlimited image was obtained by convolving the object with an Airy pattern, which bandlimited the object to 0.15 of the Nyquist frequency. Fig. 5.5(a) illustrates the error decrease as a function of the iteration count when applying the four methods described in section 5.4.3. In this example, the bandlimited image was corrupted with Gaussian noise to give an SNR of 20dB, the regularisation parameter was set to 10^{-8} and $\mathcal{N}$, the number of conjugate gradient iterations in the algorithm, was set to 5. Regularisation is essential when dealing with real data since although enforcing positivity may be sufficient to achieve regularisation, this is not always the case. The error for Nakamura's technique oscillates initially before converging to the solution. The projected optimal steepest descent technique produces a monotonic decrease. The other techniques also produced monotonic convergence with the number of iterations required by the bisection method and Brent's method being similar to Nakamura's method.

A more realistic picture of the computational requirements is obtained when the same results are plotted versus the number of FFTs required, Fig. 5.5(b). Nakamura's algorithm is the fastest, with the extra computation of an accurate linesearch providing a significant impediment to rapid convergence of Brent's method. The bisection technique was only marginally slower than Nakamura's method and so it is apparent that the improved accuracy

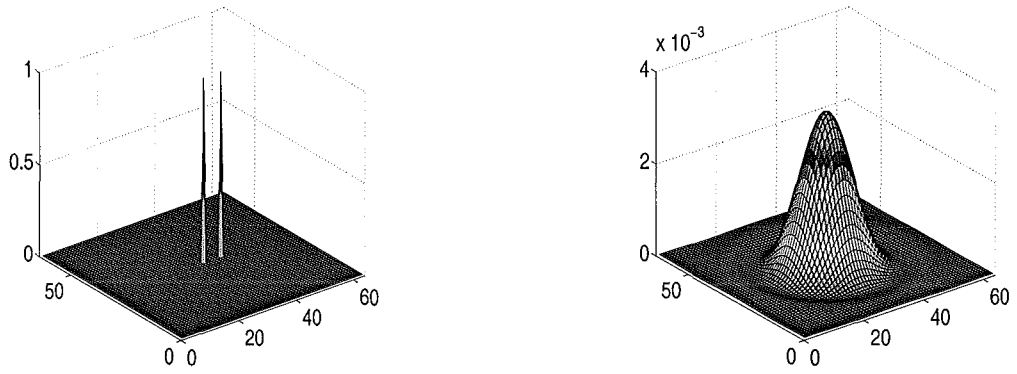

(a) (b)

Figure 5.4: *A sample problem. (a) A simulated binary star with a separation of 6 pixels. (b) The corresponding bandlimited image, the binary star can no longer be resolved.*

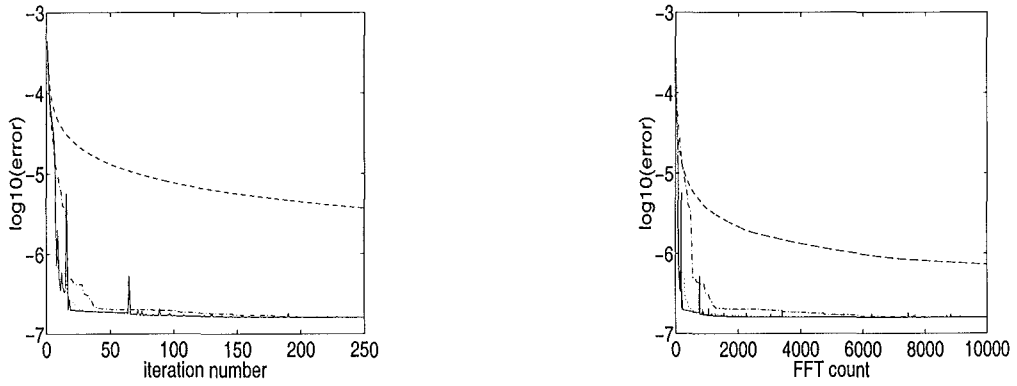

(a) (b)

Figure 5.5: *Results for a bandlimited image with a 20dB SNR, $\mathcal{N} = 5$ and $\gamma = 10^{-8}$. (a) Log10(error) versus iteration count. (b) Log10(error) versus FFT count. Projected optimal steepest descent (dashed), Nakamura's method (solid), bisection (dotted) and Brent's method (dashed - dotted).*

of the linesearch in Brent's method does not justify the extra computation it entails. The corresponding object reconstructions are shown in Fig. 5.6. All techniques, apart from projected optimal steepest descent, which has yet to converge, clearly distinguish the two peaks seen in the original object after 5000 iterations. It should be noted although the oscillations seen in Nakamura's method do not prevent final convergence here, there is no guarantee that this will be the case in all examples.

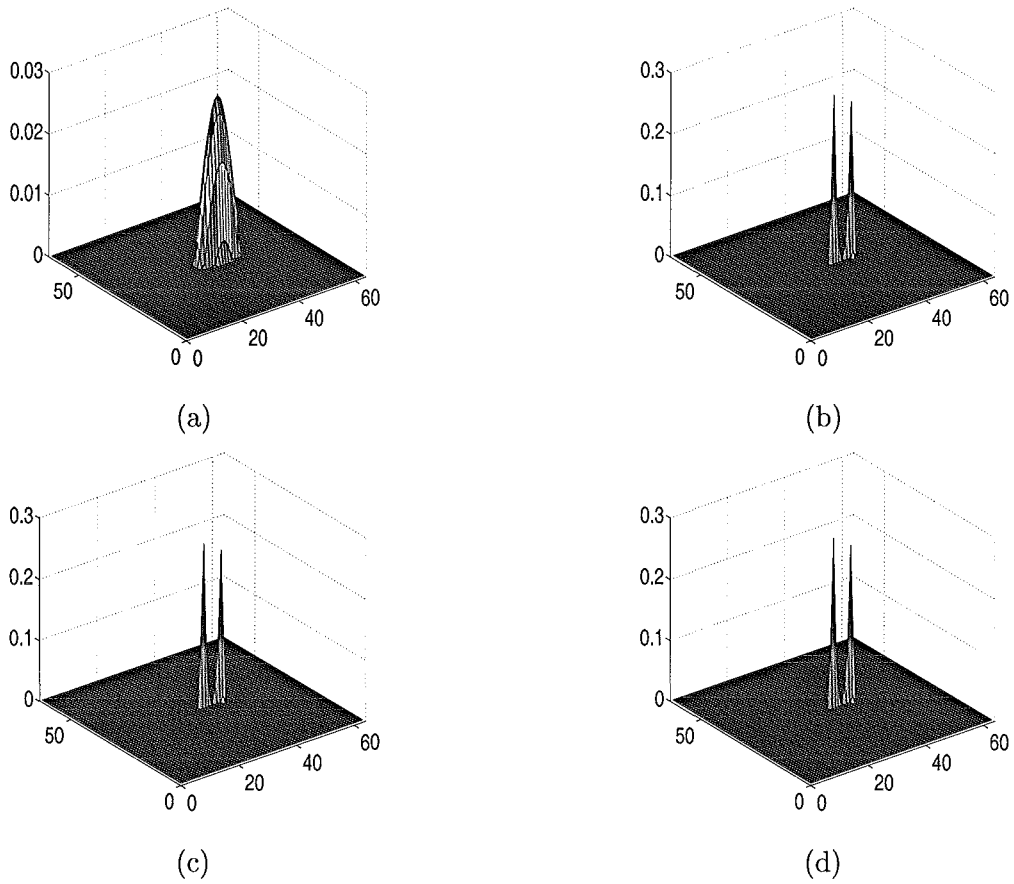

Figure 5.6: *Object reconstructions for a bandlimited image with a 20dB SNR, $\mathcal{N} = 5$, $\gamma = 10^{-8}$ and 5000 iterations. (a) Projected optimal steepest descent, (b) Nakamura's method, (c) Bisection method and (d) Brent's method.*

Finally, the effect of varying the number of conjugate gradient steps, $\mathcal{N}$, was investigated. Fig. 5.7 illustrates the error plots for conjugate gradient steps of 1, 5, 10 and 20, versus iteration and FFT count when using the bisection technique for an example with a 20dB SNR and $\gamma = 10^{-8}$. $\mathcal{N} = 5$ is the best in this case, showing that a complete solution of the conjugate gradient problem at each step is in fact undesirable. This confirms the belief that although it assures finite convergence in practice is it inefficient to perform a complete minimisation on a particular constraint set before moving to a new constraint set. The optimal value of $\mathcal{N}$, however, can be expected to depend on the particular problem.

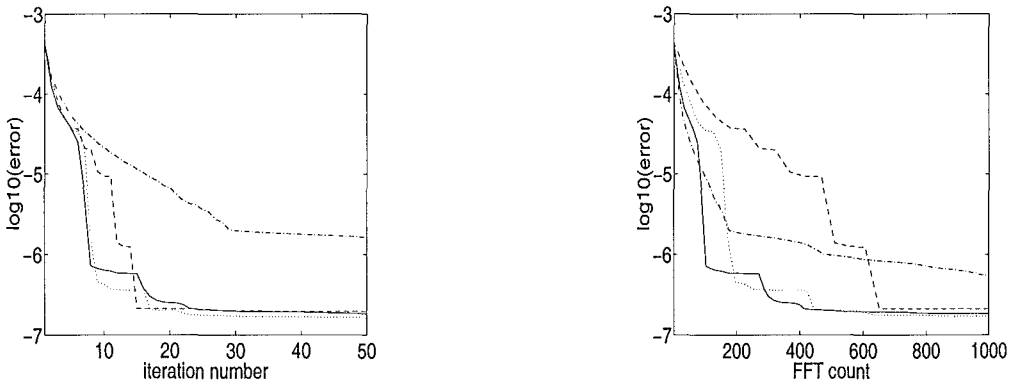

(a) (b)

Figure 5.7: *Log10(error) as a function of $\mathcal{N}$, the conjugate gradient step, using the bisection method for a bandlimited image with a 20dB SNR and $\gamma = 10^{-8}$. (a) Log10(error) versus iterations. (b) Log10(error) versus FFT count. $\mathcal{N} = 1$ (dashed-dotted), $\mathcal{N} = 5$ (solid), $\mathcal{N} = 10$ (dotted) and $\mathcal{N} = 20$ (dashed).*

5.6 Extension to Poisson and mixed noise statistics

The extension of the basic quadratic programming technique to Poisson statistics is complicated by the image dependence of the noise. The assumption of Poisson noise statistics leads to the minimisation of:

$$E = -\sum_{(x,y)} [d(x,y)\ln\hat{g}(x,y) - \hat{g}(x,y)] + \gamma\|\hat{f} \odot c\|^2. \tag{5.34}$$

A significant problem that must be overcome if an iterative minimisation scheme is to be successful is to ensure $\hat{g}$ remains positive, since a negative value means that it is no longer possible to compute the error in Eq. (5.34). In addition, in a Poisson process the underlying image must be positive. Therefore, it is sufficient to ensure that both $\hat{f}$ and h remain positive to produce a positive $\hat{g}$ as required.

An additional problem is that the error surface described by Eq. (5.34) is not convex, so minimisation of E is no longer a linear problem. A conjugate gradient minimisation for the non-convex error surface E requires a change in the calculation of the search direction update as outlined in Appendix A. In addition the step $\alpha^{(k)}$ is now found as the solution to a linesearch, with an added condition that $\hat{g}$ cannot go negative. To achieve this, the maximum allowable step that can be taken in the descent direction that still ensures a

positive estimate α_m, must be calculated from

$$f^{(k)} + \alpha_m d^{(k)} \geq 0. \tag{5.35}$$

This provides the upper bound for a region from which the optimal step value can be selected and allows use of linesearch techniques such as the golden section search [127].

A further modification is required when a constraint deleting algorithm, as opposed to a constraint adding algorithm, is employed. In this case all constraints are initially active, so the only possible starting value for $\hat{f}$ (or $\hat{h}$) is an array of zeros. This causes problems with the initial gradient calculation, since

$$\frac{\partial E}{\partial \hat{f}} = \sum_{(x,y)} \left[\left(\frac{d - \hat{g}}{\hat{g}} \right) * h + 2\gamma \hat{f}^2 \right], \tag{5.36}$$

is infinite when $\hat{f}$ is zero. The solution is therefore to use the mixed noise model gradient which corresponds to

$$\frac{\partial E}{\partial \hat{f}} = \sum_{(x,y)} \left[\left(\frac{d - \hat{g}}{\hat{g} + \sigma^2} \right) * h + 2\gamma \hat{f}^2 \right]. \tag{5.37}$$

Here σ^2 is chosen to be large enough so that $\frac{\partial E}{\partial \hat{f}}$ is of a reasonable scale, but small enough so that the search direction is not significantly altered. The addition of the Gaussian noise variance models the sensor noise inherent to real data in a method similar to that used in Lane [91]. This approach has been implemented and once again for a realistic example an impractical number of iterations were required.

5.7 Accelerating the Poisson and mixed noise techniques

Due to the non-linear nature of the deconvolution problem under the assumption of Poisson noise statistics, acceleration of this technique could not be performed using the techniques employed for Gaussian noise statistics. The complicated practical implementation necessary for Poisson ML algorithms is the main reason the equivalent Expectation-Maximisation and Richardson-Lucy algorithms are preferred. They provide a simple method for estimating the ML solution under the assumption of Poisson noise statistics.

The equivalent and well-established Expectation-Maximisation (EM) and Richardson-Lucy (RL) algorithms, discovered independently by Richardson [130] and Lucy [104] in the early 1970s and rederived for Positron Emission Tomography (PET) by Shepp and Vardi [145], have been used extensively in the restoration of astronomical images [18,143,146,175]. The standard RL update is defined in its multiplicative form as

$$\hat{f}^{(k+1)} = \left(\frac{d}{\hat{f}^{(k)} \odot h} * h \right) \hat{f}^{(k)}. \tag{5.38}$$

Eq. (5.38) can be rewritten into the following equivalent form,

$$\hat{f}^{(k+1)} = \hat{f}^{(k)} + \alpha \hat{f}^{(k)} \frac{\partial ML_p}{\partial \hat{f}^{(k)}}, \tag{5.39}$$

provided $\sum h = 1$, where $\frac{\partial ML_p}{\partial \hat{f}}$ is defined in Eq. (5.15) and $\alpha = 1$ for a standard Richardson-Lucy iteration. Eq. (5.39) shows that the RL algorithm is a scaled steepest ascent algorithm with the search direction being scaled by the current object estimate [83]. When minimising $E = -ML_p$, as in Eq. (5.34), a scaled steepest descent algorithm results, i.e.

$$\hat{f}^{(k+1)} = \hat{f}^{(k)} - \alpha \hat{f}^{(k)} \frac{\partial E}{\partial \hat{f}^{(k)}}. \tag{5.40}$$

The RL algorithm has a number of desirable properties. It has implicit positivity and support constraints due to the multiplicative nature of its updates. In addition, it also conserves energy. A disadvantage of the algorithm is its sensitivity to the initial starting estimate, as indicated by Kaufman [83]. In fact, in the absence of a good prior estimate for f, the best solutions are obtained from uniform starting estimates, where the initial step is in the direction of steepest descent. The sometimes disastrous results produced from random starting estimates indicate that the algorithm cannot be considered to be globally convergent, since a property of globally convergent algorithms is that they converge to the solution from any starting point [106]. Therefore, although the algorithm produces a monotonic increase in the log-likelihood it is not guaranteed to reach the ML solution. This is further illustrated when considering the following. Generally, when $\hat{f}$ is constrained to be positive, the aim is a solution where

$$\frac{\partial ML_p}{\partial \hat{f}} = 0 \ \ \forall \ \ \hat{f} > 0. \tag{5.41}$$

For the RL algorithm, convergence is determined by

$$\hat{f}\frac{\partial ML_p}{\partial \hat{f}} = 0 \ \ \forall \ \ \hat{f} > 0. \tag{5.42}$$

Here $\hat{f}\frac{\partial ML_p}{\partial \hat{f}}$ equal or close to 0, does not necessarily mean that $\frac{\partial ML_p}{\partial \hat{f}}$ is also zero. This is the same problem seen with the use of reparameterisation to enforce positivity in section 5.2.4 and hence suffers the same limitations.

The scaling of the gradient by a preconditioning matrix is often used to accelerate the convergence of steepest descent algorithms. A number of authors have interpreted the multiplication by $\hat{f}$ in Eq. (5.39) as a preconditioner [31, 32]. However, this scaling, often referred to as preconditioning, of the ML gradient by $\hat{f}$ as performed by the RL algorithm does not always aid the convergence of a deconvolution problem. In fact, the fastest convergence of the RL algorithm is obtained from uniform starting estimates and usually occurs within the first few iterations when the effects of preconditioning are least.

The scaling in the RL algorithm, however, ensures a positive reconstruction is obtained. If the RL scaling of the gradient is not performed, another technique must be used to ensure that the solution remains positive. Therefore, it is advantageous to modify the RL algorithm to guarantee convergence, while retaining its positivity enforcing properties. A simple addition to the RL algorithm that combines the initial speed of the RL algorithm to get close to the solution with the guaranteed convergence of the unscaled approach was made and is referred to as the modified Richardson-Lucy (MRL) algorithm. When there is no chance of hitting a constraint the search direction for that pixel remains unscaled. This approach is similar to that used in Kaufman [84], for the acceleration of least squares PET algorithms. Every q iterations, where q takes on an integer value, a step using the modified search direction, s_m, is performed, where

$$s_m = \begin{cases} -\frac{\partial ML_p}{\partial \hat{f}} & \frac{\partial ML_p}{\partial \hat{f}} > 0 \\ -\hat{f}\frac{\partial ML_p}{\partial \hat{f}} & \frac{\partial ML_p}{\partial \hat{f}} \leq 0 \end{cases} . \tag{5.43}$$

A bisection linesearch is then used to calculate the maximum step that can be taken to produce an increase in the likelihood and ensure that the updated object estimate is positive. This means that the step is initially set to 1 and is halved until the likelihood is increased.

Holmes [75] also investigated a similar approach when accelerating the RL/EM algorithm. Recall $\alpha = 1$ in Eq. (5.39) corresponds to a standard RL step with a guaranteed increase in the likelihood. As a means to accelerate the slow convergence of the algorithm α is doubled and the corresponding likelihood value is calculated. If this second likelihood value is larger than the first α is doubled again and the process repeated until the likelihood no longer increases. Holmes notes that it is important not to permit α to get too large and cause the object estimate to become negative. He suggested two ways to overcome this. First, any negative pixels in the object estimate are set equal to their value if acceleration had not been used. Second, if the α calculated using the doubling technique is greater than α_m, then α is set equal to α_m. These alternatives, also trialed, did not perform as well as the MRL method described above.

5.8 Performance of the Poisson and mixed noise algorithms

The reconstruction of a triple star was chosen to test the Poisson and mixed noise algorithms. However, the solution is still heavily dependent on the positivity constraint. The object chosen is shown in Fig. 5.8(a), with the degraded image shown in Fig. 5.8(b). The uniform and random starting points used are shown in Fig. 5.9. Figs. 5.10(a) and (b) illustrate the decrease in error as a function of iteration count when applying the RL and MRL algorithms to the starting estimates. Both the RL and MRL algorithms converge quickly to the solution from a uniform estimate. In the case of the random starting estimate, however, only the MRL algorithm gets to the solution as illustrated in Fig. 5.11.

A more realistic picture of the extra computational requirements is obtained when the same results are plotted versus the number of fast Fourier transforms (FFTs) required. Fig. 5.12 indicates that the MRL algorithm does not require much more computation than the RL algorithm to get to the solution from a uniform start. In addition, it uses only a small number of extra FFTs to obtain the solution from the random start, when the RL algorithm does not reach the solution at all.

Finally, an investigation into the effect of varying the number of standard Richardson-

Lucy iterations, q, before a modified iteration, was investigated. Fig. 5.13 illustrates the error plots for $q = 1$, 2, 3, 4 and 5 versus iteration and FFT counts. The results are very similar for each value of q, with $q = 1$ requiring the most computation as expected. Therefore, the improved convergence of the MRL method requires only a small amount of extra computation over the original method.

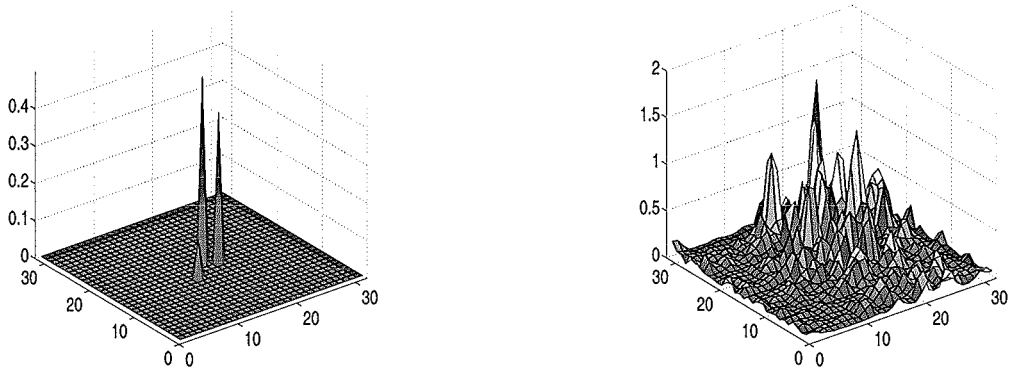

(a) (b)

Figure 5.8: *A sample problem. (a) A simulated triple star. (b) The corresponding atmospherically degraded image.*

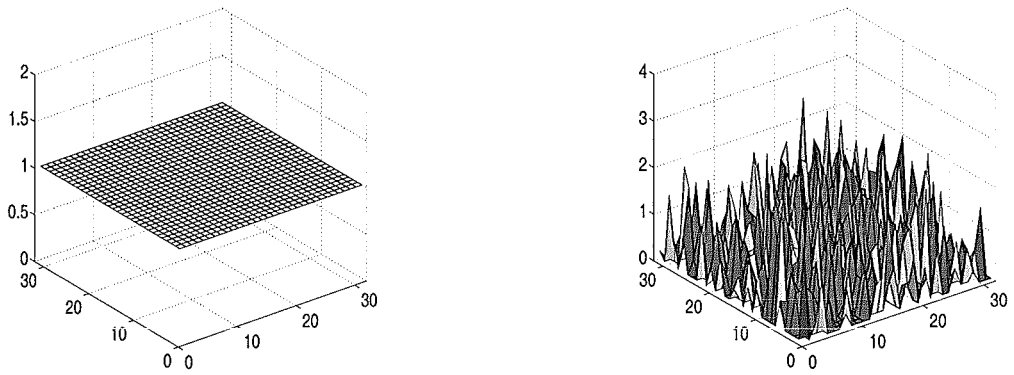

(a) (b)

Figure 5.9: *Two sample starting estimates (a) uniform and (b) random.*

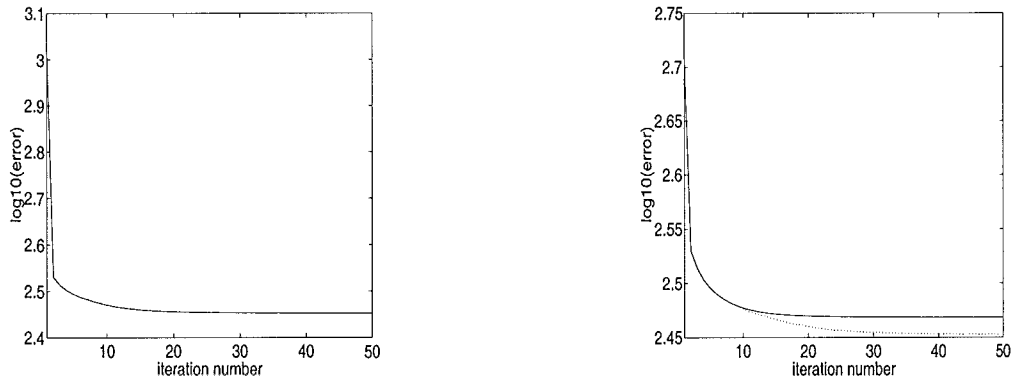

(a) (b)

Figure 5.10: *Results for degraded data containing 100 photons and q = 5. Log10(error) versus iteration count results comparing RL (solid) and MRL (dotted) algorithms for (a) uniform starting estimate and (b) random starting estimate. Note that in (a) the RL and MRL results are an almost exact match.*

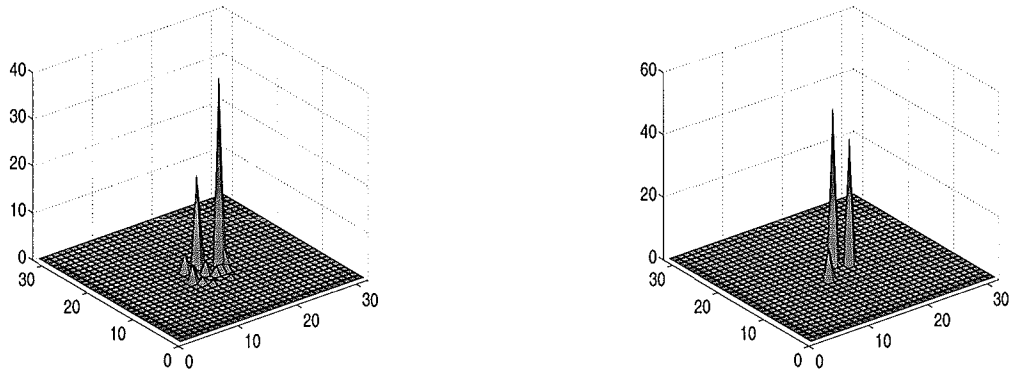

(a) (b)

Figure 5.11: *Reconstructions for degraded data containing 100 photons, q = 5 and a random starting estimate for (a) RL and (b) MRL algorithms.*

5.9 Summary

The deconvolution of a positive image comprises two parts, namely the identification of the pixels which are non-zero and the minimisation of the error over that set. It has been demonstrated that quadratic programming can be applied to this problem, regardless of the noise statistics, to produce assured convergence with a monotonic decrease in the error function. In addition, the basic Gaussian noise algorithm can be accelerated significantly

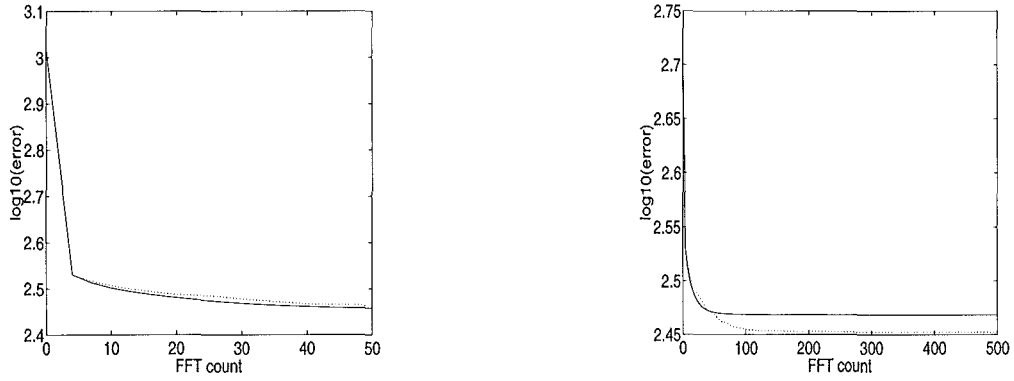

(a) (b)

Figure 5.12: *Results for degraded data containing 100 photons and $q = 5$. Log10(error) versus FFT count results comparing RL (solid) and MRL (dotted) algorithms for (a) uniform starting estimate and (b) random starting estimate.*

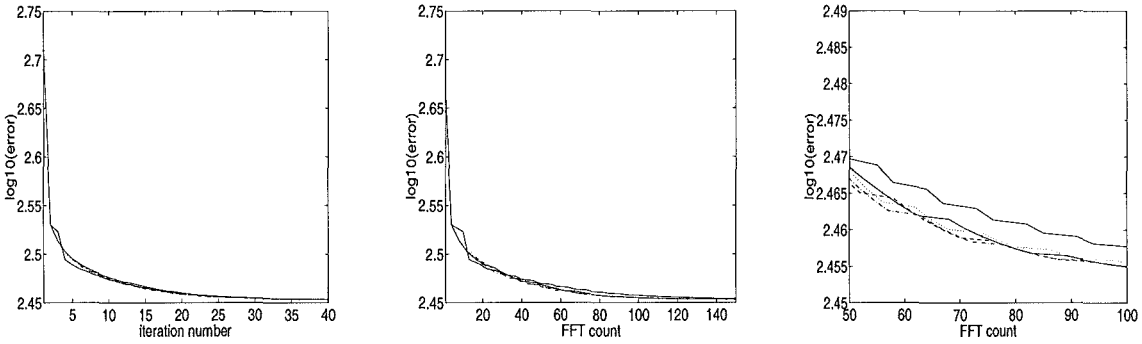

(a) (b) (c)

Figure 5.13: *Variation with q, $q = 1$(solid), 2(dotted), 3(dashed-dotted), 4(dashed) and 5(solid line with dots). (a) Log10(error) vs iteration count (b) Log10(error) vs FFT count (c) zoomed in version of (b).*

while maintaining the convergence of the partial conjugate gradient algorithm.

The best Gaussian noise algorithm was shown to be an extension of an algorithm originally proposed by Nakamura *et al* [117] with two important differences. First, the addition of a weak linesearch produces monotonic convergence. Second, it is implemented with FFTs rather than by matrix multiplication which results in a much faster implementation.

In the case of Poisson noise statistics the best algorithm was shown to be a modified Richardson-Lucy algorithm. Despite its widespread use, the Richardson-Lucy algorithm exhibits two undesirable features. Firstly, it is sensitive to the choice of starting point and secondly it is slowly convergent. Both these problems are attributable to the scaling implicit in the algorithm.

The RL algorithm does however have a number of desirable properties such as implicit positivity and support constraints. The scaling of the ML gradient is powerful in preventing the solution from violating these constraints. The best technique incorporates a modified iteration, after q standard RL iterations. Hence, it combines the initial speed and constraint avoiding properties of the RL algorithm with the guaranteed convergence of the unscaled approach.

Chapter 6

Astronomical Blind Deconvolution

Blind deconvolution techniques attempt to recover both the object and the PSF simultaneously from a noisy degraded image, thereby removing the requirement of conventional deconvolution that an accurate characterisation of the blurring is available. Both the blind deconvolution from a single degraded image and the blind deconvolution from an ensemble of differently blurred images are investigated in this chapter.

Blind deconvolution is inherently more complicated than conventional deconvolution as less information is available. *A priori* information plays an important role as it provides the additional information required to solve the problem. Previously developed deconvolution algorithms and the prior information assumed in each are reviewed and placed into a general framework. There are several issues peculiar to blind, as opposed to conventional, deconvolution and these are also discussed.

The deconvolution algorithms incorporating positivity and regularisation, developed in the previous chapter, are extended to blind deconvolution. Different methods for regularising the blind deconvolution problem are investigated including Tikhonov-Miller regularisation, smoothness constraints, a statistical prior for the PSF, a constraint on the norm of the

object, and penalised MAP approaches, both individually and in combination.

6.1 Introduction

Blind deconvolution is an important problem that may arise in many fields of research, including seismic data analysis, blind equalisation of communication channels, transmission monitoring, echo cancellation in wireless telephony and astronomical imaging [88]. The mathematical analysis is based on the linear convolution described by Eq. (5.1):

$$\begin{aligned} d(x,y) &= g(x,y) + n(x,y) \\ &= f(x,y) \odot h(x,y) + n(x,y) \end{aligned} \tag{6.1}$$

where $d(x,y)$ is the observed image, $f(x,y)$ the true image, $h(x,y)$ the space invariant blurring function or PSF, $g(x,y)$ the noise free data and $n(x,y)$ is equal to the noise on the data. In blind deconvolution the aim is to recover $f(x,y)$, $h(x,y)$ and $n(x,y)$ from the observed data $d(x,y)$. The astronomical imaging problem is a blind deconvolution problem where the blurring is a function of random atmospheric turbulence. Although the blurring of the atmosphere is unknown its statistics are known and can be used to aid the inversion of Eq. (6.1) as seen in section 6.5.3.

In order to solve for $\hat{f}(x,y)$ and $\hat{h}(x,y)$ under the assumption of Gaussian noise statistics, it is common to form a maximum-likelihood estimate which can be found by the minimisation of

$$E = \|d - \hat{f} \odot \hat{h}\|^2 \tag{6.2}$$

where $\|x\|$ defines the L_2 norm of x and $\hat{\cdot}$ is used to denote the estimated quantities. This corresponds to the well-known least squares formulation introduced in chapter 5.

The minimisation of Eq. (6.2) does not guarantee a unique solution to the blind deconvolution problem. Prior information concerning the components of the convolution is required to enable a particular solution to be selected. The incorporation of prior information converts the problem from one of ML to that of MAP. For blind deconvolution the *a priori*

information can be divided into three sections: noise statistics, object prior information and PSF prior information. The first two of these areas were introduced in chapter 5. For astronomical imaging blind deconvolution problems extra *a priori* information is available in the information contained in multiple frames, in which the object is common to each frame but the point spread function varies with the atmosphere. It should be noted that the algorithms developed here are not restricted to the solution of the astronomical imaging problem. Another application is microscopy where it is also possible to obtain multiple frames of observed data. In this case the object is a microscope image and the PSFs are dependent on the degree of defocus.

Many techniques have been proposed for blind deconvolution, including real-time and post processing techniques. Real-time techniques include wavefront sensing and adaptive optics [69]. The post processing techniques developed for this problem have included direct and iterative methods in addition to a number of non-conventional techniques. Many of the previously developed blind deconvolution algorithms, reviewed in section 6.3, use powerful constraints that require knowledge of the instrument from which they are captured. Often this information is not available or it can be difficult to obtain. Therefore this chapter investigates the potential of Gaussian MAP techniques which do not assume any knowledge of the associated imaging system.

A number of issues specific to blind deconvolution that can complicate its inversion are investigated in section 6.2. Section 6.3 contains a review of existing blind deconvolution algorithms and the prior information used in each to deal with these problems. The prior information detailed in section 6.4 is relevant to the algorithms proposed in section 6.5. Finally, the performance of these algorithms is illustrated in section 6.6, before a summary is given in section 6.7.

6.2 Problems inherent to blind deconvolution

There are several problems inherent to blind deconvolution which make finding a unique or meaningful solution difficult. If (f, h) form a solution pair, then $(\alpha f, h/\alpha)$ also form a valid

solution pair, where α is a positive constant. Shifted versions of f and h will also produce an identical convolution, i.e. $(f(x,y),h(x,y))$ and $(f(x-Dx,y-Dy),h(x+Dx,y+Dy))$. When only a single frame of data is used, there is the problem of deciding which solution is f and which is h, i.e. (f,h) and (h,f) produce identical convolutions. This particular problem is eliminated by using multiframe astronomical data, because it can be assumed that f remains unchanged and h varies. This effectively prevents h and f from being swapped.

There is also the problem of ambiguous solutions. A unique solution cannot be found if either h or f is itself a convolution. If

$$f(x,y) \approx f_1(x,y) \odot f_2(x,y) \text{ or} \tag{6.3}$$

$$h(x,y) \approx h_1(x,y) \odot h_2(x,y) \tag{6.4}$$

then instead of recovering f and h, $f_1(x,y)$ and $h(x,y)\odot f_2(x,y)$ may be recovered. Although it can be argued that it is unlikely an object or PSF is a convolution this situation could arise when imaging an object using a system comprised of multiple optical components. In this case the actual PSF could be a convolution of the PSFs of the individual systems. Consider for example a Gaussian PSF [98],

$$h(x,y) = \begin{cases} \frac{1}{2\pi\sigma^2}\exp\left(\frac{-x^2+y^2}{2\sigma^2}\right) & x^2+y^2 < 4\sigma^2 \\ 0 & \text{otherwise.} \end{cases} \tag{6.5}$$

This can in fact be represented as a convolution of two Gaussians,

$$h(x,y) = h_1(x,y) \odot h_2(x,y), \tag{6.6}$$

provided $\sigma_1^2 + \sigma_2^2 = \sigma^2$, therefore a Gaussian PSF leads to ambiguous solutions. Gaussian PSFs have been used by a number of authors, for example Yang *et al* [179] and Fish *et al* [49].

A major limiting factor to the blind deconvolution problem is the trivial solution. This is where $h = \delta, f = d$ or $h = d, f = \delta$. In the astronomical imaging case this would correspond to the imaging of a single star, which although uninteresting, can be the truth. However,

as the trivial solution is such a limiting factor, various forms of prior information have been proposed for its elimination.

6.3 A review of existing blind deconvolution algorithms

Many solutions to the blind deconvolution problem have been proposed. The algorithms reviewed below were developed for both the blind deconvolution of a single blurred image and an ensemble of differently blurred images under the assumption of Gaussian, Poisson and mixed noise statistics. Table 6.1, based on the table in Leung and Lane [101], summarises the commonly used blind deconvolution algorithms and the prior information assumed by each.

Lane and Bates [92] demonstrated a direct algorithm for the solution of Eq. (6.1) using zero sheets and they also provide a theoretical justification for the uniqueness of the deconvolution problem for two dimensions and above. From the zero sheet of $g(x, y)$ it is possible to deduce the zero sheets of $f(x, y)$ and $h(x, y)$ that uniquely determine the original object and PSF. However, this original approach proved unreliable at the levels of noise present in real data. Possible means for overcoming the difficulties associated with the practical implementation of the zero sheets method were proposed by Bates *et al* [14] and involved the direct and indirect use of the concept of the zero sheet for conventional, ensemble and single frame blind deconvolution problems. Many of these were later demonstrated by Bones *et al* [21], who presented the first successful application of these techniques to actual experimental data.

Some of the more conventional imaging techniques that have been widely used to aid the solution of the blind deconvolution problem include speckle interferometry [90], the Knox-Thompson method [86], and bispectral analysis [102, 103]. These techniques recover only object intensity information and so require phase retrieval to estimate the distortion. Phase retrieval attempts to recover phase information from intensity measurements, i.e. to recover $f(x, y)$ given a measurement of $|F(u, v)|^2$ under the constraint that $f(x, y) \geq 0$. An early iterative phase retrieval algorithm was proposed by Gerchberg and Saxton [61], however it

had a tendency to stagnate. Generalisations of this original algorithm were developed to improve its convergence properties. Variants include the well-known error-reduction and hybrid-input-output algorithms of Fienup [48].

The algorithms of Fienup were the basis of the iterative blind deconvolution (IBD) algorithm of Ayers and Dainty [6] which is regarded as the first iterative blind deconvolution algorithm. It is a Gerchberg-Saxton type algorithm, with positivity and the convolution product of f and h as constraints. An alternating minimsation approach is used (discussed in section 6.5), with simple inverse filtering to update f and h. This was modified by Davey *et al* [43] to incorporate Wiener-type filters and support instead of positivity constraints. This introduced some regularisation and permitted the reconstruction of complex-valued as well as real-valued images in the presence of noise.

However, the IBD lacks stable convergence properties, making it difficult to determine when to terminate the algorithm. Lane [94] proposed a more robust joint technique, in which the constraints are incorporated into the error metric. The problem formulation becomes that of an unconstrained minimisation problem in which the stopping criteria are well defined. The use of an error penalty term to impose positivity gives rise to what are known as soft constraints. The weighting of the terms in the error metric is investigated in a later paper by Law and Lane [98].

Blind deconvolution often requires the minimisation of a multimodal cost function, i.e. a function that contains more than one minimum. The simulated annealing algorithm of MacCallum [107] performs a joint minimisation of a multimodal cost function for f and h, subject to support and positivity constraints. It is powerful at avoiding local minima and reaching the global minimum with use of the temperature control parameter T, which is reduced every iteration. Hence the simulated annealing implementation of a least squares optimisation is analogous to the annealing of metals. Just as a liquid metal cooled sufficiently slowly reaches its absolute minimum energy state, so too does the least squares minimisation reach the global minimum of the cost function when T is reduced slowly. A disadvantage of the algorithm is the large computational cost required. For realistically

sized images, the algorithm is too computationally intensive to produce a good solution [88].

Due to the underdetermined nature of blind deconvolution it is often necessary to place a high weighting on the constraint error to achieve a solution. Thiébaut and Conan [157] modified Lane's algorithm [94] to enforce positivity exactly by reparameterisation. However, use of reparameterisation distorts a parabolic error surface resulting in one which may have local minima (see section 5.2.4). They also use an instrument constraint to constrain the PSF. Jefferies and Christou [80] modified Lane's algorithm to use Fourier modulus and multiframe constraints.

The algorithm of Yang *et al* [179] uses projection onto convex sets (POCS) concepts, in which positivity and support constraints are implemented via projection, and an alternating minimisation for f and h. However, the use of projection can cause the error E to increase and convergence to the constrained minimum is not guaranteed. In addition, this algorithm was demonstrated using a Gaussian PSF introducing ambiguous solutions to the problem as noted by Law and Lane [98]. Law and Nuygen [100] extended the algorithm of Yang *et al* to the solution of the multiple frame blind deconvolution problem.

You and Kaveh [180] developed a space-adaptive regularisation technique with the assumption of piecewise smoothness on both the object and PSF. However, the Laplacian smoothing operator used, in some cases introduced edge and ringing artifacts in the reconstructions. Consequently, they proposed the use of anisotropic regularisation to combat the problem [181], an approach that is very similar to the total variation minimisation of Chan and Wong [30].

Under the assumption of Gaussian noise statistics, it is clear that the majority of techniques that have been developed estimate h. The NASRIF (Non-negativity and support constraint recursive inverse filtering) algorithm [89] developed by Kundur and Hatzinakos, estimates h^{-1} as it gives a unique solution at the price of weak constraints. It uses positivity and support constraints for the object and PSF, assumes the PSF and its inverse are absolutely summable and the inverse filter coefficients sum to one. However, the NASRIF

algorithm is sensitive to noise and early termination of the algorithm is necessary to obtain meaningful solutions. In addition, Leung and Lane [101] encountered problems with the implementation of this technique in relation to the lack of constraints on the PSF. Recently Ng *et al* [118] refined the NASRIF algorithm by incorporating regularisation to produce the NASRRIF (Non-negativity and support constraint regularised recursive inverse filtering) algorithm. Preliminary results indicate that the incorporation of eigenvalue truncation and total variation regularisation improves the performance of the algorithm.

As a result of the shot noise present in astronomical images several Poisson noise blind deconvolution algorithms have been developed and are mainly extensions of the equivalent Expectation-Maximisation and Richardson-Lucy (EM/RL) algorithms. Fish *et al* [49] applied the standard RL algorithm, which is essentially a ML technique with positivity and conservation of energy constraints, to the blind deconvolution problem. They also introduce a semiblind deconvolution algorithm in which a form for the PSF is assumed, reducing the number of unknown variables to the few parameters which describe the PSF.

Holmes [74] employs an iterative EM/RL algorithm with constraints that exploit the circular symmetry and bandlimited nature of the PSF. Schulz [143] uses the EM/RL update as the basis for two blind deconvolution algorithms designed to bias the reconstruction away from the trivial solution. The penalised ML approach proposed uses an ad-hoc prior on the object to steer it away from a delta function solution for f. The second algorithm constrains the PSF as a parameterisation of phase errors, combined with positivity implicit in the RL algorithm and a multiframe constraint.

Sheppard *et al* [146] extended the work of Thiébaut and Conan [157] for Gaussian statistics to multiframe blind deconvolution assuming Poisson statistics and they also included different constraint formulations. This technique uses the RL/EM as a basis, with positivity, bandwidth and conservation of light energy constraints enforced by reparameterisation.

Leung and Lane [101] exploit the assumed turbulence statistics and incorporate scintillation, resulting from Kolmogorov phase distortions, into a MAP blind deconvolution algorithm

along with positivity enforced by quadratic programming, conservation of energy, and multiframe constraints. Other existing algorithms of this nature assume constant scintillation. They also proposed a weighted Gaussian or mixed noise blind deconvolution algorithm designed to maximise the following likelihood function,

$$ML_{wg} = \frac{1}{2}\sum_{k}\sum_{x,y}\frac{(d_k(x,y) - \hat{g}_k(x,y))^2}{w_k(x,y)}, \tag{6.7}$$

where $w_k(x,y)$ is the weighting. Thus providing an algorithm designed for Poisson noise statistics while at the same time retaining the least squares formulation of Gaussian noise problems. This algorithm has greater flexibility in modelling the noise, when it does not exactly fit either a Gaussian or Poisson model, as it is important to match the chosen reconstruction algorithm to the noise statistics on the observed data [91].

The EM/RL algorithm is essentially a steepest descent search with a modified search direction, hence convergence is slow. As a result many attempts have been made to accelerate the algorithm by increasing the standard Richardson-Lucy step, to use of conjugate gradient minimisation [19, 20, 75, 83, 91, 115], but are not discussed here.

6.4 Prior information

In common with conventional deconvolution (see section 5.2), the prior information relevant to blind deconvolution problems can be divided into the assumed noise statistics, the object prior information and now also the PSF prior information. There can be an infinite number of possible solutions to a blind deconvolution problem, including the trivial solution where the object estimate is a point source and the point spread function is itself the data. To narrow the number of feasible solutions constraints, on $\hat{f}$ and $\hat{h}$, must be added. The constraints common to blind deconvolution algorithms are positivity, support, regularisation and multiframe constraints. The support constraint can be used to give theoretical justification to the uniqueness of the blind deconvolution problem [92]. Although a powerful constraint it can be difficult to determine and hence is not used here.

Method	Assumptions		
	Noise	Object	Point Spread Function
Kundur & Hatzinakos	G	+ve, support	$\|\Sigma h\| < \infty, \|\Sigma h^{-1}\| < \infty$
You & Kaveh	G	+ve, piece smooth	+ve, light, piece smooth
Chan & Wong	G	+ve, piece smooth	+ve, light, sym, piece smooth
Yang et al.	G	+ve, support	+ve, support
Fish et al.	P	+ve, light	+ve, light, semiblind
Schulz ML+	P	prior, +ve, light	+ve, light, multi
Schulz phase param	P	+ve, light	+ve, light, incoherent, multi
Lane	G	loose +ve and support	loose +ve and support
Thiébaut & Conan	G	+ve and support by reparam	+ve and light by reparam, incoherent
Jefferies & Christou	G	+ve, support, Fourier modulus	+ve, support, bandlimit, multi
Sheppard et al.	P	+ve by reparam	+ve, light and bandlimit by reparam, multi
Miura et al.	P	+ve, support, KT phase, light	+ve, multi, phase by Zernike polynomials
Leung & Lane blind 1	P	+ve, light	prior, +ve, light, multi
Leung & Lane	WG	+ve	+ve, multi
Law & Nuygen	G	+ve, support	+ve, support, multi
Ng et al	G	+ve, support, piece smooth	$\|\Sigma h\| < \infty, \|\Sigma h^{-1}\| < \infty$, eig

Table 6.1: *Summary of the assumptions made on the noise model, the object, and the PSF for existing blind deconvolution techniques. P = Poisson, G = Gaussian, WG = weighted Gaussian, +ve = positivity, light = conservation of light, reparam = reparameterisation, multi = multiframe, sym = centrosymmetric, KT = Knox-Thompson, eig = eigenvalue truncation, piece smooth = piecewise smoothness, incoherent = incoherent imaging. Semi-blind refers to Fish et al's scheme where only the several parameters that characterise the PSF are estimated.*

6.4.1 Multiframe constraint

Additional *a priori* information is available by solving over an ensemble of short exposure images or speckle patterns. The temporal variation of the atmosphere in comparison to the unchanging object makes it easy to obtain ensembles of differently blurred short exposure images of the same object. Short exposure images are used for blind deconvolution as they capture the instantaneous effects of the atmosphere and hence do not suffer from a loss of

information caused by averaging the time varying distortion (see section 3.4.2). Multiple data frames provide prior information to aid the solution of the blind deconvolution problem as well as being an effective way of controlling the noise that is due to low light levels in short exposure images [146]. A multiframe constraint and the assumption of Gaussian noise statistics implies the minimisation of

$$E = \sum_{i=1}^{N} \|d_i - \hat{h}_i \odot \hat{f}\|^2 \tag{6.8}$$

where N is the number of short exposure data frames, to identify $\hat{f}$ and $\hat{h}$. The possibility of $\hat{h}$ being a delta function can be eliminated by using multiple frames [143], since the object can usually be assumed to remain unchanged from frame to frame. However, the trivial solution it not completely eliminated since $\hat{f} = \delta$ and $\hat{h}_i = d_i$ can still occur. Indeed in an astronomical setting this "trivial" solution must be treated with considerable care as an unresolvable star is often a valid solution for f.

6.4.2 Regularisation

The need for regularisation has not been well addressed in the literature on blind deconvolution despite the knowledge that the presence of noise causes the standard deconvolution problem to be ill-posed. In fact, of the early algorithms only the algorithm of Davey *et al* [43] employed regularisation, where it was implicit in the Wiener filter employed. An effect of the ill-posed nature of deconvolution is that $\hat{g}(x,y)$ is often closer to $d(x,y)$ than knowledge of the noise statistics would predict. An extreme example of this is when either $f(x,y)$ or $h(x,y)$ is estimated to be a delta function whereupon $\hat{g}(x,y)$ matches the data $d(x,y)$ perfectly. The possibility of $\hat{h}$ being a delta function can be eliminated by using multiple frames as outlined above. In the presence of noise an exact solution can only be obtained when $\hat{f}$ converges to a delta function and $\hat{f} \odot \hat{h}$ to d. It is precisely this sort of overfitting to the data that regularisation prevents in conventional deconvolution, and hence the potential for regularisation to overcome the trivial solution is investigated here.

Regularisation, first introduced in chapter 5, is essential when dealing with ill-conditioned problems. Although some forms of prior information can remove the uniqueness problem

associated with the trivial solution, in general they do not regularise the problem. The traditional approach is to use Tikhonov-Miller regularisation, where an energy constraint is imposed on both $\hat{f}$ and $\hat{h}$. Assuming N frames of data for the blind deconvolution problem this would entail minimising

$$\sum_{i=1}^{N} \|d_i(x,y) - f(x,y) \odot h_i(x,y)\|^2 + \gamma_1 \sum_{(x,y)} f(x,y)^2 + \gamma_2 \sum_{i=1}^{N} \sum_{(x,y)} h_i(x,y)^2. \tag{6.9}$$

where γ_1 and γ_2 are the regularisation weightings. Note energy constraints are equivalent to constraints on the L_2 norms of $\hat{f}$ and $\hat{h}$, so this can be expressed equivalently as

$$E = \sum_{i=1}^{N} \|\hat{h}_i - d_i \odot \hat{f}\|^2 + \gamma_1 \|\hat{f} \odot c\|^2 + \gamma_2 \sum_{i=1}^{N} \|\hat{h}_i \odot c\|^2 \tag{6.10}$$

where c is the regularisation operator which allows for the incorporation of different forms of regularisation. Setting $c = \delta$ corresponds to Tikhonov-Miller regularisation. The placing of an energy constraint on both $\hat{f}$ and $\hat{h}$ makes the problem well-conditioned. It is important to note that if, for example, γ_2 was set to zero then minimising Eq. (6.9) would also force $\hat{f}$ towards zero, which could be compensated in the first term of Eq. (6.9) by a corresponding increase in the $\hat{h}_i$. The regularisation term would then have no effect compared to $\sum_{i=1}^{N} \|d_i(x,y) - f(x,y) \odot h_i(x,y)\|^2$. This occurs because $\alpha\hat{f}$ and $\hat{h}/\alpha$ also form a solution pair, and regularising $\hat{f}$ alone simply causes $\|\hat{f}\|^2$ to tend to zero and the regularisation to become ineffective. Therefore, the selection of the regularisation parameters plays a key role in the development of practical blind deconvolution algorithms.

It is worth noting at this stage a similarity between blind deconvolution and conventional deconvolution where h is known. In conventional deconvolution it is necessary to regularise the solution to eliminate null-objects. Clearly the blind deconvolution problem also suffers from null-objects. There are, however, significant differences between blind and conventional deconvolution caused by the fact h is now variable. Firstly, it is more difficult to estimate $\|\hat{f}\|^2$ in a straightforward manner. Secondly, it is now necessary to regularise $\hat{h}$ as well. This is partly to eliminate null-objects in $\hat{h}$, but more importantly to prevent $\hat{f}$ tending towards zero as discussed above.

For the regularisation to prevent the trivial solution, it is necessary for the $\gamma_1\|\hat{f} \odot c\|^2 +$

$\gamma_2 \sum_{i=1}^{N} \|\hat{h}_i \odot c\|^2$ term obtained when $\hat{f} = \delta$ to be higher than that obtained from the true solution f. Furthermore it must be sufficiently increased to outweigh the effects of the $\sum_{i=1}^{N} \|d_i - \hat{f} \odot \hat{h}_i\|^2$ term, which is zero for the trivial solution. In order to illustrate how this problem occurs consider the following two cases (i) f is a delta function and (ii) f is a closely spaced binary with peaks of height 1 and α as illustrated in Fig. 6.1. Note that each case corresponds to the same g. From Eq. (6.10) the error term to be minimised when Tikhonov - Miller regularisation is used is

$$\begin{aligned} E &= \|d - f \odot h\|^2 + \gamma_1 \|f\|^2 + \gamma_2 \|h\|^2 \\ &= T_1 + T_2. \end{aligned} \tag{6.11}$$

When the norms are equalised,

$$T_2 = \gamma_1 \beta \|f\|^2 + \gamma_2 \frac{1}{\beta} \|h\|^2 \tag{6.12}$$

where β is the term that equalises the norms. In case (i) $T_1 = 0$ and $T_2 = 2\sqrt{\gamma_1 \gamma_2}\|d\|$. To successfully reconstruct the binary star from the observed data and avoid the trivial solution, the decrease in T_2 must outweigh the increase in T_1. In case (ii) if the data is being fitted accurately T_1 will be equal to the total noise on the system and T_2 can be calculated from Eq. (6.12). For the example in case (ii)

$$\|f\|^2 = 1^2 + \alpha^2. \tag{6.13}$$

In addition, d can be approximated by $d \approx (1+\alpha)h$, so that the regularisation term becomes

$$T_2 = 2\sqrt{\gamma_1 \gamma_2}\|d\| \sqrt{\frac{1^2 + \alpha^2}{(1+\alpha)^2}}. \tag{6.14}$$

The true solution causes the following reduction in the regularisation term for the closely spaced binary, when compared with the trivial solution,

$$2\sqrt{\gamma_1 \gamma_2}\|d\| \left(1 - \sqrt{\frac{1^2 + \alpha^2}{(1+\alpha)^2}}\right). \tag{6.15}$$

Therefore, the binary star will be successfully reconstructed if

$$2\sqrt{\gamma_1 \gamma_2}\|d\| \left(1 - \sqrt{\frac{1^2 + \alpha^2}{(1+\alpha)^2}}\right) > \text{Total Noise}. \tag{6.16}$$

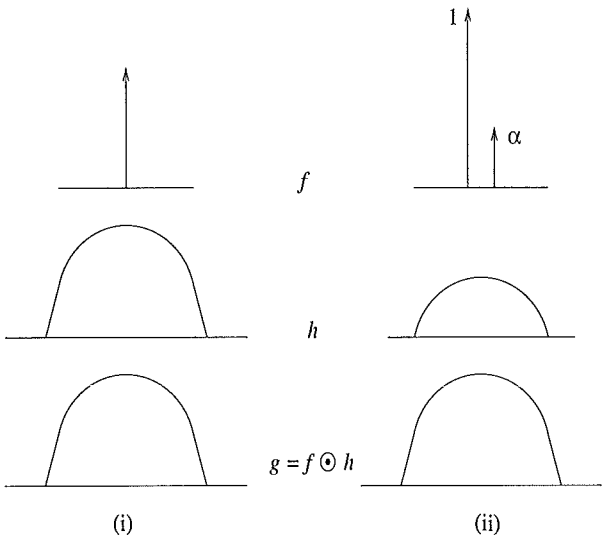

Figure 6.1: *Recovering a binary star. Case(i) f is a delta function. Case (ii) f is a binary with magnitudes of* 1 *and* α. *The convolution g is the same in each case.*

Consider now a widely spaced binary. The approximation $d \approx (1 + \alpha)h$ can no longer be made so there is no reduction in T_2 over the trivial solution for the widely spaced binary, and hence it will not be reconstructed successfully. Thus for a closely spaced binary, regularisation can avoid the trivial solution, but it has little effect for the widely spaced binary. Not surprisingly as the smaller binary component decreases in amplitude, the binary approaches a delta function, and it becomes increasingly more difficult to resolve the two components and avoid the trivial solution. These examples have illustrated the need for additional prior information to steer the reconstruction away from the trivial solution; regularisation alone is not sufficient in many cases.

6.4.3 PSF prior information

In astronomical imaging the PSF is a function of both the imaging system and the atmosphere. In addition, much of the assumed object prior information can also be applied to the PSF, for example positivity and conservation of energy constraints. Regularisation of the PSF as well as the object is also important. Support constraints, however, are not generally used because speckle images do not have clearly defined edges.

Powerful constraints for the PSF can be obtained from knowledge that the data was produced by an optical instrument imaging through atmospheric turbulence. One approach, utilised by Schulz [143] and Thiébaut and Conan [157] is to restrict h to being the PSF of an aberrated optical system. For example, Schulz parameterises the PSF by phase errors distributed over an aperture. This is a powerful prior constraint that aids considerably in the solution of Eq. (6.1), but necessitates solution of a non-linear phase problem to determine h. A less powerful, but simpler, alternative proposed by Jefferies and Christou [80] is to bandlimit the spectrum of h to that of the telescope. Other forms of instrument prior information have also been used, for instance the symmetry constraints of Holmes [74]. In all cases great care must be taken to ensure that only realistic assumptions are made, as errors introduced into the PSF by fitting the prior information and not the data will be reflected in the object estimates.

Although the introduction of an instrument constraint is useful in avoiding the trivial solution, the information required may be difficult or impossible to obtain. In addition any errors in the assumptions are reflected in errors in the reconstruction. Therefore, the algorithms proposed below use only positivity, multiple frames of data and various forms of regularisation to solve the blind deconvolution problem and avoid the trivial solution.

6.5 Proposed algorithms

A summary of existing blind deconvolution algorithms was presented in section 6.3, with the majority having a ML/MAP basis. The blind deconvolution algorithms summarised in Table 6.1 all enforce positivity, whether implicitly, by reparameterisation or projection. This section investigates MAP blind deconvolution algorithms that enforce positivity using the quadratic programming approach outlined in chapter 5 under the assumption of Gaussian noise statistics. In addition, only spatial domain constraints that assume no knowledge of the imaging system are incorporated. The proposed algorithms incorporate a multiframe constraint and prior information for both f and h. The constraints are incorporated into an error metric which is then minimised. The similar existing algorithms are included in the upper right section of Table 6.2. Note that the only multiframe Gaussian noise algorithm

Noise	Instrument/Atmosphere Constraints	No Instrument/Atmosphere Constraints
G	Thiébaut & Conan Jefferies & Christou (m)	Kundur & Hatzinakos You & Kaveh Chan & Wong Yang et al Lane Law & Nuygen (m) Ng et al
P	Schulz phase param (m) Sheppard et al (m) Miura et al Leung & Lane blind (m)	Fish et al Schulz ML+ (m)
WG	Leung and Lane WG (m)	

Table 6.2: *The existing blind deconvolution algorithms sorted by noise statistics and constraint types. Note (m) = multiframe and WG = weighted Gaussian.*

is that of Law and Nuygen [100], although the algorithm of Lane [94] can be extended to multiframe data also.

Regularised solutions of Eq. (6.1) are found using direct maximisation of a likelihood function. For simplicity an alternating variable approach to estimating $\hat{f}$ and $\hat{h}$ was taken, although extension to joint estimation as in Lane [94] and MacCallum [107] is possible. An alternating minimisation reduces the blind deconvolution problem to two linked conventional deconvolution problems (see Fig. 6.2), whereas a joint minimisation has the disadvantage of making the problem more complicated for an improvement in convergence speed. The resulting algorithms are similar in structure to Yang *et al* [179] with accelerated convergence due to optimal step length selection and use of the quadratic programming method. As a result the proposed algorithms have a common structure illustrated in Fig. 6.3. A brief description of each algorithm is provided below and a summary of the proposed

Method	Assumptions	
	Object	Point Spread Function
M1	+ve, energy	+ve, energy, multi
M2	+ve, smoothness	+ve, smoothness, multi
M3	+ve, energy	+ve, smoothness, multi
M4	+ve, penalty	+ve, energy, multi
M5	+ve, energy	+ve, statistical prior, multi
M6	+ve, $\sum f = 1$	+ve, smoothness, multi

Table 6.3: *Summary of the assumptions made on the the object, and the PSF for the proposed Gaussian noise blind deconvolution techniques. Note +ve = positivity, light = conservation of light, multi = multiframe.*

algorithms is presented in Table 6.3. The major algorithmic differences to previous methods are the enforcement of positivity using an accelerated quadratic programming approach and the incorporation of regularisation.

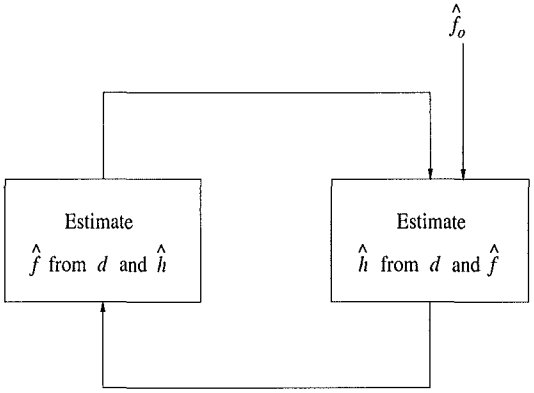

Figure 6.2: *Solving a blind deconvolution problem using alternating minimisations is equivalent to solving two linked conventional deconvolution problems.*

6.5.1 Energy and smoothness constraints

The first algorithm directly extends the quadratic programming technique, developed in chapter 5 to blind deconvolution. Positivity and energy constraints are assumed for both

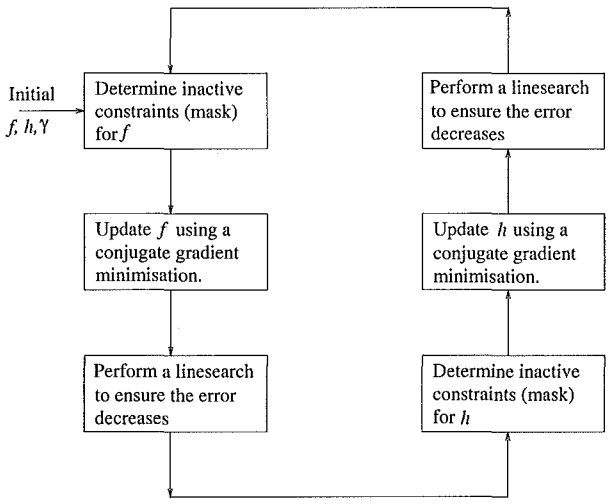

Figure 6.3: *The common structure of the proposed algorithms.*

the object and PSF. This requires minimisation of Eq. (6.10) with $c = \delta$. The piecewise smoothness assumption for the object and PSF as suggested by You and Kaveh [180] requires the minimisation of Eq. (6.10) with c equal to the Laplacian, i.e.

$$c = \begin{bmatrix} -1 & 0 & -1 \\ 0 & 4 & 0 \\ -1 & 0 & -1 \end{bmatrix}, \tag{6.17}$$

and was also implemented with the new method of positivity enforcement. Combinations of energy and smoothness constraints on $\hat{f}$ and $\hat{h}$ were also trialed. The smoothness constraint did not seem intuitively sensible, as stellar objects are typically modelled as sharp peaks on a relatively flat background. Therefore, the oversampling of $\hat{h}$ was investigated in an attempt to increase the smoothness of $\hat{h}$ and justify the application of a smoothness constraint to the problem.

6.5.2 Penalised MAP

The penalised MAP method as suggested by Schulz [143] was incorporated to steer the solution away from the delta function. The cost function to be minimised now becomes

$$E = \sum_{i=1}^{N} \|\hat{f} \odot \hat{h}_i - d_i\|^2 + \beta \ln(1 - \hat{f}) + \gamma \sum_{i=1}^{N} \|\hat{h}_i \odot c\|^2 \tag{6.18}$$

while constraining $\sum \hat{f} = 1$ and $\hat{f} \geq 0$. Should $\hat{f}$ approach a delta function the penalty term will take on the value $+\infty$. The problem however is no longer linear and this must be considered when performing the conjugate gradient minimisation. The step is now found as the solution to a linesearch, with the Newton-Raphson method [72] being used here. Starting with an initial guess denoted by α_0, the linesearch attempts to find x such that

$$\frac{\partial S(\alpha_0 + x)}{\partial \alpha_0} = 0, \tag{6.19}$$

where

$$S(\alpha_0 + x) = f^k + (\alpha_0 + x)\frac{\partial E(f^k)}{f^k}. \tag{6.20}$$

Using a Taylor series expansion for small x gives

$$\frac{\partial S(\alpha_0 + x)}{\partial \alpha_0} \approx \frac{\partial S(\alpha_0)}{\partial \alpha_0} + x\frac{\partial^2 S(\alpha_0)}{\partial \alpha_0^2}. \tag{6.21}$$

Rearranging this gives x and the update for the step, α_1, respectively,

$$x_0 = \frac{-\frac{\partial S(\alpha_0)}{\partial \alpha_0}}{\frac{\partial^2 S(\alpha_0)}{\partial \alpha_0^2}} \tag{6.22}$$

$$\alpha_1 = \alpha_0 + x_0. \tag{6.23}$$

This process is then repeated. Finally, the Polak-Ribiere update (see Appendix A) is used for β with the remaining conjugate gradient steps unchanged.

6.5.3 Statistical prior for the PSF

The use of standard regularisation and support constraints were compared with an alternative based on the statistical nature of h and a constraint on the sum of f. When using blind deconvolution to deconvolve noisy speckle images the fact that the probability of a speckle occurring at the edges is much less than the probability of it occurring in the centre is utilised. This is effectively the probability of a particular speckle pattern occurring and is generated by observing an ensemble of unresolved stars or speckle patterns and forming the covariance of the ensemble.

$$C(x', y', x'', y'') = \langle h(x', y', x'', y'') \rangle . \tag{6.24}$$

This can be achieved either analytically or more conveniently by observation of a known unresolvable star as a reference. The practical difference between the use of a guide star in adaptive optics and the observation required here is that in the former the guide star is required to be sufficiently close to the object of interest to ensure that the same turbulence is measured. In the latter the only requirement is that the observation is made through statistically similar turbulence, a much less demanding requirement.

Having obtained $C(x', y', x'', y'')$ the probability of a particular speckle image can be assessed by first forming a column vector $\mathbf{h}$ by concatenating the rows in a single vector. The corresponding covariance matrix C is formed from Eq. (6.24) and the regularisation term for the PSF h in Eq. (6.9) is replaced by

$$\sum_{i=1}^{N} \mathbf{h}_i' C^{-1} \mathbf{h}_i. \tag{6.25}$$

It is then possible to perform the regularisation using the whole C^{-1} matrix or the diagonalised approximation.

6.5.4 Constraint on the L_1 norm

Another alternative was to incorporate the constraint

$$\sum f(x, y) = 1. \tag{6.26}$$

Note this also eliminates the uniqueness difficulty as it fixes γ. This can be achieved simply by gradient projection and is compatible with the method for enforcing positivity. When combined with positivity, and an L_2 norm on h, Eq. (6.26) gives a constraint on the L_1 norm of the solution, i.e.

$$\sum |f(x, y)| = 1. \tag{6.27}$$

Together Eqs. (6.25) and (6.27) are sufficient to regularise the solution when combined with a positivity constraint on f.

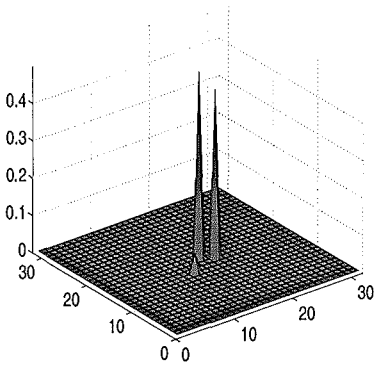

Figure 6.4: *The simulated image data.*

6.6 Performance of the proposed algorithms

Each algorithm was tested on noiseless and noisy computer simulated speckle data. The speckle data was generated from phase screens simulated with the modified midpoint displacement technique introduced in sections 4.1.5 to 4.1.7. Gaussian noise was added to the speckle images by addition of suitably weighted random numbers following a Gaussian distribution. Photon noise was added by generating random numbers following a Poisson distribution, where the mean of the distribution for each pixel was taken as the corresponding noiseless image pixel. The simulated object consisted of a binary star and a much smaller third star, see Fig. 6.4. Sampled noiseless and noisy data are illustrated in Fig. 6.5.

All algorithms were implemented using optimal step length steepest descent (equivalent to one conjugate gradient step) techniques combined with a quadratic programming constraint adding algorithm and were implemented via convolutions using the FFT. In addition to positivity, various combinations of smoothness and energy constraints and penalty terms were used to bias the solution away from a delta function. No assumptions regarding the size of the object were made, since this can then eliminate any possibility that the estimate of the size of f is unduly influencing the reconstructed estimate. In addition the effects of the number of frames, turbulence severity, starting point and noise level on the reconstruction of f are examined.

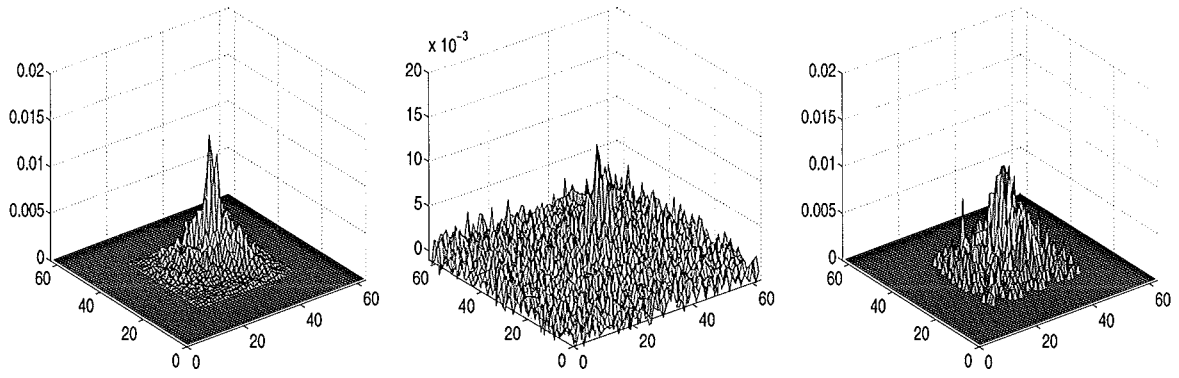

(a) (b) (c)

Figure 6.5: *Simulated speckle data. (a) Noiseless, (b) Gaussian noise degraded image (10dB SNR) and (c) Poisson noise degraded image (1000 photons).*

Fig. 6.6 illustrates the best reconstructions for each algorithm from 5 frames of data degraded by Gaussian noise giving an overall SNR of 40dB. The initial reconstructions assumed energy constraints, smoothness constraints and combinations. The reconstruction in (c) clearly illustrates all three peaks that are present in the original object. The reconstruction in (d) is poor, which is not surprising considering the f and h being considered are not smooth. The next step taken was to impose an energy constraint on f, leaving the smoothness constraint on h. This produced improved results as seen in figure 6.6 (e). In (d) and (e) the oversampling of h mentioned in section 6.5.1 did not improve the reconstructions. The penalised MAP result (see Fig. 6.6(f)) was very similar to that in (c) as was the result of using a statistical prior in (g). The object estimate in (h) however is very poor. The main problem encountered was in the choice of the regularisation parameter, γ, and the penalty factor, β. This may be a result of an implicit estimate of the size of f and h inherent in the computational implementation of these algorithms. This size or support constraint appears to reduce the regularisation required at high noise levels. As a consequence the values of γ and β were chosen empirically to give the best results.

In the results presented here, regularisation has been applied to both $\hat{f}$ and $\hat{h}$ to prevent either tending towards zero. When considering more than a single frame, $\gamma_1 = \sqrt{N}\gamma_2$ was used, where N is the number of frames. In this case it can be shown that the minimum of

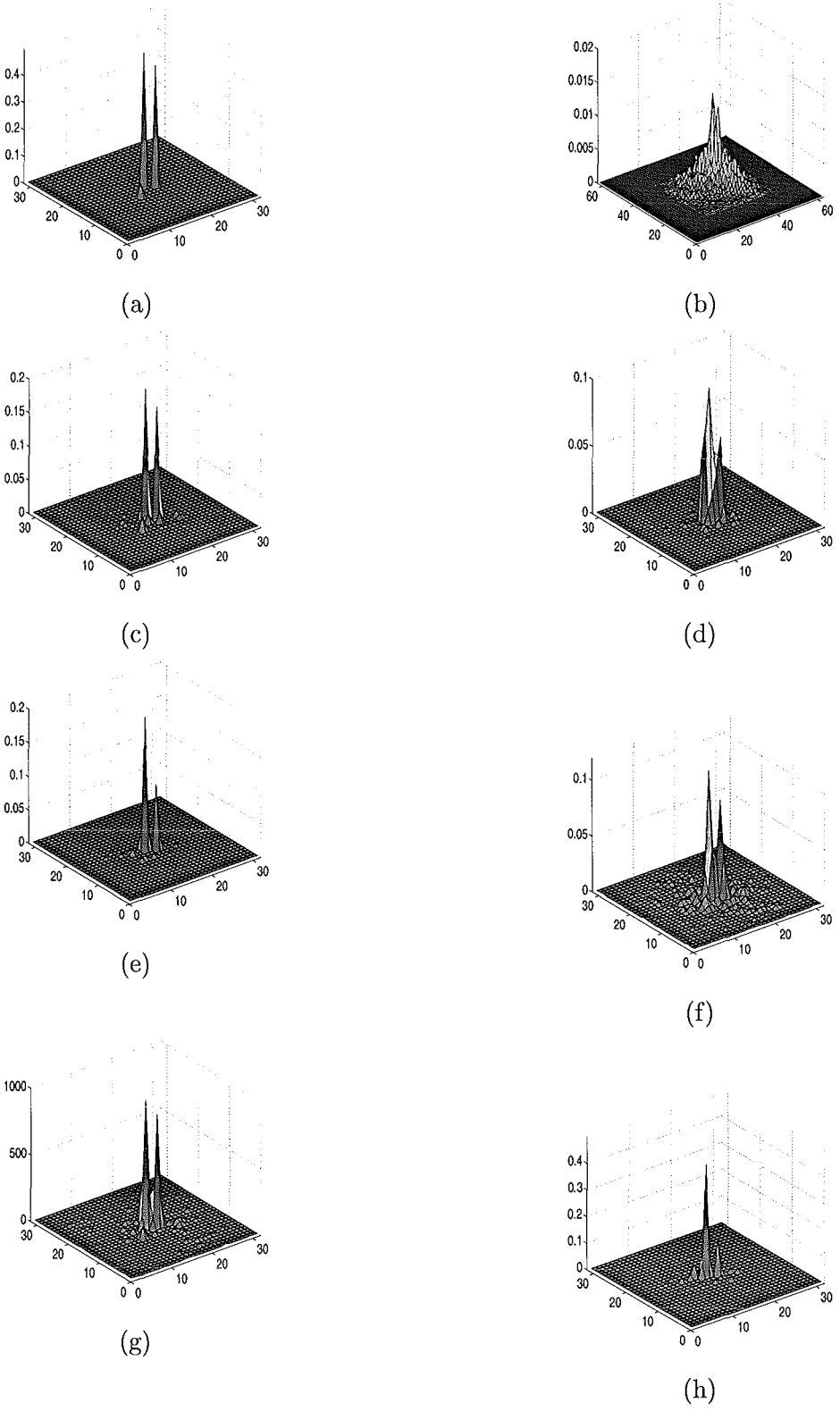

Figure 6.6: *Performance of blind deconvolution algorithm using 5 frames of observed data, (a) true image, (b) a single frame of turbulence degraded data 40dB. Estimates of the true image for (c) Energy constraints, (d) smoothness constraints, (e) Energy constraint on f, smoothness constraint on h, (f) Energy constraint on h, penalty on f, (g) Energy constraint on f, statistical prior for h and (h) Energy constraint on h, $\sum f = 1$.*

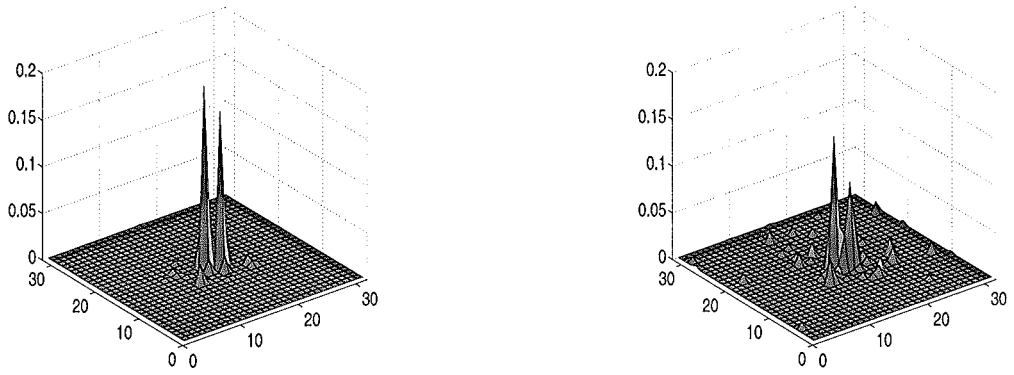

Figure 6.7: *Performance of blind deconvolution algorithm, with energy constraints on f and h for (a) 40dB SNR using 5 frames of data and (b) 20dB SNR using 10 frames of data.*

Eq (6.10) occurs when

$$\gamma_1 \|\hat{f} \odot c\|^2 = \gamma_2 \sqrt{N} \sum_{i=1}^{N} \|\hat{h}_i \odot c\|^2. \tag{6.28}$$

Using this constraint along with Parseval's theorem a lower bound on the norm of $\hat{f}$ and $\hat{h}$ can be deduced as,

$$\|f\| \geq \int |G(jw)|\, dw. \tag{6.29}$$

Since this is a lower bound, using this to fix γ_1 and γ_2 results in an overregularised solution for $\hat{f}$ and $\hat{h}$.

As the noise was increased the quality of the reconstructions decreased. Fig. 6.7 illustrates the reconstructions for M1 for data degraded by Gaussian noise of SNRs of 40dB and 20dB. Therefore, as the noise is increased more frames are needed to obtain meaningful reconstructions. The solution in Fig. 6.7(a) was achieved with 5 frames of data, whereas the solution in Fig. 6.7(b) required 10 frames of data.

Astronomical images suffer from photon noise which is fundamental to all optical systems, where photons arriving can be described by Poisson statistics. Poisson noise corrupted data was also used to determine the performance of the algorithms. Good reconstructions were obtained for high photon counts. However, the solutions started to break down round 10000

photons and produced the trivial solution as the photon count was further reduced.

The robustness and consistency of the solutions obtained by the best performing algorithms were tested by altering the turbulence severity and starting estimates for $\hat{h}$ and $\hat{f}$ respectively. Five frames of Gaussian noise degraded data of 40dB SNR were simulated for D/r_0 values of 4, 6, 8, 10, and 20. In each case an excellent reconstruction was obtained with use of a carefully selected regularisation value. The $D/r_0 = 8$ data was also reconstructed using a variety of different starting estimates for $\hat{f}$; uniform, zero, delta function and random starts. When starting with the null hypothesis that $\hat{f}$ is in fact an unresolvable point source, representable mathematically by a delta function, the prior information must indicate statistically that this is not the case and provide the most probable estimate of the actual data. The reconstructions from these varied starting points all reconstructed the original object.

Another test of algorithm robustness was the reconstruction of the object from an ensemble of 50 different speckle patterns. The best performing algorithms only, M1, M4 and M5, were tested in this manner. The algorithms M1 and M5 reconstructed the object from each of the 50 speckle patterns, although different amounts of regularisation were required in each case. The performance of M4 was more difficult to ascertain due to the difficulty in selecting values for γ and β.

6.7 Summary

Gaussian noise MAP blind deconvolution algorithms, incorporating positivity and various forms of regularisation were presented in this chapter. The basic algorithm, in each case, was obtained by extending the quadratic programming method outlined in the previous chapter to iterative blind deconvolution. A variety of regularisation and penalty terms were utilised in an attempt to avoid the trivial solution and produce good estimates for both $\hat{f}$ and $\hat{h}$.

A thorough review of early through to existing blind deconvolution techniques was also

presented. The majority of the existing iterative techniques are Bayesian techniques which include both maximum-likelihood and maximum *a posteriori* formulations. Of the algorithms reviewed, very few incorporate regularisation and only one multiple frame Gaussian noise algorithm was seen. In addition, positivity is enforced implicitly, by reparameterisation or projection in the majority of these algorithms. The extension of the quadratic programming method to blind deconvolution was therefore a logical step to make.

In addition, extension of the algorithms developed and demonstrated in this chapter to conjugate gradient methods is straightforward. Optimal step length steepest descent approaches were used since the corresponding algorithms are simpler and the use of conjugate gradient methods introduces yet another variable; the optimal number of conjugate gradient steps for each update of $\hat{f}$ and $\hat{h}$. In addition, both single and multiple frame data can be processed.

Excellent results were obtained with Tikhonov-Miller regularisation even in the presence of reasonable amounts of noise. Although use of smoothness constraints in the atmospheric setting has been suggested [180], they generally produced poor results. Even the oversampling of the PSF in an attempt to create smoother data did not aid the reconstruction. Combinations of energy and smoothness constraints produced improved results, but still did not compare to the use of simple energy constraints. The use of a penalty term for f and energy constraint for h and an energy constraint for f with a statistical prior for h were also successful. The final combination of $\sum f = 1$ and a smoothness constraint on h did not perform well. A drawback of these techniques is the choice and interaction of β and γ values is not automatic.

The prevention of the delta function solution requires more regularisation than conventional deconvolution with a consequent tendency to overregularise the solutions. For the examples presented in this chapter the incorporation of penalty terms and statistical priors was successful at avoiding the delta function solution in the presence of considerable amounts of noise. However, robust methods for selecting the regularisation parameters required for these algorithms have yet to be obtained.

In conclusion, the extension of the improved method for enforcing positivity combined with regularisation illustrates potential for the blind deconvolution of astronomical speckle images. The best results were obtained with energy constraints alone and combined with penalty and statistical prior terms. In addition, the algorithms are robust as confirmed by thorough testing on ensembles of different speckle images under a variety of different conditions.

Chapter 7

Estimation of Atmospheric Turbulence Profiles

Atmospheric turbulence severely degrades the quality and resolution of images captured by ground-based telescopes. It introduces a phase distortion in the incident wavefront, which when propagated produces an amplitude variation, known as scintillation. This scintillation cannot be compensated for by current adaptive optics devices and hence it is important to place deformable mirrors conjugate to the turbulence. Thus a knowledge of the vertical structure of the atmosphere is important to enable multiconjugate adaptive optics systems to compensate over a wide field of view. As a consequence techniques have been developed to estimate turbulence height profiles, from balloon-borne instrumentation to remote sensing approaches. However, as the structure of the turbulence can change rapidly it is important that it can be measured efficiently, therefore an optical approach is convenient.

Remote sensing techniques that have achieved some degree of success are the classical SCIDAR (scintillation detection and ranging) and generalised SCIDAR techniques proposed by Vernin and Roddier [170] and Fuchs *et al* [57] respectively. These techniques are possible because scintillation, although often small at good observing sites, contains useful informa-

tion about the structure of the atmosphere. The theory behind these techniques is discussed in section 7.1.

Although SCIDAR is an established technique there are a number of unanswered questions relating to its performance. As a result a series of simulation tools, for the simulation and improved understanding of the existing SCIDAR techniques, were developed and are presented in section 7.2. The simulation of various forms of SCIDAR data and algorithms for the estimation of accurate and meaningful turbulence profiles are also included.

The resulting techniques were tested on astronomical data obtained during a field trip to the Mount John university observatory in April of 1999. This real data proved invaluable for testing the robustness and usefulness of the simulation tools developed. It also provided first hand experience in dealing with the problems associated with the processing of real data and an indication of the turbulence structure above Mount John. The results from a number of selected data sets, representative of the measured scintillation data, are presented in section 7.3 and selected velocity profiles are presented in section 7.4.

Many of the experimental results, however, were inconsistent with the conditions observed at the time the data was captured. In an attempt to explain these anomalies and improve the existing SCIDAR techniques, an in-depth investigation into the assumptions and accuracy of the existing techniques was carried out. Improvements to the standard approach, that came about from these investigations, are presented in section 7.5. Further limitations of the SCIDAR technique are also discussed. Alternative approaches to estimating atmospheric turbulence profiles are presented in chapter 8.

7.1 Existing SCIDAR techniques

SCIDAR (scintillation detection and ranging) is a remote sensing technique used to characterise the 3D structure of the atmosphere. Remote sensing approaches are possible because

the turbulence profile, $C_N^2(h)$, is related to the scintillation covariance as [165]

$$C(\rho) = \int_0^\infty K(\rho, h) C_N^2(h) dh + n(\rho), \tag{7.1}$$

where the kernel, $K(\rho, h)$, is the theoretical autocovariance due to a single star produced by a single layer at an altitude h, with a unit C_N^2. $C(\rho)$ represents the spatial covariance function and $n(\rho)$ is the measurement noise. Eq. (7.1) can be expressed equivalently as

$$T(\rho, h) \times C_N^2(h) + n(\rho) = S(\rho), \tag{7.2}$$

where $T(\rho, h)$ contains theoretical covariance curves of spatial sampling ρ, for a range of height samples h, corresponding to a unit C_N^2 and $S(\rho)$ is a 1D slice of the 2D average covariance calculated from the observed scintillation frames. The aim is to invert the measured covariance at the aperture of the telescope to obtain an estimate of the turbulence profile $C_N^2(h)$.

Kolmogorov statistics are generally assumed for the description of atmospheric turbulence. Under this assumption the ideal scintillation covariance due to a single star, $C(\rho)$, is obtained from the Hankel transform of Eq. (4.95), i.e.

$$C(\rho) = \mathcal{H}\{W_S(f)\}. \tag{7.3}$$

Covariance curves corresponding to a single turbulent layer at heights of 2.5km, 5km, 7.5km and 10km respectively are illustrated in Fig. 7.1(a), and are simply the same curve scaled by $\sqrt{h}$. The integral in Eq. (7.3) was performed numerically for $h = 1\text{km}$, $C_N^2 = 10^{-14}$, $\lambda = 500\text{nm}$ and a sample spacing of 0.001m to give $C_{1\text{km}}(\rho)$. This result was then scaled and interpolated for the different parameter values to give the results in Fig. 7.1(a) by

$$\begin{aligned} C(\rho) &= \left(\frac{C_N^2}{10^{-14}}\right) \times \left(\frac{h}{1000}\right)^{5/6} \times \left(\frac{500 \times 10^{-9}}{\lambda}\right)^{7/6} \\ &\times \left[C_{1\text{km}}(\rho')\left[\rho' + 1 - \rho\right] + C_{1\text{km}}(\rho' + 1)\left[\rho - \rho'\right]\right]. \end{aligned} \tag{7.4}$$

Here

$$\rho' = \text{FLOOR}\left[\frac{\rho\sqrt{\left(\frac{1000}{h}\right)\left(\frac{500\times10^{-9}}{\lambda}\right)}}{0.001} + 1\right], \tag{7.5}$$

where the FLOOR operation denotes the rounding of the result inside the square brackets down to the nearest integer value. Therefore, the covariances consist of a single peak, scaled according to the distance of propagation, with larger propagation distances producing taller and broader peaks. Under the assumption of weak turbulence, the covariance for multiple turbulence layers is obtained by summing the covariances of the individual layers. This result consists only of a single smooth central peak (see Fig. 7.1(b)) and thus the inversion of the height profile using Eq. (7.2) is an ill-posed problem. A $T(\rho, h)$ matrix based on single star covariances, as illustrated in Fig. 7.1(c), has an infinite condition number indicating a singular matrix.

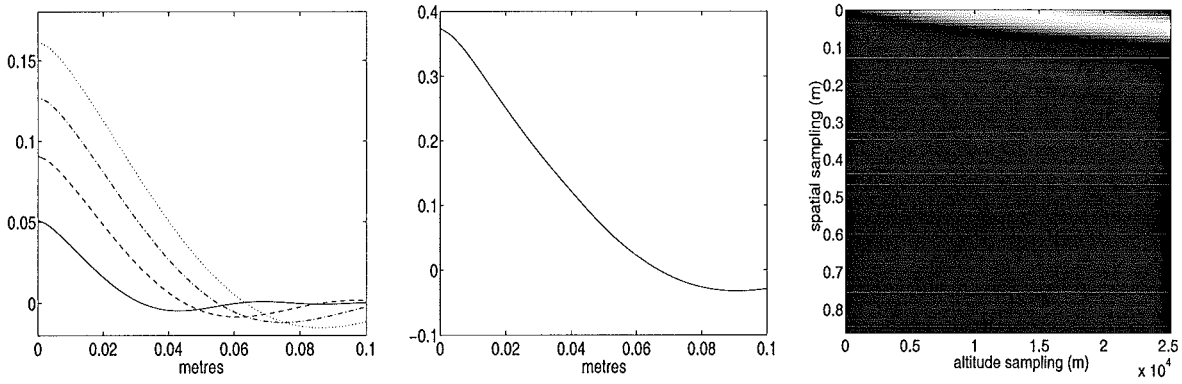

(a) (b) (c)

Figure 7.1: *Single star scintillation covariances. (a) Theoretical covariance curves for propagation distances of 2.5km (solid), 5km (dashed), 7.5km (dashed-dotted) and 10km (dotted). (b) Theoretical covariance curve corresponding to three layers at heights of 1km, 10km and 12km. (c) A sample $T(\rho, h)$ matrix containing theoretical single star covariances.*

7.1.1 Classical SCIDAR

The classical SCIDAR approach to estimating atmospheric turbulence profiles requires the observation of binary or double stars to improve the conditioning of this inverse problem. The covariance of crossed-beam scintillation data is a function of both spatial and angular variables and is denoted by $C(\rho, \theta)$. The spatioangular covariance, as it is termed, consists

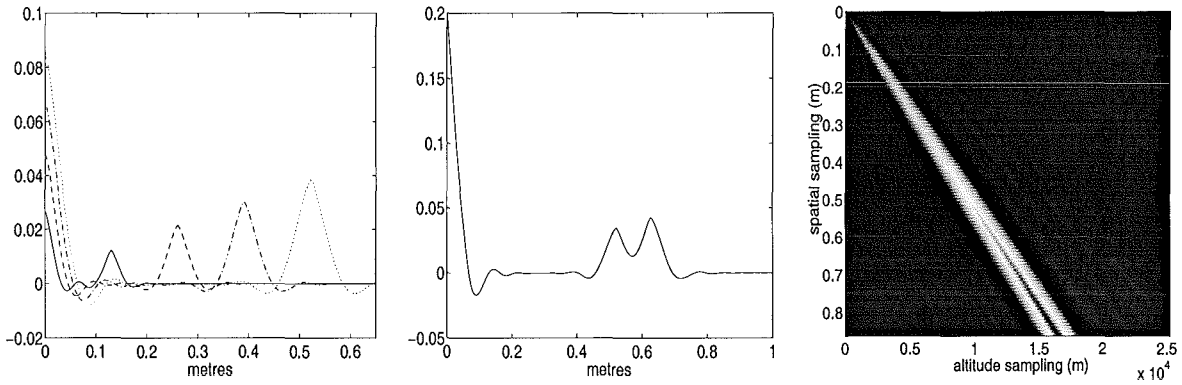

(a) (b) (c)

Figure 7.2: *Binary star scintillation covariances. (a) Theoretical covariance curves for propagation distances of 2.5km (solid), 5km (dashed), 7.5km (dashed-dotted) and 10km (dotted). (b) Theoretical covariance curve corresponding to three layers at heights of 1km, 10km and 12km. (c) A sample $T(\rho, h)$ matrix containing theoretical central peak removed binary star covariances.*

of scaled and shifted versions of the single star covariances:

$$C(\rho,\theta) = \sum_h \left(\frac{1+\alpha^2}{(1+\alpha)^2} C(\rho) + \frac{\alpha}{(1+\alpha)^2} \left(C(\rho-\theta h) + C(\rho+\theta h) \right) \right), \tag{7.6}$$

where α is the relative magnitude of the binary star and θh the separation of scintillation patterns due to each individual star. The binary star covariance curves corresponding to a single turbulent layer at 2.5km, 5km, 7.5km and 10km above the telescope aperture respectively are illustrated in Fig. 7.2(a). In addition to a central peak, each covariance curve now also contains a secondary peak separated from the central peak by a distance proportional to the height of the layer as described by Eq. (7.6). Covariances due to multiple turbulent layers consist of a single central peak and as many secondary peaks as there are layers (see Fig. 7.2(b)). The secondary peaks carry all the information relevant to the height of the turbulent layers. For this reason, current inversion techniques use a $T(\rho, h)$ matrix containing only the secondary peaks as illustrated in Fig. 7.2(c). As a result the measured data must be adjusted accordingly, so that $S(\rho)$ in Eq. (7.2) corresponds to a 1D central peak removed slice of the 2D average covariance. The slice extraction is detailed in section 7.2.2.

7.1.2 Generalised SCIDAR

The normalised scintillation variance, σ_I^2, is proportional to the 5/6th power of altitude, so for short propagation distances σ_I^2 is barely detectable. In classical SCIDAR the scintillation is measured at the telescope aperture, hence it is limited by its inability to detect low altitude turbulence. This is undesirable because boundary layer turbulence often accounts for a significant percentage of the overall turbulence at a particular site.

A solution to the low altitude detection problem of classical SCIDAR is to move the measurement plane until the scintillation is detected. Generalised SCIDAR uses a simple lens system (depicted in Fig. 7.3) to move the measurement plane beneath the telescope aperture, providing the low altitude turbulence with an additional propagation distance for it to increase to a measurable strength. This simple lens system can also be used to obtain measurements at the telescope aperture as required for the classical SCIDAR technique, by appropriate selection of the field lens $L2$.

When operating in classical SCIDAR mode, the field lens $L2$ is selected to produce an image of the desired size at the CCD. An 80mm lens was selected for the Mount John experiments. This fixes l_2' at 80mm for operation in both generalised and classical SCIDAR modes. Operation in generalised SCIDAR mode simply requires a change of field lens. The location of the virtual measurement plane for a selected field lens is given by the thin lens equation (Eq. (3.5)). Using Eq. (3.5) and Fig. 7.3 gives

$$\frac{1}{f_1} = \frac{1}{l_1} + \frac{1}{l_1'} \tag{7.7}$$

$$\text{where } l_1' = f_1 - l_2 \tag{7.8}$$

$$\text{and } \frac{1}{f_2} = \frac{1}{l_2} + \frac{1}{l_2'}. \tag{7.9}$$

Although l_2' stays fixed at 80mm, l_2 varies as the field lens is changed. When using a telescope of focal length 13.5m, and a field lens of 30mm the defocus distance, l_1, extends 3.78km beneath the telescope aperture.

A mathematical description of the generalised SCIDAR method is now included. A telescope can be modelled as a thin lens, with a focal length f. The problem of estimating the optical

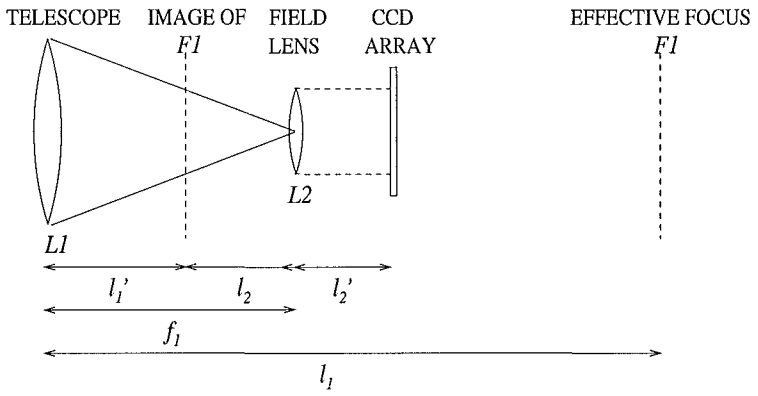

Figure 7.3: *The basic generalised SCIDAR concept.*

field at the virtual measurement plane beneath the telescope, resulting from a planar wave incident on a turbulent layer at an altitude h above the telescope aperture, is illustrated in Fig. 7.4. The complex field of an incident plane wave $U(\mathbf{x}, h+)$ immediately after passing through the phase screen at an altitude h is given by

$$U(\mathbf{x}, h-) = U(\mathbf{x}, h+)\exp\left[i\phi(\mathbf{x}, h)\right]. \tag{7.10}$$

The wavefront incident on the telescope aperture is obtained by a Fresnel propagation of $U(\mathbf{x}, h-)$ to give,

$$U(\mathbf{x}, 0+) = U(\mathbf{x}, h-) \odot h(\mathbf{x}) \tag{7.11}$$

where $h(\mathbf{x})$ is the Fresnel propagation kernel defined in Eq. (3.19). Using the Fresnel propagation equation, Eq. (4.72), this becomes

$$U(\mathbf{x}, 0+) = \frac{1}{j\lambda h}\exp\left[j\frac{\pi\mathbf{x}^2}{\lambda h}\right]\mathcal{F}\left\{U(\mathbf{x}, h-)\exp\left[j\frac{\pi\mathbf{x}^2}{\lambda h}\right]\right\}_{|\frac{\mathbf{x}}{\lambda h}} \tag{7.12}$$

$$= \frac{1}{j\lambda h}\exp\left[j\frac{\pi\mathbf{x}^2}{\lambda h}\right] \times \left[\mathcal{F}\left\{U(\mathbf{x}, h-)\right\}_{|\frac{\mathbf{x}}{\lambda h}} \odot \mathcal{F}\left\{\exp\left[j\frac{\pi\mathbf{x}^2}{\lambda h}\right]\right\}_{|\frac{\mathbf{x}}{\lambda h}}\right] \tag{7.13}$$

$$= \frac{1}{j\lambda h}\exp\left[j\frac{\pi\mathbf{x}^2}{\lambda h}\right] \times \left[\tilde{U}\left(\frac{\mathbf{x}}{\lambda h}, h-\right) \odot \exp\left[-j\frac{\pi\mathbf{x}^2}{\lambda h}\right]\right] \tag{7.14}$$

where $\tilde{U}$ denotes the Fourier transform of U and any pure phase terms have been ignored. As the wavefront passes through the telescope it is truncated by the finite extent of the mirror, $P(\mathbf{x})$, and an overall wavefront curvature is introduced giving

$$U(\mathbf{x}, 0-) = U(\mathbf{x}, 0+)P(\mathbf{x})\exp\left[-j\frac{\pi\mathbf{x}^2}{\lambda f}\right]. \tag{7.15}$$

The optical field in the virtual measurement plane is then obtained by Fresnel propagating $U(\mathbf{x}, 0-)$ over a distance of $d$km to obtain

$$U(\mathbf{x}, d) = U(\mathbf{x}, 0-) \odot h(\mathbf{x}) \tag{7.16}$$

$$= \frac{1}{j\lambda d} \exp\left[j\frac{\pi \mathbf{x}^2}{\lambda d}\right] \mathcal{F}\left\{U(\mathbf{x}, 0-) \exp\left[j\frac{\pi \mathbf{x}^2}{\lambda d}\right]\right\}_{|\frac{\mathbf{x}}{\lambda d}}. \tag{7.17}$$

The use of Eqs. (7.14), (7.15), (7.17), the thin lens equation (Eq. (3.5)), and several of the Fourier transform properties gives [58]

$$U(\mathbf{x}, d) = -\left(\frac{h}{d}\right) \exp\left[j\frac{\pi \mathbf{x}^2}{\lambda d}\right] \times \left[\mathcal{F}\{P(\mathbf{x})\}_{|\frac{\mathbf{x}}{\lambda d}} \odot U\left(-\frac{h}{d}\mathbf{x}, h-\right) \exp\left[j\frac{\pi \mathbf{x}^2}{\lambda d}\frac{h}{d}\right]\right]. \tag{7.18}$$

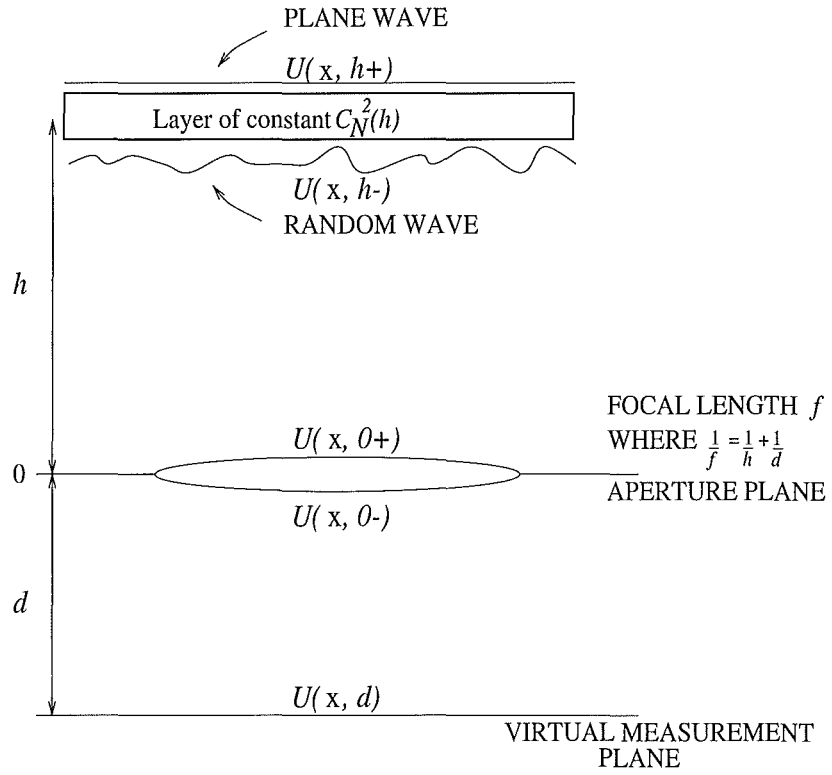

Figure 7.4: *The generalised SCIDAR problem.*

7.1.3 Scanned SCIDAR

Placement of the measurement plane is not restricted to the telescope aperture as in classical SCIDAR nor to a virtual measurement plane beneath the telescope aperture as in generalised

SCIDAR. In 1994 Fuchs *et al* [57] introduced the concept of a movable observing plane. By placing the observing plane at or close to the location of a turbulent layer, the scintillation due to that layer vanishes, while scintillation due to layers above and below it is reinforced. A measurement plane located above or below the turbulent layer by the same amount produces the same scintillation pattern, although inverted. Therefore, it is possible to "wipe out" a turbulent layer by moving the measurement plane until a null in the scintillation is detected. This concept is used as the basis of an alternative turbulence estimation technique outlined in chapter 8.

7.2 Simulation of the SCIDAR method

The development of a series of SCIDAR tools first requires the simulation of the components of the inverse problem: scintillation data, scintillation covariances and T matrices. These can then be used to investigate the performance of techniques for the inversion of Eq. (7.2) under a variety of different conditions.

Simulated scintillation patterns due to a single star for a variety of propagation distances, with a superimposed aperture representing a telescope with a 1m primary mirror and a central obstruction due to a secondary mirror of diameter 30cm, are illustrated in Fig. 7.5. These were generated directly from the theory outlined in chapter 4. The simulation of binary star scintillation patterns proved to be more difficult. An initial phase screen of dimension $(D + 6\sigma_w + bs)\text{m} \times (D + 6\sigma_w + bs)\text{m}$ was generated, where σ_w is given by Eq. (4.83) and bs, the separation of the scintillation patterns, is defined as

$$bs = h \times \sec(\zeta) \times \theta. \tag{7.19}$$

Here h is the distance of propagation or altitude of the turbulent layer above the telescope aperture, ζ is the zenith angle and θ the binary star separation in radians. After propagation over a distance h the resulting valid scintillation result has dimensions $(D+bs)\text{m}\times(D+bs)\text{m}$. Finally, pieces of size $D\text{m}\times D\text{m}$ offset by bs are extracted and added to produce a binary star scintillation pattern. This process is displayed in Fig. 7.6, with sample binary star scintillation patterns illustrated in Fig. 7.7. The simulation accuracy was confirmed by

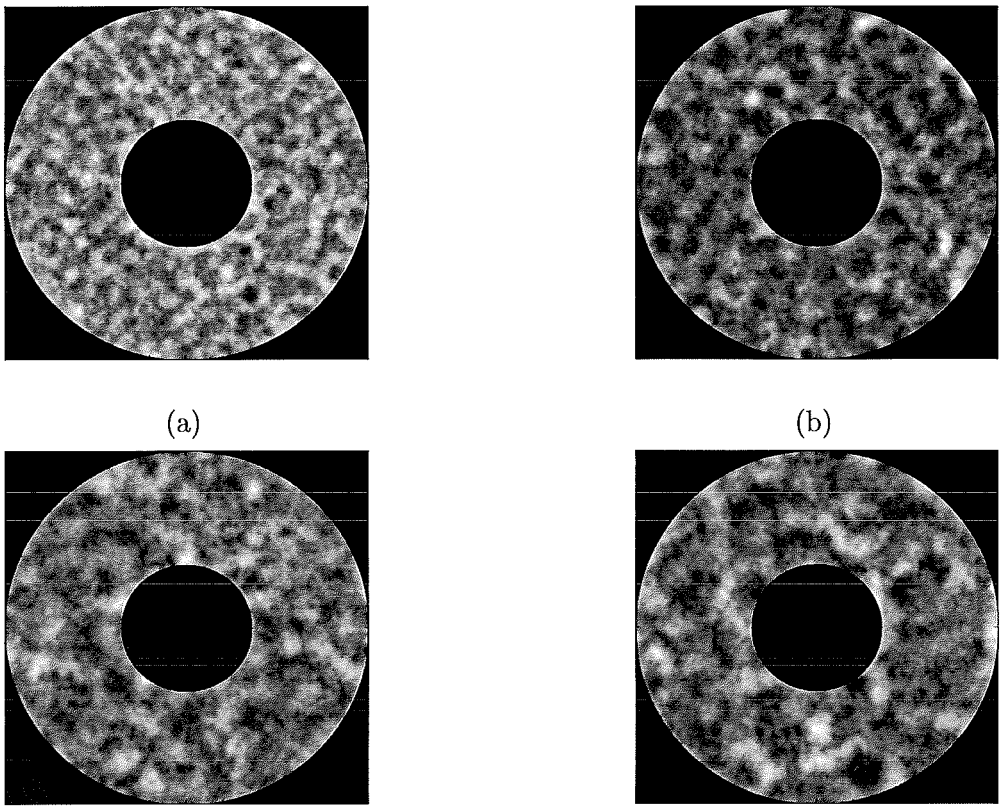

Figure 7.5: *Scintillation patterns for phase screens propagated over (a) 2.5km, (b) 5km, (c) 7.5km and (d) 10km for a 1m telescope with a 30cm central obstruction.*

comparison of the covariances generated from an ensemble of scintillation data frames with the ideal binary star covariances given by Eq. (7.6), see Fig. 7.8. A very good agreement is seen between the two curves over the altitude ranges used. This technique was also extended to the simulation of multiple turbulence layers.

The simulation of generalised SCIDAR binary star scintillation patterns was similar to the simulation of scintillation due to multiple layers of turbulence with one major difference. The scintillation captured by the telescope is truncated by the aperture before it is propagated to the virtual measurement plane beneath the telescope, as indicated in Eq. (7.18). Diffraction effects are, therefore, expected in the resulting scintillation patterns. In addition, when imaging scintillation patterns due to binary stars, the data appears in two overlapped

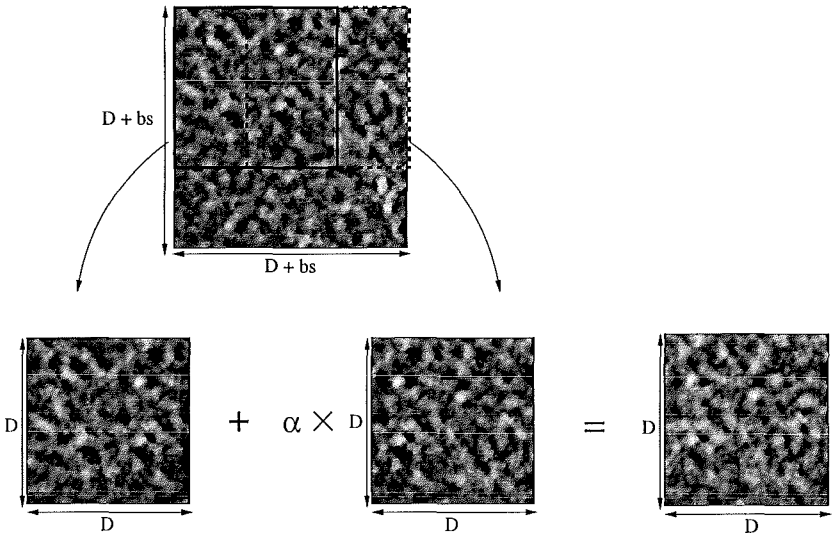

Figure 7.6: *The simulation of binary star scintillation data.*

pupils. The degree of pupil overlap is proportional to the angular separation of the binary and the distance of propagation below the telescope pupil. Simulated generalised SCIDAR data, with and without diffraction effects and superimposed apertures, is displayed in Fig. 7.9.

7.2.1 T matrix generation

The T matrix is generated from the assumed turbulence statistics, typically Kolmogorov for astronomical imaging applications. It contains a series of theoretical covariance curves for a range of height samples determined by the altitude resolution dh. For the classical and generalised SCIDAR techniques dh is a function of the pupil plane sampling, dr, the binary star separation, θ, and the zenith angle, ζ, i.e.

$$dh = \frac{dr}{\theta \sec(\zeta)}. \tag{7.20}$$

This indicates that as the separation increases the resolution also increases. However, there are restrictions imposed by the maximum height range desired [85], i.e.

$$h_{\max} = \frac{D}{\theta} \geq 20\text{km} + d \tag{7.21}$$

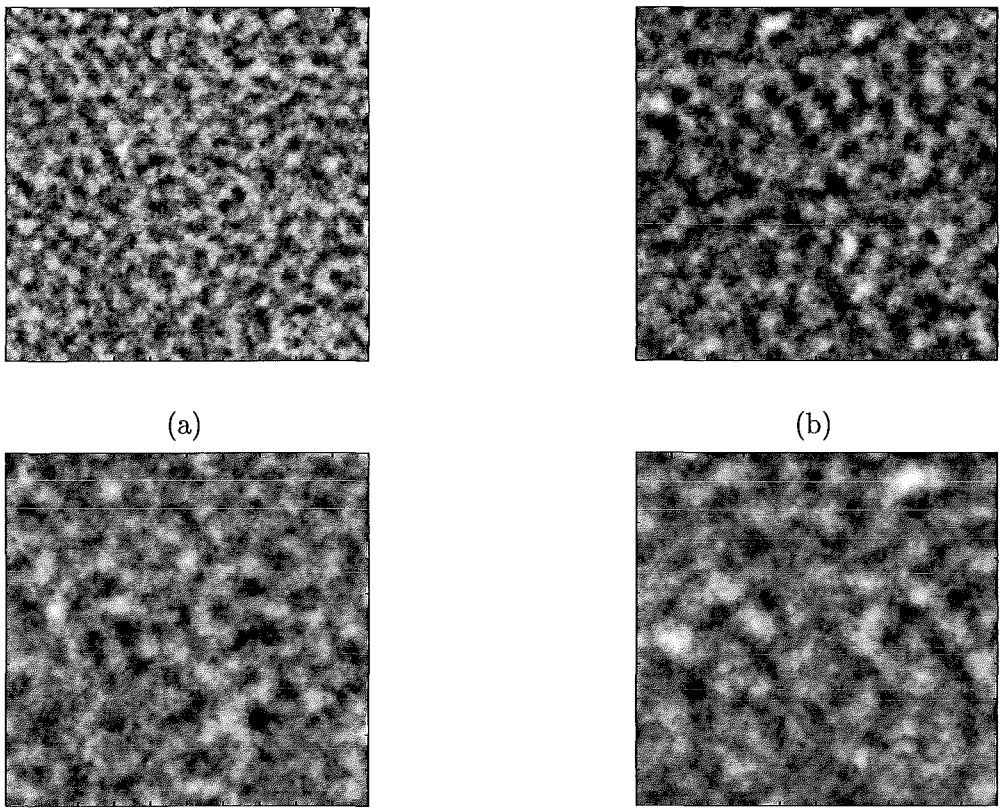

Figure 7.7: *Binary star scintillation patterns for phase screens propagated over (a) 2.5km, (b) 5km, (c) 7.5km and (d) 10km for a binary star with a separation of 10.3 arcseconds and a magnitude difference of 0.5.*

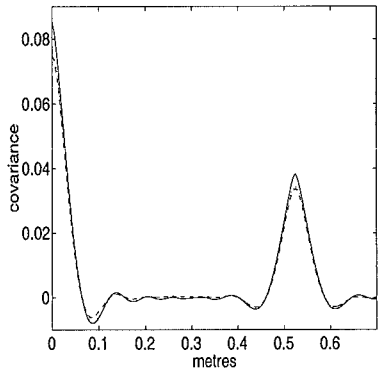

Figure 7.8: *Comparison of theoretical zero inner scale (solid), theoretical non-zero inner scale (dotted) and simulated binary star covariance curves (dashed) for $D = 1\text{m}$, $r_0 = 25\text{cm}$, $\sigma = 0.008$ and a propagation distance of 10km.*

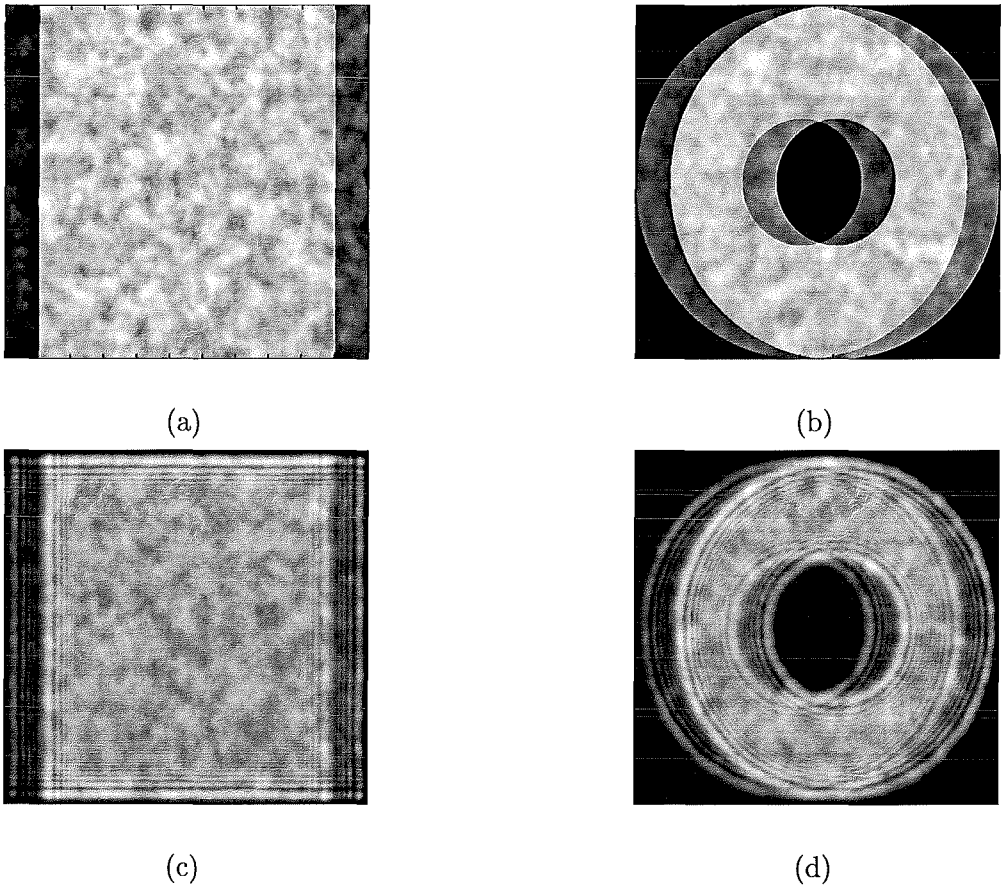

Figure 7.9: *Sample generalised SCIDAR scintillation data with and without diffraction effects and superimposed apertures. (a) No diffraction effects, no aperture, (b) no diffraction effects, superimposed aperture, (c) diffraction effects, no aperture and (d) diffraction effects, superimposed aperture.*

where d is the defocus distance, the distance from the telescope aperture to the virtual measurement plane. This states that the maximum height should be greater than the sum of the height for which the optical turbulence is assumed to be negligible and the defocus distance. For the results presented here $h_{\max}$ is taken to be 25km. This in turn places restrictions on the binary separations that can be used. A large separation although giving good altitude resolution does not give the required altitude range. Conversely, a small separation gives the required altitude range but not the desired resolution. For these reasons most of the binary stars observed were chosen to have separations of between 3 and 15 arcseconds. Sample T matrices corresponding to 3, 8, 12 and 15 arcsecond binaries are

illustrated in Fig. 7.10.

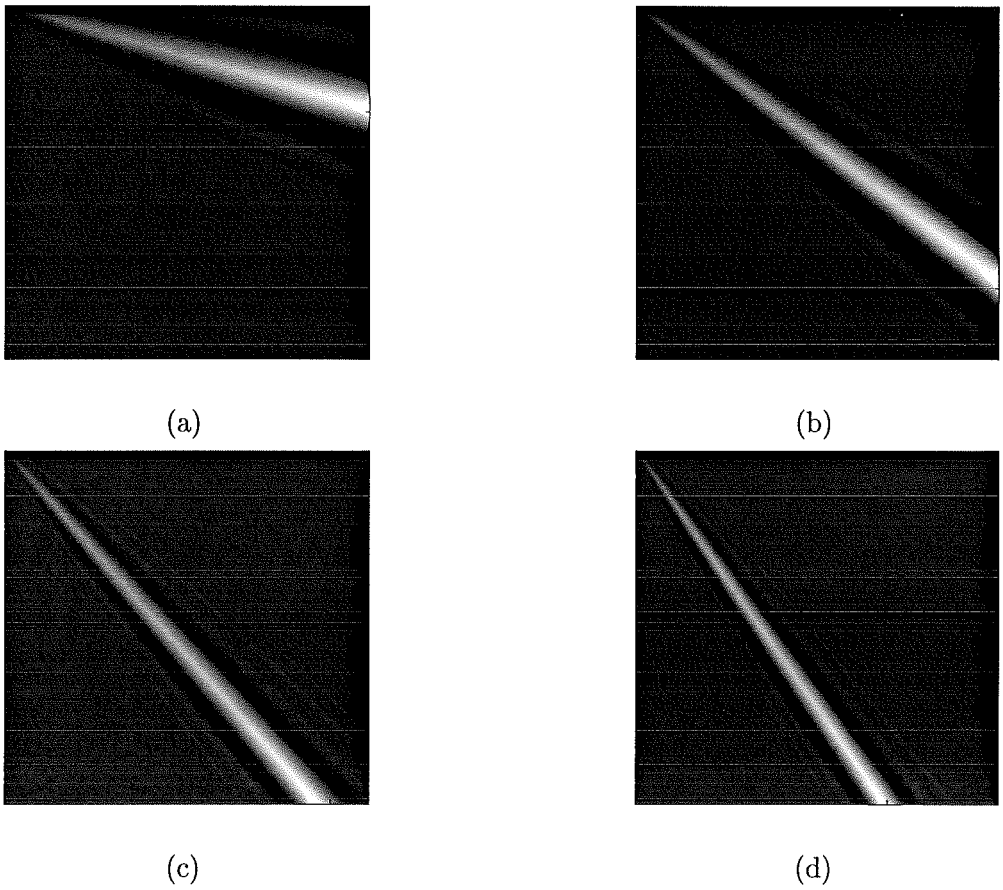

Figure 7.10: *Binary star T matrices for binary star separations of (a) 3, (b) 8, (c) 12 and (d) 15 arcseconds.*

7.2.2 Slice extraction

The right hand side of the system of equations described by Eq. (7.2), $S(\rho)$, corresponds to a 1D central peak removed slice of the 2D measured covariance data. Therefore, calculation of the central peak removed covariance slice is required for its inversion. The 2D measured covariance data is first scaled by $\frac{(1+\alpha)^2}{\alpha}$ to scale the height of the secondary peaks to one, hence

$$S(\rho) = C(\rho - \theta h). \tag{7.22}$$

A slice of the 2D covariance taken along the binary, $C_{||}(\rho, \theta)$, contains central and secondary peak information (see Fig. 7.11). Therefore, an approximation to the central peak removed slice is given as [5]

$$C(\rho - \theta h) \approx C_{||}(\rho, \theta) - C_{\perp}(\rho, \theta), \tag{7.23}$$

where $C_{\perp}(\rho, \theta)$ denotes a slice perpendicular to the direction of the binary (see Fig. 7.11).

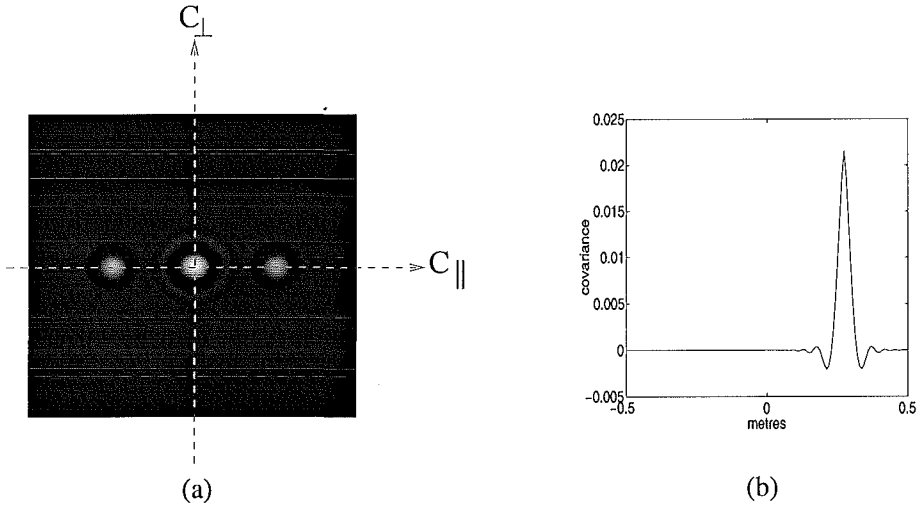

Figure 7.11: *Extracting a 1D central peak removed slice of the 2D covariance data. (a) Original 2D covariance data. (b) One sided central peak removed 1D covariance slice which corresponds to* $C_{||} - C_{\perp}$.

7.2.3 $C_N^2(h)$ estimation

Estimates of the turbulence profile, $C_N^2(h)$, can now be obtained by inverting Eq. (7.2) using the simulated components. Assuming Gaussian noise a maximum-likelihood approach to this problem reduces it to the well-known least squares formulation. Tyler and Steinhoff [161] illustrated that the profile of the atmosphere can be obtained from SCIDAR measurement data by the minimisation of the least squares error function,

$$E = \|T(\rho, h)C_N^2(h) - S(\rho)\|^2. \tag{7.24}$$

However, the problem is inherently ill-conditioned and as a result its inversion can lead to unacceptable noise amplification. A practical solution requires prior information in the form

of regularisation, where regularisation is a statement of the energy or smoothness of the solution. The positivity of the turbulence profile, $C_N^2(h)$, provides an additional constraint.

A variety of different methods for the regularisation of an ill-posed problem were investigated in section 5.2.2. Tikhonov-Miller regularisation is used here and requires the minimisation of

$$E = \|T(\rho, h)C_N^2(h) - S(\rho)\|^2 + \gamma\|C_N^2(h)\|^2. \tag{7.25}$$

Here the first term ensures a fit to the data and the second term is an assumption regarding the energy used to regularise the problem. This minimisation can be performed using standard steepest descent and conjugate gradient techniques, but unlike the use of entropy a positive solution for $C_N^2(h)$ can only be guaranteed by further constraint. Two alternatives for the minimisation of Eq. (7.25) to obtain a positive solution were investigated. In the first method an unconstrained minimisation is performed using optimal step length steepest descent, followed by projection to enforce positivity. In the second method, the accelerated quadratic programming method, introduced in chapter 5, is adapted to the inversion of Eq. (7.25).

A drawback of the techniques presented here is that they all require the selection of a regularisation parameter, γ. The effect of varying γ on the $C_N^2(h)$ estimates and the corresponding r_0 values is illustrated in the following sample problem: T is a matrix of ideal covariances, corresponding to a binary star with a separation of 7.8 arcseconds and a magnitude difference of 0 and S, corresponding to a layer at a height of approximately 10km is a column in the T matrix scaled to have a C_N^2 value of 1.9965 $\times 10^{-13}\mathrm{m}^{-2/3}$ which corresponds to an r_0 of 25cm. A solution can be obtained with $\gamma = 0$ in this case because there is no noise on the system. As the regularisation parameter is increased from 0, the width of the peak in the estimate increases and the height drops (see Fig. 7.12), with the overall area remaining relatively constant. The resulting C_N^2 and r_0 value estimates for different regularisation values confirm this and are listed in Table 7.1. Both methods returned consistent $C_N^2(h)$ and r_0 values, with the quadratic programming method illustrating a superior performance to that of the projected least squares method.

γ	Projected Least Squares		Quadratic Programming	
	C_N^2 ($m^{-2/3}$)	r_0 (cm)	C_N^2 ($m^{-2/3}$)	r_0 (cm)
0	2.81×10^{-13}	20.4	2.00×10^{-13}	25.0
0.01	2.40×10^{-13}	22.4	2.01×10^{-13}	24.9
0.1	2.45×10^{-13}	22.1	2.03×10^{-13}	24.8
1	2.42×10^{-13}	22.3	2.06×10^{-13}	24.6
10	2.27×10^{-13}	23.2	2.01×10^{-13}	24.9

Table 7.1: *Estimates of C_N^2 and r_0 as a function of the regularisation parameter, γ. Ideal values are 1.9965 $\times 10^{-13}$ $m^{-2/3}$ and 25cm.*

Noise is inherent to all real world images, whether it is in the form of image dependent or independent noise, for instance shot noise or measurement noise. Noise was added to the simulations and various noise levels were used to assess the sensitivity of the reconstruction techniques to noise. In the presence of noise, regularisation is essential to obtain a meaningful solution, as illustrated in Fig. 7.13. The sample problem introduced above was tested with SNRs of ∞dB, 40dB, 20dB and 10dB. The estimated C_N^2 and r_0 values are listed in Table 7.2, along with the regularisation values required for a solution to be obtained. As the noise is increased more regularisation is required, with a subsequent reduction in accuracy of the C_N^2 and r_0 estimates. Not surprisingly, the quadratic programming estimates are considerably closer to the ideal than the corresponding projected least squares estimates. A more in-depth look at the sensitivity of these techniques to noise is presented in chapter 8.

The results indicate that although regularisation is necessary to obtain a solution in the presence of noise, the solution is not sensitive to the value of the regularisation parameter γ. An order of magnitude difference in γ does not significantly affect the result (see Tables 7.1 and 7.2). There exist many techniques for determining γ, for example setting it equal to the noise to signal ratio as discussed in section 5.2.2. However, the values used for the SCIDAR problems in this thesis were selected to produce visually pleasing and meaningful results. In this particular application, the ideal regularisation value should allow the individual layers to be clearly distinguished, or in other words not perform so much smoothing that adjacent

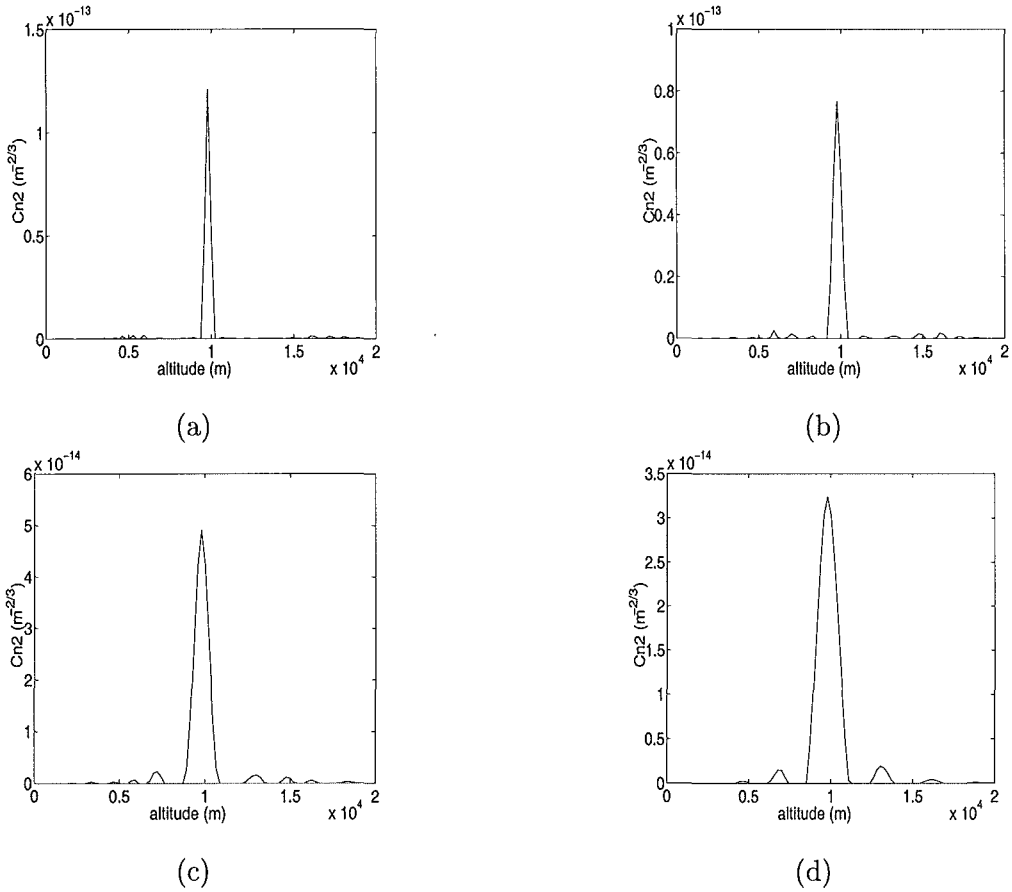

Figure 7.12: *The effect of regularisation.* $C_N^2(h)$ *estimates for (a)* $\gamma = 0.01$*, (b)* $\gamma = 0.1$*, (c)* $\gamma = 1$ *and (d)* $\gamma = 10$*.*

layers become indistinguishable from each other. In addition, it should not produce extra spurious peaks indicating turbulent layers where there are in fact none. The regularisation parameter γ was selected by trial and error to best meet the above requirements.

7.3 Experimental results

The experimental data presented in this thesis was obtained during an observing run held at the Mount John University Observatory. All experimentation was performed using the McLellan 1m telescope, which has a cassegrain focus and was operated in a 13.5m focal length configuration. The SCIDAR equipment attached to the telescope was designed and built by the Applied Optics group based at Imperial College in London. Of the 10 available

SNR (dB)	γ	Projected Least Squares		Quadratic Programming	
		C_N^2 ($m^{-2/3}$)	r_0 (cm)	C_N^2 ($m^{-2/3}$)	r_0 (cm)
∞	0	2.81×10^{-13}	20.4	2.00×10^{-13}	25
40	0	2.84×10^{-13}	20.3	2.00×10^{-13}	24.95
20	0.1	3.28×10^{-13}	18.6	2.41×10^{-13}	22.34
10	10	3.04×10^{-13}	19.4	2.55×10^{-13}	21.51

Table 7.2: *Estimates of C_N^2 and r_0 for ∞, 40, 20 and 10dB noise levels, where the ideal values are 1.9965 $\times 10^{-13} m^{-2/3}$ and 25cm.*

observing nights approximately 50% were successful.

7.3.1 Experimental setup

A block diagram of the equipment is illustrated in Fig. 7.14. The imaging system consists of an image intensifier lens-coupled to a 128×128 CCD camera, the output of which was then stored onto DAT tape. The TV finder is used to centre on the object of interest, since this is not possible with an image of the aperture. The required components were attached to an optical rail which was bolted onto the base plate of the telescope. The optical rail was then aligned with the optical axis of the telescope.

An 80mm field lens was selected for operation in classical SCIDAR mode, and resulted in the telescope pupil approximately filling the 128×128 CCD (see Fig. 7.15). The central obstruction (secondary mirror) of 0.33 metres diameter and the spider, the supports that hold the secondary mirror in place, are seen in Fig. 7.15. Also visible are what appear to be bites taken out of the edge of the primary mirror. These are in fact due to incomplete removal of the primary mirror covers during the observation. Investigation of the data gives the pupil plane sampling, dr, as 1/117, i.e. the 1m diameter was spread over 117 of the 128 pixels.

For binary separations between 4.4 arcseconds (the separation of α Cru) and 10.3 arcseconds (the separation of ξ Lup) the altitude resolution that can be achieved is between 500m and

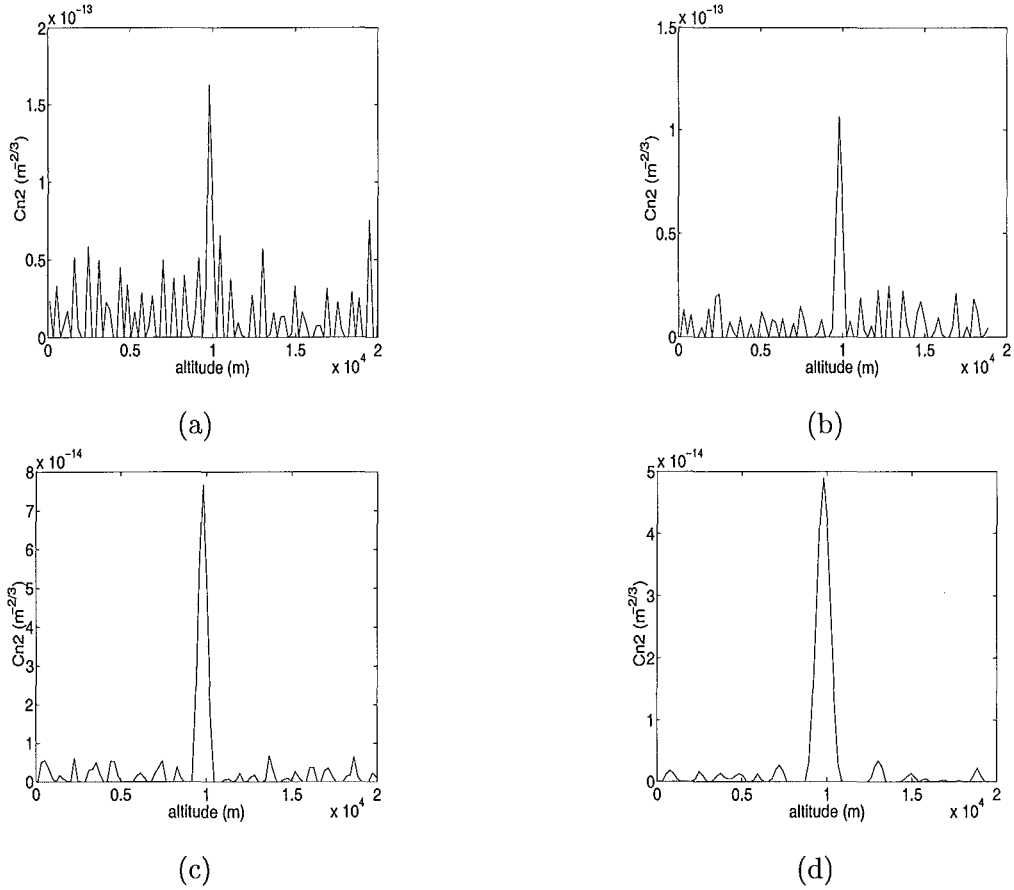

Figure 7.13: *The importance of regularisation when reconstructing noisy data. $C_N^2(h)$ estimates for data with a 20dB SNR. (a) $\gamma = 0$, (b) $\gamma = 0.01$, (c) $\gamma = 0.1$ and (d) $\gamma = 1$.*

200m. The binary stars were restricted to be within 30 degrees of the zenith so that the telescope could operate as close to vertical as possible. A magnitude difference of no more than one between the binary star components was also required to ensure that the scintillation due to each star was detected. Finally, the basic SCIDAR equipment was limited to an overall magnitude of 6 to avoid saturation and subsequent damage of the CCD. Hence filters were required when observing brighter than 6th magnitude stars. These factors placed severe limitations on the number of suitable binary stars, meaning that at any one time during the observing run only a handful of stars were available. The complete list of stars used at various stages throughout the observing run are listed in Table 7.3.

Operation in generalised SCIDAR mode required the field lens to be replaced with the

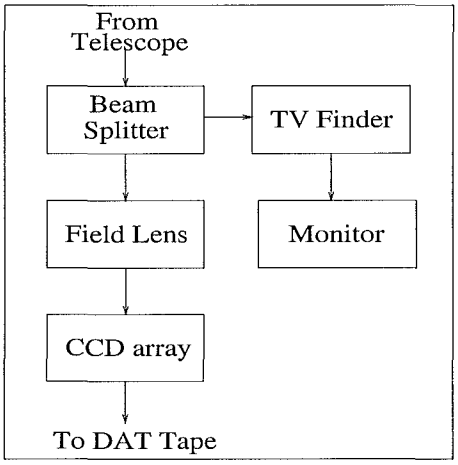

Figure 7.14: *Block diagram of the SCIDAR equipment used during the observing run at the Mount John observatory.*

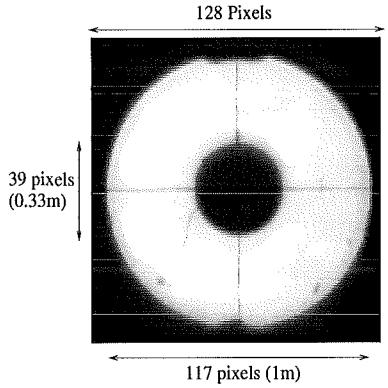

Figure 7.15: *The 1m McLellan telescope aperture.*

appropriate lens ($L2'$) for the selected defocus distance. Recall from section 7.1.2 that the distance between the field lens and the CCD array, l_2', stays fixed for operation in classical and generalised SCIDAR modes, and was set at 80mm due to selection of an 80mm field lens. Therefore, changing the field lens, from the 80mm pupil plane lens, alters the location of the corresponding conjugate plane and hence changes the defocus distance. Table 7.4 lists a number of field lens diameters and the corresponding defocus distances calculated using Eqs. (7.7) to (7.9) with $l_2' = 80$mm and $f = 13.5$m (the focal length of the McLellan 1m Telescope). Defocus distances of 2.26km and 3.78km were used throughout the observing run, corresponding to field lenses of 40mm and 30mm respectively.

YBS Number	Name	Separation (as)	Mag. Diff.
2948/2949		0.2	9.9
4135		0.4	13.7
4443/4444		0.1	9.3
4730/4731	α Cru	0.4	4.4
4898/4899	μ Cru	1.0	34.9
5120		1.0	10.1
5925/5926	ξ Lup	0.5	10.3
6187		1.2	9.6
6401/6402	36 OPH	0	4.6

Table 7.3: *Binary stars, with corresponding separations, in arcseconds, and magnitude differences, imaged during the Mount John observing run. Note that the YBS number corresponds to the number the star is listed by in the Yale Bright Star Catalogue [73].*

$L2'$ (mm)	**Defocus** (km)
10	-15.93
20	-6.82
30	-3.78
40	-2.26

Table 7.4: *Defocus distances for a number of selected field lens diameters. Note that* $f_1 = 13.5m$, $L2 = 0.08m$, $l_2' = 0.08m$.

7.3.2 Data acquisition

The scintillation data was captured in blocks of 2000 frames of 1ms exposure with one frame recorded every 2.7ms. A single data frame for each of the selected runs is illustrated in Fig. 7.16. The scintillation varies in depth over all six sample images. Darker patterns indicate more depth and correspond to stronger turbulence, a measure of the different conditions seen over the different nights the images were captured. The generalised SCIDAR data is different to the classical data, and is illustrated in Figs. 7.16(g) - (l). The edge of the pupil is no longer clear due to the pupil overlap that occurs once propagated beneath the telescope

aperture. Figs. 7.16(g), (h), (k) and (l) correspond to defocus distances of 2.26km and appear to have finer detailed structure than the data corresponding to defocus distances of 3.78km (Figs. 7.16(i) and (j)). In some cases the central obstruction is almost invisible and the edge of the aperture is often clipped by the CCD during the imaging process. This has implications during the covariance calculations.

Measurement noise is inherent to all experimental measurements. Also captured during the observing run were noise data frames (see Fig. 7.17(a)). The corresponding noise spectrum and average autocovariance of the noise are illustrated in Fig. 7.17, and indicate the measurement noise cannot be completely described by a Gaussian noise model. As a result preprocessing of the data was carried out to eliminate the non-linear noise effects before the inversion was performed.

7.3.3 Preprocessing

The average spatial covariances of the short exposure scintillation frames, the basis for the SCIDAR technique, were calculated from the measured data. Preprocessing was incorporated at this step to remove some of the non-linear effects of the noise and compensate for the fact that the data of interest was only within the finite aperture of the telescope.

Although averaging over a large ensemble of data frames helps to reduce the error due to measurement noise, further processing was performed as part of the averaging process and was made possible because noise data was captured each night. Let $d(\rho)$, where $\rho = (x, y)$, denote the observed data, which is equal to the sum of the SCIDAR data $(s(\rho) + \bar{s}(\rho))$ and the noise data $(n(\rho) + \bar{n}(\rho))$:

$$d(\rho) = s(\rho) + \bar{s}(\rho) + n(\rho) + \bar{n}(\rho). \tag{7.26}$$

Here the SCIDAR and noise data contain both zero mean scintillation data and mean scintillation components, with a mean quantity denoted by a bar above the respective quantity.

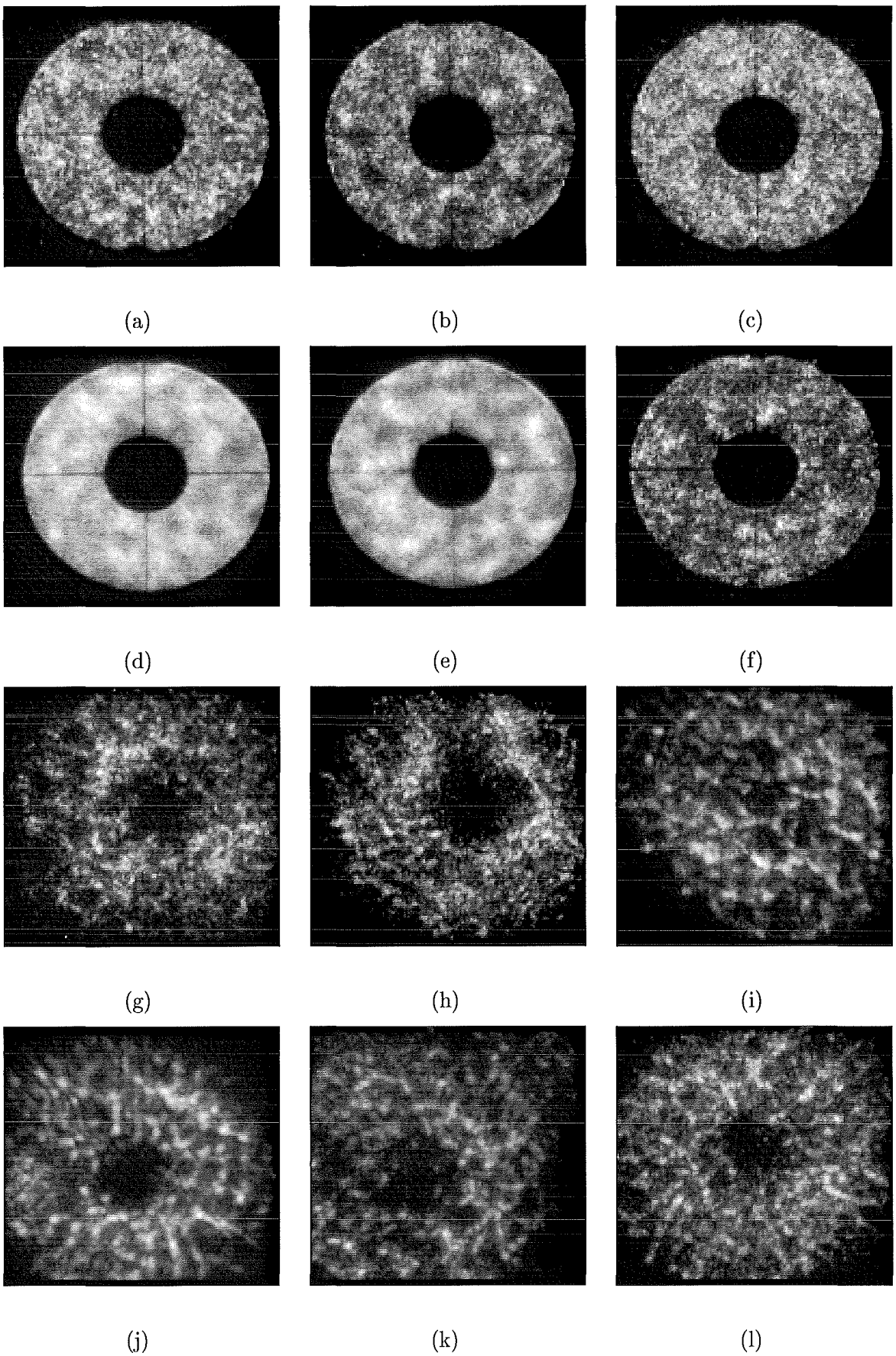

Figure 7.16: *Sample SCIDAR data frames. (a) - (f) Classical SCIDAR data and (g) - (l) Generalised SCIDAR data.*

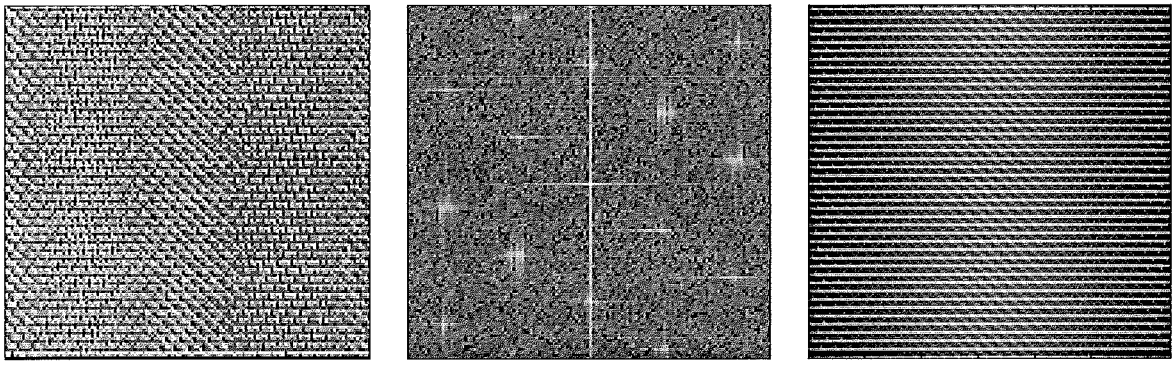

(a) (b) (c)

Figure 7.17: *Measurement noise. (a) A single noise frame, (b) corresponding noise spectrum and (c) average autocovariance of the noise.*

Using this notation the quantity of interest, the SCIDAR data covariance, is given by

$$\begin{aligned} C'(\rho) &= [[(s(\rho)+\bar{s}(\rho))-\bar{s}(\rho)]*[(s(\rho)+\bar{s}(\rho))-\bar{s}(\rho)]] \\ &= s(\rho)*s(\rho), \end{aligned} \tag{7.27}$$

where $*$ denotes the correlation operator. This can be calculated from the autocorrelations of the measured quantities,

$$\begin{aligned} A_d &= d(\rho)*d(\rho) \\ &= s(\rho)*s(\rho)+n(\rho)*n(\rho)+\bar{s}(\rho)*\bar{s}(\rho) \\ &+ \bar{n}(\rho)*\bar{n}(\rho)+\bar{s}(\rho)*\bar{n}(\rho)+\bar{n}(\rho)*\bar{s}(\rho) \end{aligned} \tag{7.28}$$

$$\begin{aligned} A_n &= (n(\rho)+\bar{n}(\rho))*(n(\rho)+\bar{n}(\rho)) \\ &= n(\rho)*n(\rho)+\bar{n}(\rho)*\bar{n}(\rho) \end{aligned} \tag{7.29}$$

$$\begin{aligned} A_{\bar{d}} &= \bar{d}(\rho)*\bar{d}(\rho) \\ &= \bar{s}(\rho)*\bar{s}(\rho)+\bar{n}(\rho)*\bar{n}(\rho) \\ &+ \bar{s}(\rho)*\bar{n}(\rho)+\bar{n}(\rho)*\bar{s}(\rho) \end{aligned} \tag{7.30}$$

$$A_{\bar{n}} = \bar{n}(\rho)*\bar{n}(\rho), \tag{7.31}$$

to give,

$$C' = A_d - A_{\bar{d}} - A_n + A_{\bar{n}}. \tag{7.32}$$

This result is then normalised by division by the autocorrelation of the average SCIDAR data to compensate for the obstruction caused by the secondary mirror of the telescope and produces an unbiased covariance measurement. The normalised scintillation covariance, C, is thus

$$\begin{aligned} C &= \frac{A_d - A_{\bar{d}} - A_n + A_{\bar{n}}}{A_{(\bar{d}-\bar{n})}} \\ &= \frac{C'}{A_{\bar{s}}}, \end{aligned} \tag{7.33}$$

where

$$A_{\bar{s}} = \left(\bar{d}(\rho) - \bar{n}(\rho)\right) * \left(\bar{d}(\rho) - \bar{n}(\rho)\right). \tag{7.34}$$

The final result of the processing is the two-dimensional intensity covariance. Average spatial intensity covariances for 6 classical and 6 generalised measurements are illustrated in Fig. 7.18. Each turbulent layer creates a *triple peak* pattern comprising a central peak plus two secondary peaks (one on each side of the central peak) at distances proportional to the height of the corresponding layer. The pupil plane spatial intensity covariances contain several peaks and indicate the presence of between 1-3 distinct turbulent layers. The altitude sampling is a function of the binary star separation for classical and generalised SCIDAR so this accounts for the variation in location of the secondary peaks. The different orientations of the covariances can be attributed to the different binaries viewed, for instance (a), (b) and (g) correspond to the same binary star and as a result have the same orientation.

The generalised spatial intensity covariances all contain only one triple peak pattern each. The variations in the triple peak patterns for these covariances are a function of the binary star separation and defocus distance, i.e. (h) corresponds to a SCIDAR defocus of 2.26km with a binary star separation of 10.3, whereas (k) corresponds to the same defocus distance but a binary star separation of 34.9 arcseconds. The different orientations again result from the different binaries observed.

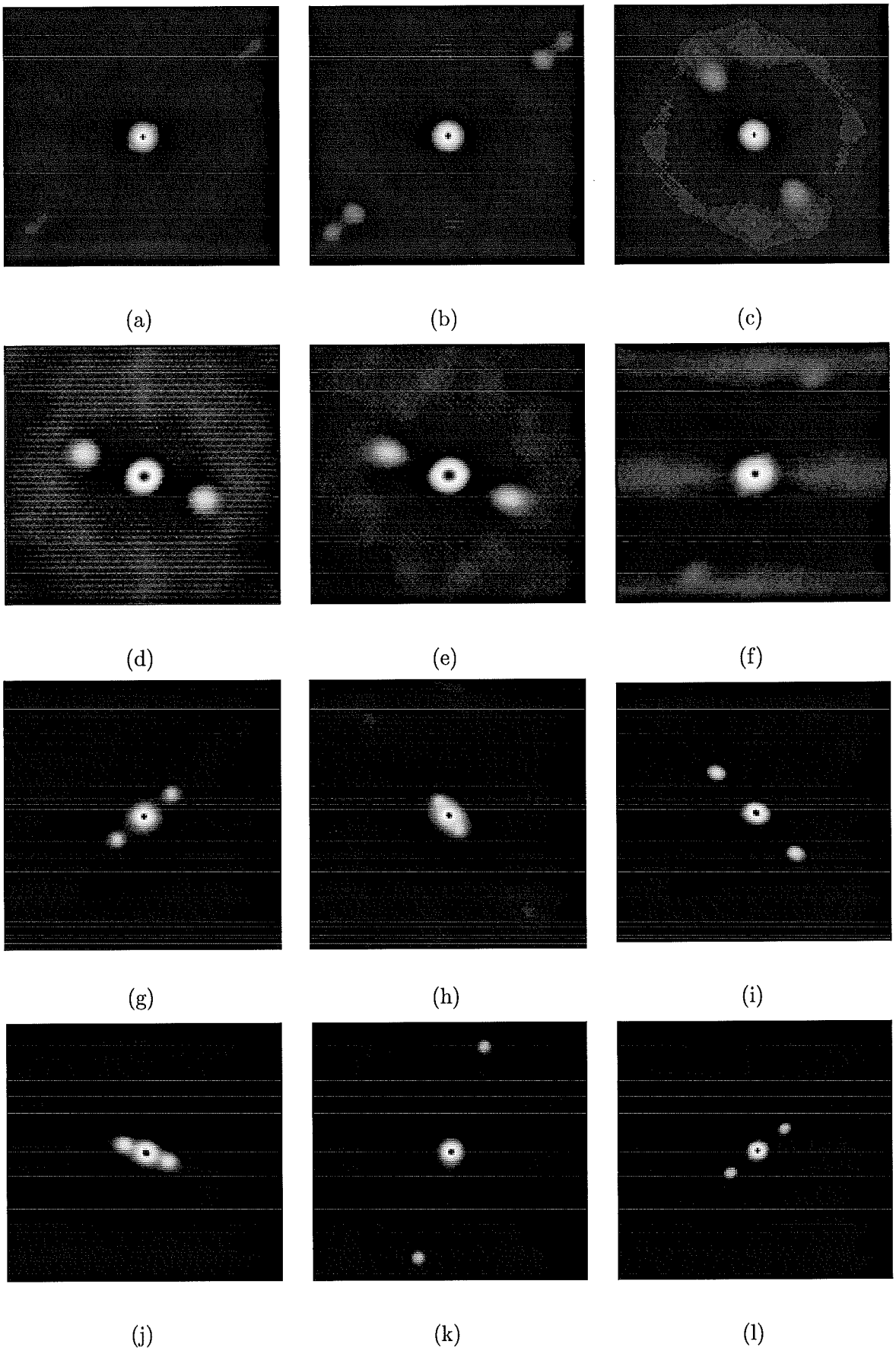

Figure 7.18: *SCIDAR covariances. (a) - (f) Classical SCIDAR covariances and (g) - (l) Generalised SCIDAR covariances*

7.3.4 Slice extraction

The next step requires taking a slice of the 2D covariance to obtain a 1D slice required for the inversion of Eq. (7.2). Although the theory was outlined in section 7.2.2, in practice this is achieved by removing a circle in the centre of the covariance, with diameter r_{mask}, that completely covers the central peak. The brightest remaining point should then correspond to one of the secondary peaks, and a slice is obtained from the centre through this point. Another slice is taken perpendicular to this slice and subtracted from it leaving the central peak removed covariance slice. When the triple peak pattern is nothing more than an elongated central peak this is very difficult, for example the peaks in the covariance in Fig. 7.18(h) are very close together. In practice this restricts the binary star separations and defocus distances that can be used. Other problems relating to the extraction of central peak removed covariance slices are discussed in section 7.5.1.

7.3.5 $C_N^2(h)$ estimation

The estimated turbulence profiles corresponding to the data and covariances in Figs. 7.16 and 7.18 respectively are illustrated in Fig. 7.19. The generalised SCIDAR profiles (Figs. 7.19(g) to (l)) all consist of a strong single peak at or close to ground level and various other peaks at the level of the noise. The fit to the data in each case is very good as illustrated in Fig. 7.20. The generalised SCIDAR profiles are an order of magnitude stronger than the classical SCIDAR profiles illustrated in Figs. 7.19(a) to (f). This is not surprising considering that the altitude at which the telescope is located (1031m above sea level) is low compared to most other observing sites, and no steps are taken to combat turbulence inside and outside the telescope dome. No high altitude information is seen in either the reconstructions or in the generalised SCIDAR covariance data. However, in many of the reconstructed profiles the ground level layer extends beneath the telescope aperture. This type of response has been noted by Avila and co-workers [4, 5]. They suggest that it is part of the response of the instrument to $C_N^2(h)$ just above the ground. In addition, splits are seen in several of the reconstruction peaks, indicating a possible mismatch between the assumed and actual turbulence statistics. Table 7.5 contains the estimated r_0 values for each profile, which range between 5cm and 30cm, and are larger than expected.

The pupil plane profiles Figs. 7.19(a) to (f) , indicate the presence of between 1 and 3 high altitude layers. In each case, these are consistent with the corresponding covariance data as indicated by the fit to the data in Fig. 7.20. The reconstructions in 7.19(a) and (b) were obtained from covariances with very little visible background disturbance and produce 3 and 2 distinct layers respectively. The layers reconstructed in Figs. 7.19(c) to (f) are not so well defined. The covariances corresponding to each of these reconstructions have significant regions of disturbance running through their respective secondary peaks which could account for the poor quality of the reconstructions. For example in (c) although a definite peak at about 12km has been reconstructed, smaller peaks either side of this peak have appeared and are not apparent from the corresponding covariance data.

The peak widths vary from profile to profile, a direct consequence of the sampling determined by the binary star separation and the amount of regularisation necessary to obtain meaningful solutions. Regardless of the size, width and shapes of the reconstructed layers the turbulence appears highly discretised and dominated by 1 to 3 distinct layers. The small peaks in the reconstruction appear to be noise as they are inconsistent with the knowledge that the turbulence exists in a finite number of layers. Also of interest is that the largest peaks in (c) to (f) indicate splits, a phenomenon also seen in many of the generalised SCIDAR reconstructions. The estimated r_0 values for the classical SCIDAR profiles start at 35cm (see Table 7.5), considerably larger than the conditions at the time suggested.

Overall, the turbulence appears to be dominated by low altitude turbulence close to the telescope pupil, which includes turbulence inside and just above the telescope dome. The high altitude turbulence is more fluid, in that the number of dominant layers can change over short periods of time as is illustrated by Figs. 7.19(a) and (b) taken 2 hours apart. In addition, there appears to be a dominant high altitude layer at approximately 10 - 12km above the telescope pupil.

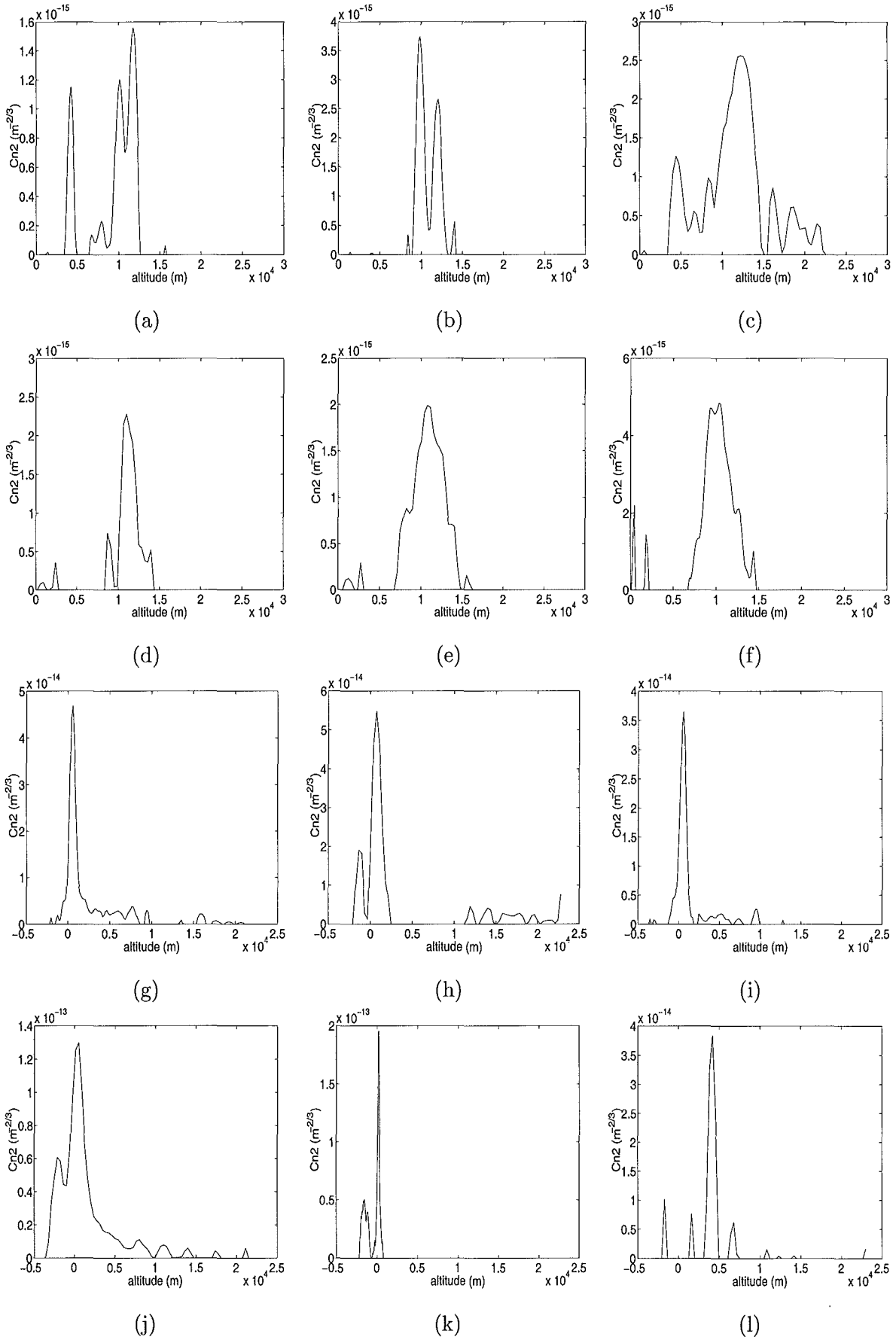

Figure 7.19: *$C_N^2(h)$ estimates reconstructed from (a) - (f) Classical SCIDAR covariance data and (g) - (l) Generalised SCIDAR covariance data.*

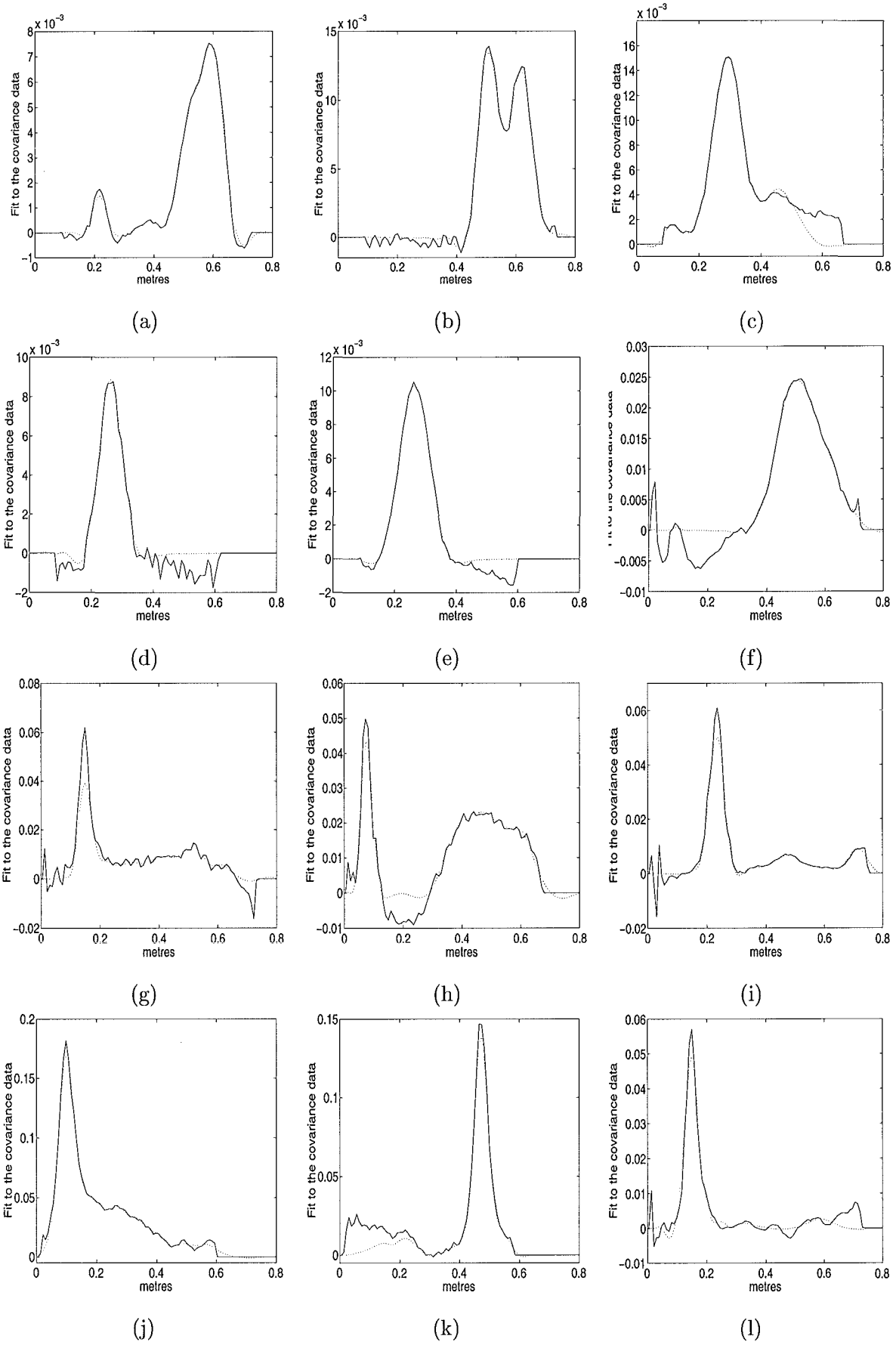

Figure 7.20: *The fit (dotted) to the covariance data (solid). (a) - (f) Classical SCIDAR and (g) - (l) Generalised SCIDAR.*

Profile	r_0 (cm)
Run 12 (Fig. 7.19)(a)	84
Run 16 (Fig. 7.19)(b)	60.8
Run 20 (Fig. 7.19)(c)	58.4
Run 28 (Fig. 7.19)(d)	115.4
Run 36 (Fig. 7.19)(e)	84.8
Run 56 (Fig. 7.19)(f)	34.4
Run 17 (Fig. 7.19)(g)	15.9
Run 21 (Fig. 7.19)(h)	18.4
Run 22 (Fig. 7.19)(i)	19.6
Run 29 (Fig. 7.19)(j)	8.2
Run 40 (Fig. 7.19)(k)	5.2
Run 42 (Fig. 7.19)(k)	31.7

Table 7.5: *r_0 estimates for the $C_N^2(h)$ profiles illustrated in Fig. 7.19.*

7.4 Estimation of the velocity profile $v(h)$

Although the estimation of $v(h)$ was not the major emphasis throughout this research, its estimation is useful for confirming layer altitudes; low altitude turbulence associated with the dome does not move, whereas high altitude turbulence is characterised by its movement. A different analysis of the short exposure scintillation data frames is required to estimate $v(h)$, the layer velocities as a function of altitude, namely a spatiotemporal analysis. The same initial steps as required for the $C_N^2(h)$ estimation are performed, however, it is the cross covariance of the data frames that is calculated, producing an average spatiotemporal covariance function. In the analysis presented here the 1st frame was correlated with the 5th, the 2nd with the 6th and so on giving dt, the time difference between correlated frames, equal to 10.6ms. The corresponding dv is given as

$$dv = \frac{dr}{dt}. \tag{7.35}$$

A data frame was captured every 2.7ms, hence $dt = 4 \times 2.7\text{ms} = 10.6\text{ms}$ and $dr = 1/117$ metres, so $dv = 0.8\text{ms}^{-1}$.

Typical average cross covariance results for pupil plane and generalised data are presented in Fig. 7.21. Fig. 7.21(a) illustrates two triple peak patterns displaced from the origin, corresponding to the two layers present. Fig. 7.21(b), however, has only one triplet located in the centre of the cross correlation result. The distance from the centre of each triplet in pixels, when multiplied by dv gives the speed of the corresponding layer. The triplets corresponding to layers at altitudes of 10km and 12km have velocities of 6.45ms^{-1} and 11.63ms^{-1} respectively. In Fig. 7.21(b) the single triplet is in the centre of the cross correlation, hence it appears to be stationary, a good indication that this turbulence is in fact associated with the telescope dome.

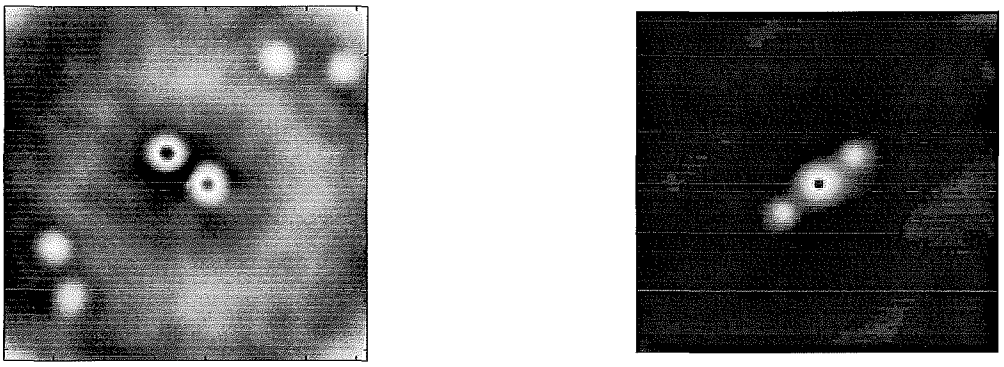

(a) (b)

Figure 7.21: *Average cross covariances for (a) classical and (b) generalised SCIDAR data.*

Although the analysis presented here was performed manually it is possible to automate the calculation of $v(h)$. Kluckers *et al* [85] outline a method for doing this which they call *template correlation.* The altitude of each layer present must first be calculated from the covariance data. This combined with the orientation of the binary allows a template for each layer to be constructed, corresponding to the ideal spatial covariance function for a layer at that height and orientation (see Fig. 7.22). The covariance of each template with the average cross covariance function returns a peak offset from the centre (zero velocity position) by an amount proportional to the velocity of the layer.

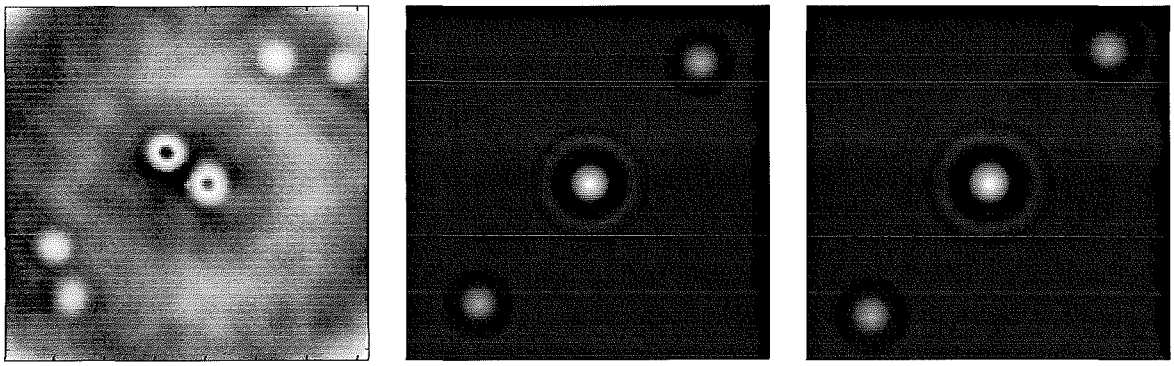

(a) (b) (c)

Figure 7.22: *Template correlation. (a) Average cross correlation data, (b) and (c) correspond to ideal spatial covariance functions for the two layers present in (a).*

7.5 Practical concerns arising from the experimental results

The results illustrated in section 7.3.5 correspond to r_0 values that do not match the *seeing* conditions observed at the time, where *seeing* refers to the ability to resolve two point objects when observed through the atmosphere. Uncompensated atmospheric seeing at a good site can be as low as 0.45 arcseconds or as high as 2 arcseconds. During particularly bad seeing conditions at Mount John the observation of a binary star of 4.4 arcseconds separation was made. From the image of the star on the monitor it was impossible to resolve the two stars, indicating seeing of worse than 4.4 arcseconds. Generally, however, the seeing was in the order of 2-3 arcseconds. Using Eq. (3.46), $\lambda = 589 \times 10^{-9}$m and average seeing of $\theta = 3$ arcseconds gives an estimate for r_0 of approximately 5cm. This is considerably smaller than the average values consistently returned for the complete turbulence profiles estimated using the generalised SCIDAR technique.

The problem of larger than expected r_0 values was also noted by Kluckers *et al* [85]. They believe it could be due to the finite spatial and temporal sampling imposed by the practical implementation of the SCIDAR method. In an attempt to obtain a high SNR in the detected intensity the level of detectable scintillation is compromised. This was investigated by adding 2 and 5 consecutive frames together respectively, corresponding to exposure times of 3.7ms and 10.9ms, to simulate different temporal sampling rates. Both classical and

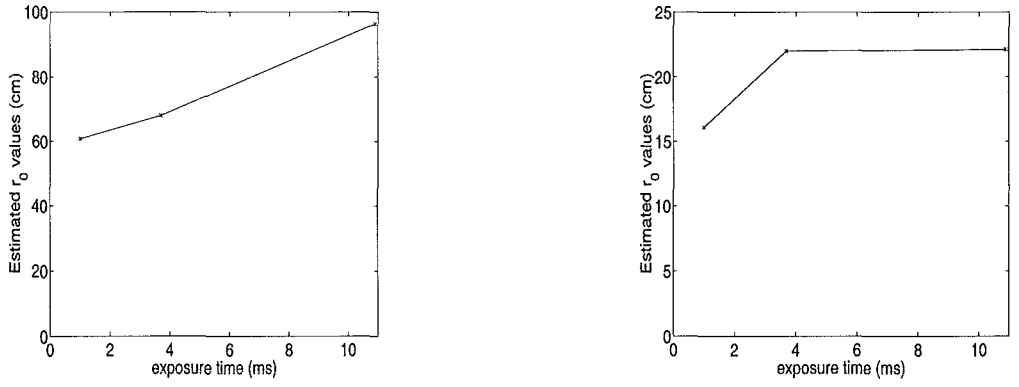

(a) (b)

Figure 7.23: *Estimated r_0 values for a variety of temporal sampling rates, for sample (a) classical SCIDAR and (b) generalised SCIDAR data.*

generalised SCIDAR data were combined, with the r_0 values estimated for exposure times of 1ms, 3.7ms and 10.9ms illustrated in Fig. 7.23. Note that the two plots are different, with the generalised SCIDAR result (Fig. 7.23(b)) indicating a much steeper drop towards temporal sampling of zero than the corresponding classical SCIDAR result (Fig. 7.23(a)). However, in each case extension of the results towards temporal sampling of zero is unlikely to result in r_0 values that match the conditions observed. Kluckers *et al* [85] also state that another possible cause of the larger than expected r_0 values is non-Kolmogorov effects, a theory that has been voiced in numerous SCIDAR papers [25, 47, 165].

The first series of tests involved simulating scintillation data corresponding to the experimental results. These were then compared with the measured scintillation data to determine the accuracy of the reconstructions presented in section 7.3.5. The scintillation simulated to match the experimental data is illustrated in Figs. 7.24 and 7.25. The match between the simulated and experimental classical SCIDAR data is less apparent than for the generalised SCIDAR data. However, it can be confirmed by comparing the size of the white areas in the simulated and experimental data. Scintillation structure of the same scale exists between the simulated and real data, a good indication that the heights of the layers are correct. However, the depth of the scintillation patterns do not match indicating the turbulence strengths have been inaccurately estimated.

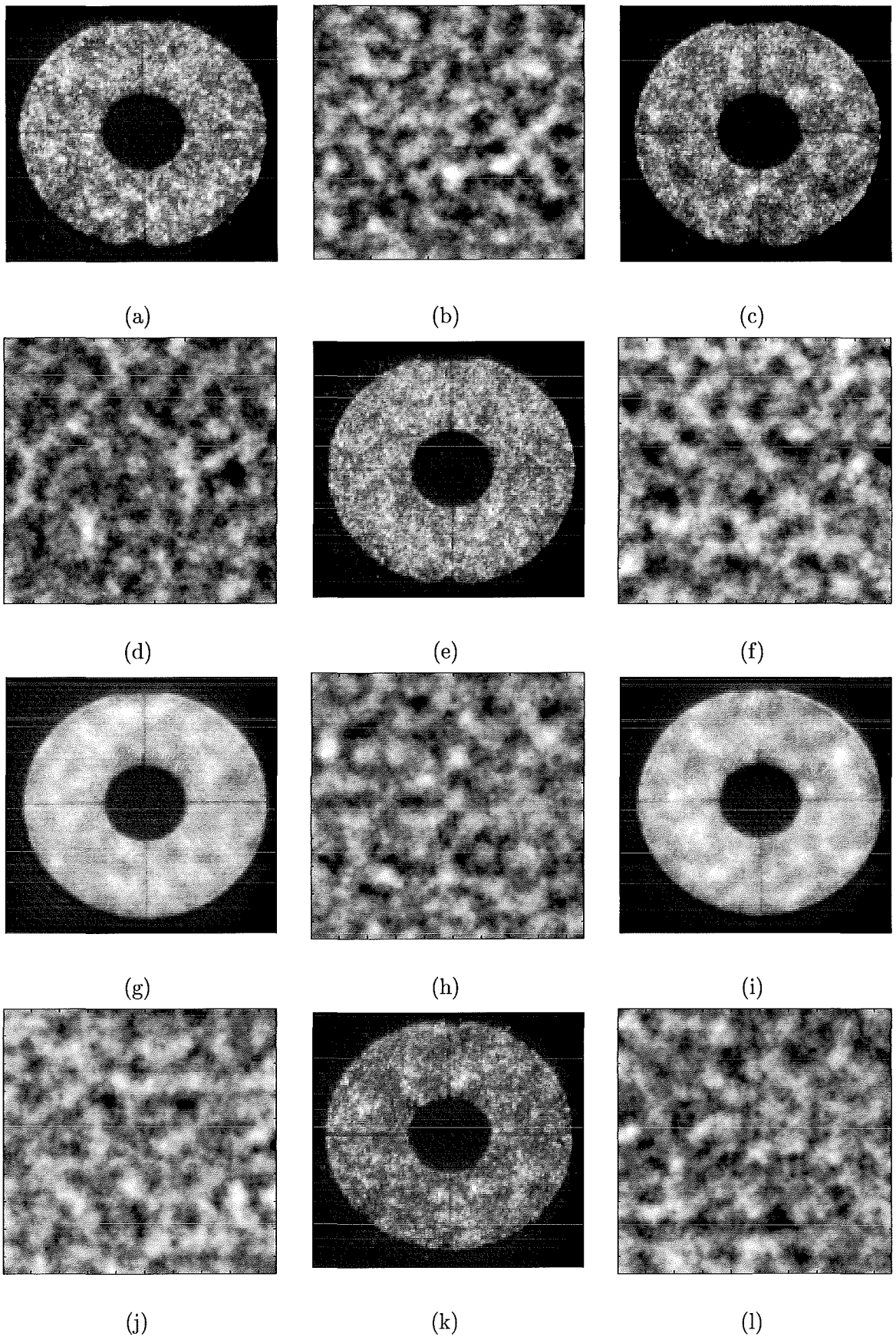

Figure 7.24: *Classical SCIDAR data. (a), (c), (e), (g), (i) and (k) experimental and (b), (d), (f), (h), (j) and (l) the corresponding simulated data.*

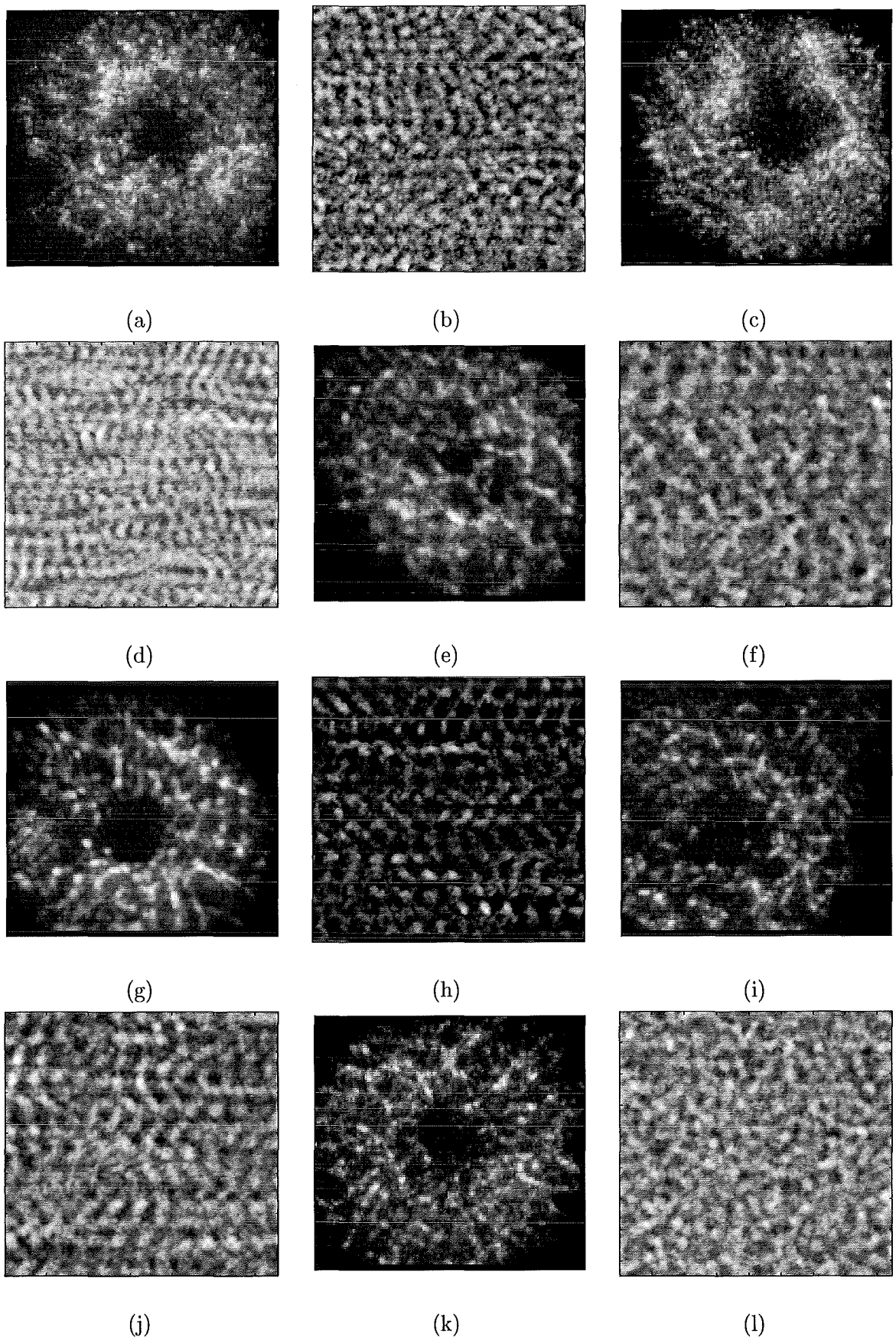

Figure 7.25: *Generalised SCIDAR data. (a), (c), (e), (g), (i) and (k) experimental and (b), (d), (f), (h), (j) and (l) the corresponding simulated data.*

Recall from Eq. (1.13) that

$$r_0 = \left[0.42k^2\sec(\zeta)\int C_N^2(h)dh\right]^{-3/5}. \tag{7.36}$$

This indicates that r_0 is purely a function of the area under the $C_N^2(h)$ profile, so as the area increases r_0 decreases and the converse is also true. Therefore, the cause of the discrepancies is directly related to inaccurate $C_N^2(h)$ profile strengths and area. Any number of factors could have caused these problems. Further, investigation was required in an attempt to account for these anomalies.

Thorough investigations of the different aspects of the inversion were performed. During this investigation several areas of concern arose. Firstly the existing techniques are limited by how the SCIDAR data is processed. Recall that normalisation of the measured covariance data by division by the autocorrelation of the average scintillation data is performed. This process gives rise to noise amplification and produces incorrect averages in the case of generalised SCIDAR data. Another drawback of these inversion techniques concerns the extraction of the 1D central peak removed covariance slices from the 2D covariance data. Incomplete removal of the central peak often occurred and can lead to a variety of problems. These areas of concern relating to the processing of the SCIDAR data are discussed in section 7.5.1 below.

It was also necessary to look beyond the processing to the assumptions made by the SCIDAR methods, to determine the limitations imposed by inaccuracies in the basis functions making up the T matrices. Each T matrix contains a series of basis functions generated from the assumed Kolmogorov scintillation statistics. The effects of deviation from the assumed statistics and other undesirable effects, such as diffraction, must also be considered when investigating a real system.

7.5.1 Data processing problem areas and solutions

The processing of the raw SCIDAR data and how it is inverted makes a considerable difference to the accuracy and resolution of the corresponding $C_N^2(h)$ estimate. Consider first

the scintillation due to a single star, $d(\rho)$, where

$$d(\rho) = m(\rho) + s(\rho). \tag{7.37}$$

Here $m(\rho)$ represents the mean data and $s(\rho)$ the zero mean scintillation data. The average ensemble covariance is equal to

$$\begin{aligned} C'(\rho) &= \langle d(\rho) * d(\rho) \rangle - \langle m(\rho) * m(\rho) \rangle \\ &= \langle s(\rho) * s(\rho) \rangle , \end{aligned} \tag{7.38}$$

where $*$ denotes the correlation operation. $C'(\rho)$ is a biased covariance estimate as $C'(\rho)$ for larger shifts, corresponding to higher altitudes and longer propagation distances, is averaged over a smaller area. This is apparent from Fig. 7.28, where the overlap of $p_1(\rho)$ and $p_2(\rho)$ decreases as the altitude increases. For propagation distances greater than $h_{\max}$, there is no correlation between the pieces of the atmosphere and hence no secondary peak is seen. However, an unbiased estimate can be obtained by dividing by the autocorrelation of the mean to give

$$C(\rho) = \frac{C'(\rho)}{\langle m(\rho) * m(\rho) \rangle}. \tag{7.39}$$

Consider now the problem illustrated in Fig. 7.28 corresponding to a binary star with components having a ratio of α and a defocus distance of $d$km, equivalent to a separation of θd at the telescope aperture. In this case the observed data is described by

$$d(\rho) \approx m(\rho) + s(\rho) + \alpha \left[m(\rho + \theta d) + s(\rho + \theta d) \right]. \tag{7.40}$$

This is an approximation since the atmosphere they pass through is slightly different. The average ensemble covariance is

$$\begin{aligned} C'(\rho) &= \langle d(\rho) * d(\rho) \rangle - \langle (m(\rho) + \alpha m(\rho + \theta d)) * (m(\rho) + \alpha m(\rho - \theta d)) \rangle \\ &= (1 + \alpha^2) \langle s(\rho) * s(\rho) \rangle + \alpha \left[\langle s(\rho) * s(\rho + \theta d) \rangle + \langle s(\rho) * s(\rho - \theta d) \rangle \right]. \end{aligned} \tag{7.41}$$

To correctly normalise this covariance each term must be normalised separately. The correct unbiased estimate of the first term is given as

$$\frac{(1 + \alpha^2) \langle s(\rho) * s(\rho) \rangle}{(1 + \alpha^2) \langle m(\rho) * m(\rho) \rangle} \tag{7.42}$$

and the normalised second and third terms respectively are

$$\frac{\alpha \langle s(\rho) * s(\rho + \theta d)\rangle}{\alpha \langle m(\rho) * m(\rho + \theta d)\rangle} \quad \text{and} \tag{7.43}$$

$$\frac{\alpha \langle s(\rho) * s(\rho - \theta d)\rangle}{\alpha \langle m(\rho) * m(\rho - \theta d)\rangle}. \tag{7.44}$$

The existing method for performing the normalisation for the binary star problem is to divide by

$$(1 + \alpha^2) \langle m(\rho) * m(\rho)\rangle + \alpha [\langle m(\rho) * m(\rho + \theta d)\rangle + \langle m(\rho) * m(\rho - \theta d)\rangle]. \tag{7.45}$$

For classical SCIDAR the defocus distance, d, is zero. Thus $\theta d = 0$ so the terms in Eq. (7.45) are identical, i.e.

$$\langle m(\rho) * m(\rho)\rangle = \langle m(\rho) * m(\rho + \theta d)\rangle = \langle m(\rho) * m(\rho - \theta d)\rangle. \tag{7.46}$$

As a result they completely overlap as shown in Fig. 7.26(a). In this case the normalisation is performed correctly. If θd is greater than twice the width of the scintillation pattern, D, the terms in Eq. (7.45) do not overlap, see Fig. 7.26(b). Hence the normalisation performed is equivalent to dividing each term in Eq. (7.41) by the corresponding normalisation term given in Eqs. (7.42) to (7.44). When $\theta d < 2D$, the terms in Eq. (7.45) partially overlap, as in Fig. 7.26(c). In this case the normalisation is performed incorrectly, different regions of the normalised covariance are too small while others remain unchanged. This under estimating of the covariance results in r_0 estimates that are too large.

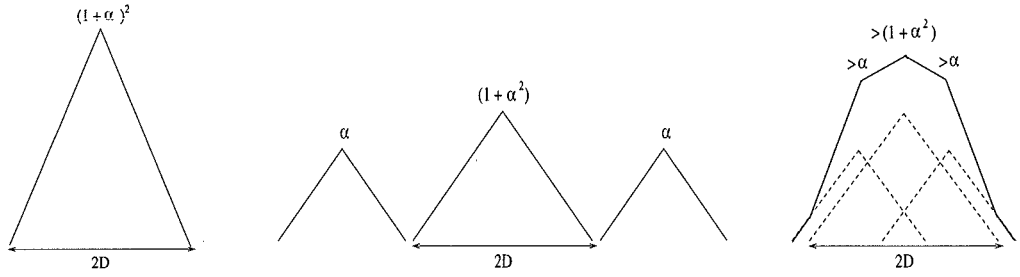

(a) (b) (c)

Figure 7.26: *Normalisation functions for (a) $\theta d = 0$, (b) $\theta d > 2D$ and (c) $\theta d < 2D$.*

Nearly all of the experimental data, captured during the observing run at Mount John, corresponds to $\theta d < 2D$. However, the r_0 estimate, corresponding to the profile in Fig. 7.19(k), was representative of the conditions observed. The reason for this is that the separation of 34.9 arcseconds was large enough to sufficiently separate the normalisation terms and enable correct normalisation to be achieved.

Generally the correct normalisation of the generalised SCIDAR covariances requires that each of the individual normalisation terms is extracted. Theoretically this can be achieved by performing a deconvolution of the function described by Eq. (7.45) with

$$\frac{(1+\alpha^2)}{\alpha}\delta(\rho) + \delta(\rho - \theta d) + \delta(\rho + \theta d) \tag{7.47}$$

to obtain an estimate of $\langle m(\rho) * m(\rho)\rangle$. The components of the deconvolution problem are illustrated in Fig. 7.27. Fig. 7.27(a) illustrates a sample normalisation term for $\theta d < 2D$, which consists of overlapped and added triangle functions. Fig. 7.27(b) contains the function described by Eq. (7.47) for the overlapped function in Fig. 7.27(a). An estimate of $\langle m(\rho) * m(\rho)\rangle$, the deconvolution output, is illustrated in Fig. 7.27(c). An alternative to deconvolution is to simultaneously image a single star to obtain $\langle m(\rho) * m(\rho)\rangle$. In either case, the estimated $\langle m(\rho) * m(\rho)\rangle$ can then be scaled and shifted as required for the normalisation of each term in Eq. (7.41).

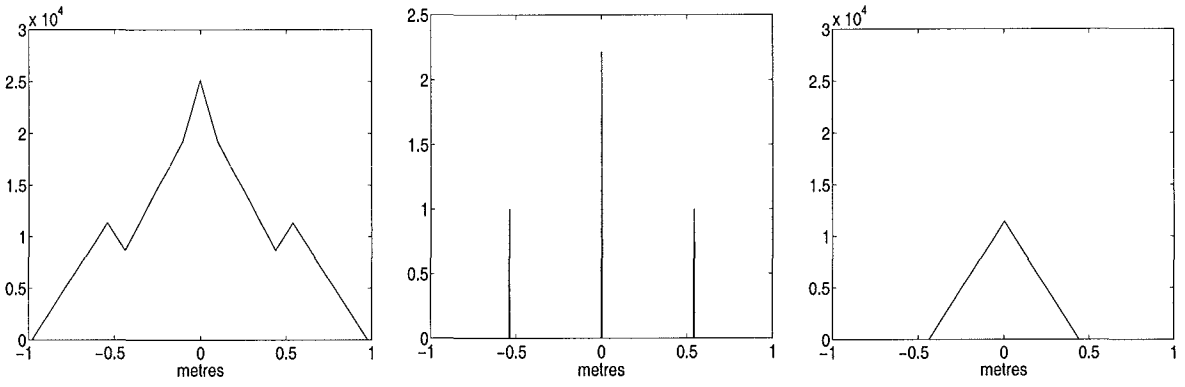

(a) (b) (c)

Figure 7.27: *Deconvolution to extract an estimate of $\langle m(\rho) * m(\rho)\rangle$. (a) Overlapped normalisation function, Eq. (7.45), (b) Eq. (7.47) and (c) Estimate of $\langle m(\rho) * m(\rho)\rangle$.*

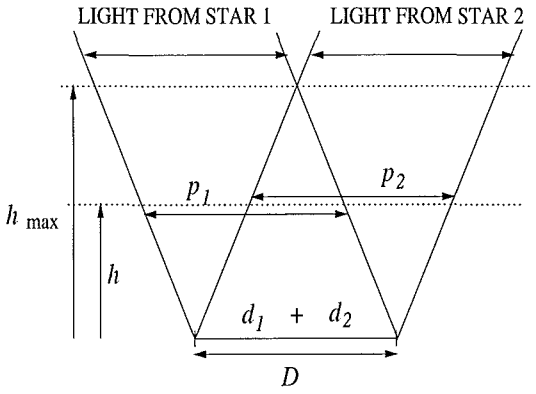

Figure 7.28: *The classical SCIDAR problem.*

Although the correct normalisation of the covariance data produces an unbiased covariance result, the division in Eq. (7.39) significantly amplifies any noise present, especially at larger shifts as illustrated in Fig. 7.29, corresponding to higher altitudes. A better approach is to solve

$$T'(\rho, h) \times C_N^2(h) + n(\rho) = S'(\rho), \tag{7.48}$$

where $T'(\rho, h)$ is defined by

$$T'(\rho, h) = T(\rho, h) \times \langle m_1(\rho) * m_2(\rho) \rangle \,, \tag{7.49}$$

thus avoiding the need for division in Eq. (7.39). Sample T and T' matrices are illustrated in Fig. 7.30. T' is intuitively more reasonable as less weighting is given to higher altitudes which are averaged over a much smaller area.

Reconstructions using both T, S and T', S' combinations were investigated. The unbiased and biased reconstructions corresponding to the slices and T matrices in Figs. 7.29 and 7.30 are illustrated in Fig. 7.31 for regularisation values of 10^{-8} and 10^{-6}. Due to the increased noise more regularisation was required to obtain a solution for the unbiased technique. In addition, the r_0 estimates for the biased reconstructions, where the correct value is 25cm, were more consistent than those estimated from the unbiased reconstructions.

The reconstructions illustrated in Fig. 7.31 were generated using the quadratic programming approach described in chapter 5. The same profiles generated using a projected least

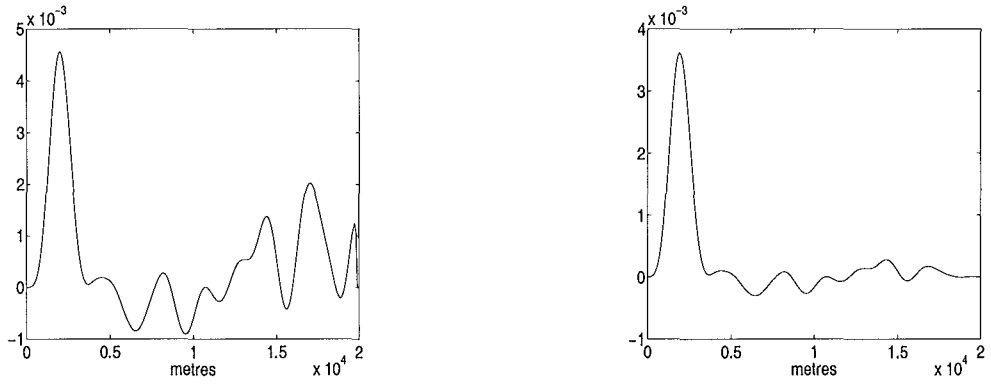

(a) (b)

Figure 7.29: *A comparison of covariance slices, (a) unbiased and (b) biased, due to an ensemble of 10 scintillation data frames propagated over 2km and imaged on a circular aperture with a large central obstruction.*

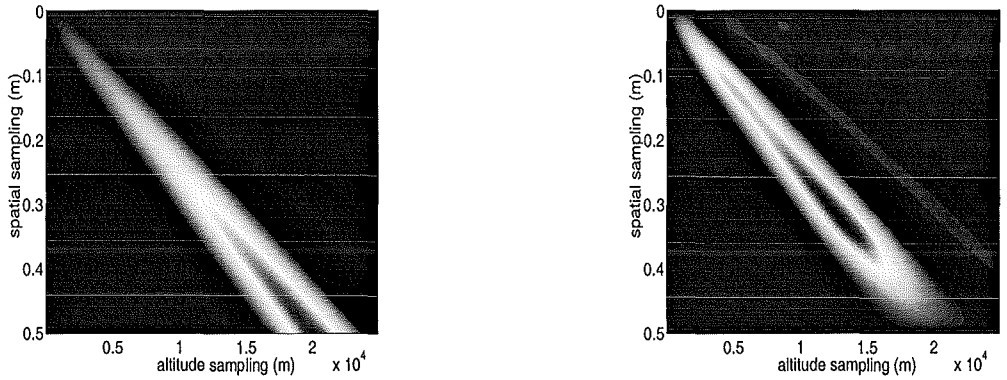

(a) (b)

Figure 7.30: *A comparison of T matrices, (a) unbiased and (b) biased.*

squares algorithm are illustrated in Fig. 7.32. The use of projection has led to the reconstruction of additional extra peaks and inaccurate r_0 estimates. These results emphasise that enforcing positivity is important in obtaining accurate and meaningful results.

The estimation of atmospheric turbulence profiles from biased experimental classical SCIDAR data was trialed, with a sample result illustrated in Fig. 7.33. The problems introduced by the superimposed border have been completely eliminated. However, the estimated r_0 values from these new reconstructions were consistently larger than the values listed in

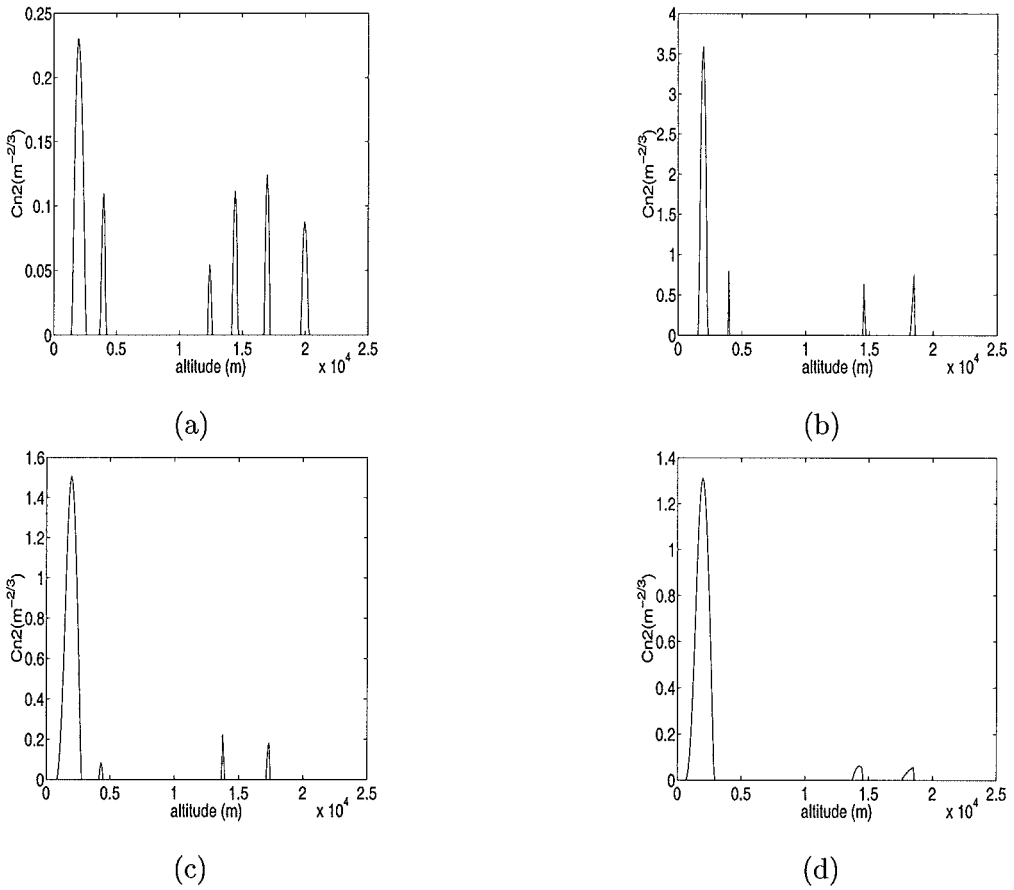

Figure 7.31: *Unbiased and biased $C_N^2(h)$ estimation using the accelerated quadratic programming method. (a) Unbiased $C_N^2(h)$ estimate for $\gamma = 1\times10^{-8}$, corresponds to an r_0 estimate of 67.8cm. (b) Biased $C_N^2(h)$ estimate for $\gamma = 1\times10^{-8}$, corresponds to an r_0 estimate of 23.3cm. (c) Unbiased $C_N^2(h)$ estimate for $\gamma = 1\times10^{-6}$, corresponds to and r_0 estimate of 25.2cm. (d) Biased $C_N^2(h)$ estimate for $\gamma = 1\times10^{-6}$, corresponds to an r_0 estimate of 25.7cm.*

Table 7.5. In addition, incomplete removal of the central peak is still a problem.

The estimation of atmospheric turbulence profiles from biased generalised SCIDAR data proved to be more difficult. It first required the extraction of $\langle m(\rho) * m(\rho)\rangle$ from Eq. (7.45) by deconvolution, as illustrated in Fig. 7.34. Fig. 7.34(a) contains the overlapped normalisation terms. A zoomed version of the function in Eq. (7.47) for this problem is shown in Fig. 7.34(b). The $\langle m(\rho) * m(\rho)\rangle$ estimate (Fig. 7.34(c)) has the correct general form when compared to a typical single star equivalent (Fig. 7.34(d)). This result was used

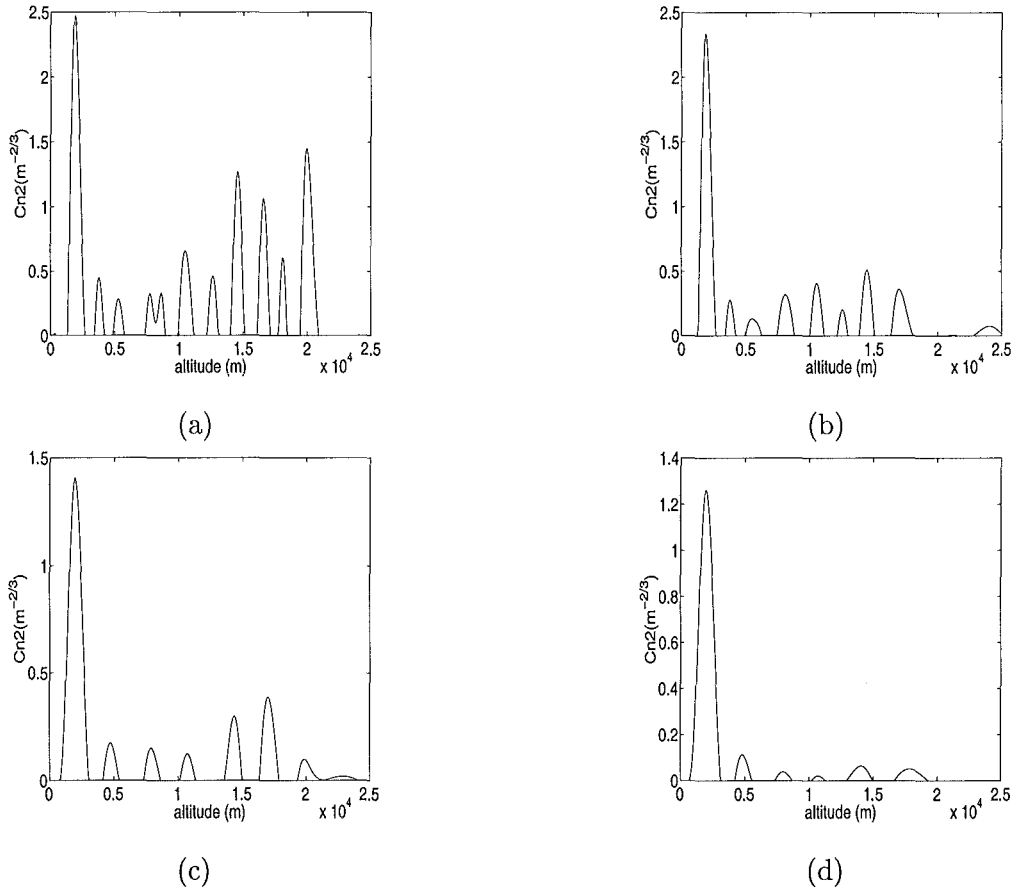

Figure 7.32: *Unbiased and biased $C_N^2(h)$ estimation with projection to enforce positivity. (a) Unbiased $C_N^2(h)$ estimate for $\gamma = 1\times10^{-8}$, corresponds to an r_0 estimate of 11.3cm. (b) Biased $C_N^2(h)$ estimate for $\gamma = 1\times10^{-8}$, corresponds to an r_0 estimate of 15.7cm. (c) Unbiased $C_N^2(h)$ estimate for $\gamma = 1\times10^{-6}$, corresponds to an r_0 estimate of 18.6cm. (d) Biased $C_N^2(h)$ estimate for $\gamma = 1\times10^{-6}$, corresponds to an r_0 estimate of 23.2cm.*

to weight the T matrix in the inversion to obtain T'. The resulting profile is illustrated in Fig. 7.35(a). The appearance of the profile is similar to its reconstruction using the original method (reproduced in Fig. 7.35(b)), however, the estimated r_0 is now 6.2cm.

A further processing problem involved determining the position of one of the secondary peaks from the covariance data. The position of the secondary peak is selected as the brightest point in the data after the central peak has been removed. It is used in the extraction of a 1D covariance slice from the 2D covariance data as described in section

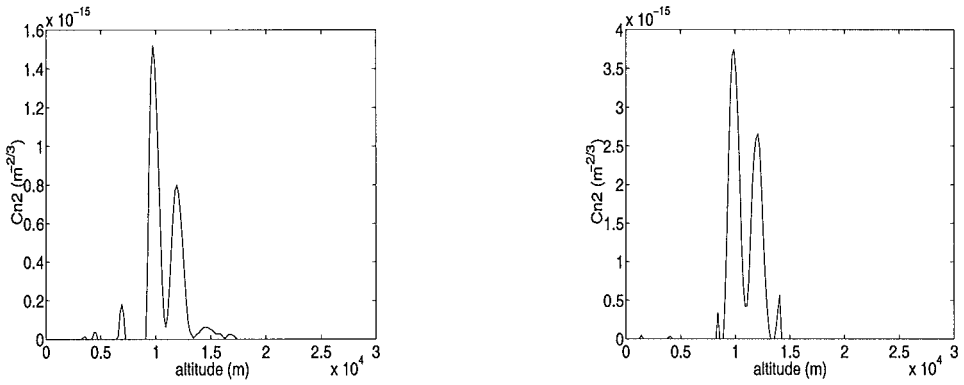

(a) (b)

Figure 7.33: *$C_N^2(h)$ estimate for Run 16 from (a) Biased data and (b) Unbiased data. Estimates for r_0 are 115cm and 60.8cm respectively.*

7.3.4. Noise amplification can result from the normalisation of the covariance data, even with the use of a mask to prevent significant noise amplification, producing pixels with values greater than the secondary peak (see Fig. 7.36). The brightest pixel in the image no longer corresponds to the secondary peak. When this happens, the slice from the centre of the image through this point is not guaranteed to contain information regarding the secondary peak. In this case the corresponding reconstruction is not representative of the data.

The first method for combating this problem was to increase the useful area inside the border. This often proved to be enough. However a mask was still required for the calculation and inevitably some of the data produced peaks that were not included within the largest possible area. An alternative solution was that outlined above for improving the normalisation of the covariance data as it also eliminates the problems due to the superimposed border.

There were also a large number of practical difficulties associated with the removal of the central peak from the measured covariance data. Firstly, in many cases the central peak was not circular. Hence slices perpendicular and parallel to the binary did not match well. Fig. 7.37 shows covariance slices containing tall thin peaks at low altitudes, resulting from

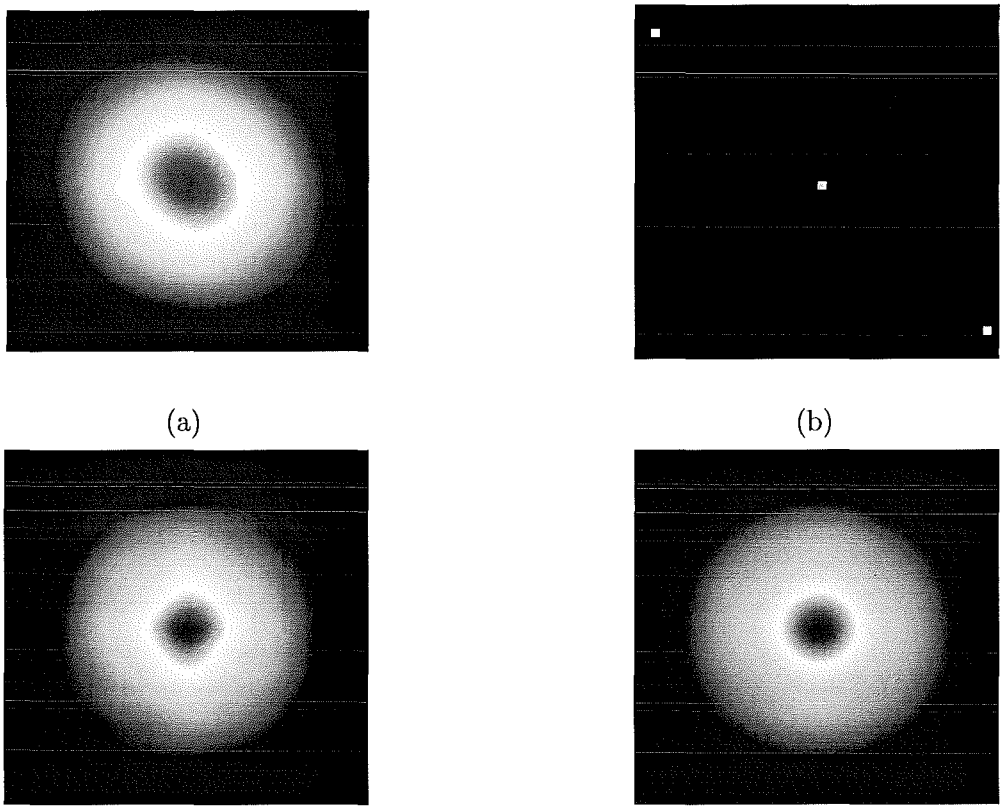

(a) (b)

(c) (d)

Figure 7.34: *Deconvolution of Eq.(7.45) for* $\langle m(\rho) * m(\rho)\rangle$ *for Run 22. (a) The function described by Eq. (7.45) for this problem, (b) a zoomed version of* $\frac{(1+\alpha^2)}{\alpha}\delta(\rho)+\delta(\rho-\theta d)+\delta(\rho+\theta d)$ *and (c) estimated* $\langle m(\rho) * m(\rho)\rangle$ *and (d) a sample* $\theta d = 0$ *result for comparison.*

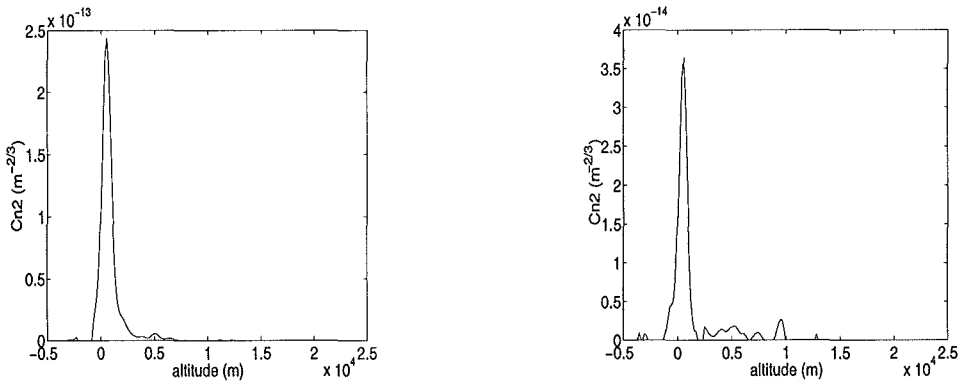

(a) (b)

Figure 7.35: $C_N^2(h)$ *estimates for Run 22 from (a) Biased data and (b) Unbiased data. Estimates for* r_0 *are 6.2cm and 19.6cm respectively.*

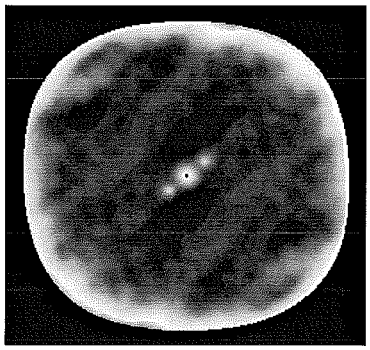

Figure 7.36: *A normalised covariance result. The normalisation can produce pixels with values greater in amplitude than the central and secondary peaks.*

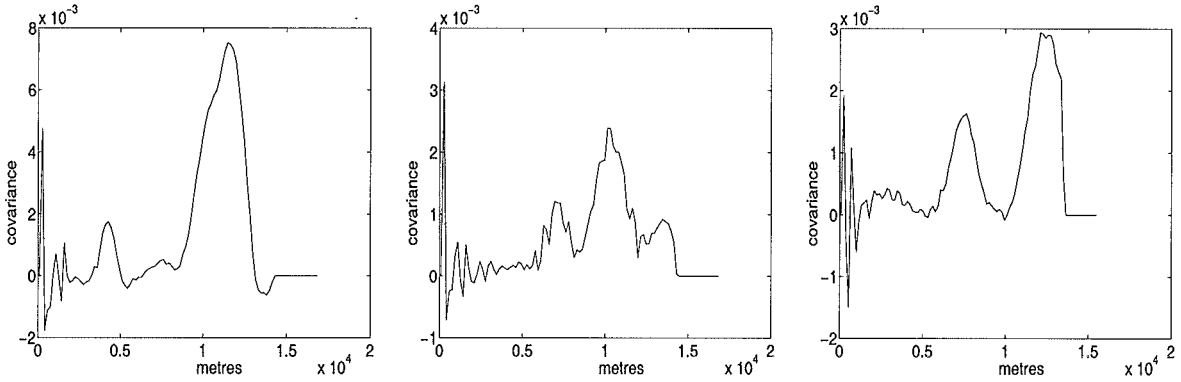

Figure 7.37: *Incomplete removal of central peak during extraction of 1D covariance slices.*

the unsuccessful removal of the central peak in each case. These peaks are incorrectly reconstructed as very large low altitude layers. To combat this problem, the first r_{mask} samples were set to zero manually, considerably slowing down the reconstruction process.

The obvious solution to this problem was to perform the inversion using a T or T' matrix containing both central and secondary peaks, thus eliminating the need to remove the central peak. Therefore, attempts to eliminate the problem of incomplete removal of the central peak were made. However, these were unsuccessful for classical SCIDAR data, perhaps because the secondary peaks are very small in comparison to the central peak, as illustrated in Fig. 7.38 for a typical covariance slice. Another possibility is that the

assumed covariances are not accurate, i.e. the central and secondary peaks do not have the correct relative heights in fitting with the assumed statistics. In addition, the generalised SCIDAR problem required the central and secondary peaks in the T matrix to be weighted individually before a reconstruction could be performed.

A sample complete generalised SCIDAR T matrix is illustrated in Fig. 7.39(a). Note that the central peak has a much larger weighting than the secondary peak, which is almost invisible, as expected. The reconstruction achieved using the sample T matrix and the complete slice (Fig. 7.39(b)) is illustrated in Fig. 7.39(c). A layer just above the telescope aperture has been successfully reconstructed. However, the r_0 value estimated is 1cm which is very small. This appears to be due to the fact that the central and secondary peaks are out of proportion for Kolmogorov statistics and the best fit to the data does not match it very well. This processing method, however, did not suffer from the problem of incomplete central peak removal.

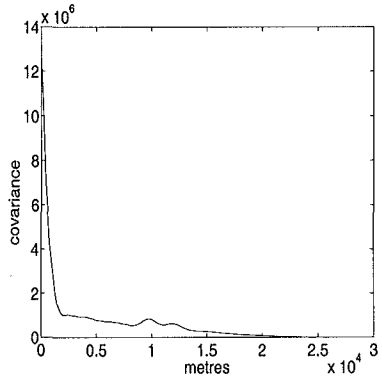

Figure 7.38: *A sample 1D classical SCIDAR covariance slice with the central peak intact.*

7.5.2 Different power spectra

A large amount of research has gone into confirming that high altitude turbulence often follows Kolmogorov statistics [25, 47, 170]. Although well developed turbulence is thought to follow Kolmogorov statistics, for developing turbulence and the breaking wave motion characteristic of upper altitude turbulence structure another power law may apply [25]. In

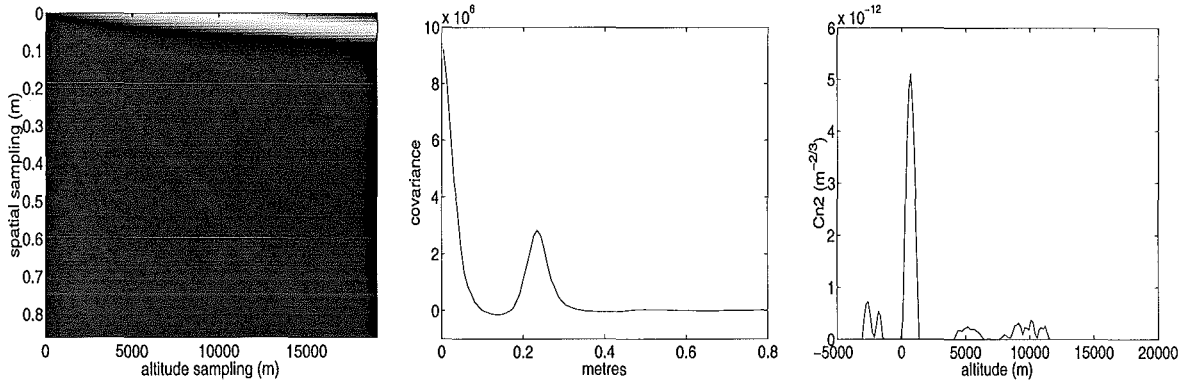

(a) (b) (c)

Figure 7.39: *Generalised SCIDAR reconstruction using both central and secondary peaks. (a) Complete T matrix, (b) complete covariance slice and (c) reconstruction.*

particular low altitude turbulence is thought to arise from the mixing of air of different temperatures from inside and outside the telescope dome. Deviation from Kolmogorov statistics has often been noted, for instance Strohbehn [153] reports that measurements of β in Eq. (4.97) made by Kropfli *et al* and Konrad indicate β values of 3.2 - 4.1 and 3.3 - 5.4 respectively, where $\beta = 3.67$ corresponds to Kolmogorov turbulence. Correct modelling would, therefore, require the actual turbulence statistics to be determined and the covariance curves that make up the T matrix changed appropriately.

Non-Kolmogorov turbulence was originally acknowledged as a problem in the single star case and its effects were investigated by Strohbehn in Refs. [152] and [153]. As discussed in chapter 4 the scintillation covariance does not appear to provide a direct measure of the tip-tilt component of the measured distortion. This information must be inferred from what is known about the statistics of the turbulence. Phase distortions of equal strengths, but obeying different power laws, contain different percentages of tip-tilt distortion. Any uncertainty in the form of the spectrum affects the determination of $C_N^2(h)$. Therefore, reconstruction of a covariance slice corresponding to $\beta = 12/3$, under the assumption of Kolmogorov statistics, underestimates the tip-tilt distortion and overestimates the size of r_0.

Reconstructions for a single turbulent layer simulated with different β values, located at 10km above the telescope, for the binary star problem were investigated. In each case a peak was reconstructed at the correct altitude for all power laws. However, the layer strengths varied from 10^{-13} to 10^{-14} and the corresponding r_0 values varied from 12cm to 33cm, with the correct value being 25cm. As expected a 12/3 power law underestimated the turbulence strength and 9/3 and 10/3 power laws overestimated it. This variation in estimated r_0 values indicates that the existing SCIDAR techniques, although powerful for estimating the heights of turbulent layers, can produce inaccurate turbulence strengths.

7.5.3 Diffraction and motion effects

The T matrices for classical and generalised SCIDAR are given by the ideal binary star covariance curves assuming Kolmogorov statistics. Diffraction effects are inherent in applications where information is truncated and then propagated. In the case of generalised SCIDAR, the incoming wavefronts are truncated by the telescope aperture before further propagation to a virtual plane, several kilometres beneath the telescope. The complex field after propagation to the virtual measurement plane $U(\mathbf{x}, d)$ is given by Eq. (7.17). Fuchs *et al* [58] argue that the effect of the limited aperture can be neglected when $D >> (\lambda h)^{1/2}$ and $D >> \frac{\lambda h}{r_0}$. These requirements mean that $D >>$ 10cm for $\lambda = 0.5$ μm, $h =$ 20km and $r_0 =$ 10cm. However, in the case of a small cassegrain telescope these conditions are not met. Consider a 1m telescope with a large central obstruction where the largest distance between any two edges, defined as the effective diameter D_E, is in the order of 30cm (see Fig. 7.40). An r_0 of 10cm requires $D_E >>$ 10cm, but 30cm is not considerably larger than 10cm. In addition, Avila *et al* [5], noted a diffraction pattern close to the borders of the Nordic Optical Telescope (NOT) pupil for data due to a generalised SCIDAR measurement plane located 3.4km beneath the telescope aperture. Finally, the pupil overlap inherent to the generalised SCIDAR technique further decreases the undistorted pupil data. These all suggest that the effects of the limited aperture cannot be ignored.

A series of covariance curves for the propagation of truncated distorted wavefronts beneath the telescope aperture were generated to determine the extent of the diffraction effects. For

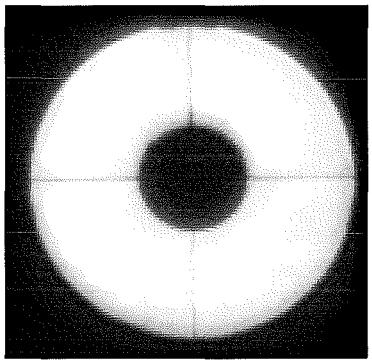

Figure 7.40: *Average scintillation measurement for 1m McLellan telescope.*

example, Fig. 7.41 illustrates simulated covariance curves for propagation of a truncated phase distorted wavefront over propagation distances of 2km, 5km and 10km all compared with the ideal simulated result. These results indicate that the truncation of the complex field during propagation results in an overall bias in the resulting covariance. The further the propagation distance after truncation the larger the bias introduced.

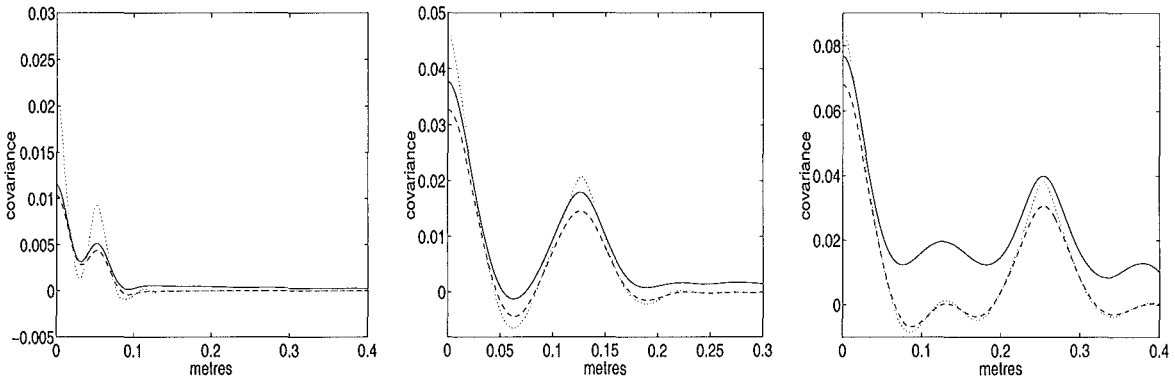

(a) (b) (c)

Figure 7.41: *Comparison of ideal (dotted), ideal non-zero inner scale (dashed) and simulated (solid) covariance curves when truncated wavefronts are propagated over (a) 2km, (b) 5km and (c) 10km.*

Random centroid motion inherent to imaging through atmospheric turbulence was also investigated. This is because approximately 90% of the phase distortion is in the tip and tilt of the wavefront, which cause the centroid motion. As a result movement of the telescope

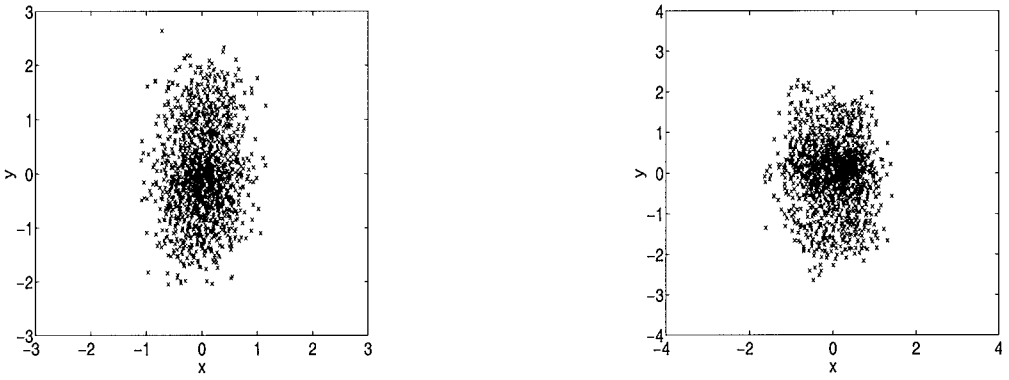

(a) (b)

Figure 7.42: *Random centroid motion of experimental data. (a) Sample classical SCIDAR data and (b) sample generalised SCIDAR data. The clearly elongated centroid distribution indicates telescope motion.*

pupil on the CCD as the turbulence evolved with time was expected. To determine the magnitude of the motion, centroids of 2000 data frames for a number of classical and generalised SCIDAR runs were calculated. The resulting plots illustrated in Fig. 7.42 are interesting in that the centroid motion is not symmetric, but elongated indicating motion of the telescope itself.

Random centroid motion not exceeding 20 pixels was added to simulated scintillation data and tested for a variety of different motion scenarios. When the two overlapped scintillation patterns are each simulated with the same random motion a larger overall bias is seen in the corresponding covariance curves, see Fig. 7.43(a), with the central and secondary peaks remaining in proportion. When each scintillation pattern is allowed to move independently, an overall bias is still noted and there is also a significant decrease in the relative height of the secondary peak. When diffraction and motion are combined, their effects add as illustrated in Fig. 7.44. Since current techniques use only the secondary peak in the calculation of $C_N^2(h)$ profiles, they will therefore indicate stronger turbulence than is in fact present. The correct approach would be to include diffraction and motion effects into the T matrix.

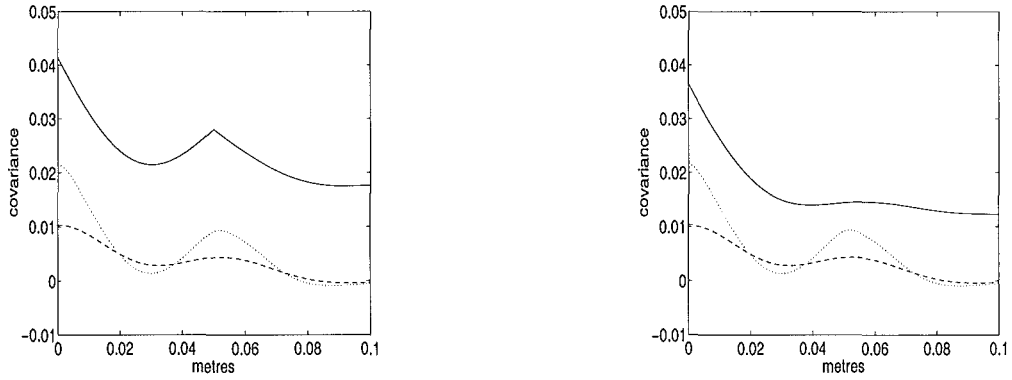

(a) (b)

Figure 7.43: *Comparison of ideal (dotted), non-zero inner scale (dashed) and simulated (solid) covariance curves for the effects of random centroid motion. (a) Dependent motion and (b) independent motion.*

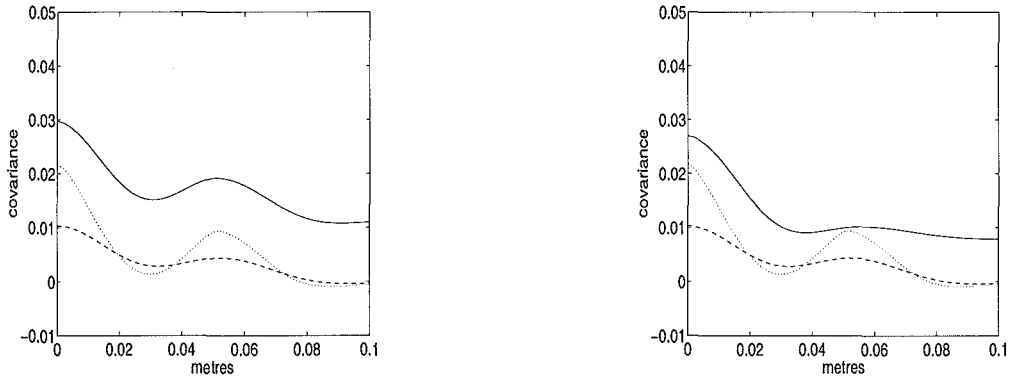

(a) (b)

Figure 7.44: *Comparison of ideal (dotted), non-zero inner scale (dashed) and simulated (solid) covariance curves for the effects of diffraction and random centroid motion. (a) Dependent motion and (b) independent motion.*

7.6 Summary

The development of a series of SCIDAR simulation tools outlined in the early part of this chapter was successful. These tools enabled a thorough investigation into the existing SCIDAR methods and the associated drawbacks. Improvements to the existing method resulted from this work and also provided the motivation for investigating alternative techniques presented in the following chapter.

The inversion required for estimation of the parameters which completely describe atmospheric turbulence is very ill-conditioned. The current SCIDAR methods overcome this problem by measuring scintillation due to a binary star as well as the incorporation of regularisation. Although the common approach to performing the inversion is to use maximum entropy based techniques, as they not only regularise the problem but also guarantee a positive solution, a non-linear minimisation is required. The application of quadratic programming methods to this problem proved to be successful and can be implemented using standard minimisation methods.

The processing of the Mount John data highlighted a number of discrepancies between the reconstructed turbulence profiles and the conditions observed at the time the data was captured, in terms of the estimated turbulence severity. This prompted further investigations into the processing and assumptions made by the SCIDAR techniques and unearthed a number of problem areas. It was shown that various aspects of the data processing considerably altered the results obtained. Alternative processing methods were proposed and trialed, with some success, in an attempt to remedy these problems. Even with this new processing further investigations were required. The accuracy of the basis functions making up the T matrix were also investigated. The effects of non-Kolmogorov statistics, diffraction and motion can lead to large differences between the measured and assumed statistics, and are areas that require further research.

In conclusion, the classical and generalised SCIDAR methods are powerful at estimating turbulent layer heights, but the turbulence severity estimates can be inaccurate for a variety of reasons. The need to assume a specific power law model is a definite drawback of these techniques. In addition, the practical difficulties associated with finding suitable binary stars is a major limitation of these techniques.

Chapter 8

Alternative Atmospheric Turbulence Profile Estimation

A number of problems with the current methods of turbulence estimation were discussed in chapter 7, and as a consequence this chapter looks at different techniques for estimating the optical properties of the atmosphere. The estimation of atmospheric turbulence profiles is necessary for the development of advanced adaptive optics technologies, particularly those aimed at imaging over a wide field of view. The classical and generalised SCIDAR methods, investigated in some detail in chapter 7, use crossed-beam scintillation measurements to improve the conditioning of the inversion required to estimate these parameters. Unfortunately the need to find binary stars of a suitable brightness and separation is a major limitation of these techniques. Another limitation of the SCIDAR technique is the potential for inaccurate layer strength estimation, due partly to the assumptions made by the technique. Furthermore, the covariance measures fundamental to the method appear to be blind to the tip-tilt components of the distortion, which are known to contribute towards approximately 90% of the overall distortion introduced by the atmosphere in the case of Kolmogorov statistics.

The first alternative investigated in section 8.1 is how measuring the scintillation from a single star at a number of different planes, obtained by propagating the wavefront over different distances, can be used to improve the conditioning of the inverse problem. This has the major advantage that only a single bright star needs to be observed, thus eliminating the need to find suitable binaries to profile the atmosphere.

Other alternatives to the SCIDAR technique are the well-established differential image motion monitor (DIMM) and Hartmann-DIMM (HDIMM) techniques for estimating the overall turbulence seeing, r_0. The second profile estimation technique, investigated in section 8.2, was mentioned by Bally *et al* [10] and combines the functionality of the SCIDAR technique with the HDIMM. Where the existing SCIDAR techniques use the correlation between scintillation patterns, this technique uses the correlation of the slopes of the two binary star components. The advantage of this technique over the SCIDAR methods is the higher SNR that can be achieved, as it requires only that an image is formed. As a consequence the restrictions on suitable binary stars are considerably reduced compared to the SCIDAR methods.

8.1 Single star SCIDAR

8.1.1 Noise performance of the SCIDAR method

The use of crossed beam scintillation measurements improves the conditioning of the inverse problem described by Eq. (7.2). An investigation of the sensitivity of single star and crossed beam techniques to noise illustrates this and is achieved by decomposing the corresponding $m \times n$ T matrix:

$$T = \mathbf{U}\Lambda\mathbf{V}^T, \tag{8.1}$$

where Λ is a diagonal matrix containing the singular values of T, $\mathbf{U} = (U_1, U_2, \ldots U_m)$, where the U_i are the left singular vectors of T and $\mathbf{V} = (V_1, V_2, \ldots V_n)$, where the V_i are the right singular vectors of T.

The singular values of the T matrix for binary separations of 0 to 10 arcseconds are illus-

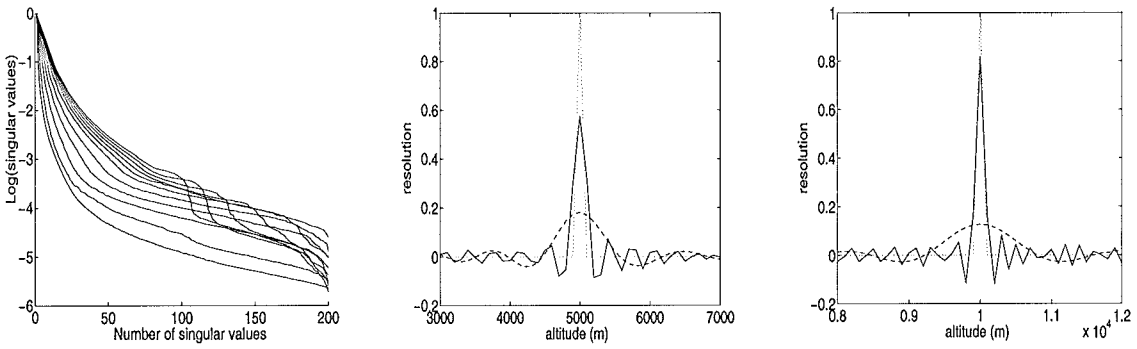

(a) (b) (c)

Figure 8.1: *(a) Comparison of singular values for increasing binary separation. The lowest curve corresponds to a separation of 0 arcseconds and the highest a separation of 10 arcseconds. A comparison of ideal (dotted), binary star with a 5 arcsecond separation (solid) and single star (dashed) resolutions for (b) 5km and (c) 10km respectively.*

trated in Fig. 8.1(a). Note that a separation of 0 arcseconds corresponds to the single star result. As the separation is increased the singular value spread decreases. Assuming a noise floor of 40dB the single star curve indicates that only the first 35 singular values are above the noise floor and hence only the first 35 singular vectors can be used for the inversion, whereas for a separation of 5 arcseconds the first 160 singular vectors can be used. The incorporation of the remaining singular vectors only adds to the noise amplification of the inversion. The reduction in the singular functions available for reconstruction has a large effect on the resolution that can be achieved. Figs. 8.1(b) and (c) illustrate the ideal, binary star of 5 arcsecond separation and single star resolutions for two different altitudes. The ideal case corresponds to a delta function at the corresponding altitude. The binary star resolution improves as the altitude increases, indicating a greater sensitivity to noise at low altitudes as noted by Tyler and Steinhoff [161]. By contrast, the single star resolution is consistently poor.

8.1.2 Proposed technique

The use of crossed beam scintillation measurements is one method for improving the conditioning of the inversion of Eq. (7.2). Unfortunately the need to find binary stars of

a suitable brightness and separation is a major limitation of these techniques. As an alternative, measuring the scintillation from a single star at a number of different planes is investigated as a means for improving the conditioning of the inverse problem.

However, before the proposed technique can be discussed it is necessary to investigate the sampling of the single star problem. Recall that the singular values for the binary star problem indicate an increase in resolution with increasing separation. This, combined with the fact that only the secondary peak is used for the inversion, means that adequate altitude sampling, dh, is simply a function of the binary star separation. Close to the zenith

$$dh = \frac{dr}{\theta}, \tag{8.2}$$

where dr is the spatial sampling and θ the binary star separation. Determining adequate sampling for the single star problem is not so straightforward. In this case the covariance data consists only of a central peak. It is important, therefore, that the central peak is sampled sufficiently to allow different measurements of it to be clearly distinguished. To do this the decomposition of the single star T matrix was investigated for altitude resolutions of 50m, 100m, 200m, 500m and 1000m. This produced 400, 200, 100, 40 and 20 singular vectors respectively. An inspection of the singular vectors for altitude sampling of 100m given in Fig. 8.2(a) indicates that only the first 50 are significant. Fig. 8.2(b) illustrates the number of significant singular vectors for each of the sampling intervals investigated. No increase in the number of meaningful singular vectors is gained in going from altitude sampling of 100m to 50m. Therefore, for the remaining single star simulations in this chapter 100m resolution is used.

With multiple measurement planes the problem to be solved now becomes

$$T_A(\rho, h) \times C_N^2(h) + n(\rho) = S_A(\rho), \tag{8.3}$$

where a subscript A denotes an augmented matrix containing M single star measurements, i.e.

$$T_A = [T_1 T_2 \ ... \ T_M]^T, \tag{8.4}$$

$$S_A = [S_1 S_2 \ ... \ S_M]^T, \tag{8.5}$$

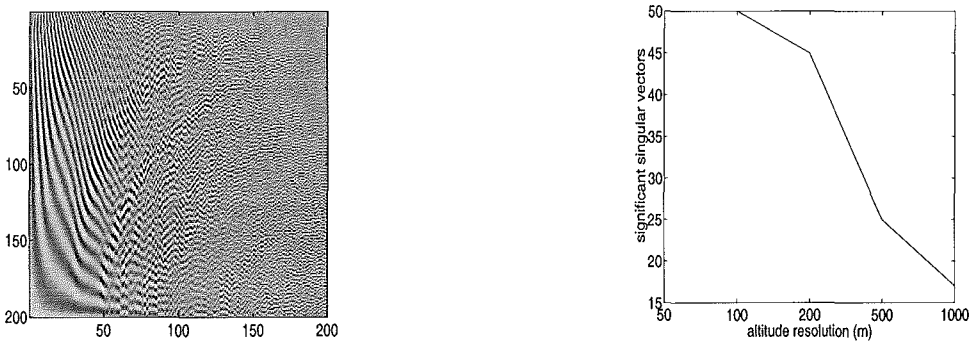

(a) (b)

Figure 8.2: *(a) Singular vectors for an altitude resolution of 100m. Only the first 50 appear significant. (b) Significant singular vectors for a variety of altitude resolutions.*

and $n(\rho)$ again denotes the noise on the system. S_A is obtained by reordering the matrix of single star covariance measurements into a vector. The analysis required is no different from the existing techniques but the performance varies significantly.

The introduction of one additional measurement plane at some altitude above the telescope aperture does not improve the overall singular value spread or the conditioning of the problem. However, it does increase the resolution that can be obtained at that altitude in the inversion of Eq. (7.1), as it "wipes out" any turbulence there (see section 7.1.3). A comparison of the resolutions for ideal, crossed beam, single star with a measurement plane at the aperture and single star with measurement planes at the aperture and 5km above the aperture examples are illustrated in Fig. 8.3. The augmented single star system returns an achievable resolution close to the ideal at 5km, with no significant improvement at 10km. The extension of this technique to a large number of measurement planes should, therefore, produce good resolution at all altitudes. Apart from multiple measurement planes a possibility is to tilt the CCD, each row thus capturing 1D scintillation data corresponding to different propagation distances. One-dimensional scintillation data is sufficient for the single star problem because the covariance in this case is radially symmetric.

The single star covariance matrices T_i for $i = 1, 2, \ldots M$ contain theoretical covariances that are offset from the origin by the distance between the measurement layer and the telescope

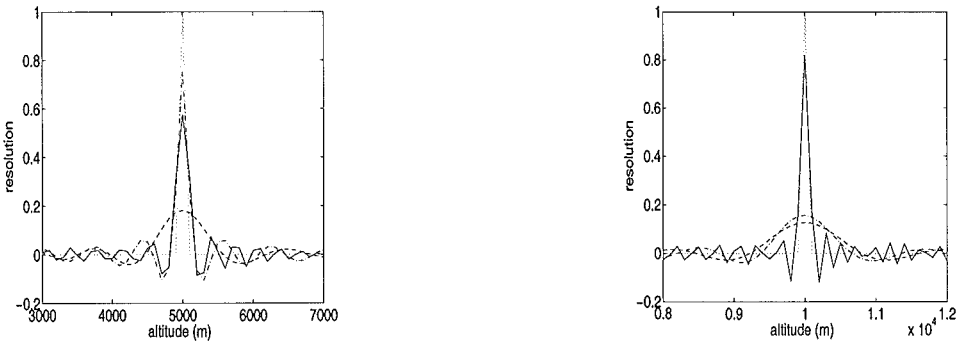

(a) (b)

Figure 8.3: *A comparison of ideal (dotted), binary star with a 5 arc-second separation (solid), single star with a measurement plane at the telescope aperture (dashed) and single star with measurement planes at the telescope aperture and 5km above the aperture (dashed-dotted) resolutions for a turbulent layer located at (a) 5km and (b) 10km.*

aperture. Consider the sample T_A matrix, illustrated in Fig. 8.4, corresponding to eleven measurement planes located at 0km (telescope aperture) to 10km above the aperture in increments of 1km. Fig. 8.4 shows a series of nulls corresponding to the respective heights of the measurement planes. When combined with the other basis functions these nulls produce the associated peak sharpening illustrated in Fig. 8.3(a). S_A for this problem contains eleven 1D covariance slices, end to end, corresponding to the average covariances calculated from the scintillation measurements made at each plane. The T_A matrix required for this inversion is very large requiring a considerable, although feasible, amount of computation.

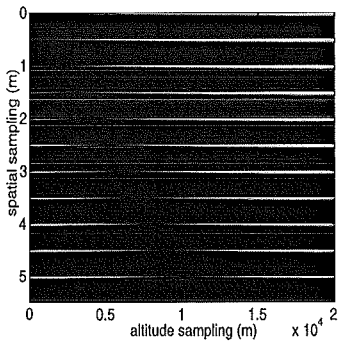

Figure 8.4: *A sample $T_A(\rho, h)$ matrix containing theoretical single star covariances for eleven measurement planes located at 0km to 10km in 1km increments.*

8.1.3 Performance

This technique was demonstrated for a simple three measurement plane combination, with the planes located at the aperture, 5km above the aperture and 10km above the aperture. Three turbulent layers at 1km, 10km and 12km were simulated as a typical profile may contain two high altitude layers and a boundary layer. The layer at 10km is at the altitude of one of the measurement planes, therefore, there should be a marked improvement in the reconstruction of the layer at 10km over the layers at 1km and 12km. Each layer has a C_N^2 value of $1\times10^{-13}\mathrm{m}^{-2/3}$ corresponding to an overall r_0 of 20.15cm. Using

$$T_A = \mathbf{U}_A \Lambda_A \mathbf{V}_A^T, \tag{8.6}$$

a pseudo-inverse of T_A was computed by

$$T_{A_N}^+ = \mathbf{V}_A \Lambda_{A_N}^{-1} \mathbf{U}_A^T, \tag{8.7}$$

where

$$\Lambda_{A_N}^{-1}(k,k) = \begin{cases} 1/\Lambda_A(k,k) & \Lambda_A(k,k) > \text{noise floor} \\ 0 & \text{otherwise} \end{cases}. \tag{8.8}$$

Note a subscript N is used to signify the number of singular vectors above the noise floor. The inversion can then be performed as

$$C_N^2(h) = T_{A_N}^+(\rho,h) S(\rho), \tag{8.9}$$

which is illustrated in Fig. 8.5(a) and returns an r_0 estimate of 20.22cm. This direct solution contains negative elements and, therefore, is not physically realisable. Enforcing positivity by projection gives the profile illustrated in Fig. 8.5(b) with a corresponding r_0 of 15.57cm. Since projection simply sets the negative elements to zero it does not conserve the energy contained in the solution and as a result the estimated r_0 value is altered considerably. An alternative is to solve

$$T_{A_N}(\rho,h) \times C_N^2(h) + n(\rho) = S_A(\rho), \tag{8.10}$$

where

$$T_{A_N} = \mathbf{U}_A \Lambda_{A_N} \mathbf{V}_A^T, \tag{8.11}$$

using the accelerated quadratic programming method outlined in chapter 5. This produces the result in Fig. 8.5(c) and an r_0 estimate of 20.01cm. In each case it should be noted

that when the layer height corresponds to the height of one of the measurement planes the resolution achieved at that altitude is very close to ideal. Note also that the enforcement of positivity has a significant effect on the resolution obtained.

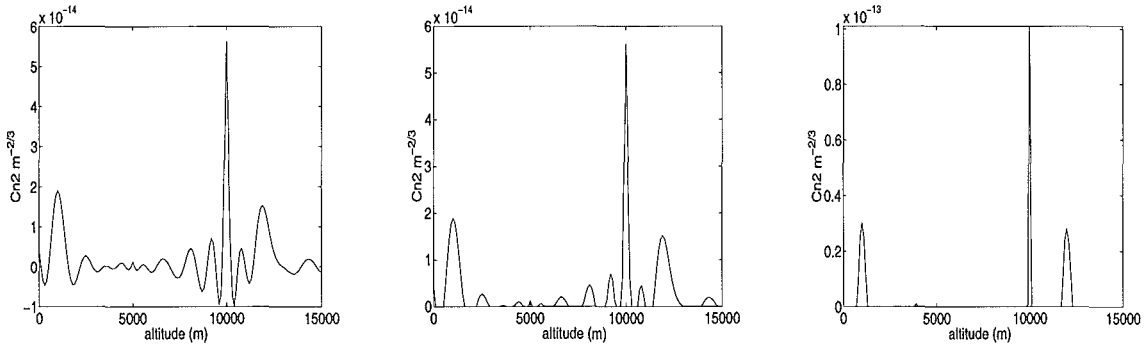

(a) (b) (c)

Figure 8.5: *Estimation of turbulence profiles for an SNR of 40dB for a single star with measurement planes at 0km, 5km and 10km. The turbulent layers are located at 1km, 10km and 12km. (a) Direct reconstruction, (b) direct reconstruction with projection and (c) quadratic programming reconstruction.*

8.2 Atmospheric turbulence estimation from slope measurements

A well-established technique for measuring the seeing conditions at a particular site is to use a differential image motion monitor (DIMM) [142]. The basic idea behind the technique involves measuring wavefront slopes over two small pupils some distance apart. This allows dual star images to be obtained whose relative motion gives a measure of the local wavefront tilts. In addition, since it is only the relative motion which is important, telescope tracking errors do not affect the results.

Direct measurements necessary to characterise atmospheric turbulence can also be made using a Shack-Hartmann wavefront sensor (SHWS) [10, 147], where a SHWS is generally used to measure wavefront phase perturbations. The Shack-Hartmann wavefront sensor is the most common type of wavefront sensor in use in adaptive optics systems due to its

simplicity, flexibility and widespread application [128]. It subdivides the incident wavefront using an array of lenslets as illustrated in Fig. 8.6, generating a set of subapertures. An image, referred to as a *spot*, is formed by each lenslet. In the absence of atmospheric turbulence, each image would be centred in the corresponding subaperture as illustrated by Fig. 8.7(a). However, in reality each spot is shifted from this central position by a quantity proportional to the local slope of the wavefront, see Fig. 8.7(b). The displacements in x and y directions of the spots around the central position can be directly related back to the slope of the incident wavefront. These centroid measurements can then be used to obtain the statistics of the phase fluctuations. Methods for estimating r_0 include calculating the covariance or differential variances of pairs of centroids [119].

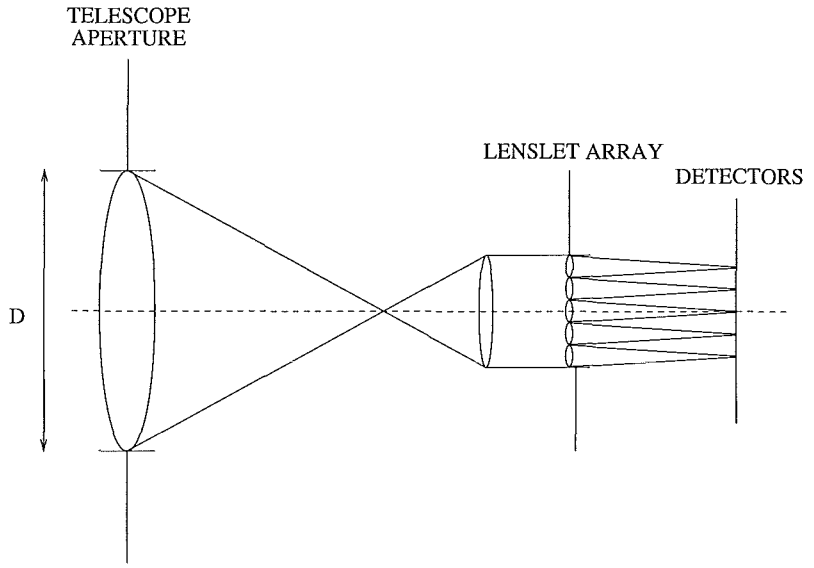

Figure 8.6: *Relationship between the telescope aperture and a Shack-Hartmann array of lenslets.*

An extension of this idea to turbulence profile estimation by the imaging of binary stars with a Hartmann differential image motion monitor (HDIMM) was mentioned by Bally *et al* [10]. When using a Shack-Hartmann wavefront sensor each component of the binary star produces a separate image in each subaperture, see Fig. 8.8. The light from each component of the binary star passes through the same turbulence, as illustrated in Fig. 8.9 for turbulent layers at different altitudes. Therefore, just as the scintillation due to each

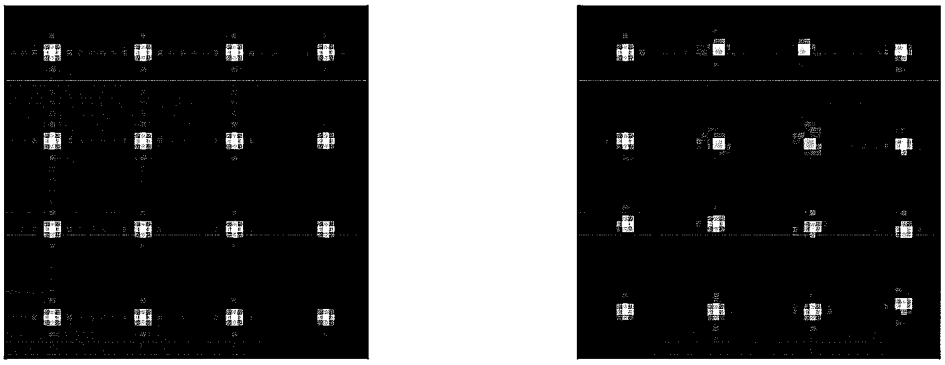

(a) (b)

Figure 8.7: *Typical Shack-Hartmann speckle images for a 4 × 4 lenslet array (a) without turbulence and (b) with turbulence.*

binary star component is correlated, so too are the slopes of the wavefronts due to each component. Since an overall slope corresponds to motion of the image (see section 3.4.2), this means that there is correlation in the movement of the spots due to each star. For example a layer at ground level (see Fig. 8.9(c)) results in images due to each binary star component that are exactly correlated and hence move in synchronisation. As the height of the turbulent layer increases (see Figs. 8.9(a) and (b)), the slopes seen by each component of the binary star become better correlated at a distance bs (defined in Eq. (7.19)). Therefore, measurement of the correlation of the centroid variances for each of these images can then be used to determine turbulent layer altitudes.

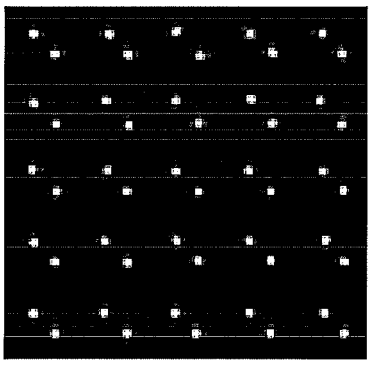

Figure 8.8: *Typical Shack-Hartmann speckle image for a 5 × 5 lenslet array when imaging a binary star.*

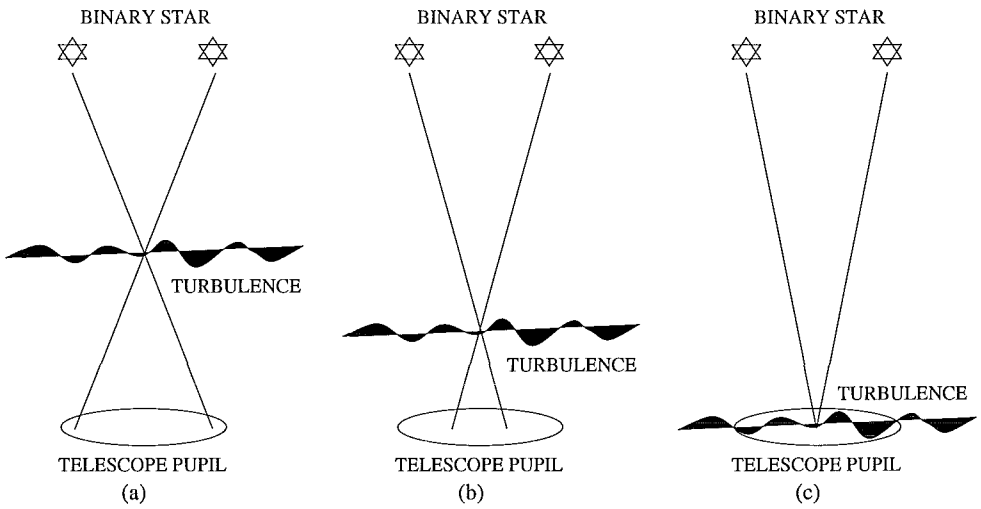

Figure 8.9: *Wavefront slope correlation for (a) high, (b) medium and (c) low altitude turbulent layers.*

The estimation of layer height information is achieved by inverting

$$S \times H(h) = S_m, \tag{8.12}$$

for $H(h)$ the turbulence height profile. Here S is a matrix of theoretical centroid variance correlations and S_m is the correlation of the measured centroid variances. Note that Eq. (8.12) has a very similar form to Eq. (7.2). For an $N \times N$ Shack-Hartmann array, S_m is a vector containing $4N^4$ elements. The theoretical slope correlation matrix, S, is calculated from results in Wallner [171].

The slope across the nth lenslet, s_n, is a weighted average of the local wavefront slope and is defined by [171]

$$s_n = \int_{-\infty}^{\infty} W_{sn}(\mathbf{x}) \left[\phi_n^s(\mathbf{x}) + v(\mathbf{x})\right] d\mathbf{x} \tag{8.13}$$

$$= \int_{-\infty}^{\infty} \left[-W_{sn}^s(\mathbf{x})\phi(\mathbf{x}) + W_{sn}(\mathbf{x})v(\mathbf{x})\right] d\mathbf{x}, \tag{8.14}$$

where $W_{sn}(\mathbf{x})$ is the weighting function for the nth lenslet, $\phi_n^s(\mathbf{x})$ is the slope of the wavefront phase in the direction of slope sensitivity of the nth lenslet, $W_{sn}^s(\mathbf{x})$ is the derivative of $W_{sn}(\mathbf{x})$ in the direction of slope sensitivity and $v(\mathbf{x})$ is the noise. A typical lenslet weighting function and its derivatives in the x and y directions are illustrated in Fig. 8.10. Therefore, Eq. (8.14) states that the wavefront slope across the lenslet is the integral of the difference

in the phase along the edges of the aperture in the direction of sensitivity. For lenslet 1 of dimensions $D \times D$, in Fig. 8.11, the x direction slope is equal to

$$s_1 = \int_{-\frac{D}{2}}^{\frac{D}{2}} \frac{\phi(-\frac{D}{2}, y) - \phi(\frac{D}{2}, y)}{D} dy. \tag{8.15}$$

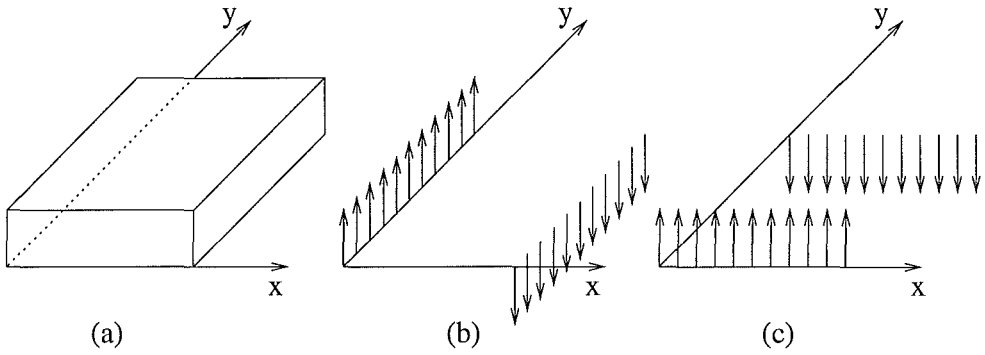

Figure 8.10: *(a) A typical lenslet weighting function and its derivatives in (b) x and (c) y directions.*

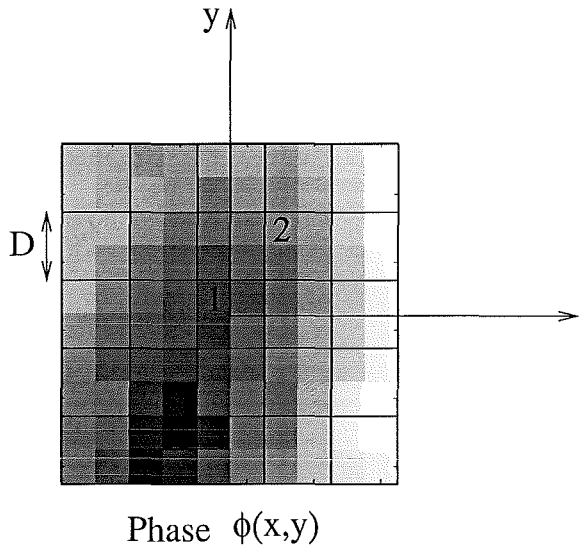

Figure 8.11: *The phase across a 5×5 lenslet array.*

The quantity of interest here is the correlation of lenslet slopes which is given by [171]

$$\begin{aligned} S_{nn'} &= \langle s_n s_{n'} \rangle \\ &= \int_{-\infty}^{\infty} \int_{-\infty}^{\infty} [W_{sn}^s(\mathbf{x}') W_{sn'}^s(\mathbf{x}'') \langle \phi(\mathbf{x}') \phi(\mathbf{x}'') \rangle \end{aligned} \tag{8.16}$$

$$+ \quad W_{sn}(\mathbf{x}')W_{sn'}(\mathbf{x}'')\left\langle v(\mathbf{x}')v(\mathbf{x}'')\right\rangle]\, d\mathbf{x}'d\mathbf{x}'' \tag{8.17}$$

$$= \int_{-\infty}^{\infty}\int_{-\infty}^{\infty}[-1/2W_{sn}^{s}(\mathbf{x}')W_{sn'}^{s}(\mathbf{x}'')D_p(\mathbf{x}',\mathbf{x}'')$$

$$+ \quad W_{sn}(\mathbf{x}')W_{sn'}(\mathbf{x}'')\left\langle v(\mathbf{x}')v(\mathbf{x}'')\right\rangle d\mathbf{x}'d\mathbf{x}''] \tag{8.18}$$

where D_p is the phase structure function, introduced in chapter 3, and defined as

$$D_p(x_1,x_2,y_1,y_2) = 6.88\left((x_1-x_2)^2+(y_1-y_2)^2\right)^{5/6} r_0^{-5/3}. \tag{8.19}$$

It is now possible to calculate from Eq. (8.17) the correlation in x direction slopes between lenslets 1 and 2 in Fig. 8.11 as

$$\begin{aligned} S_{12} &= \frac{1}{2}\int_{-\frac{D}{2}}^{\frac{D}{2}}\int_{\frac{D}{2}}^{\frac{3D}{2}}\frac{\phi(-\frac{D}{2},y_1)\phi(\frac{3D}{2},y_2)}{D^2}dy_1dy_2 \\ &+ \frac{1}{2}\int_{-\frac{D}{2}}^{\frac{D}{2}}\int_{\frac{D}{2}}^{\frac{3D}{2}}\frac{\phi(\frac{D}{2},y_1)\phi(\frac{D}{2},y_2)}{D^2}dy_1dy_2 \\ &- \frac{1}{2}\int_{-\frac{D}{2}}^{\frac{D}{2}}\int_{\frac{D}{2}}^{\frac{3D}{2}}\frac{\phi(-\frac{D}{2},y_1)\phi(\frac{D}{2},y_2)}{D^2}dy_1dy_2 \\ &- \frac{1}{2}\int_{-\frac{D}{2}}^{\frac{D}{2}}\int_{\frac{D}{2}}^{\frac{3D}{2}}\frac{\phi(\frac{D}{2},y_1)\phi(\frac{3D}{2},y_2)}{D^2}dy_1dy_2. \end{aligned} \tag{8.20}$$

The expression in Eq. (8.20) is also equal to

$$\begin{aligned} S_{12} &= \frac{1}{2}\int_{-\frac{D}{2}}^{\frac{D}{2}}\int_{\frac{D}{2}}^{\frac{3D}{2}}D_p\left(-\frac{D}{2},\frac{3D}{2},y_1,y_2\right)dy_1dy_2 \\ &+ \frac{1}{2}\int_{-\frac{D}{2}}^{\frac{D}{2}}\int_{\frac{D}{2}}^{\frac{3D}{2}}D_p\left(\frac{D}{2},\frac{D}{2},y_1,y_2\right)dy_1dy_2 \\ &- \frac{1}{2}\int_{-\frac{D}{2}}^{\frac{D}{2}}\int_{\frac{D}{2}}^{\frac{3D}{2}}D_p\left(-\frac{D}{2},\frac{D}{2},y_1,y_2\right)dy_1dy_2 \\ &- \frac{1}{2}\int_{-\frac{D}{2}}^{\frac{D}{2}}\int_{\frac{D}{2}}^{\frac{3D}{2}}D_p\left(\frac{D}{2},\frac{3D}{2},y_1,y_2\right)dy_1dy_2, \end{aligned} \tag{8.21}$$

by Eq. (8.18).

The extension to the correlation of binary star slopes is straightforward. The displacement of the binary star spots (dx,dy), see Fig. 8.12, is a function of the turbulent layer height. The correlation between the binary star spots can be calculated as

$$S_{11'} = \frac{1}{2}\int_{-\frac{D}{2}}^{\frac{D}{2}}\int_{-\frac{D}{2}+dy}^{\frac{D}{2}+dy}D_p\left(-\frac{D}{2},\frac{D}{2}+dx,y_1,y_2\right)dy_1dy_2$$

$$+ \frac{1}{2}\int_{-\frac{D}{2}}^{\frac{D}{2}}\int_{-\frac{D}{2}+dy}^{\frac{D}{2}+dy} D_p\left(\frac{D}{2}, -\frac{D}{2}+dx, y_1, y_2\right) dy_1 dy_2$$
$$- \frac{1}{2}\int_{-\frac{D}{2}}^{\frac{D}{2}}\int_{-\frac{D}{2}+dy}^{\frac{D}{2}+dy} D_p\left(-\frac{D}{2}, -\frac{D}{2}+dx, y_1, y_2\right) dy_1 dy_2$$
$$- \frac{1}{2}\int_{-\frac{D}{2}}^{\frac{D}{2}}\int_{-\frac{D}{2}+dy}^{\frac{D}{2}+dy} D_p\left(\frac{D}{2}, \frac{D}{2}+dx, y_1, y_2\right) dy_1 dy_2. \quad (8.22)$$

The S matrix is generated using these results and contains x and y slope correlations for spot displacements corresponding to altitudes of 0 to 20km. Each column contains the analytic result for a different separation at the aperture which in turn corresponds to an altitude within the desired range.

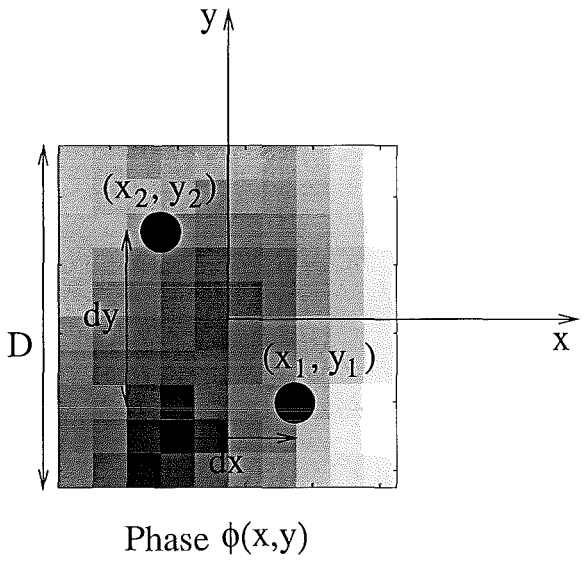

Figure 8.12: *Spot displacement in a single lenslet when imaging a binary star.*

8.2.1 Performance

The performance of this technique was tested by simulation of a sample problem. A 5 × 5 Shack-Hartmann lenslet array, where each lenslet had physical dimensions of 5cm × 5cm and a gridsize of 12 pixels by 12 pixels (corresponding to speckle patterns of dimensions 24 pixels by 24 pixels), was used to image a binary star with components of equal brightness and a separation of 3 arcseconds. A turbulent layer at an altitude of 5km was simulated producing a separation of the spots in each speckle image of 7.3cm, corresponding to 17

pixels.

The ensemble centroid variances and covariances for the images in each lenslet, which provide a measure of the turbulence, were calculated by

$$\sigma_x^2 = \left\langle (x_i - x_{ci})(x_i - x_{ci})^T \right\rangle \tag{8.23}$$

$$\sigma_{x'}^2 = \left\langle (x'_i - x'_{ci})(x'_i - x'_{ci})^T \right\rangle \tag{8.24}$$

$$\sigma_{xx'}^2 = \left\langle (x_i - x_{ci})(x'_i - x'_{ci})^T \right\rangle \tag{8.25}$$

$$\sigma_{x'x}^2 = \left\langle (x'_i - x'_{ci})(x_i - x_{ci})^T \right\rangle \tag{8.26}$$

where i = 1 ... N^2 and $(x_i - x_{ci}), (x'_i - x'_{ci})$ represent the displacements of the measured spot centroids in each lenslet from their ideal positions as illustrated in Fig. 8.13. Similar equations can also be derived for the displacements in the y direction. The combining and reshaping of these measurements produces a vector of length 2500 for this problem. The matrices defined by Eqs. (8.23) to (8.26) are displayed in Fig. 8.14 for a turbulent layer at an altitude of 2km.

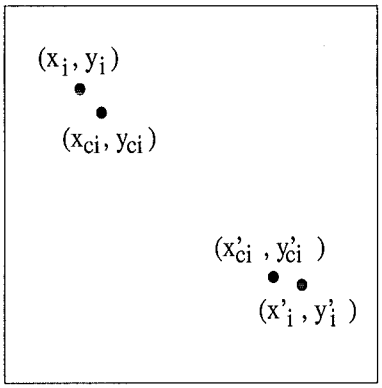

Figure 8.13: *Typical Shack-Hartmann speckle image in a single lenslet when imaging a binary star.*

An altitude sampling of 200m was used for simulation purposes over an altitude range of 20km producing an S matrix of dimensions 2500×100. The inversion of Eq. (8.12) can now be obtained using the quadratic programming methods outlined in chapter 5. The reconstruction for this problem in Fig. 8.15 illustrates a dominant peak at an altitude of 5km as desired and a much smaller noise peak. An equivalent reconstruction can also be

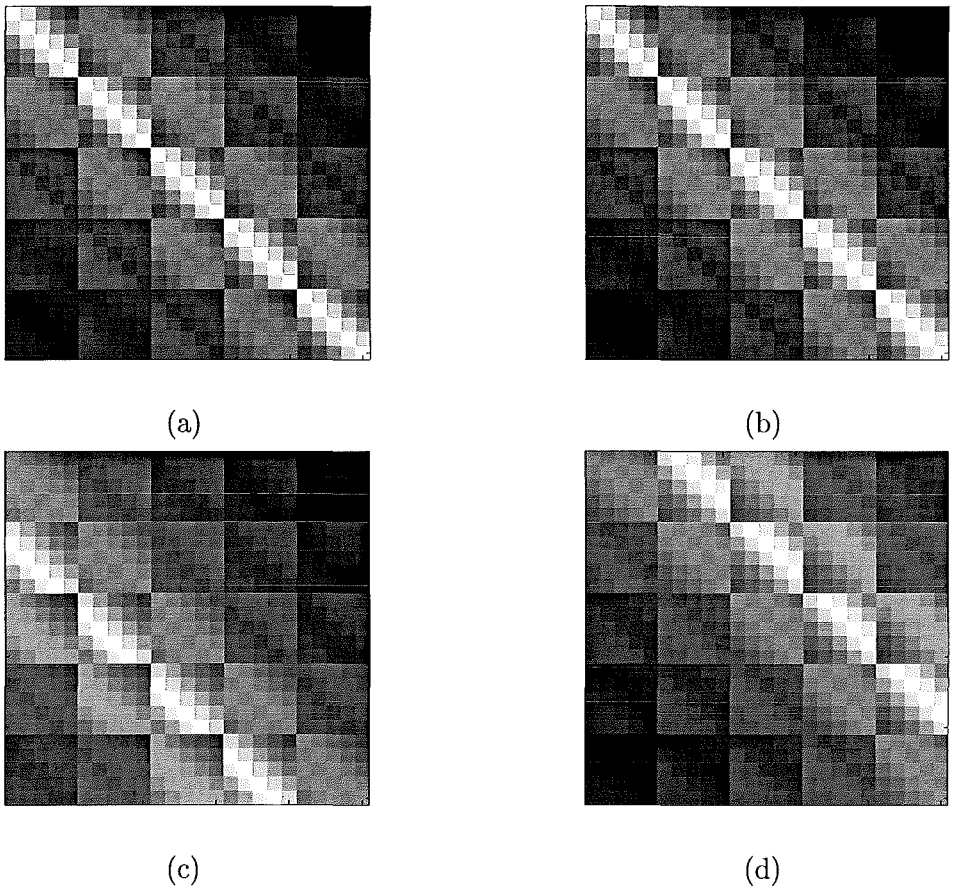

Figure 8.14: *Sample slope correlation terms corresponding to (a) σ_x^2, (b) $\sigma_{x'}^2$, (c) $\sigma_{xx'}^2$ and (d) $\sigma_{x'x}^2$.*

obtained by performing the inversion using only the information in Eqs. (8.25) and (8.26).

8.3 Summary

Adaptive optics systems attached to ground based telescopes have been used successfully to compensate for the wavefront distortion introduced by the atmosphere. For effective operation, however, a 3D characterisation of the atmosphere is required. The problem posed by the need to invert the measured covariance at the aperture of the telescope to the turbulence profile is very ill-conditioned, and so the existing techniques for estimating atmospheric turbulence profiles require the observation of binary stars to improve the conditioning of the inverse problem. The strict requirements of the generalised SCIDAR method provided the

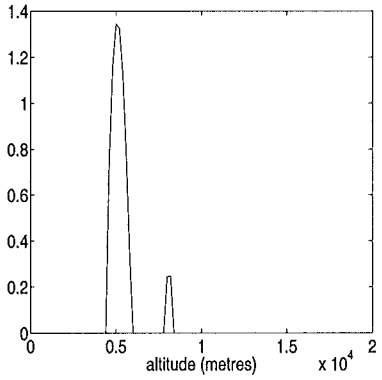

Figure 8.15: *Reconstruction for a turbulent layer at an altitude of 5km.*

motivation for the development of a feasible single star method and an investigation of existing alternatives.

The measurement of single star scintillation at a number of different planes provides a huge improvement in the resolution of the reconstruction at these altitudes. The different measurement planes required for the implementation of this technique can be achieved with a small modification to the existing optics and existing inversion algorithms can be applied to estimate the profiles. This technique is limited, as the classical and generalised SCIDAR methods are, by its sensitivity to external effects such as non-Kolmogorov statistics and the need to assume a power law model. However, it does require only a single star. In addition, there is potential to combine the single star method with curvature sensing and hence overcome the difficulties associated with the assumed statistics.

A technique combining the functionality of a DIMM with the SCIDAR method as discussed by Bally *et al* [10] was also investigated. The technique was demonstrated in this chapter and shown to successfully estimate turbulent layer heights. Extension to layer strengths and velocities is also possible. An advantage is that the implementation of this technique only requires standard off-the-shelf equipment. However, as with other techniques a power law model must be assumed to enable the slope statistics to be directly related to the wavefront phase statistics.

In conclusion, there exist many methods for improving the estimation of optical turbulence profiles. The theory indicates that the SCIDAR method can be extended to measurements made from a single bright star. The remote sensing of wavefront tilt information is yet another alternative and offers some advantages over the remote sensing of scintillation data. However, all existing and proposed methods are limited by the need to assume a form for the turbulence statistics. An obvious solution to combat this is to simultaneously perform these techniques with wavefront sensing to provide a direct estimate of the phase distortion and hence remove the uncertainty associated with the assumption of a specific power law.

Chapter 9

Conclusions and Future Research

This thesis discusses the problems associated with the imaging of light that has passed through atmospheric turbulence and investigates the compensation and removal of these effects. The first part of this chapter summarises and concludes the research presented in chapters 4, 5, 6, 7, and 8. Suggestions for ongoing and future research in related areas are presented in the second part of the chapter.

9.1 Conclusions

The imaging of wavefronts which suffer from both phase and intensity variations is a direct consequence of imaging through the atmosphere. Methods for improving the quality of images obtained by ground-based telescopes include the post processing of short exposure images and the real-time compensation achieved with the use of adaptive optics systems.

These techniques typically require the solution of an inverse problem. An integral part of any inversion is the study of the corresponding forward problem, the events, assumptions and processes that combined produce the distorted data. Knowledge of the forward problem is often attained by simulation. Improved methods for the simulation of atmospheric

turbulence and the subsequent propagation of phase distorted wavefronts to the telescope aperture were presented. The extension of these techniques to non-Kolmogorov statistics was also demonstrated. These then provided the necessary tools for the simulation of short exposure speckle images and scintillation patterns required for the development and testing of post processing and SCIDAR techniques respectively.

The conventional and blind deconvolution of atmospheric speckle images were investigated in chapters 5 and 6. Conventional deconvolution algorithms are suitable for situations in which the exact nature of the blurring, or distortion, is known. When the blurring is unknown, a blind deconvolution problem results. For each problem the necessary inversion is very ill-conditioned, requiring the addition of *a priori* information, for instance the use of a positivity constraint, which is commonly applied in astronomical imaging. Enforcing positivity by reformulating the deconvolution problem as one of quadratic programming was shown to be superior to the popular projection and reparameterisation methods and required only a small amount of additional computation for the assumption of Gaussian noise statistics. For Poisson noise statistics the scaling inherent in the RL algorithm proved very powerful for avoiding negative and hence meaningless solutions. A simple modification to the standard RL algorithm combined the desirable features of the RL algorithm with the guaranteed convergence of the quadratic programming method.

A review of existing blind deconvolution algorithms indicated very few multiple frame Gaussian noise based algorithms. The logical extension of the quadratic programming algorithm to iterative blind deconvolution was relatively straightforward as iterative blind deconvolution often reduces to two linked conventional deconvolution problems. The extension to iterative blind deconvolution, with the inclusion of a variety of regularisation options, led to the development of a series of MAP blind deconvolution algorithms. The use of energy constraints alone and combined with penalty terms and statistical priors produced the best reconstructions from atmospheric speckle images. Although both the conventional deconvolution and blind deconvolution techniques presented in chapters 5 and 6 are illustrated for the astronomical imaging problem they have a much wider application. For example, the basic quadratic programming method was applied to a number of different

inversion problems throughout this thesis.

Single and multiple conjugate adaptive optics technologies, which aim to compensate for the distortion introduced by the atmosphere in real-time, would benefit from knowledge of the vertical structure of the atmosphere. The processing of experimental SCIDAR data, in chapter 7, highlighted a variety of problems associated with this technique including aspects related to the data acquisition, data processing and assumptions inherent to the method. Alternative processing methods were proposed and trialed in an attempt to combat these problems. A thorough investigation into the effects of inaccurate and incomplete assumptions indicated that the layer height estimation is reliable, but the turbulence strength estimation is not. The covariance measure is a contributing factor in this area as it does not appear to directly measure the wavefront tip and tilt components, known to contribute significantly to the overall distortion. Finally, a major limitation of the technique is the need to image binary stars of a suitable separation and brightness.

The problems with the practical implementation of the SCIDAR method provided the motivation for the development and investigation of different approaches for the estimation of turbulence structure. The well-established DIMM and HDIMM technologies, used for estimating the turbulence coherence length, were extended to the estimation of atmospheric turbulence profiles. To obtain complete turbulence profiles, however, these still require the imaging of a binary star. The extension of the SCIDAR technique to use of single star scintillation was also investigated and demonstrated. However, the need to assume a form for the turbulence phase statistics is still a limitation of all current and proposed methods. Therefore, there is a definite need for further development of these techniques.

9.2 Future research

Many of the powerful astronomical blind deconvolution algorithms use information about the imaging optics and/or the atmosphere to constrain the solution away from the undesirable outcomes inherent to the problem. However, care must be taken as the incorporation of incorrect prior information can lead to unrealistic results. In addition, there exist many

problems for which this information is not available. In these instances general algorithms, that will return meaningful solutions for the minimum amount of prior information, are required. The results in chapter 6 illustrate the potential for robust Gaussian noise algorithms requiring only small amounts of prior information. For astronomical imaging applications, Poisson noise algorithms are more appropriate. All existing Poisson noise techniques reviewed use EM/RL updates with additional constraints. However, the standard RL method suffers from a number of problems. The incorporation of the modified RL update into existing Poisson noise algorithms should produce powerful and robust techniques for very little additional cost. Finally, further testing of these algorithms on a variety of different test objects, including real data and extended objects, is desirable to confirm their effectiveness.

A drawback of the techniques presented in chapter 6 is the selection of a value for the regularisation parameter. Improved and robust techniques for doing this would be an advantage. The joint minimisation of f and h with positivity enforced by quadratic programming is another area for future work. Finally, the determination of a fundamental limit to reconstruction resolution and quality that can be achieved with this type of algorithm would be of considerable interest.

Clearly, there are many possibilities for further research in the area of atmospheric turbulence profile estimation. The SCIDAR technique although theoretically sound requires further refinement for more accurate practical implementation. In addition, the potential for practical implementation of the single star method proposed in chapter 8 requires further research. The use of single stars, seen in abundance when viewing the sky at night with the naked eye, would be a considerable advantage to these techniques.

An interesting research possibility as foreshadowed in chapter 8 would be to combine single star SCIDAR, or the existing SCIDAR methods, with wavefront sensing techniques. The addition of an extra measurement plane, beneath the telescope aperture as in generalised SCIDAR, to the single star problem to match a plane an equal distance above the aperture would provide enough information to enable simultaneous curvature sensing to be performed. Not only does this have the potential to provide a corresponding estimate of the

actual phase distortion, thereby eliminating the need to assume a specific power law, but also the 3D mapping of the turbulence at a particular site. This would be a big step towards the ultimate goal, a real-time technique for the estimation of atmospheric turbulence that does not depend strongly on the assumed turbulence statistics.

It is therefore worth investigating whether SCIDAR methods can be implemented in real-time in combination with an AO system. As the turbulence is continually changing it would be advantageous to combine real-time techniques for estimating the turbulence structure with the control system of a single or multiple conjugate system. This would allow the deformable mirror or mirrors to be conjugated to the average seeing layer or layers as they change and hence further improve the quality of the recorded images.

The imaging of a binary star using an HDIMM is another potentially powerful turbulence estimation technique, although there appears to be no further mention of this technique apart from its original source of Bally *et al* [10]. Particularly so in that its implementation requires only standard readily available optical components. A comparison of this technique with the SCIDAR method would be beneficial in determining its sensitivity to noise and non-Kolmogorov effects for instance that are such limiting factors of the SCIDAR technique.

Appendix A

Optimisation Approaches

The use of maximum-likelihood (ML) and maximum *a posteriori* (MAP) techniques require the minimisation of an error function or the maximisation of a likelihood function. A variety of techniques including steepest descent, optimal step length steepest descent and conjugate gradient techniques can be used.

A.1 The method of steepest descent (the gradient method)

The steepest descent method also known as the gradient method is a simple algorithm often used when minimising a function of several variables. A drawback of the technique is its slow convergence and as a result other algorithms have been developed that attempt to modify the basic descent direction so as to produce an algorithm with superior convergence properties.

Consider the minimisation of an error function $E(f)$. The method of steepest descent is defined by

$$f^{(k+1)} = f^{(k)} - \alpha^{(k)} s^{(k)} \tag{A.1}$$

where $\alpha^{(k)}$ is the non-negative step, $s^{(k)} = \frac{\partial E}{\partial f^{(k)}}$ is the gradient of E with respect to $f^{(k)}$.

From an initial starting point a step is taken in the direction of negative gradient. This new estimate is then used to update the search direction and the process is repeated.

When the error function to be minimised is quadratic it may take on one of the following equivalent forms:

$$E(f) = \frac{1}{2} f^T Q f - f^T b \tag{A.2}$$

or

$$E(f) = \frac{1}{2} \|Hf - d\|^2. \tag{A.3}$$

where $Q = H^T H$ and $b = H^T d$. The minimisation of each of these error functions is equivalent to solving $Qf = b$ for f. In the quadratic case it is possible to take this a step further and calculate an optimal value for $\alpha^{(k)}$ for each iteration. A standard result for this optimal $\alpha^{(k)}$ as given in Luenberger [106] is

$$\alpha^{(k)} = \frac{(s^{(k)})^T s^{(k)}}{(s^{(k)})^T Q s^{(k)}}. \tag{A.4}$$

A.2 The conjugate gradient method

The conjugate gradient method is also a descent method used for minimising quadratic problems of the forms given in Eqs. (A.2) and (A.3). The conjugate gradient method is similar to the method of steepest descent and requires the following steps:

$$\begin{aligned}
y^{(0)} &= b - Q x^{(0)} \\
f^{(k+1)} &= f^{(k)} + \alpha^{(k)} y^{(k)} && \text{(A.5)} \\
\alpha^{(k)} &= -\frac{(s^{(k)})^T y^{(k)}}{(y^{(k)})^T Q y^{(k)}} && \text{(A.6)} \\
s^{(k)} &= Q x^{(k)} - b && \text{(A.7)} \\
y^{(k+1)} &= -s^{(k+1)} + \beta^{(k)} y^{(k)} && \text{(A.8)} \\
\beta^{(k)} &= \frac{(s^{(k)})^T Q y^{(k)}}{(y^{(k)})^T Q y^{(k)}}. && \text{(A.9)}
\end{aligned}$$

Here $y^{(k)}$ represents the search direction, $s^{(k)}$ represents the gradient, $\beta^{(k)}$ is used to update the search direction and Q is an $n \times n$ symmetric positive definite matrix [106]. Note the deviation from the notation of Luenberger [106] for the search direction, y instead of d,

and gradient, s instead of g. This is to avoid confusion with $d(\mathbf{x})$ the observed data and $g(\mathbf{x})$ the noise free convolution of $f(\mathbf{x})$ and $h(\mathbf{x})$. At each iteration the search direction taken by the algorithm is a linear combination of the current gradient and the previous search directions. The step size is recalculated each iteration as in optimal step length steepest descent to guarantee the minimum of the subspace spanned by the current and previous search direction vectors is reached. In addition, a single conjugate gradient step is equivalent to optimal step length steepest descent. The solution is guaranteed in no more than N iterations for a vector of length N and it is at least a good as that obtained using the steepest descent approach from the same starting point.

A.3 The non-quadratic conjugate gradient method

The conjugate gradient method can also be extended to non-quadratic problems by the introduction of suitable approximations. The step, $\alpha^{(k)}$, must now be generated as the solution to a linesearch. There exist many different possible linesearches, for example the Newton-Raphson method [72]. It is also necessary to use an alternative update for $\beta^{(k+1)}$. The update for $\beta^{(k+1)}$ used throughout this thesis is the Polak-Ribiere update [106],

$$\beta^{(k+1)} = \frac{(s^{(k+1)} - s^{(k)})^T (s^{(k+1)})}{(s^{(k)})^T s^{(k)}}. \tag{A.10}$$

A.4 FFT based conjugate gradient minimisation

The theoretical development of this theory has been in matrix form. This section shows how each step of the conjugate gradient algorithm can be implemented quickly using convolutions and on a specific constraint set if required. Note that when performing convolutions via the FFT, the components of the convolution must be zeropacked to the size of the resultant convolution, in order to increase their sampling rate in Fourier space. Minimising Eq. (A.2) is equivalent to solving

$$Q\hat{f} = b \tag{A.11}$$

for $\hat{f}$, where $Q = (H^T H + \gamma I)$ when using Tikhonov-Miller regularisation and $b = H^T d$. Given a starting estimate $\hat{f}^{(0)}$, the steps for solving for $\hat{f}^{(k)}$ are outlined below. Note that

the uppercase of a quantity corresponds to its Fourier transform, e.g.

$$H = \mathcal{F}\{h\} = \int_{-\infty}^{\infty}\int_{-\infty}^{\infty} h(x,y)\exp(j2\pi(ux+vy))dxdy, \tag{A.12}$$

and

$$h = \mathcal{F}^{-1}\{H\} = \int_{-\infty}^{\infty}\int_{-\infty}^{\infty} H(u,v)\exp(-j2\pi(ux+vy))dudv. \tag{A.13}$$

In addition, the active and inactive constraints can be easily selected by an element by element multiplication with a suitable mask, $\mathcal{M}$, comprising a 0 at pixels corresponding to an active constraint and a 1 at pixels corresponding to an inactive constraint. For problems not requiring a quadratic programming solution $\mathcal{M}$ can be set equal to a matrix of 1s with the steps outlined below reducing to the standard conjugate gradient algorithm.

Step 1.

Compute the initial search direction, $d^{(0)}$,

$$d^{(0)} = -s^{(0)} = \mathcal{M}(b - Q\hat{f}^{(0)}), \tag{A.14}$$

where $s^{(0)}$ is the initial gradient, $Q = (H^T H + \gamma I)$, $b = H^T d$ and $\mathcal{M}$ represents the current constraint set. Multiplication by Q corresponds to convolving $\hat{f}^{(0)}$ with the autocorrelation of h and adding $\gamma\hat{f}^{(0)}$ to the result. This can be implemented using

$$Q\hat{f}^{(0)} = (H^T H + \gamma I)\hat{f}^{(0)} = \mathcal{F}^{-1}\left\{[\mathcal{F}\{h\}^* \mathcal{F}\{h\}]\mathcal{F}\left\{\hat{f}^{(0)}\right\}\right\} + \gamma\hat{f}^{(0)}. \tag{A.15}$$

The term $H^T d$ can be computed using

$$H^T d = \mathcal{F}^{-1}\{\mathcal{F}\{h\}^* \mathcal{F}\{d\}\} \tag{A.16}$$

where a superscript $*$ denotes conjugation.

Step 2.

The current mask is used to update the estimate, $\hat{f}^{(k)}$, by

$$\hat{f}^{(k+1)} = \mathcal{M}\left(\hat{f}^{(k)} + \alpha^{(k)} y^{(k)}\right), \tag{A.17}$$

where $\alpha^{(k)}$ is given by Eq. (A.6). The $Qy^{(k)}$ product in Eq. (A.6) can be calculated as in Eq. (A.15).

Step 3.

Update the search direction, $y^{(k)}$, by

$$y^{(k+1)} = -s^{(k+1)} + \beta^{(k)} y^{(k)} \tag{A.18}$$

where

$$s^{(k+1)} = \mathcal{M}(s^{(k)} + \alpha^{(k)} Q y^{(k)}) \tag{A.19}$$

and β^k is given by Eq. (A.9). The $Q\hat{f}^{(k+1)}$ and $Qy^{(k)}$ products can be calculated as in Eq. (A.15).

Step 4.

Complete the minimisation on the current constraint set $\mathcal{M}$ by repeating steps 2 and 3 for the desired number, $\mathcal{N}$, of conjugate gradient iterations.

Bibliography

[1] M. J. Adcock and N. Jones, "Atmospheric Propagation Simulation", http://op.ph.ic.ac.uk/users/miles/see/see.html, 1997.

[2] N. Ahmed, T. Natarajan and K. R. Rao, "Discrete Cosine Transform", *IEEE Trans. Computers*, Correspondence, pp 90–93, January 1974.

[3] H. C. Andrews and B. R. Hunt, *Digital Image Restoration*, Prentice Hall Signal Processing Series (Alan V. Oppenheim - Series Editor), Prentice-Hall, Inc., Englewood Cliffs, New Jersey, 1977.

[4] R. Avila, J. Vernin and S. Cuevas, "Turbulence Profiles with Generalized Scidar at San Pedro Martir Observatory and Isoplanatism Studies", *Pub. Astron. Soc. Pac.*, Vol. **110**, pp 1106–1116, September 1998.

[5] R. Avila, J. Vernin and E. Masciadri, "Whole Atmospheric Turbulence profiling with generalized scidar", *Appl. Opt.*, Vol. **36**, No. 30, pp 7898–7905, October 1997.

[6] G. R. Ayers and J. C. Dainty, "Iterative blind deconvolution method and its applications", *Opt. Lett.*, Vol. **13**, No. 7, pp 547–549, July 1988.

[7] G. R. Ayers, M. J. Northcott and J. C. Dainty, "Knox-Thompson and triple correlation imaging through atmospheric turbulence", *J. Opt. Soc. Am. A*, Vol. **5**, No. 7, pp 963–985, July 1988.

[8] M. Azouit and J. Vernin, "Remote Investigation of Tropospheric Turbulence by Two-Dimensional Analysis of Stellar Scintillation", *J. Atmos. Sci.*, Vol. **37**, pp 1550–1557, July 1980.

[9] H. W. Babcock, "The possibility of compensating astronomical seeing", *Pub. Astron. Soc. Pac.*, Vol. **65**, No. 386, pp 229–236, 1953.

[10] J. Bally, D. Theil, Y. Billawala, D. Potter, R. F. Loewenstein, F. Mrozek and J. P. Lloyd, "A Hartmann Differential Image Motion Monitor (H-Dimm) for Atmospheric Turbulence Characterisation", *Pub. Astron. Soc. Aust.*, Vol. **13**, No. 1, pp 22–27, 1996.

[11] M. R. Banham and A. K. Katsaggelos, "Digital Image Restoration", *IEEE Sig. Pro. Magazine*, pp 24–41, 1997.

[12] B. V. Barlow, *The Astronomical Telescope*, Wykeham Publications, London, 1975.

[13] R. H. T. Bates and M. J. McDonnell, *Image Restoration and Reconstruction*, Clarendon Press, Oxford, England, 1989.

[14] R. H. T. Bates, B. K. Quek and C. R. Parker, "Some implications of zero sheets for blind deconvolution and phase retrieval", *J. Opt. Soc. Am. A*, Vol. **7**, No. 3, pp 468–479, March 1990.

[15] J. M. Beckers, "Adaptive Optics for Astronomy: Principles, Performance and Applications", *Annu. Rev. Astron. Astrophys.*, Vol. **31**, pp 13–62, 1993.

[16] T. E. Bell (Editor), "Electronics and the Stars", *IEEE Spectrum Mag.*, pp 16–24, August 1995.

[17] M. Bertero and P. Boccacci, *Introduction to Inverse Problems in Imaging*, Institute of Physics (IOP) Publishing, Bristol, UK, 1998.

[18] M. Bertero, F. Maggio, E. R. Pike and D. Fish, "Assessment of Methods Used for HST Image Reconstruction", in *The Restoration of HST Images and Spectra II* (Editors - R. J. Hansich and R. L. White), Space Telescope Science Institute, pp 300–306, 1994.

[19] D. S. C. Biggs and M. Andrews, "Conjugate gradient acceleration of maximum-likelihood image restoration", *Electron. Lett.*, Vol. **31**, No. 23, pp 1985–1986, November 1995.

[20] D. S. C. Biggs and M. Andrews, "Acceleration of iterative image restortation algorithms", *Appl. Opt.*, Vol. **36**, No. 8, pp 1766–1775, March 1997.

[21] P. J. Bones, C. R. Parker, B. L. Satherly and R. W. Watson, "Deconvolution and phase retrieval with use of zero sheets", *J. Opt. Soc. Am. A*, Vol. **12**, No. 9, pp 1842–1857, September 1995.

[22] B. G. Boone, *Signal Processing using optics: fundamentals, devices, architectures and applications*, Oxford University Press, New York, 1998.

[23] M. Born and E. Wolf, *Principles of Optics*, Pergamon Press, fifth edition, 1975.

[24] R. N. Bracewell, *The Fourier transform and its applications*, McGraw-Hill, New York, 2nd edition, 1986.

[25] J. L. Bufton, "Comparison of Vertical Profile Turbulence Structure with Stellar Observations", *Appl. Opt.*, Vol. **12**, No. 8, pp 1785–1793, August 1973.

[26] J. L. Caccia, M. Azouit and J. Vernin, "Wind and C_N^2 profiling by single-star scintillation analysis", *Appl. Opt.*, Vol. **26**, No. 7, pp 1288–1294, April 1987.

[27] J.-L. Caccia, J. Vernin and M. Azouit, "Structure function C_N^2 profiling by two-color stellar scintillation with atmospheric dispersion", *Appl. Opt.*, Vol. **27**, No. 11, pp 2229–2235, June 1988.

[28] J. L. Caccia and J. Vernin, "Wind fluctuation measurements in the buoyancy range by Stellar Scintillation Analysis", *J. Geophys. Res.*, Vol. **95**, No. D9, pp 13683–13690, August 1990.

[29] K. R. Castleman, *Digital Image Processing*, Prentice Hall, Inc., Englewood Cliffs, New Jersey, 1979.

[30] T. F. Chan and C.-K. Wong, "Total Variation Blind Deconvolution", *IEEE Trans. Image Process.*, Vol. **7**, No. 3, pp 370–375, March 1998.

[31] G. Chinn and S.-C. Huang, "A General Class of Preconditioners for Statistical Iterative Reconstruction of Emission Computed Tomography", *IEEE Trans. Med. Imaging*, Vol. **16**, No. 1, pp 1–10, February 1997.

[32] N. Clinthorne, T.-S. Pan, P.-C. Chiao, W. L. Rogers and J. A. Stamos, "Preconditioning Methods for Improved Convergence Rates in Iterative Reconstructions", *IEEE Trans. Med. Im.*, Vol. **12**, No. 1, pp 78–83, March 1993.

[33] Wm. A. Coles, J. P. Filice, R. G. Frelich and M. Yadlowsky, "Simulation of wave propagation in three-dimensional random media", *Appl. Opt.*, Vol. **34**, No. 12, pp 2089–2101, 1995.

[34] G. P. Collins, "Making stars to see stars: Dod adaptive optics work is declassified", *Phys. Today*, Vol. **45**, pp 17–21, February 1992.

[35] T. J. Connolly and R. G. Lane, "Gradient methods for superresolution", *International conference on image processing (IEEE Signal Processing Society), Santa Barbara, California*, Vol. **1**, pp 917–920, 1997.

[36] T. J. Connolly and R. G. Lane, "Constrained regularization methods for superresolution", *International Conference on Image Processing (IEEE Signal Processing Society), Chicago, Illinois, USA*, Vol. **3**, pp 727–731, October 4 - 7 1998.

[37] J. W. Cooley and J. W. Tukey, "An algorithm for the machine calculation of complex Fourier Series", *Math. Comp.*, Vol. **19**, pp 297–300, 1965.

[38] C. E. Coulman, J. Vernin and A. Fuchs, "Optical seeing - mechanism of formation of thin turbulent laminae in the atmosphere", *Appl. Opt.*, Vol. **34**, No. 24, pp 5461–5475, August 1995.

[39] I. J. D. Craig and J. C. Brown, *Inverse Problems in Astronomy - A guide to inversion strategies for remotely sensed data*, Adam Hilger Ltd, Bristol, England, 1986.

[40] J. C. Dainty and J. R. Fienup, "Phase Retrieval and Image Reconstruction for Astronomy", in *Image Recovery: Theory and Application* (Editor - H. Stark), Academic Press, Inc., Orlando, Florida, pp 231–275, 1987.

[41] F. Dalaudier, M. Crochet and C. Sidi, "Direct comparison between in situ and radar measurements of temperture fluctuation spectra: A puzzling result", *Radio Sci.*, Vol. **24**, pp 311–324, 1989.

[42] F. Dalaudier, C. Sidi, M. Crochet and J. Vernin, "Direct Evidence of Sheets in the Atmospheric Temperature Field", *J. Atmos. Sci.*, Vol. **51**, No. 2, pp 237–248, January 1994.

[43] B. L. K. Davey, R. G. Lane and R. H. T. Bates, "Blind deconvolution of noisy complex-valued image", *Opt. Commun.*, Vol. **69**, No. 5-6, pp 353–356, January 1989.

[44] C. A. Davis and D. L. Walters, "Atmospheric inner-scale effects on normalized irradiance variance", *Appl. Opt.*, Vol. **33**, No. 36, pp 8406–8111, December 1994.

[45] L. Debnath, *Integral transforms and their applications*, CRC Press, Inc., 1995.

[46] R. Ditteon, *Modern Geometrical Optics*, John Wiley and Sons, Inc., New York, 1998.

[47] D. Dravins, L. Lindegren, E. Mezey and A. T. Young, "Atmospheric Intensity Scintillation of Stars. III. Effects for Different Telescope Apertures", *Pub. Astron. Soc. Pac.*, Vol. **110**, pp 610–633, May 1998.

[48] J. R. Fienup, "Phase retrieval algorithms: a comparison", *Appl. Opt.*, Vol. **21**, No. 15, pp 2758–2769, August 1982.

[49] D. A. Fish, A. M. Brinicombe, E. R. Pike and J. G. Walker, "Blind deconvolution by means of the Richardson-Lucy algorithm", *J. Opt. Soc. Am. A*, Vol. **12**, No. 1, pp 58–65, January 1995.

[50] S. M. Flatté, G.-Y. Wang and J. Martin, "Irradiance variance of optical waves through atmospheric turbulence by numerical simulation and comparison with experiment", *J. Opt. Soc. Am. A*, Vol. **10**, No. 11, pp 2363–2370, November 1993.

[51] H. T. Flint, *Geometrical Optics*, Methuen & Co. Ltd., London, 1936.

[52] R. Foy and A. Labeyrie, "Feasibility of adaptive telescope with laser probe", *Astron. Astrophys.*, Vol. **152**, pp L29–L31, 1985.

[53] R. G. Frelich, "Estimation of the parameters of the atmospheric spectrum using measurements of the spatial intensity covariance", *Appl. Opt.*, Vol. **27**, No. 11, pp 2194–2198, June 1988.

[54] D. L. Fried, "Statistics of a geometric representation of wavefront distortion", *J. Opt. Soc. Am.*, Vol. **55**, No. 11, pp 1427–1435, November 1965.

[55] D. L. Fried, "Optical resolution through a randomly inhomogeneous medium for very long and very short exposures", *J. Opt. Soc. Am.*, Vol. **56**, No. 10, pp 1372–1379, 1966.

[56] D. L. Fried and J. F. Belsher, "Analysis of fundamental limits to artificial-guide-star adaptive-optics-system performance for astronomical imaging", *J. Opt. Soc. Am. A*, Vol. **11**, No. 1, pp 277–287, January 1994.

[57] J. Vernin, M. Tallon and A. Fuchs, "Folding of the vertical atmospheric turbulence profile using an optical technique of movable observing plane", *Proceedings of the SPIE*, Vol. **2222**, pp 682–692, 1994.

[58] A. Fuchs, M. Tallon and J. Vernin, "Focusing on a Turbulent Layer: Principle of the Generalized SCIDAR", *Pub. Astron. Soc. Pac.*, Vol. **110**, pp 86–91, January 1998.

[59] T. Fusco, J.-M. Conan, V. Michau, L. M. Mugnier and G. Rousset, "Optimal phase reconstruction in large field of view: application to multiconjugate adaptive optics systems", *SPIE's 45th Annual Meeting "Propagation and Imaging through the Atmosphere IV" Conference, San Diego*, 30 July - 4 August 2000.

[60] J. D. Gaskill, *Linear Systems, Fourier Transforms and Optics*, John Wiley and Sons, Inc., USA, 1978.

[61] R. Gerchberg and W. Saxton, "A practical algorithm for the determination of phase from image and diffraction plane picture", *Optik*, Vol. **35**, pp 237–246, 1972.

[62] A. Glindemann, "Improved Performance of Adaptive Optics in the visible", *J. Opt. Soc. Am. A*, Vol. **11**, No. 4, pp 1370–1375, 1994.

[63] A. Glindemann, R. G. Lane and J. C. Dainty, "Simulation of time evolving speckle patterns using Kolmogorov statistics", *J. Mod. Opt.*, Vol. **40**, No. 12, pp 2381–2388, 1993.

[64] T. Goldring and L. Carlson, "Analysis and implementation of non-Kolmogorov phase screens appropriate to structured environments" *SPIE proceedings on Nonlinear Optical Beam Manipulation and High Energy Beam Propagation Through the Atmosphere*, Vol. **1060**, pp 244-264, 1989.

[65] R. C. Gonzalez and P. A. Wintz, *Digital Image Processing*, Addison-Wesley, Reading, Massachusetts, 2nd edition, 1987.

[66] J. W. Goodman, *Introduction to Fourier Optics*, McGraw-Hill book company, USA, 1968.

[67] J. W. Goodman, *Statistical Optics*, John Wiley and Sons, 1985.

[68] J. W. Goodman, *Introduction to Fourier Optics*, The McGraw-Hill Companies, USA, 1996.

[69] J. W. Hardy, "Active optics: A new technololgy for the control of light", *Proc. IEEE*, Vol. **66**, No. 6, pp 651–697, June 1978.

[70] J. W. Hardy, *Adaptive Optics for Astronomical Telescopes*, Oxford University Press, New York, 1998.

[71] S. Haykin, *Communication Systems*, John Wiley and Sons, Inc., New York, 3rd edition, 1994.

[72] F. B. Hildebrand, *Advanced Calculus for Applications*, Prentice-Hall, Inc., Englewood Cliffs, New Jersey, 1976.

[73] D. Hoffleit (with collaboration of Carlos Jaschek), *The Bright Star Catalogue*, Yale University Observatory, New Haven, Connecticut, USA, 1982.

[74] T. J. Holmes, "Blind deconvolution of quantum limited incoherent imagery: maximum-likelihood approach", *J. Opt. Soc. Am. A*, Vol. **9**, No. 7, pp 1053–1061, July 1992.

[75] T. J. Holmes and Y.-H. Liu, "Acceleration of maximum-likelihood image restoration for fluorescence microscopy and other noncoherent imagery", *J. Opt. Soc. Am. A*, Vol. **8**, No. 6, pp 893–907, June 1991.

[76] P. Horowitz, "Asymptotic theory of unstable resonator modes", *J. Opt. Soc. Am.*, Vol. **63**, No. 12, pp 1528–1543, December 1973.

[77] B. Hulburd and D. Sandler, "Segmented mirrors for atmospheric compensation", *Opt. Eng.*, Vol. **29**, No. 10, pp 1186–1190, October 1990.

[78] B. R. Hunt, "The application of constrained least squares estimation to image restoration by digital computer", *IEEE Trans. Comput.*, Vol. **C-22**, No. 9, pp 805–812, September 1973.

[79] A. K. Jain, *Fundamentals of Digital Image Processing*, Prentice Hall, Inc., Englewood Cliffs, New Jersey, 1989.

[80] S. M. Jeffries and J. C. Christou, "Restoration of astronomical images by iterative blind deconvolution", *Astrophys. J.*, Vol. **415**, pp 862–874, October 1995.

[81] D. C. Johnston and B. M. Welsh, "Analysis of multiconjugate adaptive optics", *J. Opt. Soc. Am. A*, Vol. **11**, No. 1, pp 394–408, January 1994.

[82] M. G. Kang and A. K. Katsaggelos, "Simultaneous iterative image restoration and evaluation of the regularization parameter", *IEEE Trans. Signal Process*, Vol. 40, No. 9, pp 2329–2334, 1992.

[83] L. Kaufman, "Implementing and Accelerating the EM Algorithm for Positron Emisson Tomography", *IEEE Trans. Med. Im.*, Vol. **MI-6**, No. 1, pp 37–51, March 1987.

[84] L. Kaufman, "Maximum Likelihood, Least Squares and Penalized Least Squares for PET", *IEEE Trans. Med. Im.*, Vol. **12**, No. 2, pp 200–214, June 1993.

[85] V. A. Kluckers, N. J. Wooder, T. W. Nicholls, M. A. Adcock, I. Munro and J. C. Dainty, "Profiling of Atmospheric turbulence strength and velocity using a generalised SCIDAR technique", *Astron. Astrophys. Suppl. Ser.*, Vol. **130**, pp 141–155, 1998.

[86] K. T. Knox and B. J. Thompson, "Recovery of images from atmospherically degraded short exposure photographs", *Astrophys. J.*, Vol. **193**, pp L45–48, October 1974.

[87] A. Kolmogorov, "The local structure of turbulence in incompressible viscous fluid for very large Reynold's numbers", in *Turbulence - Classic papers in statistical theory*, Editors S. K. Friedlander and Topper, Wiley Interscience, New York, pp 151–155, 1961.

[88] D. Kundur and D. Hatzinakos, "Blind image deconvolution", *IEEE Signal Proc. Mag.*, Vol. **13**, pp 43–64, 1996.

[89] D. Kundur and D. Hatzinakos, "A Novel Blind Deconvolution Scheme for Image Restoration Using Recursive Filtering", *IEEE Trans. Signal Process.*, Vol. **46**, No. 2, pp 375–389, February 1998.

[90] A. Labeyrie, "Attainment of diffraction limited resolution in large telescopes by Fourier analysing speckle patterns in star images", *Astron. Astrophys.*, Vol. **6**, pp 85–87, 1970.

[91] R. G. Lane, "Methods for maximum-likelihood deconvolution", *J. Opt. Soc. Am. A*, Vol. **13**, No. 10, pp 1992–1998, October 1996.

[92] R. G. Lane and R. H. T. Bates, "Automatic multidimensional deconvolution", *J. Opt. Soc. Am. A*, Vol. **4**, No. 1, pp 180–188, January 1987.

[93] R. G. Lane and A. Glindemann, "Comparison of computer post processing and low order adaptive optics", *Digital Image Recovery and Synthesis II, Proc. SPIE*, Vol. **2029**, pp 275–286, 1993.

[94] R. G. Lane, A. Glindemann and J. C. Dainty, "Simulation of a Kolmogorov Phase Screen", *Waves Random Media*, Vol. **2**, pp 209–224, 1992.

[95] R. G. Lane and R. Irwan, "Phase retrieval as a means of wavefront sensing", *International conference on image processing (IEEE Signal processing society), Santa Barbara*, Vol. **2**, pp 242–245, 1997.

[96] R. G. Lane, R. A. Johnston, R. Irwan and T. J. Connolly, "Regularized blind deconvolution", *in Signal Recovery and Synthesis, OSA Technical Digest Series, (Optical Society of America, Washington DC)*, Vol. **11**, pp 5–7, 1998.

[97] R. G. Lane and M. Tallon, "Wave-front reconstruction using a Shack-Hartmann sensor", *Appl. Opt.*, Vol. **31**, No. 32, pp 6902–6908, November 1992.

[98] N. F. Law and R. G. Lane, "Blind deconvolution using least squares minimisation", *Opt. Commun.*, Vol. **128**, pp 341–352, 1996.

[99] N. F. Law and R. G. Lane, "Wavefront estimation at low light levels", *Opt. Commun.*, Vol. **126**, pp 19–24, 1996.

[100] N. F. Law and D. T. Nguyen, "Multiple frame projection based blind deconvolution", *Elect. Letts.*, Vol. **31**, No. 20, pp 1734–1735, September 1995.

[101] W. Y. V. Leung and R. G. Lane, "Blind deconvolution of images blurred by atmospheric speckle", *SPIE's 45th Annual Meeting "Propagation and Imaging through the Atmosphere IV" Conference, San Diego*, 30 July - 4 August 2000.

[102] A. W. Lohmann, G. Weigelt and B. Wirnitzer, "Speckle masking in astronomy: triple correlation theory and applications", *Appl. Opt.*, Vol. **22**, No. 24, pp 4028–4037, December 1983.

[103] A. W. Lohmann and B. Wirnitzer, "Triple correlations", *Proc. IEEE*, Vol. **72**, No. 7, pp 889–901, July 1984.

[104] L. B. Lucy, "An iterative technique for the rectification of observed distributions", *Astron. J*, Vol. **79**, No. 6, pp 745–754, June 1974.

[105] D. G. Luenberger, *Optimization by vector space methods*, John Wiley and Sons, New York, 1969.

[106] D. G. Luenberger, *Linear and Nonlinear Programming*, Addison-Wesley Publishing Company, United States of America, 2nd edition, 1984.

[107] B. C. MacCallum, "Blind deconvolution by simulated annealing", *Opt. Commun.*, Vol. **75**, pp 101–105, 1990.

[108] K. A. Marsh and J. M. Richardson, "The objective function implicit in the CLEAN algorithm", *Astron. Astrophys.*, Vol. **182**, pp 174–178, 1987.

[109] J. M. Martin and S. M. Flatté, "Intensity images and statistics from numerical simulation of wave propagation in 3D-random media", *Appl. Opt.*, Vol. **27**, No. 11, pp 2111–2126, June 1988.

[110] J. M. Martin and S. M. Flatté, "Simulation of point-source scintillation through three-dimensional random media", *J. Opt. Soc. Am. A*, Vol. **7**, No. 5, pp 838–847, May 1990.

[111] E. Masciadri, J. Vernin and P. Bougeault, "3D mapping of optical turbulence using an atmospheric numerical model. II. First results at Cerro Paranal", *Astron. Astrophys. Suppl. Ser.*, Vol. **137**, pp 203–216, May 1999.

[112] Mathematica, Wolfram Research, Inc., version 3.0.2.0.

[113] Matlab, The Mathworks, Inc., version 5.3.1.29215a (r11.1).

[114] B. L. McGlamery, "Computer simulation studies of compensation of turbulence degraded images", *Proc. SPIE/OSA, Image Processing*, Vol. **74**, pp 225 – 233, 1976.

[115] E. S. Meinel, "Origins of linear and nonlinear recursive restoration algorithms", *J. Opt. Soc. Am. A*, Vol. **3**, No. 6, pp 787–799, June 1986.

[116] J. W. Miles, *Integral transforms in applied mathematics*, Cambridge University Press, Cambridge, England, 1971.

[117] O. Nakamura, S. Kawata and S. Minami, "Optical microscope tomography. II. Nonnegative constraint by a gradient-projection method", *J. Opt. Soc. Am. A*, Vol. **5**, No. 4, pp 554–561, April 1988.

[118] M. K. Ng, R. J. Plemmons and S. Qiao, "Regularization of RIF Blind Image Deconvolution", *IEEE Trans. Image Proc.*, Vol. **9**, No. 6, pp 1130–1134, June 2000.

[119] T. W. Nicholls, G. D. Boreman and J. C. Dainty, "Use of a Shack-Hartmann Wave-Front sensor to Measure Deviations from a Kolmogorov Phase Spectrum", *Opt. Letts.*, Vol. **20**, No. 24, pp 2460–2462, 1995.

[120] R. Nityananda and R. Narayan, "Maximum Entropy Image Restoration - A Practical Non-Information-Theoretic Approach", *Astron. Astrophys.*, Vol. **3**, pp 419–450, 1982.

[121] R. J. Noll, "Zernike polynomials and atmospheric turbulence", *J. Opt. Soc. Am. A*, Vol. **66**, No. 3, pp 207–211, March 1976.

[122] R. R. Parenti, "Adaptive Optics for Astronomy", *Linc. Lab. J.*, Vol. **5**, No. 1, pp 93–114, 1992.

[123] R. R. Parenti and R. J. Sasiela, "Laser-guide-star systems for astronomical applications", *J. Opt. Soc. Am. A*, Vol. **11**, No. 1, pp 288–309, January 1994.

[124] H. O. Peitgen and D. Saupe (editors), *The Science of Fractal Images*, Springer-Verlag, London, 1988.

[125] M. Piana and M. Bertero, "Projected Landweber method and preconditioning", *Inverse Probl.*, Vol. **13**, pp 441–463, 1997.

[126] W. K. Pratt, *Digital Image Processing*, John Wiley and Sons, Inc., New York, 2nd edition, 1991.

[127] W. H. Press, S. A. Teukolsky, W. T. Vetterling and B. P. Flannery, *Numerical Recipes in C - The art of scientific computing*, Cambridge University Press, Cambridge; New York, 2nd edition, 1992.

[128] J. Primot, G. Rousset and J. C. Fontanella, "Deconvolution from wave-front sensing: a new technique for compensating turbulence-degraded images", *J. Opt. Soc. Am. A*, Vol. **7**, No. 9, pp 1598–1608, 1990.

[129] R. Racine and B. L. Ellerbroek, "Profiles of night-time turbulence above Mauna Kea and isoplanatism extension in adaptive optics", *Proc. SPIE*, Vol. **2534**, pp 248–257, 1995.

[130] W. H. Richardson, "Bayesian-Based Iterative Method of Image Restoration", *J. Opt. Soc. Am. A*, Vol. **62**, No. 1, pp 55–59, January 1972.

[131] I. Ridpath (Editor), *A Dictionary of Astronomy*, Oxford University Press, New York, 1997.

[132] A. Rocca, F. Roddier and J. Vernin, "Detection of Atmospheric turbulent layers by spatiotemporal and spatioangular correlation measurements of stellar-light scintillation", *J. Opt. Soc. Am. A*, Vol. **64**, No. 7, pp 1000–1004, July 1974.

[133] C. Roddier and J. Vernin, "Relative contribution of upper and lower atmosphere to integrated refractive index profiles", *Appl. Opt.*, Vol. **16**, No. 8, pp 2253–2256, August 1977.

[134] F. Roddier, "Effects of Atmospheric Turbulence in Optical Astronomy", in *Progress in Optics* (Editor E. Wolf), Vol. 19, Elsevier, pp 281–376, 1981.

[135] F. Roddier, "Curvature sensing and compensation: a new concept in adaptive optics", *Appl. Opt.*, Vol. **27**, pp 1223–1225, 1988.

[136] F. Roddier, *Adaptive Optics in Astronomy*, Cambridge University Press, 1999.

[137] N. Roddier, "Atmospheric wavefront simulation using Zernike polynomials", *Optical Engineering*, Vol. **29**, No. 10, pp 1174–1180, October 1990.

[138] M. C. Roggemann and C. L. Matson, "Power spectrum and Fourier phase spectrum estimation by using fully and partially compensating adaptive optics and bispectrum processing", *J. Opt. Soc. Am. A*, Vol. **9**, No. 9, pp 1525–1535, September 1992.

[139] M. C. Roggemann and B. Welsh, *Imaging through turbulence*, CRC Press Inc., 1996.

[140] M. C. Roggemann and T. J. Schulz, "Algorithm to increase the largest aberration which can be reconstructed from Hartmann sensor measurements", *Appl. Opt.*, Vol. **37**, No. 20, pp 4321–4329, July 1998.

[141] J. A. Rubio, A. Belmonte and A. Comerón, "Numerical simulation of long-path spherical wave propagation in three-dimensional random media", *Opt. Eng.*, Vol. **38**, No. 9, pp 1462–1469, 1999.

[142] M. Sarazin and F. Roddier, "The ESO differential image motion monitor", *Astron. Astrophys.*, Vol. **227**, No. 12, pp 294–300, 1990.

[143] T. J. Schulz, "Multiframe blind deconvolution of astronomical images", *J. Opt. Soc. Am. A*, Vol. **10**, No. 5, pp 1064–1073, May 1993.

[144] C. Schwartz, G. Baum and E. N. Ribak, "Turbulence-degraded wavefronts as fractal surfaces", *J. Opt. Soc. Am. A*, Vol. **11**, No. 1, pp 444–451, 1994.

[145] L. A. Shepp and Y. Vardi, Maximum-Likelihood reconstruction for Emission Tomography, *IEEE Trans. Med. Im.*, Vol. **MI-1**, No. 2, pp 113–122, October 1982.

[146] D. G. Sheppard, B. R. Hunt and M. W. Marcellin, "Iterative multiframe superresolution algorithms for atmospheric-turbulence-degraded imagery", *J. Opt. Soc. Am. A*, Vol. **15**, No. 4, pp 396–407, April 1998.

[147] E. E. Silbaugh, B. M. Welsh and M. C. Roggemann, "Characterization of atmospheric turbulence pahse statistics using wave-front slope measurements", *J. Opt. Soc. Am. A*, Vol. **13**, No. 12, pp 2453–2460, December 1996.

[148] W. H. Southwell, "Wave-front estimation from wave-front slope measurements", *J. Opt. Soc. Am.*, Vol. **70**, No. 8, pp 998–1006, August 1980.

[149] H. Stark and J. W. Woods, *Probability, Random Processes and Estimation Theory for Engineers*,Prentice Hall, Inc., 2nd edition, 1994.

[150] J. Stein (Editor) and L. Urdang (Managing Editor), *The Random House Dictionary of the English Language*, Vol. **1** (A-N), Random House, New York, 1967.

[151] G. Strang, *Linear Algebra and its applications*, Harcourt Brace Javanovich, Inc., 3rd edition, 1988.

[152] J. W. Strohbehn, "Remote Sensing of Clear-Air Turbulence", *J. Opt. Soc. Am.*, Vol. **60**, No. 7, pp 948–950, July 1970.

[153] J. W. Strohbehn, "Optical and millimeter line-of-sight propagation effects in the turbulent atmosphere", *Bound.-Layer Meteorol.*, Vol. **4**, pp 397–422, 1973.

[154] M. Tallon and R. Foy, "Adaptive telescope with laser probe: isoplanatism and cone effect", *Astron. Astrophys.*, Vol. **235**, pp 549–557, 1990.

[155] A. Tarantola, *Inverse Problem Theory - Methods for data fitting and model parameter estimation*, Elsevier Science Publishers, 1987.

[156] V. I. Tatarskii, *Wave Propagation in a Turbulent Medium*, McGraw-Hill Book Company, USA, 1961.

[157] E. Thiébaut and J. M. Conan, "Strict a priori constraints for maximum-likelihood blind deconvolution", *J. Opt. Soc. Am. A*, Vol. **12**, No. 3, pp 485–492, March 1995.

[158] D. M. Titterington, "General structure of regularization procedures in image reconstruction", *Astron. Astrophys.*, Vol. **144**, pp 381–387, 1985.

[159] G. A. Tyler, "Noise effects in crossed beam C_n^2 estimation", *Adaptive Optics for Large Telescopes, OSA Technical Digest Series*, Vol. **19**, pp 8–119, 1992.

[160] G. A. Tyler, "Merging: a new method for tomography through random media", *J. Opt. Soc. Am. A*, Vol. **11**, No. 1, pp 409–424, January 1994.

[161] G. A. Tyler and K. E. Steinhoff, "SCIDAR: Measurement Characteristics and Noise Amplification Properties", *tOSC Report No. TR-755R, Placentia, CA*, July 1987.

[162] R. K. Tyson, *Principles of Adaptive Optics*, Academic Press Limited, 1991.

[163] T. E. VanZandt, J. L. Green, K. S. Gage and W. L. Clark, "Vertical profiles of refractivity turbulence structure constant: Comparison of observations by the Sunset Radar with a new theoretical model", *Radio Sci*, Vol. **13**, No. 5, pp 819–829, September - October 1978.

[164] G. Vdovin, *Lightpipes : beam propagation toolbox*, Electronic Instrumentation lab, Delft University of Technology, Version 1.1, 1993-1996.

[165] J. Vernin, "Atmospheric Turbulence Profiles", *Wave Propagation in Random Media (Scintillation)*, pp 248–260, 1993.

[166] J. Vernin and M. Azouit, "Traitement d'image adapté au speckle atmosphérique. I. Formation du speckle en atmosphère turbulente. Propriétés statistiques", *J. Opt. (Paris)*, Vol. **14**, No. 1, pp 5–9, 1983.

[167] J. Vernin, R. Barletti, G. Ceppatelli, L. Paternò, A. Righini and N. Speroni, "Optical remote sensing of atmospheric turbulence: a comparison with simultaneous thermal measurements", *Appl. Opt.*, Vol. **18**, No. 2, pp 243–247, January 1979.

[168] J. Vernin, M. Crochet, M. Azouit and O. Ghebrebrhan, "SCIDAR/Radar simultaneous measurements of atmospheric turbulence", *Radio Sci.*, Vol. **25**, No. 5, pp 953–959, September-October 1990.

[169] J. Vernin and C. Munoz-Tunon, "Optical Seeing at La Palma Observatory. II. Intensive site testing campaign at the Nordic Optical Telescope", *Astron. Astrophys.*, Vol. **284**, pp 311–318, 1994.

[170] J. Vernin and F. Roddier, "Experimental determination of two dimensional spatiotemporal power spectra of stellar light scintillation - evidence for a multilayer structure of the air turbulence in the upper troposphere", *J. Opt. Soc. Am. A*, Vol. **63**, pp 270–273, 1973.

[171] E. Wallner, "Optimal wave-front correction using slope measurements", *J. Opt. Soc. Am.*, Vol. **73**, No. 12, pp 1771–1776, 1983.

[172] A. B. Watson, "Image Compression Using the Discrete Cosine Transform", *The Mathematica Journal*, Vol. **4**, No. 1, pp 81–88, 1994.

[173] W. T. Welford, *Aberrations of the Symmetrical Optical System*, Academic Press, 1974.

[174] W. T. Welford, *Optics*, Oxford University Press, New York, 2nd edition, 1981.

[175] R. L. White, "Image Restoration Using the Damped Richardson-Lucy Method", in *The Restoration of HST Images and Spectra II* (Editors - R. J. Hanisch and R. L. White), Space Telescope Science Institute, pp 104–110, 1994.

[176] K. W. Wolf, *Integral Transforms in Science and Engineering*, Plenum Press, New York, USA, 1979.

[177] P. W. Wong and C. Herley, "Area-based interpolation for scaling of images from a CCD", *International conference on image processing (IEEE Signal Processing Society), Santa Barbara, California*, Vol. **1**, pp 905–908, 1997.

[178] J. C. Wyant, "Use of an ac hetrodyne lateral shear interfermeter with real-time wavefront correction systems", *Appl. Opt.*, Vol. **14**, No. 11, pp 2622–2626, November 1975.

[179] Y. Yang, N. P. Galatsanos and H. Stark, "Projection-based blind deconvolution", *J. Opt. Soc. Am. A*, Vol. **11**, No. 9, pp 2401–2409, September 1994.

[180] Y.-L You and M. Kaveh, "A Regularization Approach to Joint Blur Identification and Image Restoration", *IEEE Trans. Im. Process.*, Vol. **5**, No. 3, pp 416–428, March 1996.

[181] Y.-L. You and M. Kaveh, "Blind Image Restoration by Anisotropic Regularization", *IEEE Trans. Image Process.*, Vol. **8**, No. 3, pp 396–407, March 1999.

[182] *Encyclopaedia of Mathematics*, Vol. **2** (C), Kluwer Academic Publishers, Dordrecht, Boston, London, 1988.

[183] *The Oxford English Dictionary*, Vol. **V** (H-K), Oxford University Press, 1961.

[184] *The decade of discovery in Astronomy and Astrophysics*, National Academy Press, Washington D.C., 1991.